SYNTHESIS, CHARACTERIZATION AND IN-VIVO TESTING OF PHOTOACTIVATABLE INSULIN DEPOTS FOR CONTINUOUSLY VARIABLE AND MINIMALLY INVASIVE INSULIN DELIVERY

A DISSERTATION IN
Pharmaceutical Sciences and
Chemistry

Presented to the faculty of the University
of Missouri-Kansas City in partial fulfillment of
the requirements for the degree

DOCTOR OF PHILOSOPHY

by
BHAGYESH R. SARODE
B.Pharm., Institute of Chemical Technology, India, 2011

Kansas City, Missouri
2019

SYNTHESIS, CHARACTERIZATION AND IN-VIVO TESTING OF PHOTOACTIVATABLE INSULIN DEPOTS FOR CONTINUOUSLY VARIABLE AND MINIMALLY INVASIVE INSULIN DELIVERY

Bhagyesh R. Sarode, Candidate for the Doctor of Philosophy degree

University of Missouri-Kansas City, 2019

ABSTRACT

Proteins are macromolecules involved in a diverse array of functions. Mutations or abnormal levels of proteins are indicated in several diseases. Despite showing early promise, the translation of protein therapeutics into the clinics has been challenging. The stability of these macromolecules, their delivery, and penetration inside the cells have been the main hurdles limiting their true potential. In the dissertation, various strategies to overcome such protein delivery challenges are discussed.

Insulin is a lifesaving peptide for millions of diabetics around the world. Despite significant progress in insulin therapies, the quality of life in diabetics is constrained by the burden of multiple daily injections, invasive nature of therapy and inability to control the blood glucose tightly. To address these concerns, we constructed a photoactivatable insulin depot (PAD). In the approach, an insoluble depot of modified insulin was created by linking insulin covalently to photolabile caging moieties. Transcutaneous irradiation breaks the bond to release insulin from the depot into the systemic circulation. Chapter 3 describes the first successful testing on our PAD technology in diabetic animal models. In Chapters 2 and 4, I describe second-generation materials incorporating more efficient photolabile groups utilizing visible light wavelengths and PAD material with greater

insulin loading. These changes improved the overall performance by several folds when tested *in-vivo*.

Chapter 5 discusses the strategies addressed to deliver siRNA inside cells for effective light-activated RNA interference (LARI). LARI can be used for studying biology and cellular processes.

Once administered, proteins are prone to degradation by ubiquitous proteases, limiting their circulation time and therapeutic effect significantly. Chapter 6 discusses prodrug strategies to temporarily modify proteins to shield them against proteases. We envisioned cross-linking amino acid residues on the surface via small crosslinkers. The tight bridges would hinder proteases from binding to proteins and unwinding the helices preventing their proteolysis. We also attempted integration of this approach to achieve intracellular protein delivery which is another obstacle in protein delivery. Here, the cross-linking was performed via disulfide linkages. The disulfide groups would be reduced once inside the cells, yielding native proteins.

APPROVAL PAGE

The faculty listed below, appointed by the Dean of School of Graduate Studies have examined the dissertation titled "Synthesis, Characterization and In-vivo Testing of Photoactivatable Insulin Depots for Continuously Variable and Minimally Invasive Insulin Delivery" presented by Bhagyesh R. Sarode, candidate for the Doctor of Philosophy degree, and certify that in their opinion it is worthy of acceptance.

Supervisory Committee

Simon H. Friedman, Ph.D., Committee Chair
Department of Pharmaceutical Sciences

Kun Cheng, Ph.D.
Department of Pharmaceutical Sciences

William Gutheil, Ph.D.
Department of Pharmaceutical Sciences

Russell Melchert, Ph.D.
Department of Pharmaceutical Sciences

J. David Van Horn, Ph.D.
Department of Chemistry

TABLE OF CONTENTS

LIST OF ILLUSTRATIONS

Figures Pages

LIST OF TABLES

Tables Pages

ACKNOWLEDGMENTS

My most sincere and deepest gratitude goes to my mentor Professor Simon H. Friedman, whose mentorship and guidance has made this journey possible. I will always be grateful for receiving excellent scientific training under his tutelage. His enthusiasm for science, constant support and encouragement at every stage of my Ph.D. career has made my Ph.D. journey immensely fulfilling and memorable. I am very impressed by his moral principles, philosophies, humbleness, and generosity. The time and efforts taken by Professor Friedman for mentoring us and cultivating a positive learning environment really inspired me towards science.

I would like to sincerely thank my supervisory committee members Prof. William Gutheil, Prof. Kun Cheng, Prof. Russell Melchert and Prof. J. David Van Horn for serving on my committee. I really appreciate their valuable time, suggestions and discussions. I am grateful to Dr. Karen Kover, Pei and Maria for their help in performing the *in-vivo* studies.

I am grateful to my beloved parents, my brother and sister-in-law for their constant love and support without which this journey would have been impossible. I appreciate them for providing me the necessary guidance, resources and steering me in the right direction.

I am very thankful to all the members of the Friedman Laboratory. I thank Nitin for teaching me basic lab procedures from systematically writing lab notebooks to important lab techniques such as assay development, working with radioactivity and peptide synthesis. I thank Piyush and Dipu for guiding and training me in the Insulin Project. I thank Ashish for training me in the LARI project. Along with them, I am

thankful to Karthik, Swetha, Parth and Mayank for collaboration on different projects and interesting scientific discussions. I will always relish the wonderful memories spent with all of them.

I am grateful to Dr. Ashim Mitra and Dr. Dhananjay Pal for training and providing access to the cell culture facility. I would like to specifically thank Dr. William Gutheil for help regarding the mass spectrometry. I would like to thank Dr. Mridul Mukherjee for allowing me to use his gel-doc equipment and Dr. Kun Cheng to use the fluorescent microscope in this lab. I am also thankful to Dr. Celestin Youan for allowing us to use the particle size analyzer. I appreciate administrative help provided by School of Pharmacy staff Joyce Johnson, Sharon Self, Shana Eisentrager, Jeannie Westmoreland, and Tamica Lige. Finally, I am grateful for NIH, NSF and UMKC School of Pharmacy for providing the funding and resources.

I sincerely thank my close friends Vijay, Ashutosh, Chinmay, Kedar, Shivani, Pratik, Akshay, Rajvinder, Sameer, Prajakta, Rachna, Nitish, Navid and Deya for being a positive influence in my life.

Dedicated to my family,

for their love, support, and patience.

CHAPTER 1

INTRODUCTION: PHOTOACTIVATABLE INSULIN DEPOT

Insulin and glucose metabolism

Insulin is a peptide hormone secreted by beta cells of Islets of the pancreas. It plays a pivotal role in the regulation of carbohydrates, fats, and amino acids metabolism as shown in Figure 1. Primarily, it lowers the blood glucose levels by promoting its absorption into liver, fat and muscle cells. It also regulates glucose levels by inhibiting glucose release from the liver.[1]

When blood glucose levels are elevated after carbohydrate-rich meals, insulin restores it to the normal range through several mechanisms by acting on muscle cells, fat cells, and the liver. Insulin promotes the uptake of glucose in muscle cells and fat cells via insulin dependent GLUT-4 transporters. Upon binding of insulin to the cell surface receptor, glucose enters the cell via GLUT-4 transporters by facilitated diffusion. Once inside, glucose gets phosphorylated to glucose-6-phosphate and gets trapped inside. Insulin is then stored in the form of glycogen in the muscle tissues. This way insulin promotes glycogen synthesis. It also aids in decreasing protein breakdown. In fat cells, insulin promotes lipogenesis while inhibiting lipolysis. In the liver, insulin inhibits the release of glucose. There, insulin promotes glycogen synthesis while preventing gluconeogenesis. In the whole body, muscle cells are accountable for 60-70% of insulin-mediated glucose uptake, fat cells 10% and the liver 30%.[2,3] In contrast, the glucose uptake in the brain tissue is not dependent on insulin.[4]

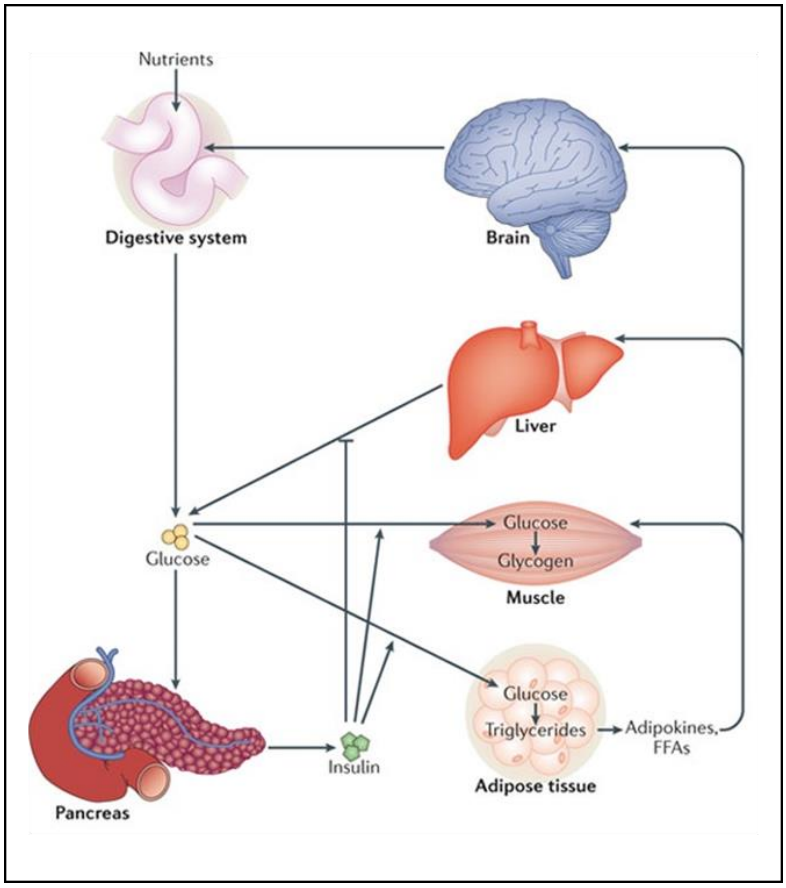

Figure 1: Regulation of glucose metabolism by insulin. Reprinted by permission from Springer Nature.[5]

Insulin structure, its biosynthesis, and secretion

Insulin is a small peptide with a molecular weight of 5808 Da. It is composed of 51 amino acids (AA), chain A is made up of 21 AA, and chain B consists of 30 AA as shown in Figure 2. Three disulfide bridges are present among cysteine residues. Insulin structure is highly conserved across many different species in nature. Several AA residues on both chain A and B are involved in the binding of insulin to its receptor.[6] Although insulin is a 51 AA peptide, the peptide that is translated from the insulin gene is 110 AA long, known as preproinsulin. Preproinsulin is converted to proinsulin by the action of an enzyme which

cleaves a signal peptide. Proinsulin further undergoes folding, and disulfide linkages are formed by the action of different enzymes.[7] Proinsulin has an additional C chain along with chain A and B. This C-peptide is cleaved by another protease to give mature insulin protein. Glucose is an important molecule which acts as a stimulus for the transcription and translation of insulin.[8]

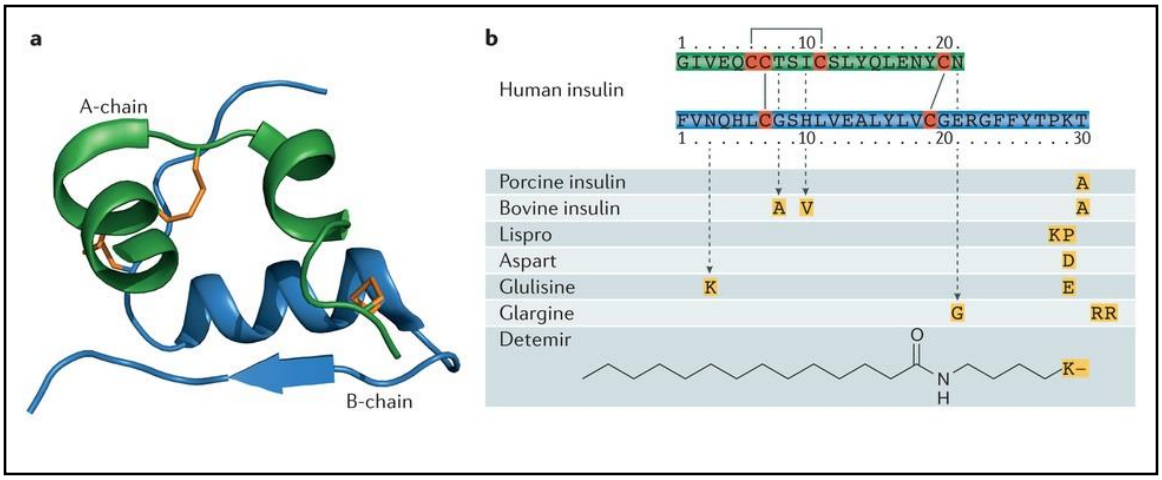

Figure 2: Structure of human insulin. The top segment (on the right) is chain A (21 amino acids), and the bottom chain is chain B with (30 amino acids). The cysteines (in red) are bridged by disulfide linkages. Other insulin analogs with their AA substitutions are also shown. Reprinted by permission from Springer Nature.[9]

Because insulin must be quickly released by the body in response to elevated blood sugar levels, β cells in the pancreas keep insulin stored in the form of insoluble crystalline insulin hexamers. Insulin hexamers are stable due to complexation with zinc cations through histidine residues. The concentration of insulin in the hexamers is approximately 40 mM.[10] Insulin is secreted from the β cells mainly in response to increased glucose levels but certain amino acids, free fatty acids can also act as triggers (Figure 3). The hormones such as leptin, glucagon-like-peptide-1 (GLP-1) play a role in the regulation of insulin secretion as well. From the β cells, insulin secretion is regulated by glucose concentrations and ATP/ADP balance. The ATP/ADP ratio inside the cells is closely linked with K_{ATP}

channels, which regulate the flux of potassium in the cell. At low glucose concentrations, the K_{ATP} channels allow free outflow of K^+ ions. This outflow of K^+ ions allows the cell to maintain a negative resting potential. However, at high glucose concentrations, more glucose gets metabolized through glycolysis which leads to higher production of ATP. More ATP synthesis leads to higher ATP/ADP ratio. Because K_{ATP} channels are linked with this ATP/ADP ratio, it stops the outflow of K^+ ions. When the channels are stopped, the membrane potential depolarizes, which causes the Ca^{2+} channel to open and release insulin from the vesicles.[10]

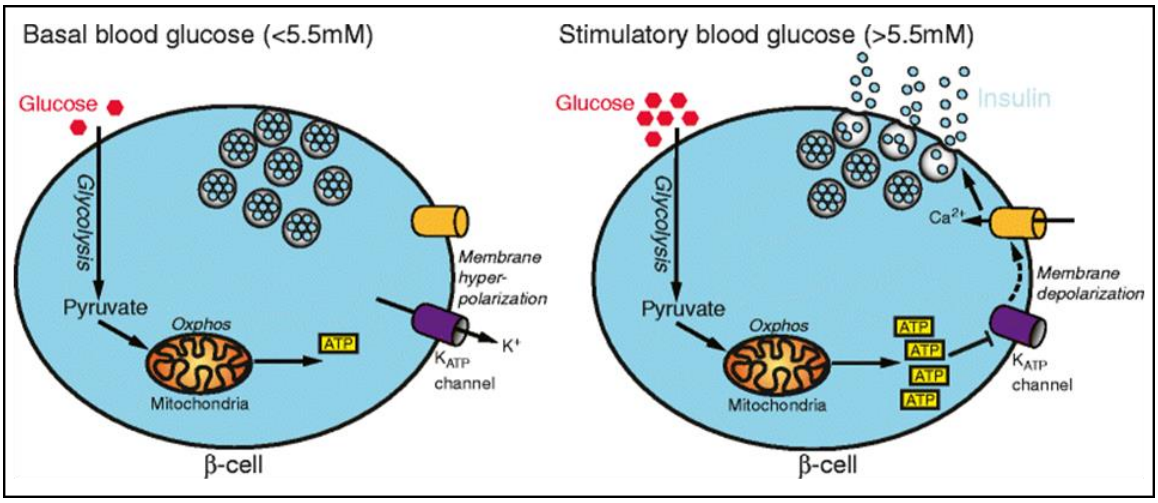

Figure 3: The mechanism of insulin secretion by the β cell of the pancreas in response to glucose. When glucose is at an elevated concentration (right figure), ATP/ADP ratio in the cell is increased which leads to membrane depolarization and release of insulin from the vesicles in the cells.[11]

Insulin is secreted from the β cells in an oscillating manner. There are two types of oscillatory secretory patterns; one is ultradian oscillations which occur over a period of 1-2 hours, and another is through rapid oscillations which occur over a short period of 10-15 minutes.[12] Millions of β cells in the pancreas synchronize insulin secretions so that they are in the same phase of the oscillation. These oscillatory secretions are more efficient in

the regulation of blood glucose than administration of multiple discrete injections of insulin throughout the day. This pattern of pulsatile insulin release is something which could be considered while designing insulin delivery systems. Most of the current insulin delivery systems follow different pharmacokinetic profiles than that of endogenous insulin.[13]

Diabetes mellitus

Diabetes mellitus (DM) is a group of disorders characterized by elevated blood glucose levels for prolonged periods of times. Figure 4 and Figure 5 describe the differences in DM 1 and 2 respectively. DM is caused due to either deficiency of insulin in the body or the resistance to the produced insulin. High glucose concentration in the blood is damaging to many organs and results in a variety of serious complications. Acute complications include diabetic ketoacidosis, coma or death. Long-term complications include diabetic retinopathy, nephropathy, cardiovascular complications, and foot ulcers.[14] A fasting plasma glucose value of 6.1 mM (110 mg dL^{-1}) and above is considered abnormal and in the diabetic range.[15,16]

Type 1 DM is characterized by an insufficient amount of insulin production in the body. The processes which destroy β cells of the pancreatic islets are responsible for type 1 DM. The underlying causes of type 1 DM are not yet fully understood, but the autoimmune system destroys β cells.[17] Lack of insulin results in high blood glucose and complications mentioned above. About 5-10% of the diabetic population has type 1 DM. In the U.S. alone, approximately 3 million people are affected by the type 1 DM.[18] Because insulin is no longer produced in the body of patients, the patient must rely on treatments such as insulin therapies, β cell replacement therapies, and follow special diets, etc.

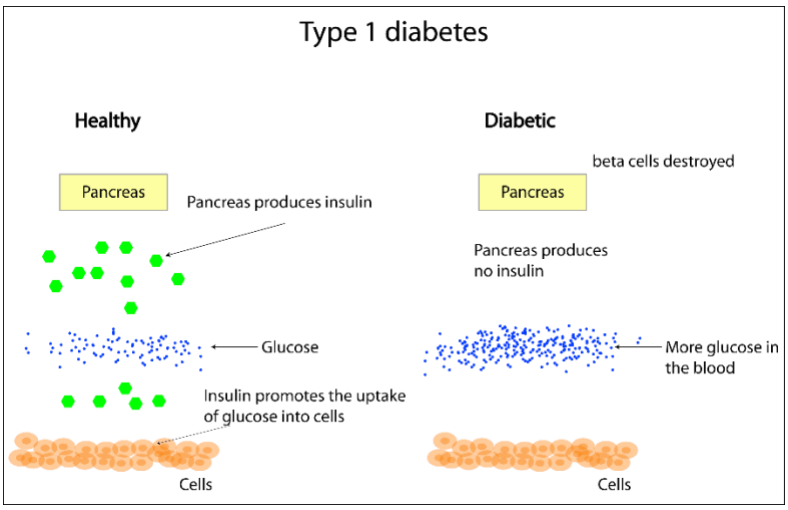

Figure 4: Type 1 diabetes.

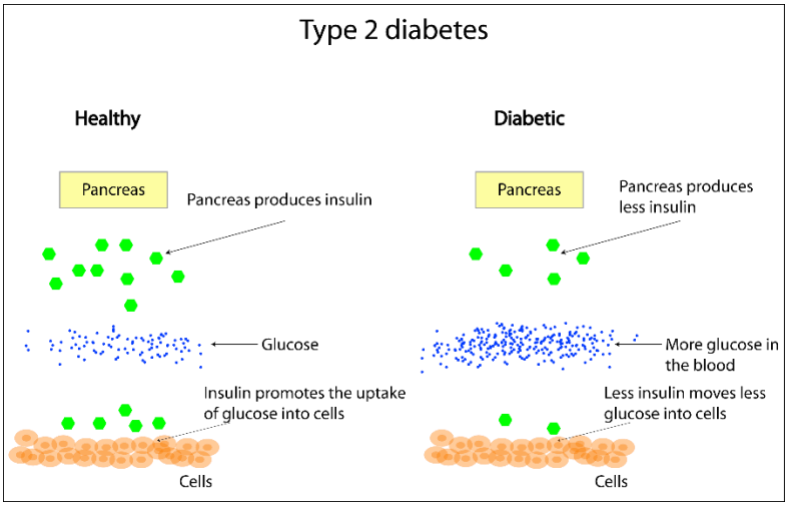

Figure 5: Type 2 diabetes.

Type 2 DM is characterized by insulin resistance, high blood glucose levels and lack of insulin. Both genetic and lifestyle factors can predispose a person towards type 2 DM. Approximately 90% of the total diabetic population suffer from type 2 DM. Complications of type 2 DM include similar disorders – cardiovascular complications, diabetic retinopathy, kidney problems and so forth. The onset of type 2 diabetes can be delayed through regular exercise, physical activity, and proper nutrition.[19]

Insulin analogs

Type 1 diabetes is managed by taking insulin externally as the body fails to secrete an adequate amount of insulin. As insulin is a protein, it undergoes rapid degradation when taken orally. Insulin is degraded by a harsh environment presented by the stomach as well as the presence of ubiquitous proteases present in the gut. Hence it is most commonly injected via the subcutaneous route. A landmark study published in 1993 named Diabetes Control and Complications Trial (DCCT) demonstrated that patients undergoing intensive insulin therapy or using continuous glucose monitoring (CGM) to tightly control blood glucose levels have a significantly lower risk of developing retinopathy, nephropathy, and albuminuria than in patients who rely on traditional insulin therapy.[20]

Along with the invention of recombinant DNA technology, various insulin analogs have been prepared. Insulin analogs are designed to have altered physical and pharmacokinetic properties. Figure 6 describes the pharmacokinetic profiles of various insulin analogs. For example, fast-acting insulin analogs (e.g., Lispro, Aspart) enter bloodstream just within 15-20 minutes after administration. They typically function by preventing insulin aggregation and allowing it to be predominantly in a monomeric form. Aggregated insulin in the form of hexamers is inactive while the monomers are active therapeutically. Mutations in these analogs prevent the hexamers formation and thus directly deliver a larger amount of monomeric insulin quickly in the bloodstream.[21] In addition, long-acting insulin (e.g., Lantus, Degludec) have been developed whose effect could last for more than 24 hours. These formulations typically work by slowing the diffusion of insulin into the body from the site of injection either due to increased protein binding or changes in its isoelectric point. The common mechanism of long-acting insulin

formulations is via complexing insulin with zinc so that it forms insulin hexamers. The hexamers are inactive and dissociate slowly from the depot site to form monomeric insulin molecules. Thus, insulin absorption is delayed, and its effect is prolonged.[21] Similarly, there are intermediate-acting insulin formulations (e.g. NPH insulin). In the clinical settings, different insulins are mixed in optimal proportions and prescribed to patients as per their needs.[22]

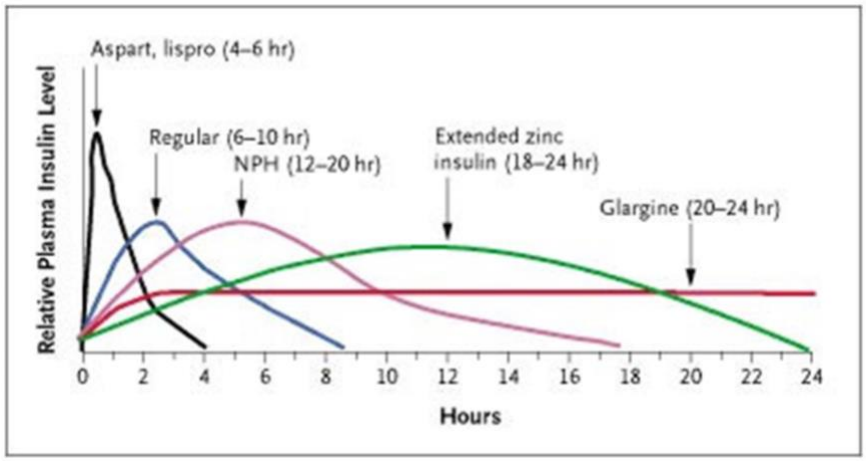

Figure 6: Pharmacokinetic profiles of various insulin analogs. Reproduced with permission from, Copyright Massachusetts Medical Society.[23]

Methods to deliver insulin

Figure 7 shows several different routes and approaches to deliver insulin in the body into the systemic circulation. Most of these routes are being investigated for insulin delivery, but the subcutaneous (SC) route is the most practical way for administration and hence it is being used clinically.

Insulin syringes, insulin pumps, and insulin pens are common devices being used currently for the delivery. Insulin syringe design has undergone several changes over the years. Nowadays, the syringes are smaller, relative pain-free with micro-fine needles, and

easy to use, etc., yet there are still barriers to overcome. For example, the accuracy of the dosage, the frequency of injection is typically 2-3 times a day, and a proper injection technique is required to be learned by the patient, etc.

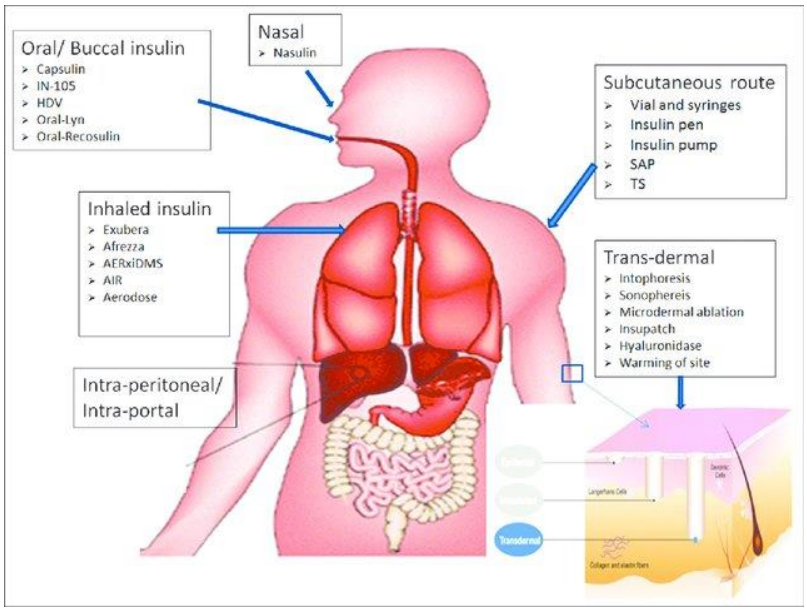

Figure 7: Methods to deliver insulin through different routes.[24]

Insulin pumps are convenient alternatives to insulin syringes. In insulin pumps, a cannula is inserted into the body SC through which insulin can be infused. Tubing is connected to the other end of the cannula which goes inside a reservoir of insulin. The amount of insulin required can be precisely infused using insulin pumps. The main advantage of the insulin pump over insulin injections is that the requirement of multiple daily injections is averted.[25] Several other benefits include precise infusion of the dose (as minimum as a fraction of a unit of insulin), a bolus dose can be planned ahead based on the intake of carbohydrates, supply a continuous and variable amount of insulin, overall increase in the quality of life and it allows flexible lifestyles.[26,27] Unfortunately, insulin pumps have their own limitations – sometimes there is an allergic reaction to the tape or a

scar tissue forms near the site of injection. Much insulin is wasted since pumps require a larger reservoir particularly at the time of changing it. In the case of cannula malfunction or other problems near the site of injection, insulin leakage can occur.[28] We are developing an alternative delivery system which retains the advantages of insulin pumps while eliminating the challenges.

The photoactivatable depot (PAD) approach

To overcome the limitations of syringes and insulin pumps, we have conceived of an idea to deliver insulin in a minimally invasive manner called a photoactivatable insulin depot (PAD). The schematic is in Figure 8. The concept is to make a shallow depot of photolabile insulin in the dermal layer. Here photolabile insulin refers to the insulin that is covalently modified with a photocleavable linker. Upon exposure of light, the photocleavable moiety detaches from insulin and triggers the release of insulin from the site of the depot. Once injected, this depot can be irradiated from the top transcutaneously using an LED. After irradiation on the skin, insulin will be released from the site into the systemic circulation. In the absence of light, no insulin will be released. Since the nature of light penetration through the skin is non-invasive, this approach is minimally invasive as opposed to insulin syringes which require multiple daily injections or a permanently inserted cannula in the case of insulin pumps. In addition, insulin dose can be precisely controlled by controlling the exact number of photons hitting the depot minute-by-minute. The number of photons could be regulated either by changing the light intensity or the duration of exposure. Ultimately the PAD approach can be coupled with continuous glucose monitoring (CGM) to make it into a part of the artificial pancreas. This would ensure continuous and variable supply of insulin which could be controlled minute-by-

minute and could maintain tighter control over fluctuating blood glucose.

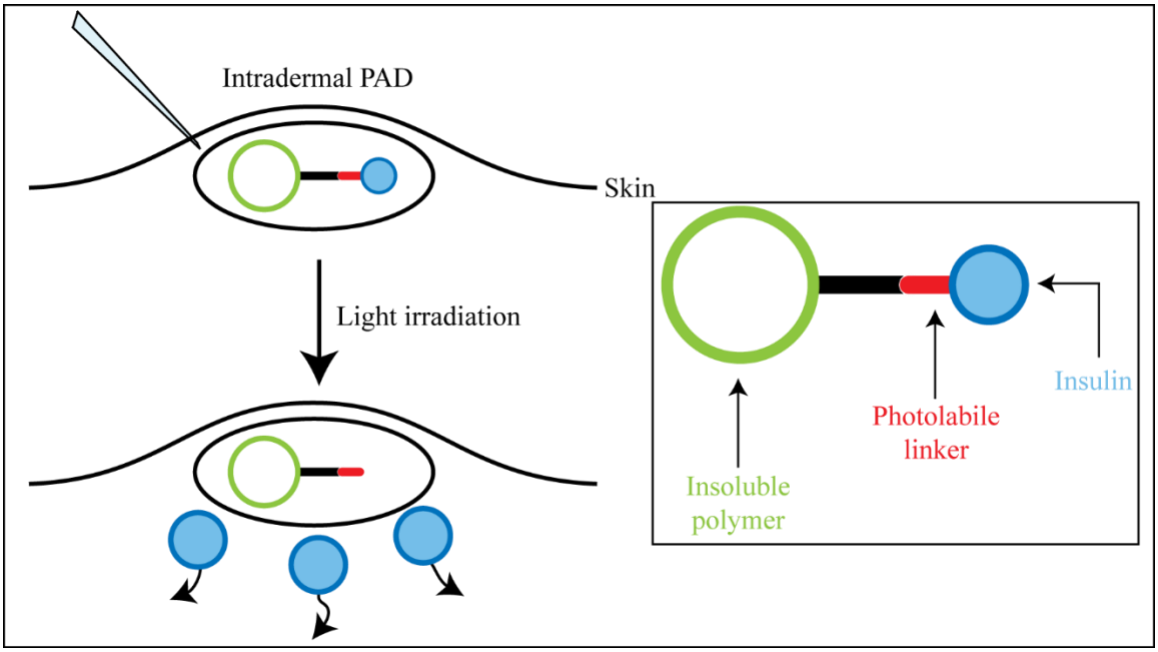

Figure 8: Photoactivatable depot and its components.

The PAD approach provides these benefits over currently available approaches –

i. The depot can hold days' worth of insulin in a single injection; this will reduce the need for the number of daily injections dramatically.

ii. The insulin release is proportional to the amount of light. Hence insulin release can be controlled easily by manipulating light intensity or duration of exposure.

iii. As the blood glucose levels fluctuate frequently, the amount of insulin should vary accordingly. These fluctuations in blood glucose can be minimized by multiple irradiations of the depot based on the knowledge of blood sugar. Insulin syringes have limitations in achieving tight control of blood glucose.

The first-generation material consisted of three parts; an insoluble polymer, a photolabile linker, and insulin.[29] The role of an insoluble polymer is to hold the depot material at the site of injection. Photolabile insulin would otherwise diffuse from the depot

site upon injection. To prevent it from migrating away from the site, it is immobilized on bulky material like an insoluble polymer. Ideally, this polymer would be a biodegradable material which will be degraded once all insulin is used up. The biodegradable polymer could be made up of a non-toxic and biocompatible material such as hyaluronic acid, poly-amino acid polymers or any other natural polymers. The photolabile group could be any chemical group which can be conjugated covalently to insulin and should release insulin by breaking the covalent linkage upon absorption of light of certain wavelengths. Several such photolabile groups have been reported in the literature.[30]

The depot could be injected into an arm or any other convenient site. An LED could be fit into a small belt or pouch which could be wrapped around the depot site. The depot could be injected intradermally rather than subcutaneously. Because an intradermal depot would be shallower than subcutaneous, more photons would be hitting the depot from the top. We suspect that an intradermal depot would help prevent diffusion of PAD material from the injection site due to its thickness. All of these factors would ensure maximum PAD efficiency.

Synthesis of first-generation PAD material

For the synthesis of first-generation material, mainly two approaches were pursued as shown in Figure 9. Divergent synthesis, in which, the chemistry was performed on an insoluble polymer to conjugate a photolabile group in the first step. Then in the final step insulin was conjugated to the photolabile group. In contrast, in the convergent synthesis approach, insulin was conjugated (caged) with the photolabile group first. Then this caged insulin was immobilized onto the polymeric material. Both routes were explored in our lab. Each approach had its own challenges and advantages.

The rationale for pursuing the divergent approach was as follows –

i. Insulin is required only in the final synthetic step. This reduces the total quantity of insulin required during synthesis as it is being utilized only in the last step.
ii. The chances of denaturation of insulin are reduced.
iii. Since there are no tedious purification steps involved in the solid phase synthesis, the synthesis takes lesser time to finish.
iv. This approach could be utilized directly for other protein molecules as well without further optimization.

On the other hand, convergent synthesis has its own merits -

i. Here caged insulin is easy to synthesize. The lab has expertise in conjugating photolabile groups with nucleic acids, the same chemistry was extended towards proteins and peptides. Caged insulin can be studied and characterized to determine photocleavage kinetics, the exact site of caging on insulin and the total number of modification.
ii. Furthermore, distinct caged insulin species can be readily purified using HPLC,

characterized and used in subsequent reactions as required.

iii. Because the material can be purified at each step, reactions are cleaner and can be analyzed at each step. The main disadvantage is that much insulin gets wasted during each step and purification. It also increases its chances of undergoing denaturation like any other protein and may render it inactive by the final step. The material and chemical groups selected here will be discussed first followed by each of the approaches in details.

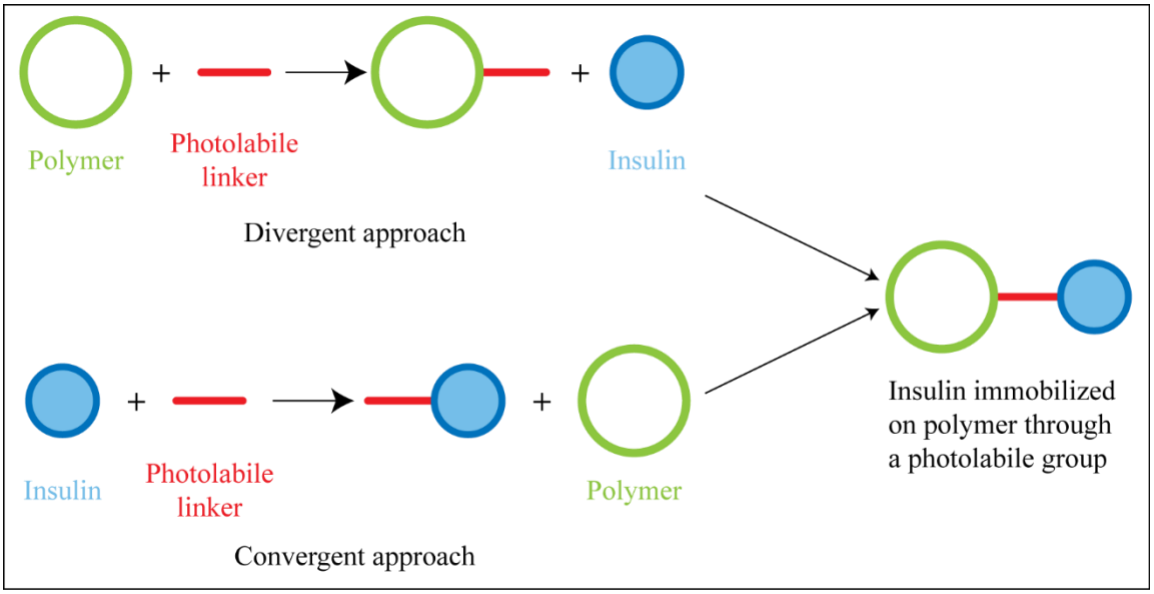

Figure 9: Synthetic approaches attempted for first-generation materials.

To start this synthesis, we decided to use solid phase synthesis (SPS) resin as an insoluble polymer. The solid phase resin offers the following advantages, and hence it was chosen: i) The SPS chemistry has been well refined over the years to give high yielding reactions. ii) These resins have higher surface/volume ratio; loading density is much greater and hence more insulin can be immobilized on the resin. iii) Many kinds of chemical reactions have been shown to work on a solid phase.[31] Traditionally polystyrene has been the material of choice for synthesis. However, polystyrene is neither tolerable when

injected into the body, nor it is biodegradable. Hence other alternative such as chitosan, sepharose, cellulose, etc. were considered but synthesis turned out to be challenging with them. Hence, for the synthesis of PAD material, polyethylene glycol (PEG) based resin had been used. PEG rink amide resin is sold under brand name ChemMatrix® (PCAS BioMatrix Inc, Catalog number 7-600-1310) shown in Figure 10.

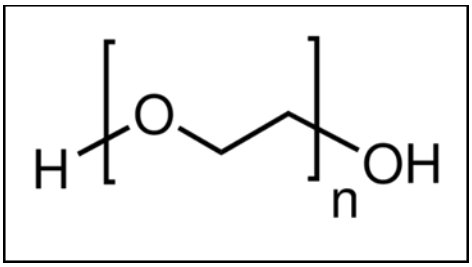

Figure 10: Structure of polyethylene glycol. ChemMatrix resin is made up of cross-linked PEG.

The Friedman laboratory has used O-nitrobenzyl group (Figure 11) extensively in the past for the application of light-activated RNA interference.[32–35] 1-(4,5-dimethoxy-2-nitrophenyl)ethyl (DMNPE) was based on the work reported by C. Holmes.[36] An ortho-nitro group is responsible for DMNPE's photocleaving properties. It has been coupled to insulin using an ester linkage which undergoes cleavage upon irradiation. Ester linkage can be formed using diazo which reacts with a carboxylic acid of insulin. Insulin has a total of six carboxylic acid groups – two terminal and four from glutamic acid side chains.

Both the approaches, synthetic routes and the work performed in the lab previously is described below.

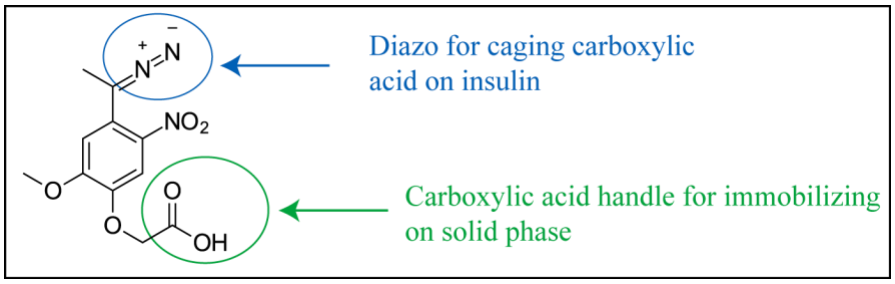

Figure 11: Structure of the bifunctional photolabile group. Diazo is used for conjugation with insulin, and the carboxylic acid side was employed for immobilizing it on the solid phase.

Divergent approach

In the divergent approach as shown in Figure 12, the synthesis was initiated by modifying ChemMatrix resin with a spacer linker such as 6-aminohexanoic acid. The spacer was added to increase the distance between insulin and the resin surface and to prevent overcrowding and steric issues. The second step was to conjugate (4-Acetyl-2-methoxy-5-nitrophenoxy)acetic acid (commonly referred to as nitro keto acid (NKA) in the lab) onto it. The aim was to convert ketone from NKA into the reactive diazo via hydrazone route. The synthesis up to the hydrazine step was successfully carried out previously on both polystyrene and ChemMatrix resin (unpublished data). The next step was to oxidize hydrazine to diazo using an oxidizing agent like MnO_2. The oxidation, when carried out in the solution phase, takes approximately 45 minutes and MnO_2 can be removed easily by filtration. However, when attempted on the solid phase, the reaction failed, and the separation was tedious as tiny MnO_2 particles remained bound to the resin tightly and couldn't be washed off. Hence the synthesis scheme was slightly modified using tosyl hydrazone in which MnO_2 is not required. Here, the ketone can be converted first into a tosyl hydrazone. This hydrazone can be converted into diazo using trimethylamine

(TEA).[37] In this case, both tosyl hydrazone and TEA can be washed off easily from the resin, unlike MnO_2.

This reaction between insulin and diazo formed through tosyl hydrazone route worked successfully only once and wasn't reproducible. The exact mass of the insulin conjugate was observed in the mass spectrometer (MS) upon completion of all reactions and post-TFA cleavage but it couldn't be reproduced afterward. Because of the following issues, this wasn't pursued further –

i. The final reaction of conjugation with insulin was not reproducible, and the yield was minimal.
ii. The insulin conjugate was not very stable, and some amount of free insulin was also observed along with the mass of the conjugate.
iii. The conversion of the ketone to hydrazone in the third step was very slow, and it took almost a week for reaction completion. As an alternative to TEA, peroxyacetic acid was also used as a reagent for conversion of hydrazone to diazo. Peroxyacetic acid was successful in diazo transformation in the solution phase but failed when attempted on the solid phase.

At this point, because the diazo approach was not yielding any promising results, it was decided to use other functionality to cage insulin. Instead of carboxylic acid groups, amines can also be utilized for this purpose as shown in Figure 13. The amino group can be conjugated to an alcohol functionality through a carbamate ester linkage using 1,1'-carbonyldiimidazole (CDI). The primary amine of B29 lysine of insulin is suggested to be reactive and we thought that this amine could be targeted.[38] The ketone from NKA can be converted into primary alcohol by a reducing agent like $NaBH_4$. This reaction was a very

high yielding reaction and was completed with 3-4 hours. However, in the final step, the carbamate ester could not be formed with insulin on the solid phase. When a small molecule containing a primary amine was used as a substitute for insulin, the reaction was successful with higher yields. Significant efforts were put by varying reactions conditions – solvents, pH, concentrations, temperatures, timings, but no reaction was observed with insulin. It was suggested that maybe the amines on insulin are less accessible or less reactive. In summary, the first approach failed for immobilizing insulin on the resin. Perhaps it would be useful to review literature related to the conjugation of insulin using amines. It might provide helpful insights into why this route did not work and possible solutions.

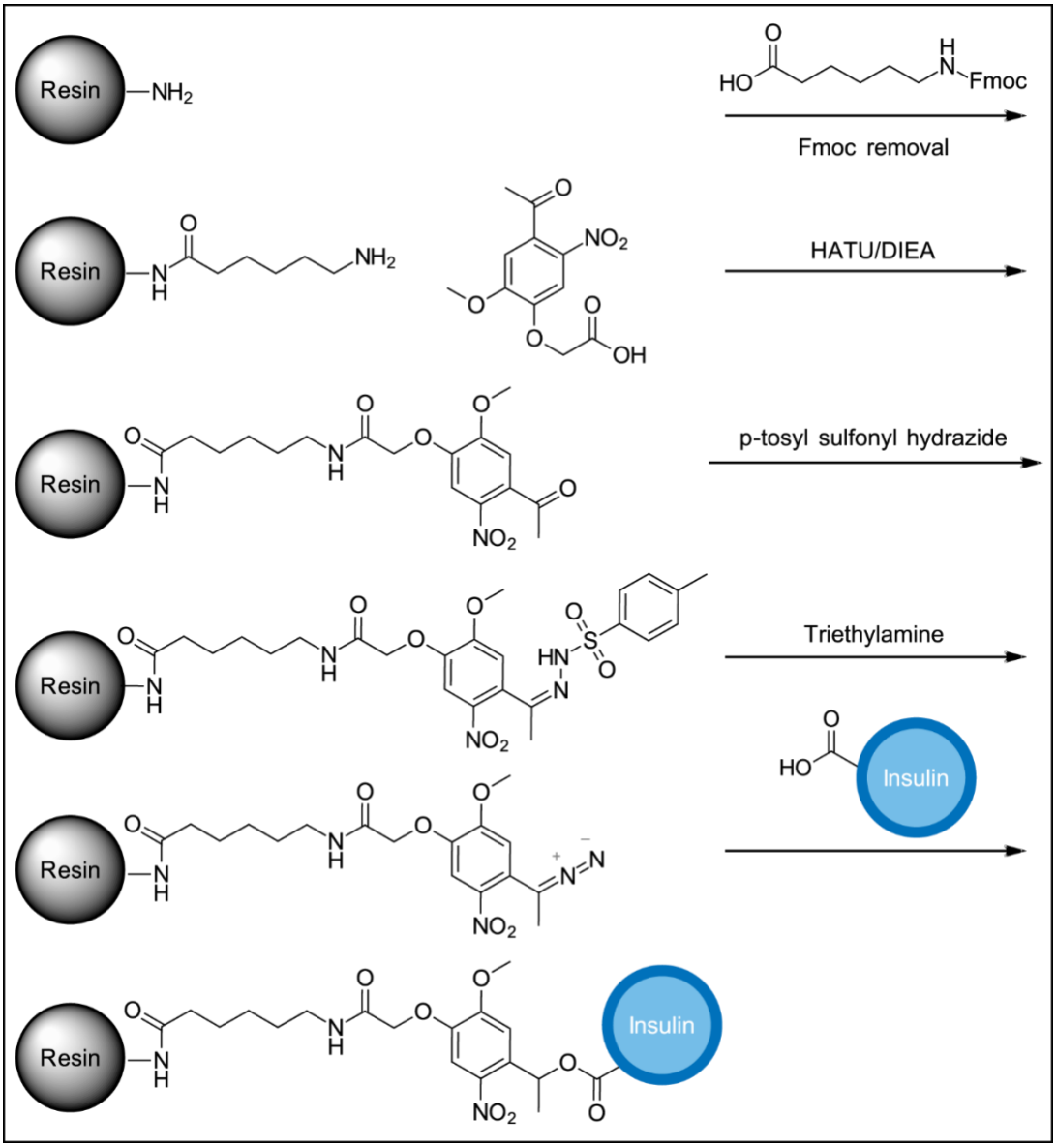

Figure 12: Immobilization of insulin on the resin through the diazo route.

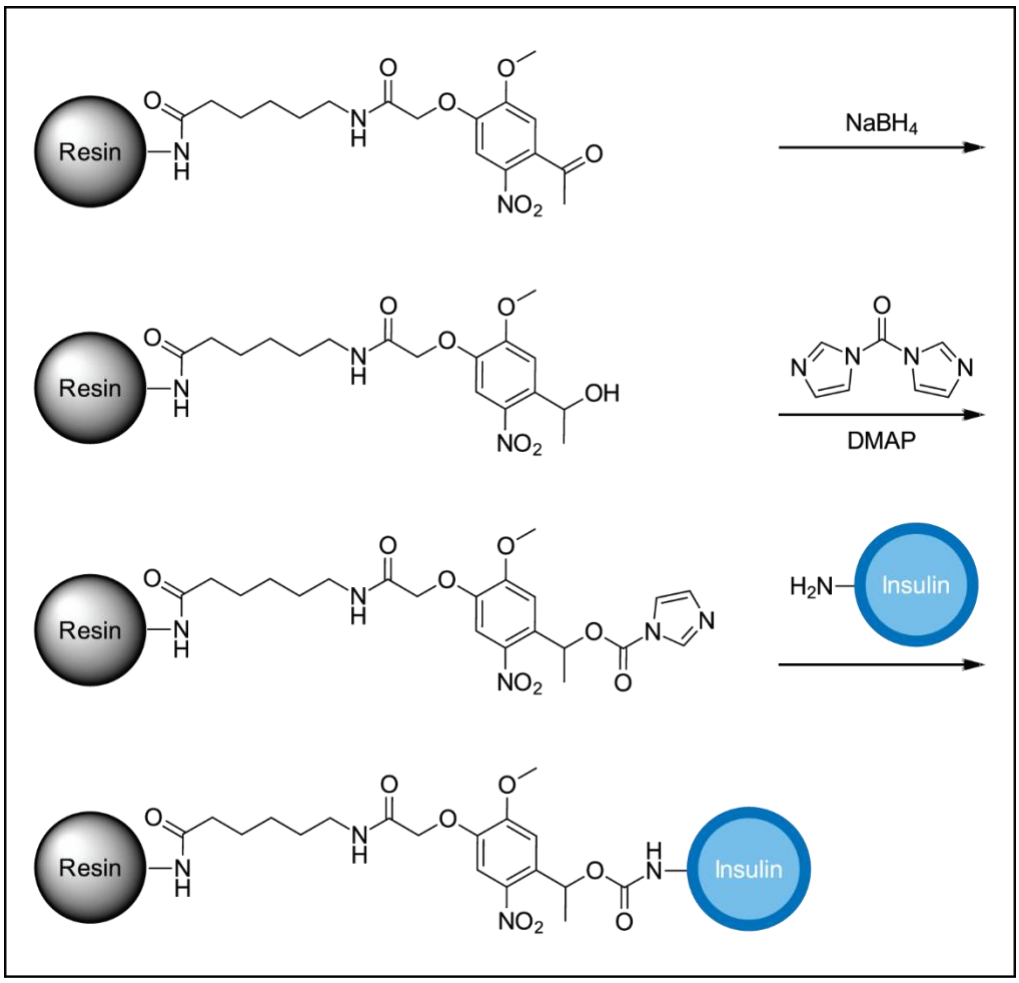

Figure 13: Insulin immobilization through the imidazole carbamate route. It is a modification of the synthetic route shown in Figure 12.

Convergent approach

In the convergent approach (Figure 14), insulin was first caged using DMNPE diazo in the solution phase. This formed conjugate was then immobilized on the resin. This work has been successfully confirmed in the lab.[29] To immobilize caged insulin on the resin, click chemistry was used. The click reaction utilized was first reported by the Bertozzi lab and readily takes place between an azide and an alkyne; it could be carried out with or without requiring any catalysts.[39] Insulin was caged using the photolabile group bearing an

azide functionality. This azide can be conjugated to the resin bearing alkyne functionality through a triazole linkage. First copper was used for the catalysis, but Cu-assisted click chemistry was unsuccessful. Hence copper-free click chemistry was used with a strained alkyne, dibenzo cyclooctyne (DBCO) in this case.[40] The synthesis scheme is outlined in Figure 14. Briefly, NKA was first conjugated to a bifunctional PEG-based linker having an azide group (which will be used for the click chemistry). Then, ketone was converted to diazo via hydrazone route. Once the diazo was formed, it was reacted with insulin to give conjugated insulin, named, DMNPE insulin mono-azide (DIMA). DBCO acid was coupled to resin first and then allowed to react with DIMA via click reaction to yield resin bound insulin. The immobilized insulin was characterized by two methods – one by performing TFA cleavage of the entire construct and analyzing it by MS, and secondly by performing photolysis of the resin bound conjugate to show the release of native insulin. Both treatments yielded correct masses when analyzed by mass spectrometry. For the irradiation experiment, the light of 365 nm wavelength was used. In one experiment, this material was subjected to alternating periods of light and darkness – as there was no leaching of insulin observed from the material which suggested that the release was solely due to the photocleavage. When the material was irradiated with alternating periods of illumination and darkness, no insulin was released in the dark; the release was seen only in the lit-state. The dark/light alternate release pattern is very crucial and relevant to the real-life application because insulin should only be released from the depot when the body needs it in response to rising glucose levels. It should not be released during the dark period, i.e., when it is not being irradiated. In Chapter 3, we will discuss attempts to test the i-PAD hypothesis in an animal model.

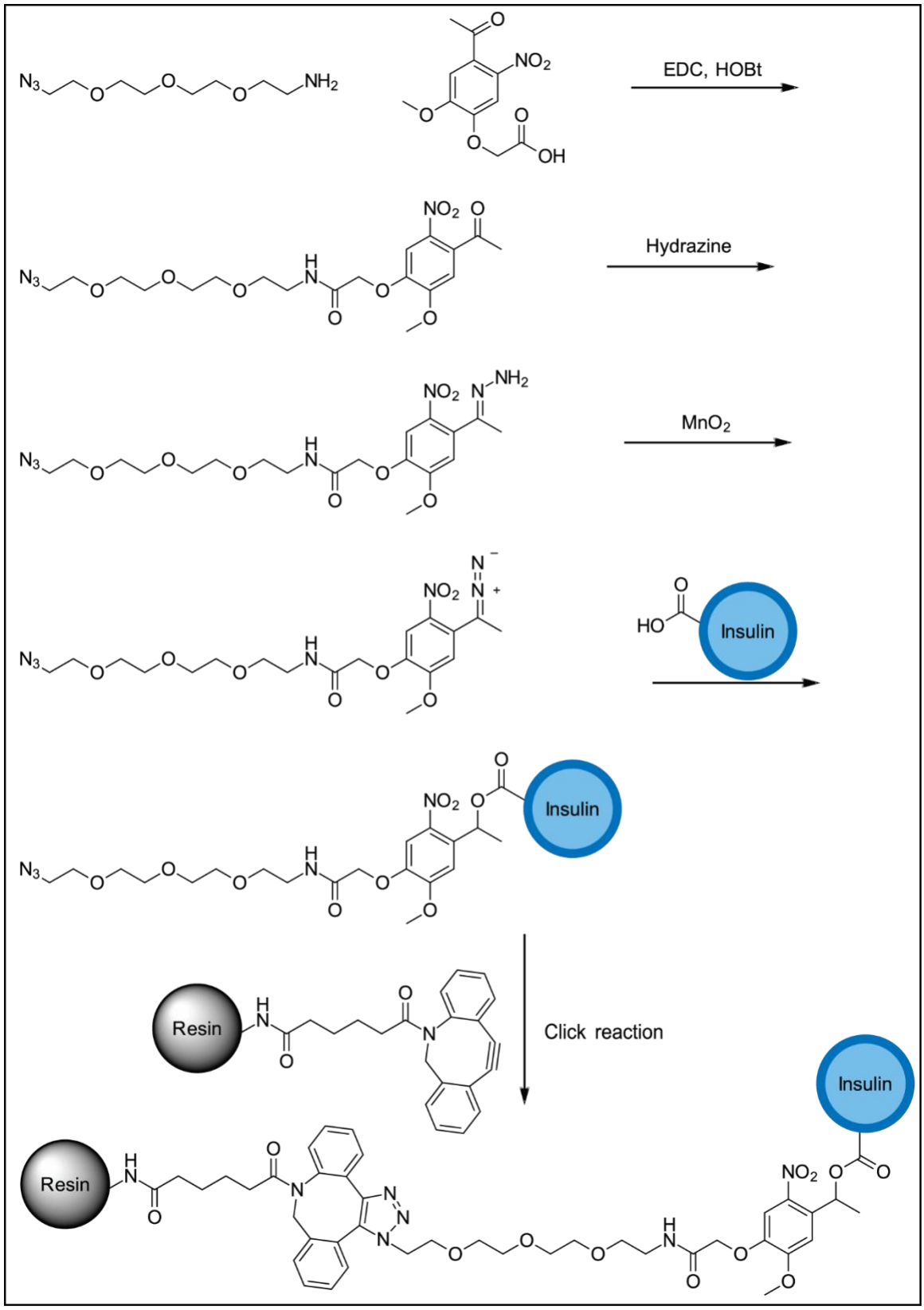

Figure 14: The convergent approach of insulin immobilization.

CHAPTER 2

SYNTHESIS OF INSULIN MACROPOLYMER

What were the limitations of first-generation PAD material?

The first-generation material here refers to the material described earlier and is published from this lab.[29] It involves immobilizing caged insulin on an insoluble polymer. The insoluble polymer chosen in the first-generation material was a PEG-based resin (ChemMatrix®). It was preferred because it has a very high loading density of approximately 0.5 mmol/g, high surface/volume ratio, biocompatibility, and PEG material is FDA approved.[41] It served as a basis for demonstrating the proof of concept that insulin can be tethered onto the resin surface and cleaved specifically using 365 nm light in a controlled manner. However, there were many potential problems with this material –

i. PEG is not biodegradable. Because insulin depot will require repetitive administration, PEG will keep on accumulating at the injection site or in the body elsewhere unless it undergoes biodegradation. Also, because of the larger size of ChemMatrix resin (< 200 µm), elimination from the body would be difficult. PEG is biocompatible and doesn't show toxicity at low doses, but it has a potential for toxicity at higher doses.[42] Accumulation after a few doses would give rise to toxicity as there is no obvious pathway for the clearance of PEG beads.

ii. Insulin density in the final conjugate is very low (<10% w/w). Because the majority of the volume is occupied by the resin, it limits the amount of insulin that can be given in a single injection.

iii. Because of the larger particle size of the resin, it cannot be injected using a conventional 31G needle which is used in insulin syringes. For this, a larger needle

size of 22-23G would be required, which might be painful. It might be challenging to inject depot in thin dermis layer precisely. Because of all these limitations, we started looking for ways how we could prepare PAD material without the need for the solid phase polymer. The insulin macropolymer approach described in Figure 15 was pursued to address these limitations.

The insulin macropolymer approach

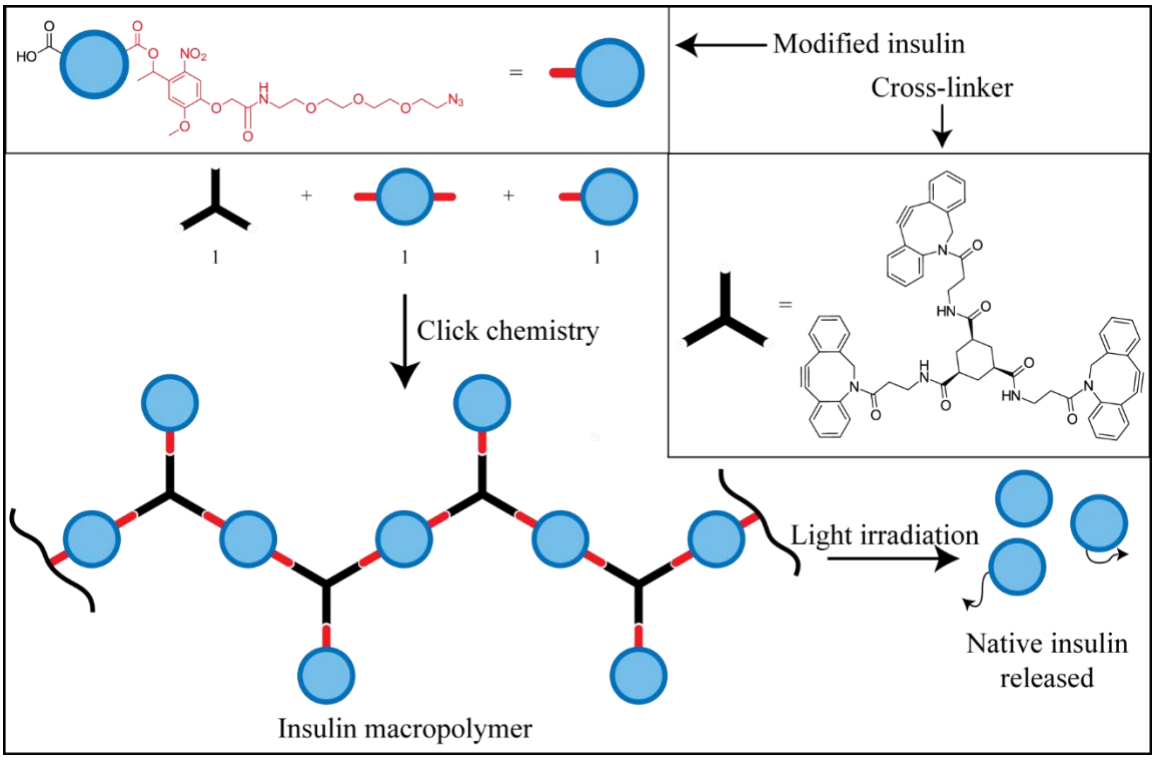

Figure 15: The insulin macropolymer approach.

The insulin macropolymer approach is described above in Figure 15. The idea here was to form a photocleavable polymer made up of insulin where insulin itself acts as a monomer in the polymerization process, hence the name macropolymer. DMNPE insulin mono-azide (DIMA), DMNPE insulin di-azide (DIDA) and a tris-DBCO (TD) linker

containing three strained alkynes were synthesized to achieve this. Mixing them in 1:1:1 proportion, we expected to see random polymerization with higher molecular constructs. We hoped that these constructs would form a precipitate in aqueous solutions because of the higher MW, hydrophobicity and due to aggregation. From this suspension, we expected insulin to be released in a controlled fashion upon light stimulation. The advantages of this approach over first-generation material were the following –

i. It gets rid of the requirement of the resin in the PAD approach. Also, it would eliminate all the problems associated with the usage of the resin and PEG material.
ii. Because the particle size could be controlled while preparing, it would be easily injectable as opposed to bulky ChemMatrix resin.
iii. Because insulin is a monomer in the polymerization process, it will occupy the majority of the mass in the final macropolymer (~ 85% w/w). It would significantly increase insulin density, hence total insulin loading and dose. This strategy would allow injecting more insulin moles per injection.
iv. As a result, the lifetime of the depot would increase significantly.

The principal mechanism of polymerization is via click chemistry. We utilized copper-free click chemistry in our synthesis approach. The click chemistry has been used for making polymers for biomedical applications using small molecules, peptides, proteins, hydrogels, etc.[43] The polymerization attempts using click chemistry have been reviewed extensively in the literature.[44–48]

Synthesis of insulin macropolymer components

In this section, the synthesis of DIMA, DIDA, and tris-DBCO moieties is described. DIMA and DIDA were synthesized as reported earlier in the lab. To cage insulin, DMNPE

diazo azide (DDA) was synthesized first, and its reaction with insulin was optimized to give DIMA and DIDA. Figure 16 outlines the synthetic steps for DDA.

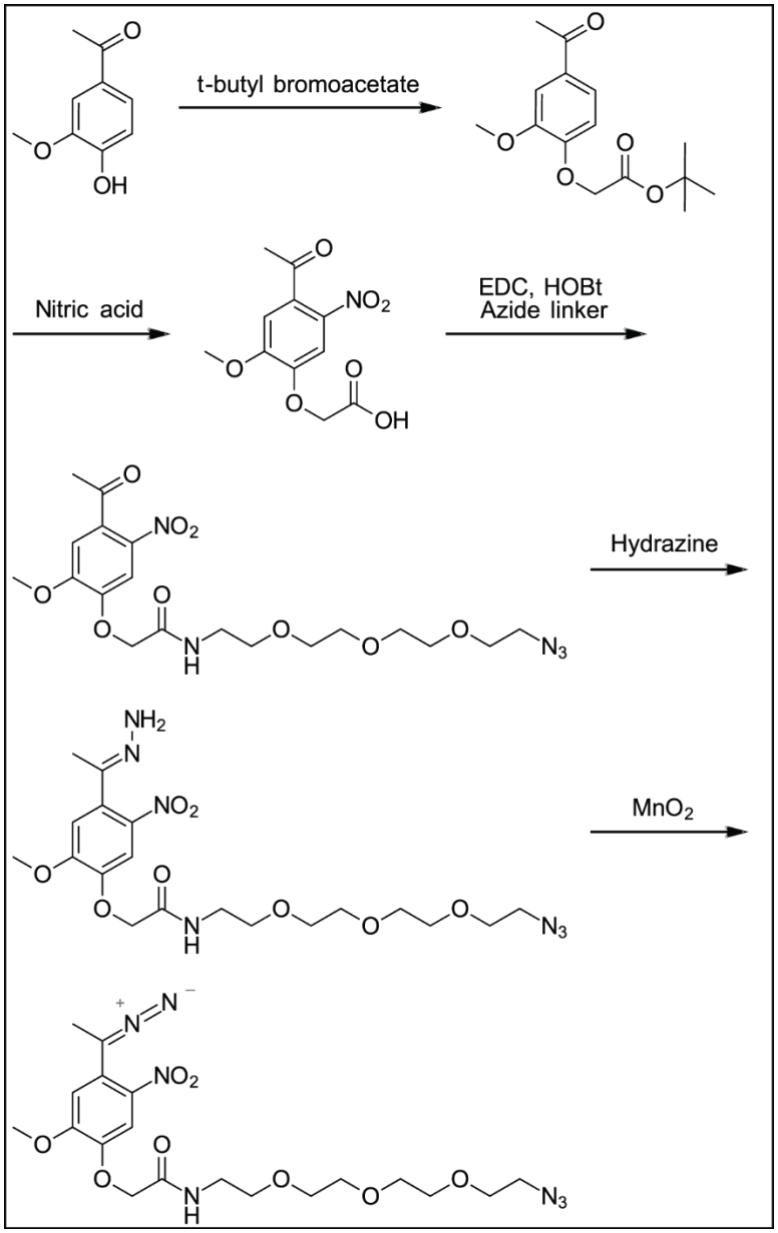

Figure 16: Synthesis of DDA.

Briefly, we started with acetovanillone (Sigma-Aldrich, catalog # A10809). We first alkylated acetovanillone using t-butyl bromoacetate (Sigma-Aldrich, catalog # 124230). The purpose of this step was to introduce a carboxylic acid functionality to turn DMNPE

into a bifunctional caging group. In the second step, nitration was performed to introduce a nitro group which is essential for the photocleavage activity of DMNPE. In the same step, the t-butyl ester hydrolyzed to give a free carboxylic acid. In the third step, an azide moiety was added so that it could be utilized in the click reaction. The conjugation was performed via an amide linkage. In the fourth step, the ketone is converted to hydrazone using hydrazine monohydrate. In the final step, hydrazone was converted to the reactive diazo using an oxidizing agent, MnO_2.

tert-Butyl (4-acetyl-2-methoxyphenoxy)acetate

Acetovanillone (5.25 g, 31.6 mmol), t-butyl bromoacetate (5.1 mL, 34.5 mmol) and K_2CO_3 (7.2 g, 52 mmol) were mixed in a round bottom flask (RBF) and stirred at room temperature for 48 hours in 35 mL DMF. After 48 hours, water was added to dissolve the salts and, partitioned between ethyl acetate (EtOAc) and saturated NaCl. The organic layer was washed once again with saturated NaCl, dried over $MgSO_4$, filtered and dried. Yield = 8.1 g (92%); analytical method – reversed-phase HPLC (flow rate 1 mL min^{-1}, runtime 29 min with 5 min post-run), solvent A (0.1% TFA in H_2O), solvent B (0.1% TFA in ACN), gradient 0% B to 100 % B over 29 min, C18 Hypersil column (5 μm, 250 × 4.6 mm, Agilent), retention time: 18.8 min (Figure 17); ESI-MS (m/z): $[MH]^+$ $C_{15}H_{20}O_5$ calculated for 281.1; found, 281.2 (Figure 18).

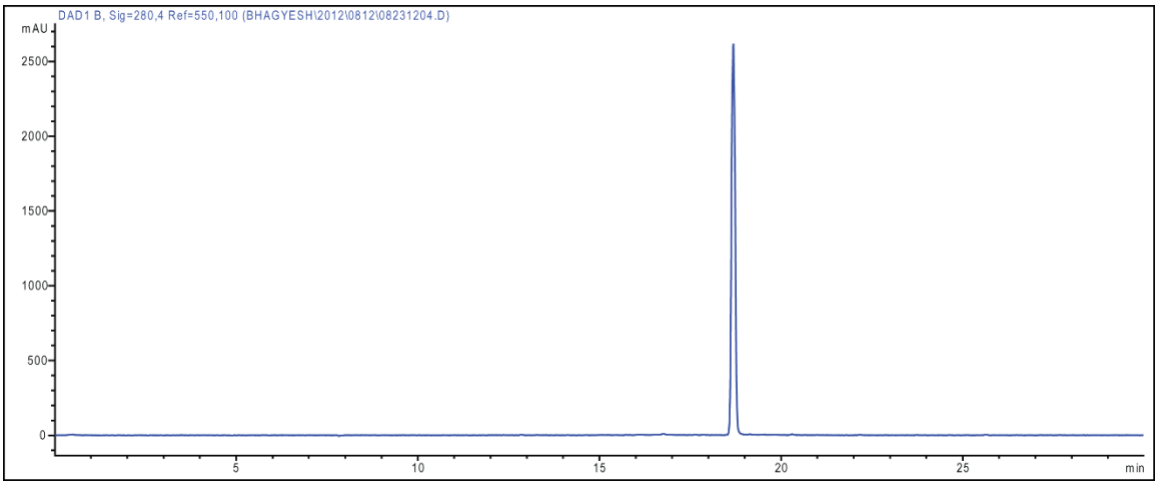

Figure 17: HPLC chromatogram of purified tert-butyl (4-acetyl-2-methoxyphenoxy)acetate.

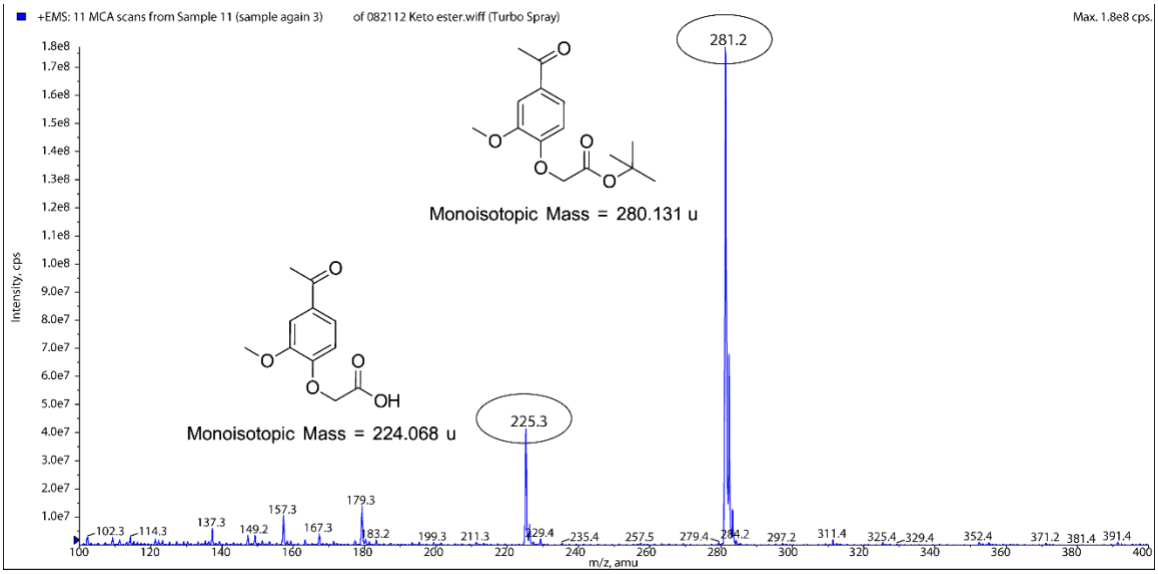

Figure 18: MS of tert-butyl (4-acetyl-2-methoxyphenoxy)acetate $[MH]^+$=281.2, the ester gets fragmented during ionization, the fragmented product is seen at $[MH]^+$=225.3.

(4-Acetyl-2-methoxy-5-nitrophenoxy)acetic Acid (nitro keto acid (NKA))

One gram (3.57 mmol) of ketoester was dissolved in 4.7 mL of acetic anhydride. This mixture was cooled in the fridge before using. Simultaneously, in a 25 mL cold RBF, three mL of 70% nitric acid and two mL acetic anhydride were mixed and kept in ice for

cooling. The chilled solution of keto-ester in acetic anhydride was added to the mixture dropwise. It was kept in an ice bath for the first two hours and then was stirred at room temperature for the next four hours. The precipitate was seen. After a total of 6 hours of reaction, the mixture was transferred to a beaker containing a small amount of ice and kept at 4 °C overnight. Next day, the precipitate was collected by filtration and washed twice with cold water and dried. Yield (0.61 g, 63.5%); ^{1}H NMR (400 MHz, DMSO-d_6); ppm 2.53 (s, 3 H) 3.95 (s, 3 H) 4.91 (s, 2 H) 7.26 (s, 1 H) 7.60 (s, 1 H) 13.3 (s, 1 H, br) (Figure 19); ESI-MS (m/z): $[MH]^+$ calculated for $C_{11}H_{11}NO_7$, 270.1; found, 270.1 (Figure 20).

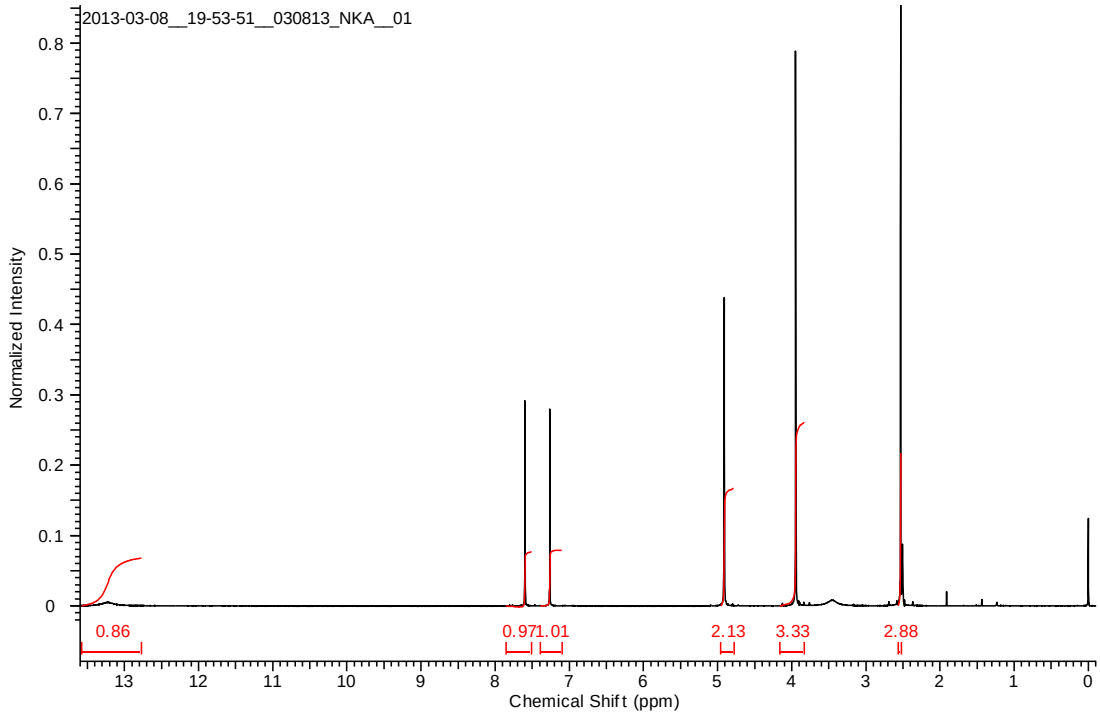

Figure 19: Proton NMR of (4-acetyl-2-methoxy-5-nitrophenoxy)acetic Acid.

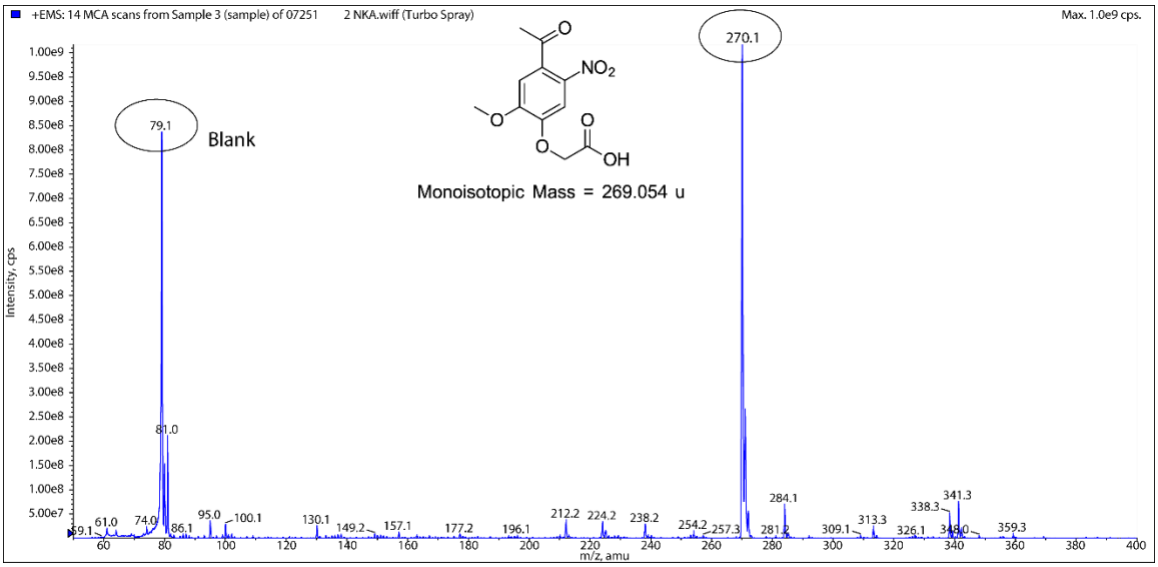

Figure 20: MS of (4-acetyl-2-methoxy-5-nitrophenoxy)acetic acid. The product is seen at $[MH]^+$=270.1

2-(4-Acetyl-2-methoxy-5-nitro-phenoxy)-N-(2-{2-[2-(2-azido-ethoxy)-ethoxy]-ethoxy}-ethyl)-acetamide

NKA (200.8 mg, 748 µmol), 11-azido-3,6,9-trioxaundecan-1-amine (Sigma-Aldrich, catalog # 17758, 150.8 µL, 760 µmol), hydroxybenzotrizole hydrate (Peptide International, catalog # KBT-1021-PI, 226.4 mg, 1.48 mmol) were dissolved in 2.7 mL anhydrous DMF. To this solution, 1-ethyl-3-(3-dimethylaminopropyl)carbodiimide hydrochloride (ThermoFisher Scientific, 245.6 mg, 1.28 mmol) was added. The reaction was run overnight. The crude reaction mixture was partitioned between EtOAc and water. The organic layer was then washed first with saturated $NaHCO_3$, followed by another wash with 1N HCl. Finally, it was washed with a saturated NaCl solution. Then EtOAc layer was dried over $MgSO_4$, filtered and dried using rotavap to obtain a viscous yellow solid. Yield (0.309 g, 89.4%); analytical method – reversed-phase HPLC (flow rate 1 mL min^{-1}, runtime 29 min with 5 min post-run), solvent A (0.1% TFA in H_2O), solvent B (0.1% TFA

in ACN), gradient 0% B to 100 % B over 29 min, C18 Hypersil column (5 µm, 250 × 4.6 mm, Agilent), retention time: 17.9 min (Figure 21); ESI (m/z): $[MH]^+$ calc. $C_{19}H_{27}N_5O_9$ for, 470.2; found, 470.2 (Figure 22).

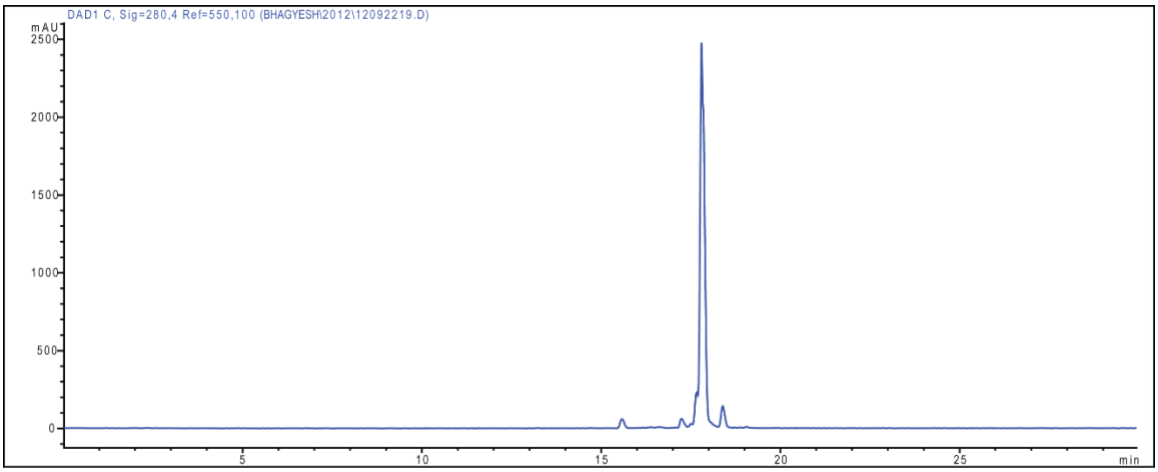

Figure 21: HPLC chromatogram of keto azide.

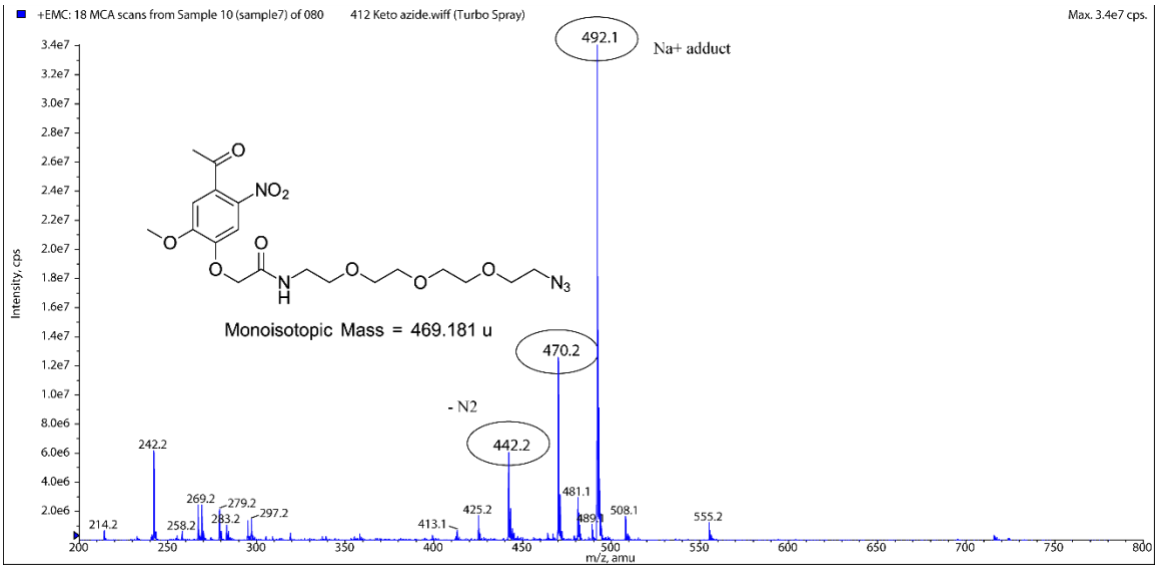

Figure 22: MS of 2-(4-acetyl-2-methoxy-5-nitro-phenoxy)-N-(2-{2-[2-(2-azido-ethoxy)-ethoxy]-ethoxy}-ethyl)-acetamide. The product is seen at $[MH]^+$=470.2.

N-(2-{2-[2-(2-azido-ethoxy)-ethoxy]-ethoxy}-ethyl)-2-[4-(1-hydrazono-ethyl)-2-methoxy-5-nitro-phenoxy]-acetamide

(120 mg, 255.7 µmol) of 2-(4-Acetyl-2-methoxy-5-nitro-phenoxy)-N-(2-{2-[2-(2-azido-ethoxy)-ethoxy]-ethoxy}-ethyl)-acetamide was dissolved in the 9.6 mL mixture of acetonitrile: ethanol (1:1). To this, glacial acetic acid (162.4 µL, 1.42 mmol) and hydrazine monohydrate (Sigma-Aldrich, 162.4 µL, 3.35 mmol) were added. The reaction was performed in a closed sealed vial at 90 °C for 5 hours. After 5 hours, the reaction mixture was evaporated using rotavap. The crude mixture was dissolved in 5% methanol (MeOH) in dichloromethane (DCM) and purified using flash chromatography.

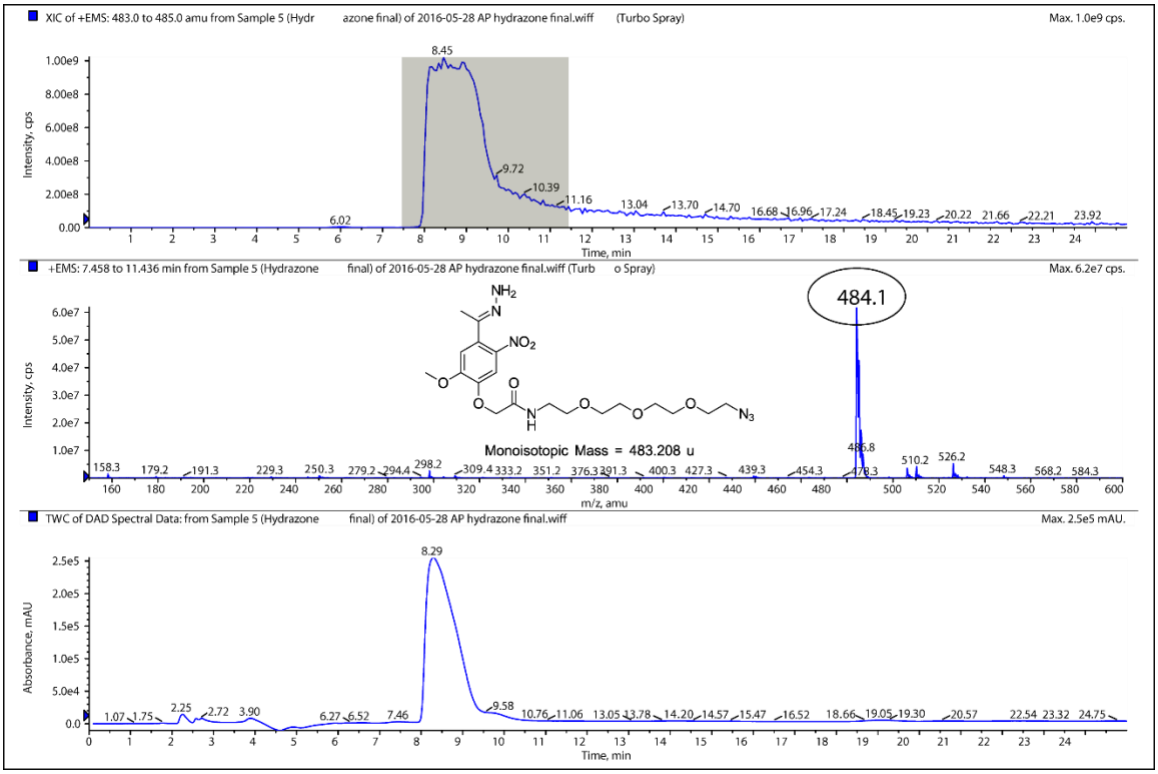

Figure 23: LCMS of N-(2-{2-[2-(2-azido-ethoxy)-ethoxy]-ethoxy}-ethyl)-2-[4-(1-hydrazono-ethyl)-2-methoxy-5-nitro-phenoxy]-acetamide. The product is seen at $[MH]^+$=484.1 at the retention time of 8.29 minutes.

Yield (63.3 mg, 51.2%); TLC (EtOAc/MeOH, 75:25 v/v): R_f = 0.37 and 0.48; analytical method – reversed-phase HPLC-MS (flow rate 0.4 mL min^{-1}, runtime 25 min with 5 min

post-run), solvent A (0.1% FA in H_2O), solvent B (0.1% FA in ACN), gradient 30 % B isocratic over 25 min, C18 Hypersil column (5 µm, 150 × 3.2 mm, Agilent), retention time: 8.29 min; ESI−MS (m/z): $[MH]^+$ calculated for $C_{19}H_{29}N_7O_8$, 484.2; found, 484.1 (Figure 23).

The diazo group is unstable, highly reactive and easily gets hydrolyzed in the presence of water. Hence, it was always prepared immediately before the caging reaction. Depending on the scale of reaction and how many DMNPE per insulin were required, the ratio of insulin: diazo was varied accordingly. Higher the diazo equivalents, more modifications on insulin were seen. The exact yield of hydrazone to the diazo reaction is not yet measured in our lab; the diazo is unstable and it is challenging to measure the yield correctly. It is assumed that this yield is approximately 80% and 1.2 equivalents of hydrazone to insulin were taken instead of 1 equivalent. For the macropolymer approach, we needed only DIMA and DIDA species but no other higher modifications. Hence a series of reactions with varying insulin: diazo ratios were set up and analyzed. The condition which yielded optimum results was selected for this project. The reactions and results are described below.

N-(2-{2-[2-(2-azido-ethoxy)-ethoxy]-ethoxy}-ethyl)-2-[4-(1-diazo-ethyl)-2-methoxy-5-nitro-phenoxy]-acetamide

5 equivalents of diazo for caging insulin

269 µL (100 mM solution in anhydrous DMSO, 26.9 µmol) of N-(2-{2-[2-(2-Azido-ethoxy)-ethoxy]-ethoxy}-ethyl)-2-[4-(1-hydrazono-ethyl)-2-methoxy-5-nitro-phenoxy]-acetamide was mixed with 26.8 mg MnO_2 and vortexed for 45 min in the dark. The red-black mixture was centrifuged, and the supernatant was filtered through Celite 545

using glass-wool/glass-pipette. The pipette was washed with anhydrous DMSO thrice to get a final volume of 870 µL. The successful diazo conversion was indicated by red color formation. In another tube, 25 mg (4.3 µmol, Sigma-Aldrich, catalog # SAFC-91077C) of insulin was dissolved in 1 mL of anhydrous DMSO. The filtered diazo solution was added to insulin. The volume was made up to 2.15 mL by adding DMSO to make the final concentration of insulin 2 mM. The reaction was performed in the dark for 24 hours. After 24 hours, DMSO was evaporated using freeze-drying. The dried residue was dissolved in 0.01N HCl. This solution was analyzed using HPLC. The fractions were collected from HPLC and infused into MS to determine how many DMNPE groups were conjugated per insulin molecule. Analytical method – reversed-phase HPLC (flow rate 1 mL min^{-1}, runtime 29 min with 5 min post-run), solvent A (0.1% TFA in H_2O), solvent B (0.1% TFA in ACN), gradient 0% B to 100 % B over 29 min, C18 Hypersil column (5 µm, 250 × 4.6 mm, Agilent). The results are shown in Figure 24.

2x diazo + insulin caging

107 µL (100 mM solution in anhydrous DMSO, 10.75 µmol) of N-(2-{2-[2-(2-Azido-ethoxy)-ethoxy]-ethoxy}-ethyl)-2-[4-(1-hydrazono-ethyl)-2-methoxy-5-nitro-phenoxy]-acetamide was mixed with 11 mg MnO_2 and allowed to vortex for 45 min in dark. The diazo was filtered using a celite-glass wool filter. Insulin (25 mg, 4.3 µmol) was dissolved in 1 mL anhydrous DMSO. The diazo with a total volume of 0.78 mL after filtration was mixed with insulin solution and diluted to make a volume of 2.15 mL and insulin concentration was 2 mM. The mixture after 24 hours of the reaction was processed as mentioned above and filtered through 5 kDa MWCO filters. The numbers of modifications were determined by running it on HPLC, collecting HPLC fractions and

infusing individual fractions in MS. The HPLC method was slightly modified to run on a semi-prep column to purify in larger quantity. Purification method – reversed-phase HPLC (flow rate 2 mL min^{-1}, runtime 45 min with 5 min post-run), solvent A (0.1% TFA in H_2O), solvent B (0.1% TFA in ACN), gradient 0% B to 75 % B over 45 min, C18 Hypersil column (5 μm, 250 × 10 mm, Phenomenex). The data are shown in Figure 25.

Two equivalents of diazo yielded optimum results – this ratio produced only DIMA and DIDA and no higher modifications on insulin. Since we wanted only these two species for macropolymer, this ratio was used in subsequent syntheses to cage insulin at 0.1-0.2-gram scale to obtain larger quantities of DIMA and DIDA. The concentration of insulin was kept the same at 2 mM whether it was performed on a smaller or larger scale. The DIMA and DIDA were purified by multiple HPLC runs, and the fractions were combined. Final stock solutions were prepared in DMSO.

DIMA and DIDA characterization

DIMA Analytical method – reversed-phase HPLC (flow rate 1 mL min^{-1}, runtime 30 min with 5 min post-run), solvent A (0.1% TFA in H_2O), solvent B (0.1% TFA in ACN), gradient 0% B to 100 % B over 30 min, C18 Hypersil column (5 μm, 250 × 4.6 mm), retention time: 18-19 min (Figure 26); ESI-MS (m/z): $[M]^+$ calculated for, 6262.0; found, 6259.0 (Figure 27); Extinction coefficient (at 280 nm) = 8400 $M^{-1}cm^{-1}$.

DIDA Analytical method – reversed-phase HPLC (flow rate 1 mL min^{-1}, runtime 30 min with 5 min post-run), solvent A (0.1% TFA in H_2O), solvent B (0.1% TFA in ACN), gradient 0% B to 100 % B over 30 min, C18 Hypersil column (5 μm, 250 × 4.6 mm), retention time: 18-20 min (Figure 28); ESI-MS (m/z): $[M]^+$ calculated for, 6714.0; found, 6712.0 (Figure 29); Extinction coefficient (at 280 nm) = 11700 $M^{-1}cm^{-1}$.

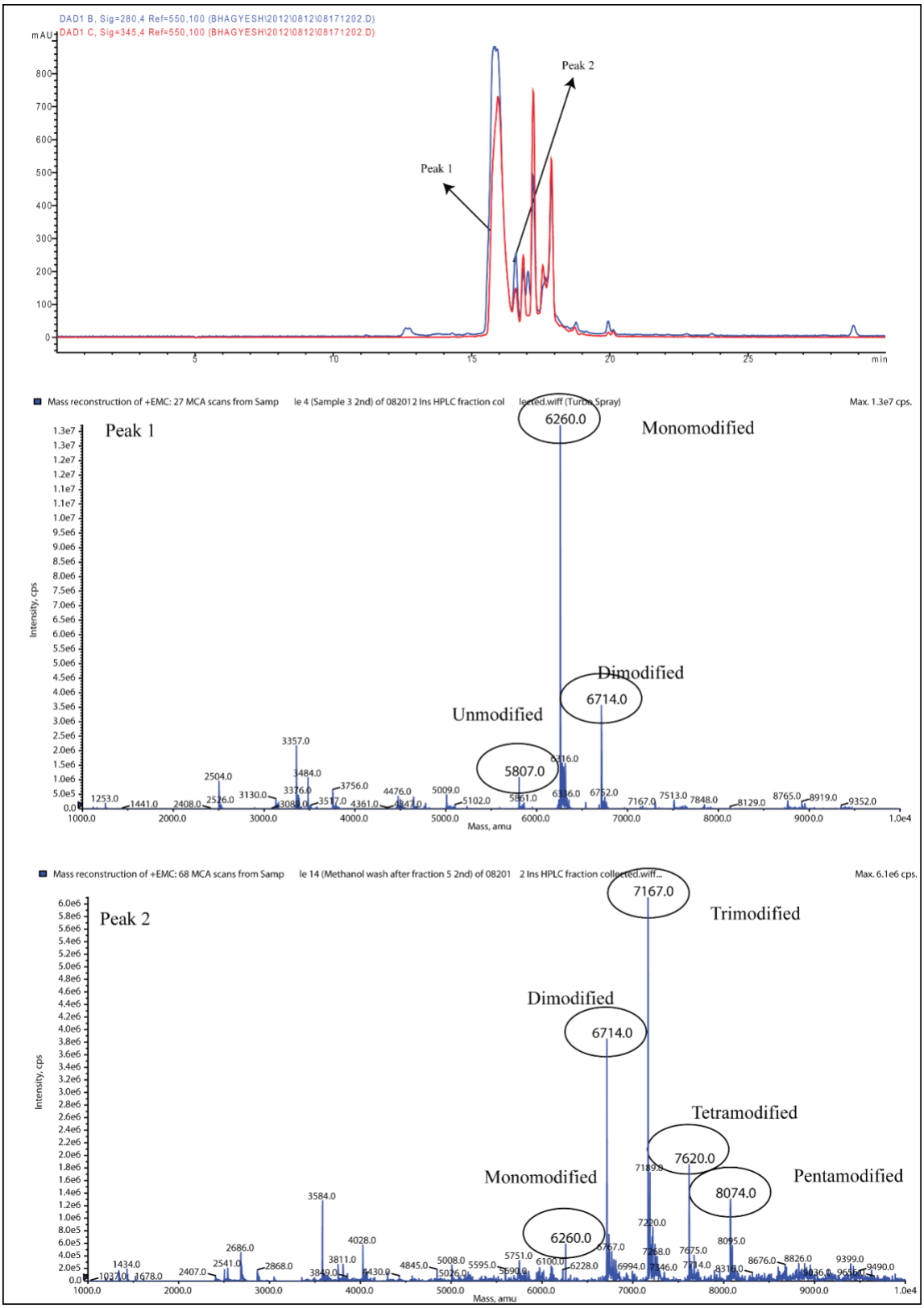

Figure 24: HPLC of crude mixture 5:1 (diazo: insulin) reaction and MS infusion of collected individual fractions.

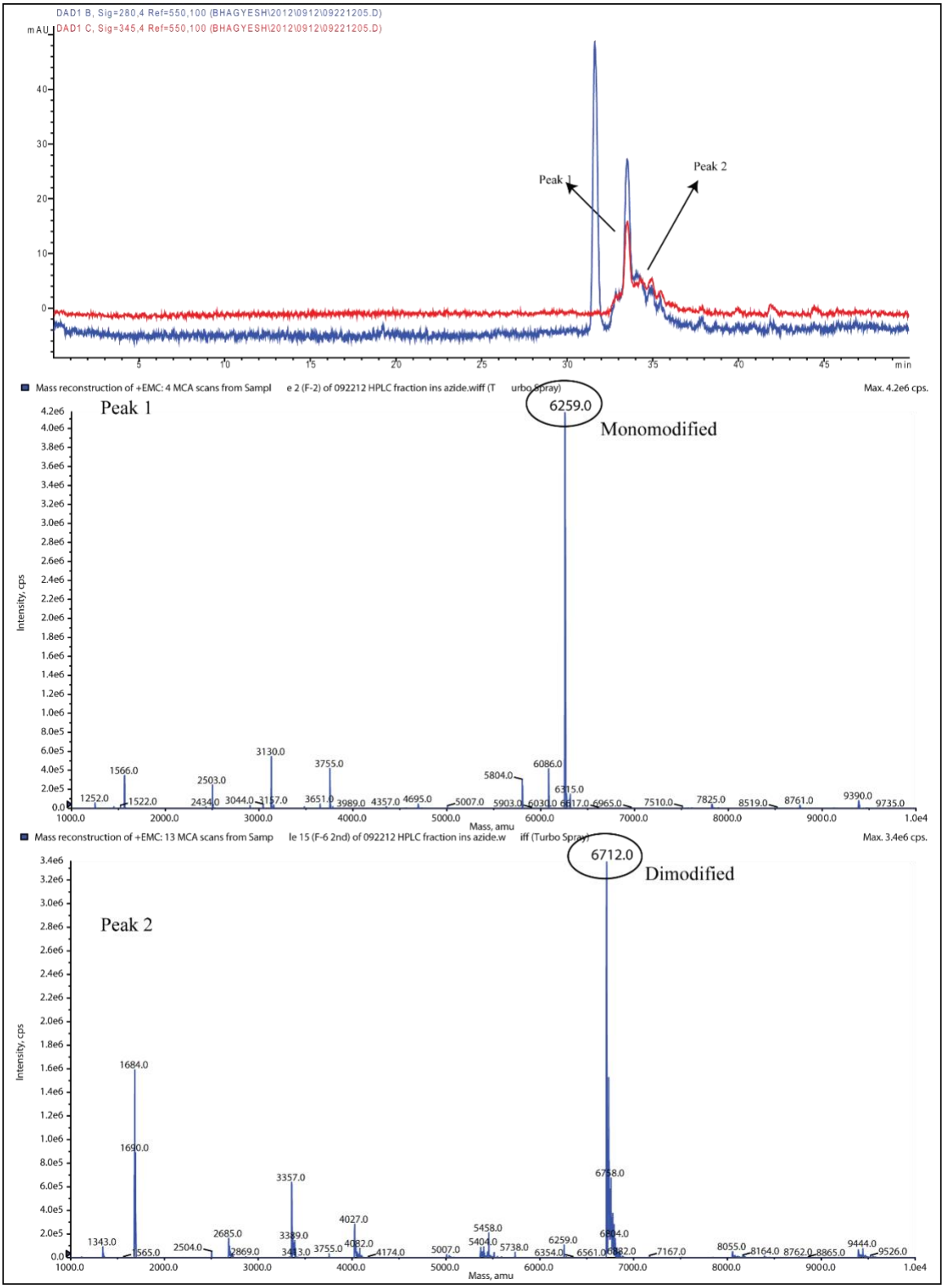

Figure 25: HPLC of crude mixture 2:1 (diazo: insulin) reaction and MS infusion of collected individual fractions.

DIMA HPLC and MS

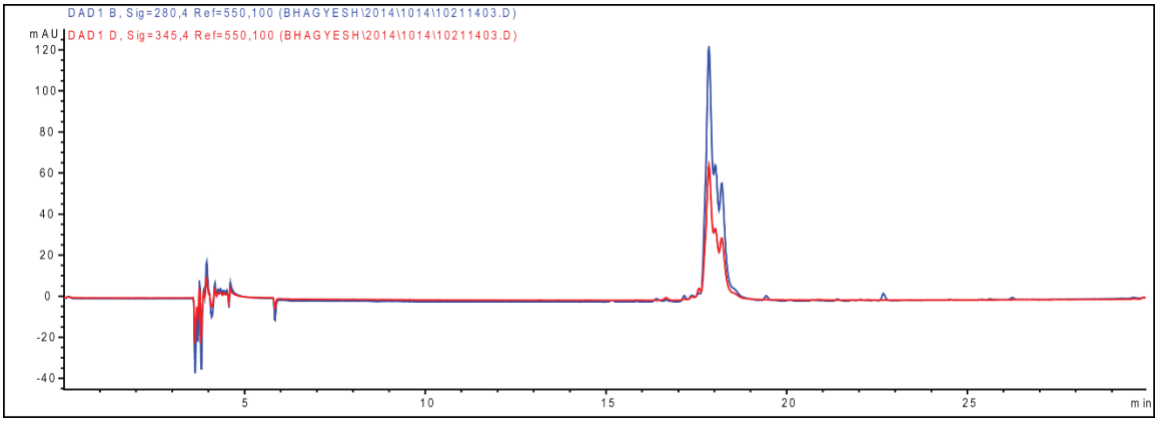

Figure 26: HPLC chromatogram of purified DIMA.

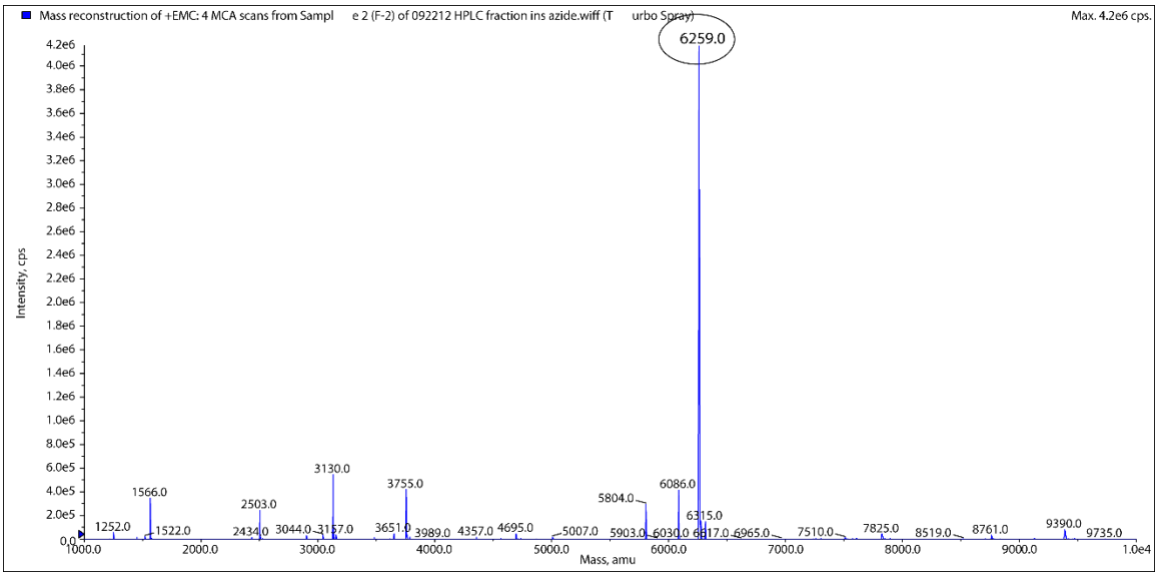

Figure 27: MS of purified DIMA. The product is seen at $[M]^+$=6259.0, calc. 6262.0.

DIDA HPLC and MS

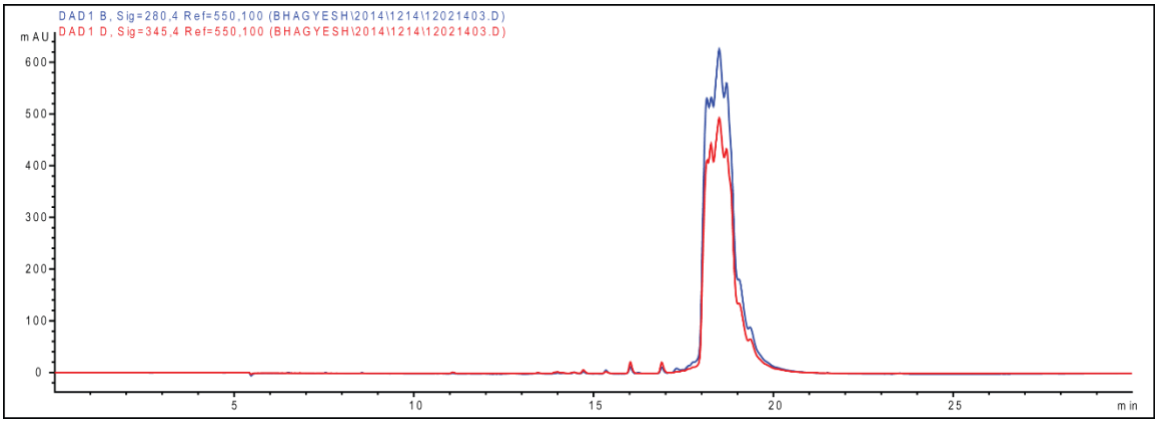

Figure 28: HPLC chromatogram of purified DIDA.

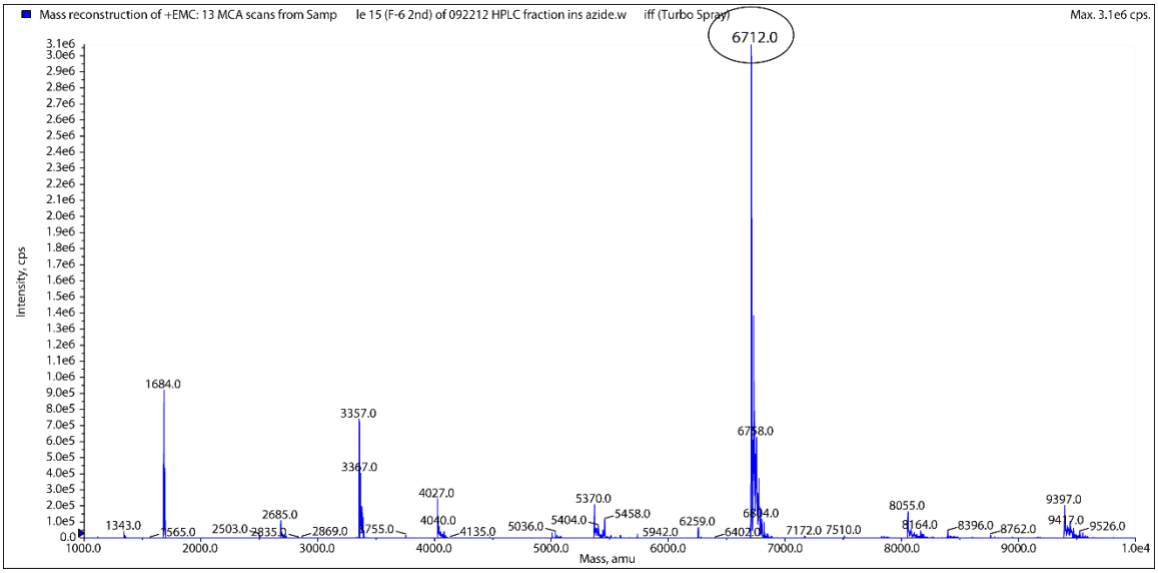

Figure 29: MS of DIDA. The product is seen at $[M]^+$=6712.0, calc. 6714.0.

Synthesis of tris-DBCO linker

To synthesize the tris-DBCO (TD) linker (Figure 30), (tren) Tris (2-aminoethyl)amine (Acros Organics, catalog # AC314791000, 10 µmol, 1.46 µL), DBCO acid (Click Chemistry Tools, catalog # A101-100, 45 µmol, 15 mg), hydroxybenzotrizole hydrate (90 µmol, 13.8 mg) were dissolved in 0.3 mL anhydrous DMF. After that 1-ethyl-

3-(3-dimethylaminopropyl) carbodiimide hydrochloride (76.5 µmol, 14. 7 mg) was added to the mixture with additional 0.5 mL anhydrous DMF and vortexed overnight. It was called TD linker 1 (TDL1). It was purified using HPLC.

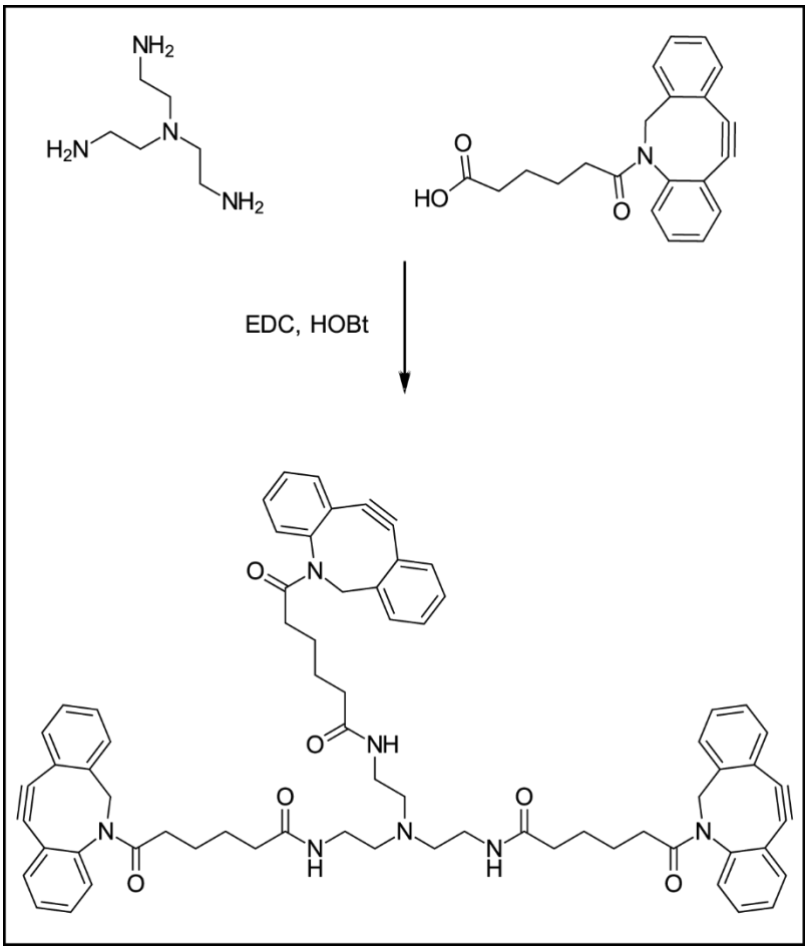

Figure 30: Synthesis of 1-{2-azatricyclo[10.4.0.04,9]hexadeca-1(16),4,6,8,12,14-hexaen-10-yn-2-yl}-6-(2-{bis[2-(6-{2-azatricyclo[10.4.0.04,9]hexadeca-1(16),4,6,8,12,14-hexaen-10-yn-2-yl}-6-oxohexanoylamino)ethyl]amino}ethylamino)-1,6-hexanedione.

HPLC purification method – reversed-phase HPLC (flow rate 2 mL/min, runtime 40 minutes), solvent A (0.1% TFA in H_2O), solvent B (0.1% TFA in ACN), gradient 0% B to 100% B over 30 minutes, isocratic 100% B for 10 minutes, C18 Hypersil column (5 µm, 250 × 10 mm, Phenomenex), retention time: 29.83 min (Figure 31); ESI−MS (m/z): $[MH]^+$ calculated for $C_{63}H_{54}N_6O_6$, 1092.5; found, 1092.5 (Figure 32). The purified material was

also analyzed using the same method mentioned here on HPLC.

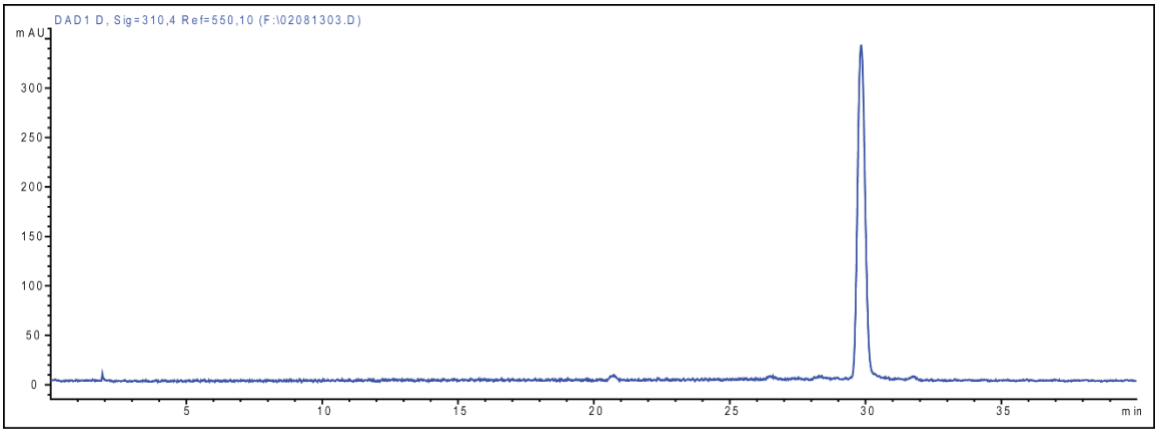

Figure 31: HPLC chromatogram TDL1.

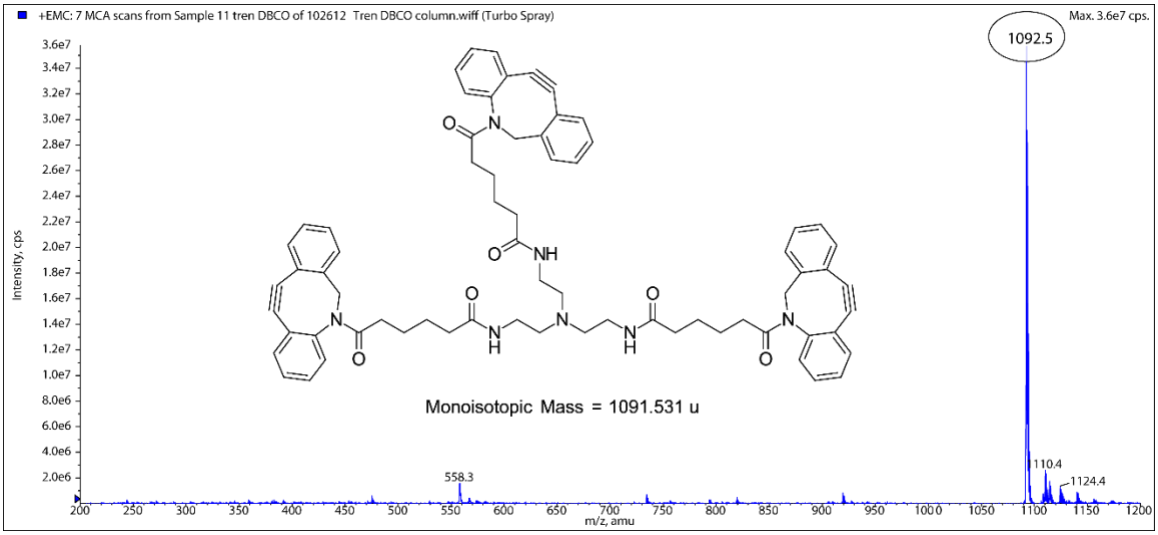

Figure 32: MS infusion of TDL1. The product is seen at $[MH]^+$=1092.5.

TD linker 2 synthesis

We had difficulty in purifying TDL1 via liquid-liquid extraction or via flash chromatography, hence it was purified using a semi-prep column on HPLC. We thought, if we synthesize more non-polar TD linker, it would be easier to purify it using aqueous-organic phase separation, as it would partition in organic phase predominantly. We then replaced tren with cyclohexanetricarboxylic acid. Hence, TDL2 (Figure 33) was

synthesized.

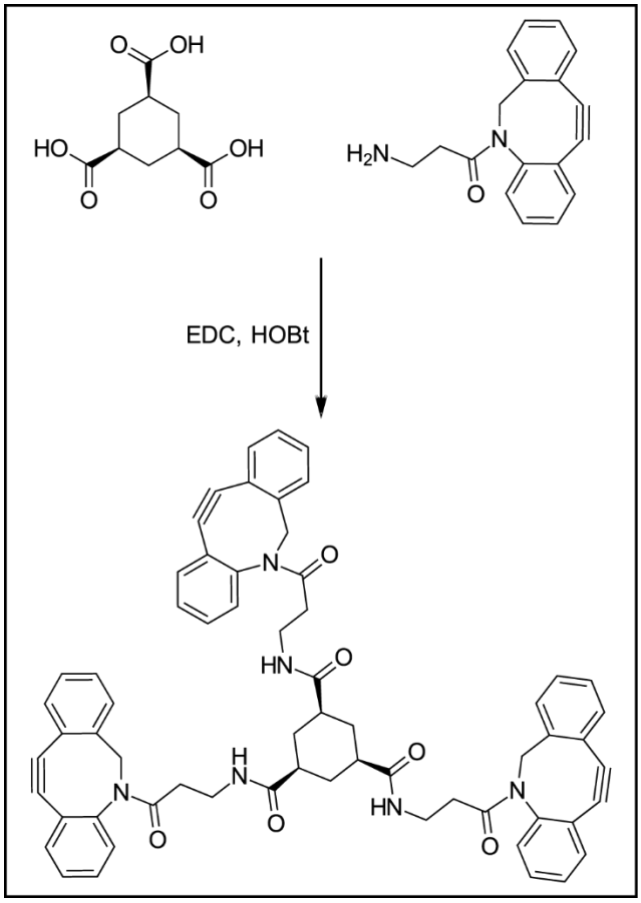

Figure 33: TDL2 synthesis scheme

1,3,5-cyclohexanetricarboxylic acid (CTA) (Sigma Aldrich, 344346-1G, 6.94 mg, 32.1 μmol), DBCO amine (Click Chemistry Tools, 40.6 mg, 146.9 μmol) and HOBt hydrate (22 mg, 143.6 μmol) were dissolved in 0.3 mL of anhydrous DMF. Once the solution became clear, EDC (29 mg, 151.2 μmol) was added, vortexed and allowed to react for 18 hours. As we modified TDL1 by introducing a cyclohexane moiety, we were expecting to purify it by aqueous-organic phase extraction due to its hydrophobicity. However, we couldn't isolate it using that method. Also, when attempted via HPLC purification, the presence of TFA in HPLC solvents is not recommended since even trace

amounts of TFA (or any acid) is found to degrade DBCO ring. First, the presence of product was confirmed by purifying a fraction on reversed phase HPLC and infusing it into MS. Once the correct fraction was identified, it was purified on a larger scale using a semi-prep column. The collected fractions were dried using a rotavap. HPLC purification method – reversed-phase HPLC (flow rate 2 mL/min, runtime 40 minutes), solvent A (H_2O), solvent B (ACN, gradient 0% B to 100% B over 30 minutes, isocratic 100% B for 10 minutes, 5-minute post run with 100% A, C18 column (5 μm, 250 × 10 mm, Phenomenex). Yield 14.1 mg (44.4%); UV/vis (methanol): 312 nm (34500 M^{-1} cm^{-1}); analytical run method – reversed-phase HPLC−MS (flow rate 0.4 mL/min, runtime 35 minutes), solvent A (0.1% FA in H_2O), solvent B (0.1% FA in ACN), gradient 0% B to 50% B over 15 minutes, gradient 50% B to 100% B over 30 minutes, isocratic 100% B for 3 minutes, 100% B to 0% B over 2 minute, C18 Hypersil column (5 μm, 100 × 4.6 mm, Varian), retention time: 22.31 min; ESI−MS (m/z): $[MH]^+$ calculated for $C_{63}H_{54}N_6O_6$, 991.4; found, 991.5 (Figure 34); reversed phase HPLC (flow rate 1 mL/min, runtime 35 minutes), solvent A (0.1% TFA in H_2O), solvent B (0.1% TFA in ACN), gradient 0% B to 100% B over 30 minutes, isocratic 100% B for 5 minutes, C18 Hypersil column (5 μm, 100 × 4.6 mm, Varian), retention time: 27.48 min (Figure 35); ^1H NMR (400 MHz, DMSO-d_6) d ppm 1.04 - 1.18 (m, 1H) 1.23 (s, 2H) 1.42 (d, J=11.71 Hz, 1H) 1.76 - 1.93 (m, 2H) 2.38 (tt, J=14.93, 7.13 Hz, 1H) 2.83 - 3.00 (m, 1H) 3.01 - 3.17 (m, 1H) 3.62 (d, J=14.06 Hz, 1H) 5.03 (d, J=14.06 Hz, 1H) 7.15 - 7.82 (m, 10H); ^{13}C NMR (100 MHz, DMSO-d_6):174.3, 170.6, 151.8, 148.8, 132.8, 129.9, 129.3, 128.6, 128.4, 128.1, 127.2, 125.6, 122.8, 121.9, 114.8, 108.5, 55.2, 42.9, 35.4, 34.6, 31.7, 29.4, 29.1 (Figure 36).

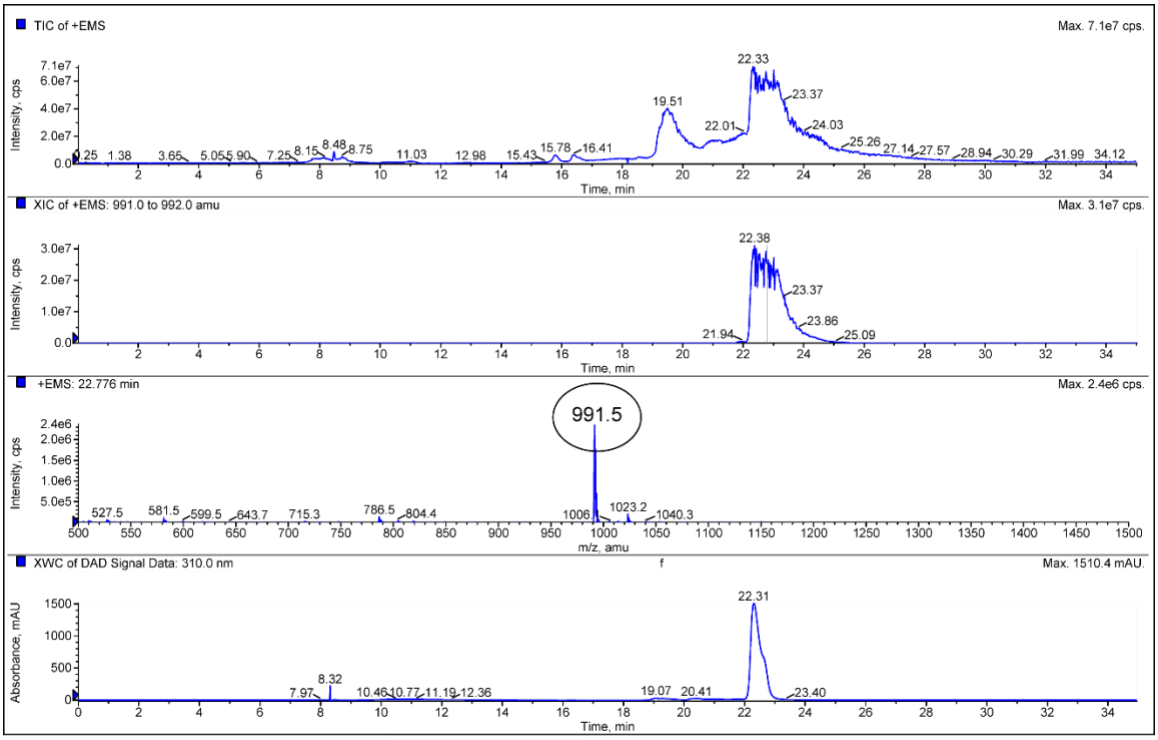

Figure 34: LCMS of TDL2. The product is seen at $[MH]^+$=991.5 at the retention time of 22.31 minutes.

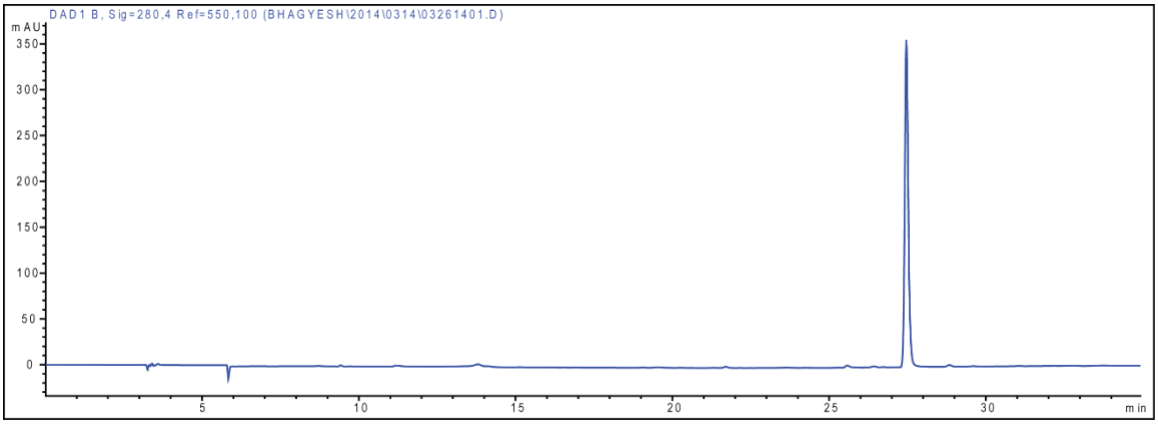

Figure 35: HPLC chromatogram of TDL2.

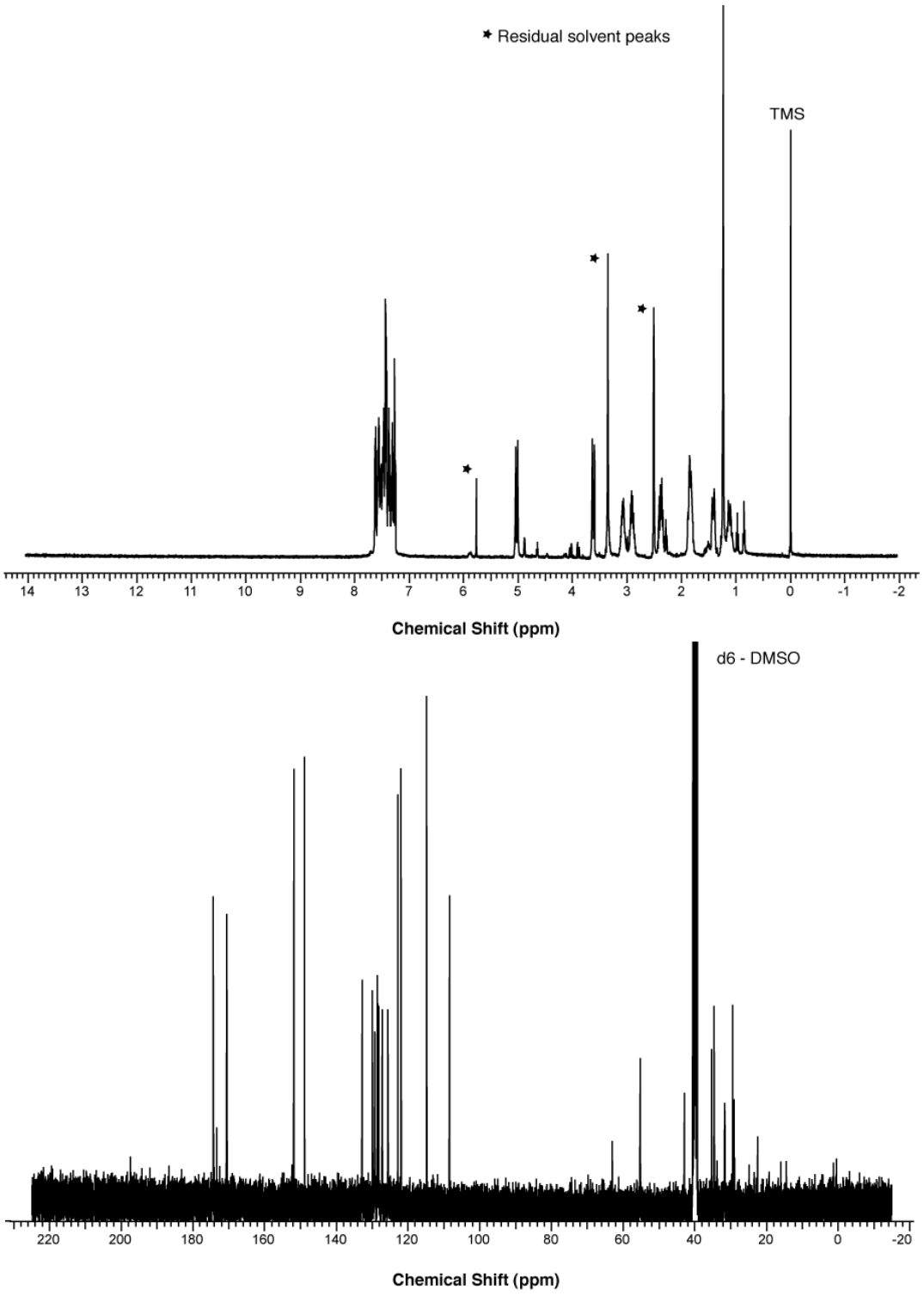

Figure 36: Proton (top) and ^{13}C (bottom) NMR of TDL2.

Instability of DBCO ring in the presence of strong acids

It has been our persistent observation that DBCO ring is highly unstable in the presence of strong acids, it degrades within minutes to hours. Although we observe this, the pathway or mechanism of how it happens is not clear. We hypothesize that the amide bond here may not be a canonical amide, it may not have the planar geometry as seen in regular amide bonds due to its position in the DBCO ring. Hence, it might be susceptible to acid hydrolysis. Regular amides have very long half-lives in the presence of acids but this one might be an exception. When we attempted to purify TD linkers using liquid-liquid extraction, despite being very non-polar, it always partitioned into 1N HCl layer instead of EtOAc. If our hypothesis is correct, in the presence of acids, the nitrogen in the amide gets protonated as it is not a typical amide. At this point, the amide undergoes hydrolysis which is the reason for ring degradation. Hence the HPLC purification method was used without adding TFA to HPLC solvents. In the presence of TFA, the purified material degraded very quickly. However, when TFA was eliminated in HPLC solvents, the product was stable and could be stored in -20 °C freezer for years without any issues of degradation. The proposed hydrolysis and the hydrolyzed products are shown in Figure 37.

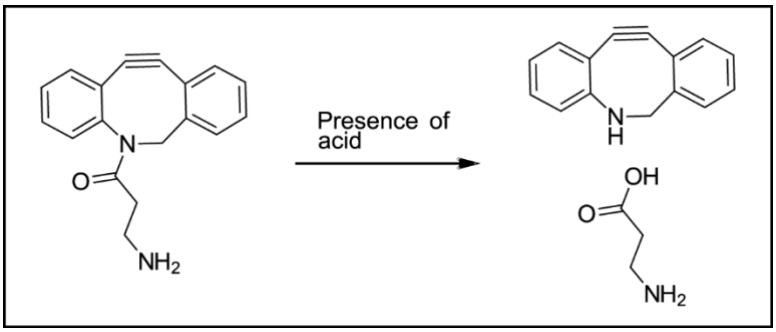

Figure 37: Hypothesis about the instability of DBCO ring in the presence of acids. The amide here may not be a regular planar amide bond; hence it might be susceptible to attack by strong acids to cause hydrolysis.

DMNPE insulin trimer synthesis and photolysis

Insulin macropolymer synthesis is a complex reaction with many possible products; hence, we decided to start with the synthesis of simpler molecules like insulin trimer as shown in Figure 38. The trimer is a molecule in which we conjugate three molecules of DIMA on all three alkynes of TD linker, hence the name trimer. The DIMA and TDL2 were synthesized and purified as described above. The stock solutions were prepared in DMSO, and the concentrations were measured using the UV-vis spectroscopy.

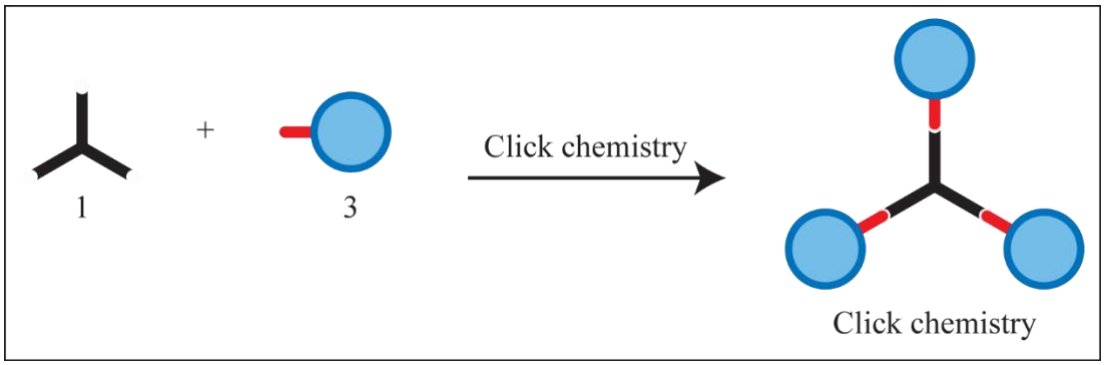

Figure 38: Synthesis of DMNPE insulin trimer.

Synthesis of DMNPE insulin trimer

DIMA (61 µL, 462 nmol) was mixed with TDL 2 (16.1 µL, 140 nmol). The stock solutions of these were prepared in DMSO. The reaction was run for 48 hours at 37 °C in the dark protected from light. The trimer was used directly without further purification. In the analysis via MS and gel, a small amount of dimer was observed in MS analysis. ESI−MS (m/z): $[M]^+$ for dimer calculated, 13513.0; found, 13512.0, $[M]^+$ for trimer calculated, 19774.0; found, 19771.0 (Figure 39).

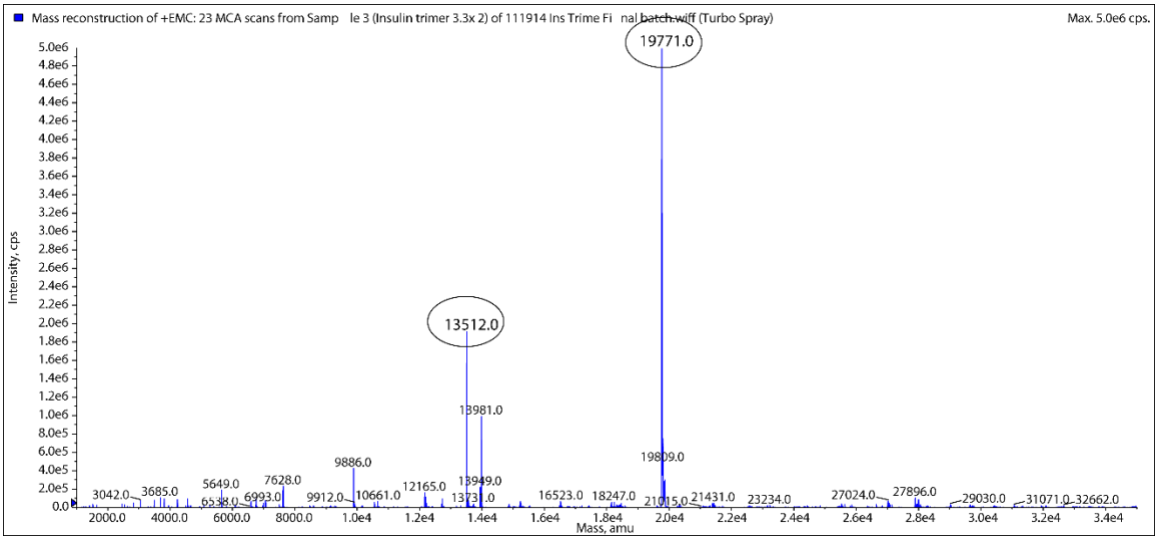

Figure 39: MS infusion of the trimer reaction mixture. The insulin trimer $[M]^+$ is seen at 19771.0 (calc. $[M]^+$ = 19774.0) and insulin dimer $[M]^+$ is seen at 13512.0 (calc. $[M]^+$ = 13513.0).

DMNPE insulin trimer photolysis in DMSO

In addition to the MS analysis of trimer, it was also analyzed by SDS-PAGE. The trimer sample prepared above was run on a gel (Criterion TGX Any kDa precast gel from Bio-rad) using Criterion vertical midi-format electrophoresis cell (Bio-rad) at 150V. The samples in DMSO were withdrawn and mixed in 1:1 with Laemmli loading buffer. This mixture was loaded in a gel. Upon running on a gel, two bands were observed. These correspond to dimer and trimer. In parallel, the crude reaction mixture in DMSO was photolyzed using a Blak-Ray lamp (Model XX-15L, 30 watts) source. For this photolysis, 3.85 µL of the reaction mixture was diluted to 35 µL in DMSO and aliquoted into a 96 well-plate (BD Falcon). The mixture was irradiated from the top using the UV-vis lamp at a 10 cm distance. 5 µL samples were withdrawn at 0, 1, 2, 4, 6, 8 minutes time points and diluted with 5 µL of Laemmli loading buffer. This 10 µL mixture was run on SDS-PAGE (Figure 40).

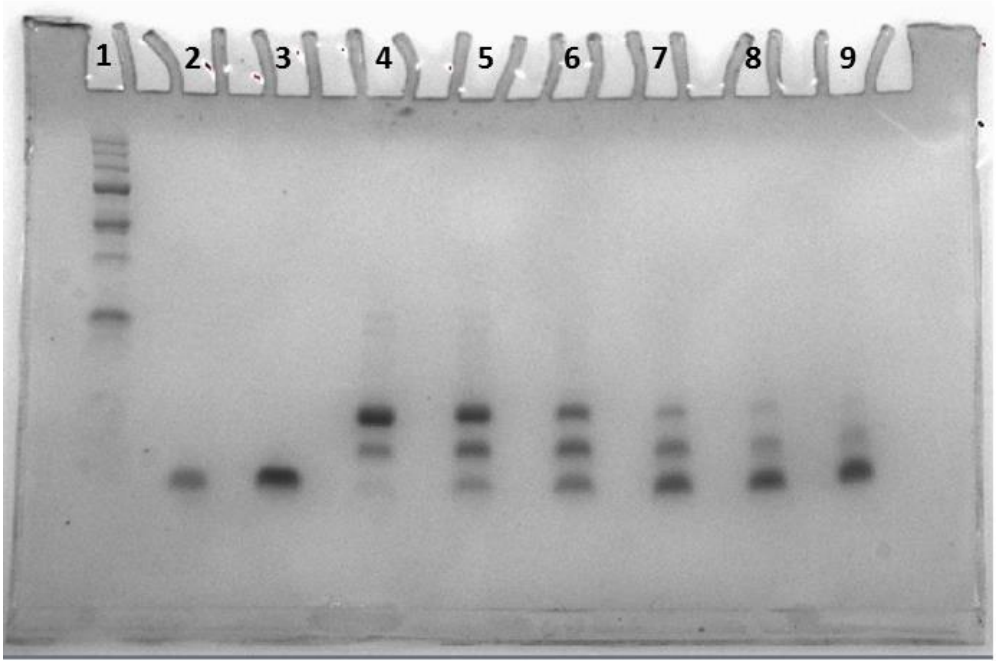

Figure 40: Characterization of DMNPE insulin trimer using SDS-PAGE. Lane 1-molecular weight ladder, lane 2-insulin std., lane 3-insulin mixed with TDL2 in 3:1 ratio, lane 4-DMNPE insulin trimer crude mixture at t=0, lane 5-mixture at t=1 min, lane 6-mixture at t=2 min, lane 7-mixture at t=4 min, lane 8-mixture at t=6 min, lane 9-mixture at t=8 min after photolysis in DMSO using the lamp.

In lane #3 of the gel, insulin was mixed with TDL2 in 3:1 ratio. Only one band is visible in that lane corresponding to insulin. However, when DIMA was mixed with TDL2 in the same proportion, we saw two new bands. The highest band corresponds to the trimer and another to the dimer. The mixture was then photolyzed from the top using the blak-ray lamp at a 10-cm distance. As the sample was being irradiated, the top band gradually disappeared, and the bottom band became darker. It suggested that trimer was being photocleaved by light to give native insulin molecules. The bottom band is consistent with the position of insulin band. The final time point at t=8 min was also infused in MS to detect insulin. It only showed a single mass of insulin: ESI (m/z); $[M]^+$ calculated, 5808.0; found, 5807.0 (Figure 41).

The 3 bands on the trimer gel were quantified using Photoshop®. The bottom band is a superposition of two bands which correspond native insulin and insulin monomer (resulting from the photolysis of insulin dimer).

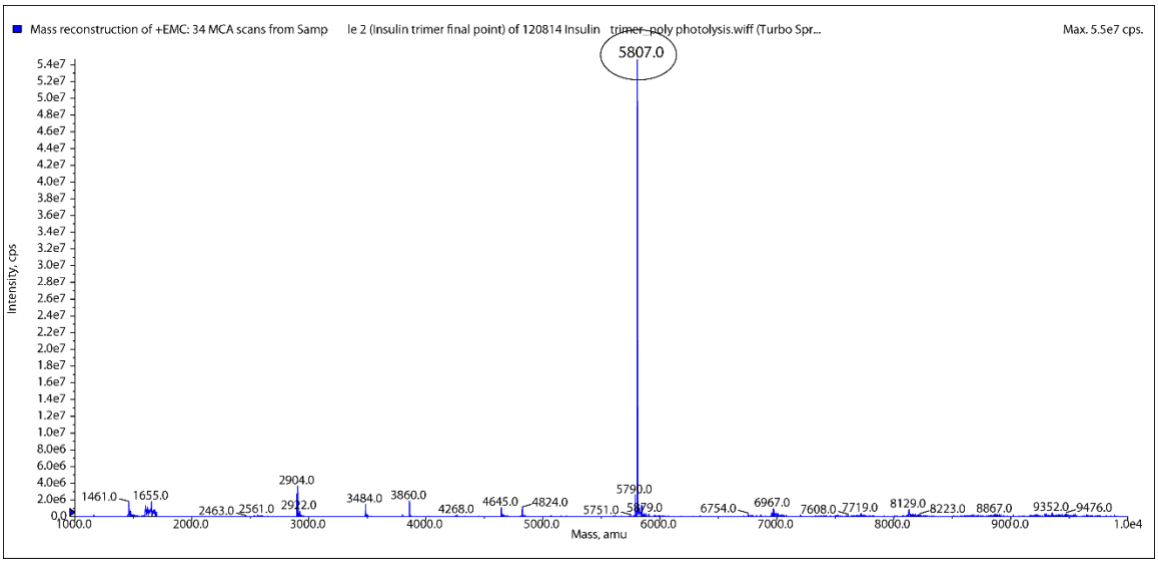

Figure 41: MS infusion of the final time point from the photolysis of DMNPE insulin trimer. The product is seen at $[M]^+$=5807.0, calc. for 5808.0.

Kinetics of insulin trimer photolysis in DMSO

Because native insulin and insulin monomer cannot be quantitated individually, they are being considered as one species in deriving equations of the kinetics of this. In Figure 42, A refers to insulin trimer, B refers to insulin dimer, and C refers to both insulin + insulin monomer. The sequential photolysis of A→ B→ C can be fit using the equations below.[49] The concentration of each species was determined by normalizing total insulin concentration to 0.66 mM. The concentration here of A, B and C refers not to the concentration of each species but the concentration of insulin present in each species. The curve fitting was performed using Kaleidagraph® software.

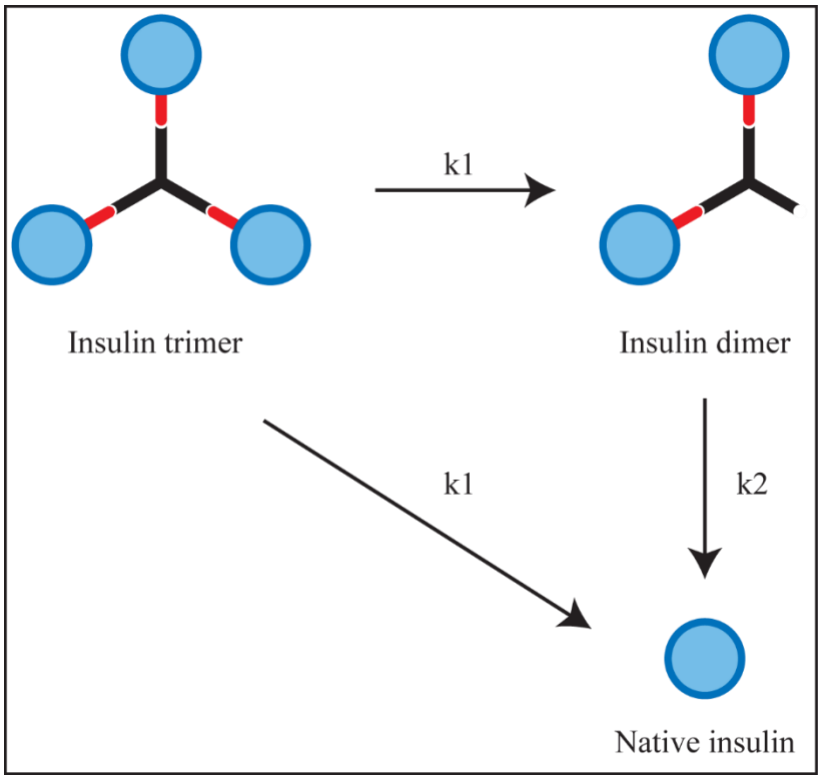

Figure 42: Photocleavage of insulin trimer. When insulin trimer is irradiated, it gets converted into dimer and one molecule of insulin. When dimer undergoes photolysis, it gets converted to monomer and one molecule of insulin. However, insulin monomer and insulin have the same mobility on the gel; they are considered as one species.

$$A = A0.e^{-k1.t}$$

$$B = B0.e^{-k2.t} + (\frac{A0.k1}{k2-k1})(e^{-k1.t} - e^{-k2.t})$$

$$C = C0 + A0(2 - e^{-k1.t}) + B0(1 - e^{-k2.t}) + \frac{A0}{k2-k1}(k1.e^{-k2.t} - k2.e^{-k1t})$$

Where A0, B0, and C0 are concentrations of A, B, and C at t=0 respectively. This was determined by quantitation of gel bands and knowledge of insulin concentration in the mixture.

A0 is 81.7% of total (.00066 M) = .00053922 M

B0 is 14.5% of total = .0000957 M

C0 is 3.77% of total = .000024882 M

M0 is the time in minutes, and M1 and M2 are rate constants for the degradation of A and B respectively. Each set of data (A, B and C) was fit to the appropriate equation given above, and resulted in the following fit values for k_1 and k_2 (fit errors in parenthesis):

A $k_1 = .47\ min^{-1}$ (.035)

B $k_1 = .39\ min^{-1}$ (.028), $k_2 = .35\ min^{-1}$ (.015)

C $k_1 = .21\ min^{-1}$ (.015), $k_2 = .016\ min^{-1}$ (.0076)

These results (shown in Figure 43) demonstrated that trimer material was synthesized and undergoing photolysis as it is expected from this kind of substance. It sequentially underwent photocleavage reactions from trimer to dimer to monomer and finally to native insulin. The sequential reactions (A→ B→ C) follow the first order kinetics. The kinetic constants are very close. The transitions can be detected using SDS-PAGE as shown above. The native insulin released at the end was also analyzed by MS and showed an exact mass corresponding to insulin.

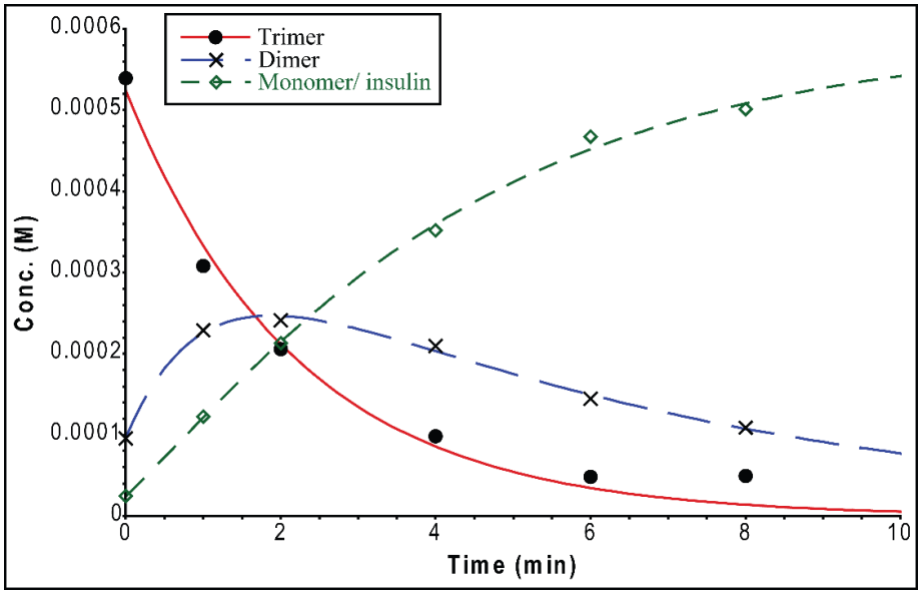

Figure 43: Curve fitting of sequential photocleavage of trimer→dimer→monomer/ insulin.

The above experiment was performed in DMSO in which the trimer is soluble. However, in the real-world, DMSO will be replaced by bodily fluids which are aqueous. It is critical that trimer material remains insoluble in such aqueous solutions if we want to retain it at the site after injection. Otherwise, after injection, the material would diffuse away from the site. To test this hypothesis, the trimer material which was originally synthesized in DMSO was dried using a freeze dryer. PBS was added to the dried residue, the trimer material precipitated out, and the solution became turbid. PBS was used because of its composition, osmolarity is closer to plasma. The way the material behaves in PBS might give us an idea of how it would behave in a patient. The photocleavage of this trimer material was tested using a 365 nm LED designed by Dr. Friedman.

Photocleavage of DMNPE insulin trimer in PBS

The trimer crude mixture (containing 66 nmol of DIMA) was added to two HPLC glass inserts (one for the experimental and one for the control). HPLC glass vial insert (flat bottom glass vial inserts 250 µL, diameter 3.4 mm (inner), 4.5 mm (outer), height 30.5 mm (Agilent, 5183-2090) was used. The original reaction mixture in DMSO was added to these vials and freeze-dried overnight to get rid of all DMSO. Then 100 µL PBS was added to it, and the pellet which was at the bottom was scratched out using a needle to suspend the trimer material uniformly in PBS. For t=0, the sample in the insert was vortexed, centrifuged and half of it was withdrawn and replaced with fresh PBS. This procedure was repeated at the time of collection for each time point. The experimental samples were irradiated from the bottom by keeping the glass insert right on top of the LED, refer to Figure 44. The control samples were kept in the dark, not exposed to light.

Figure 44: Setup for photolysis of samples. The samples were photolyzed in a glass insert and kept right on top of 365 nm LED as shown on the right.

HPLC was not used for analysis because analyte was released was not concentrated enough. Also, there was a concern whether other trimer components might get solubilized and elute at the same retention time as insulin. This would make the analysis challenging. The supernatant was analyzed using MS. Because we were anticipating a much lower quantity of insulin in the material, we pooled all the supernatant solutions for MS analysis. This pooled solution was spin-filtered using 5000 Da MWCO filter to remove salts from PBS. The salts prevent ionization of insulin in MS. After spin filtration, the sample was dissolved in 0.01 N HCl and infused in MS. The molecular ion $[M]^+$ of insulin was calculated, 5808.0; found, 5809.0 (Figure 45). The samples were also analyzed by SDS-PAGE to confirm the presence of insulin in the supernatant. Because of the small quantity of insulin, it could not be detected using Coomassie blue staining. Hence, we used silver staining (Thermo Fisher Scientific), which is much more sensitive and has a lower limit of detection than Coomassie blue staining. For gel data, refer to Figure 46. The samples were finally analyzed using ELISA to measure the concentration of released insulin present in the supernatant at each time point.

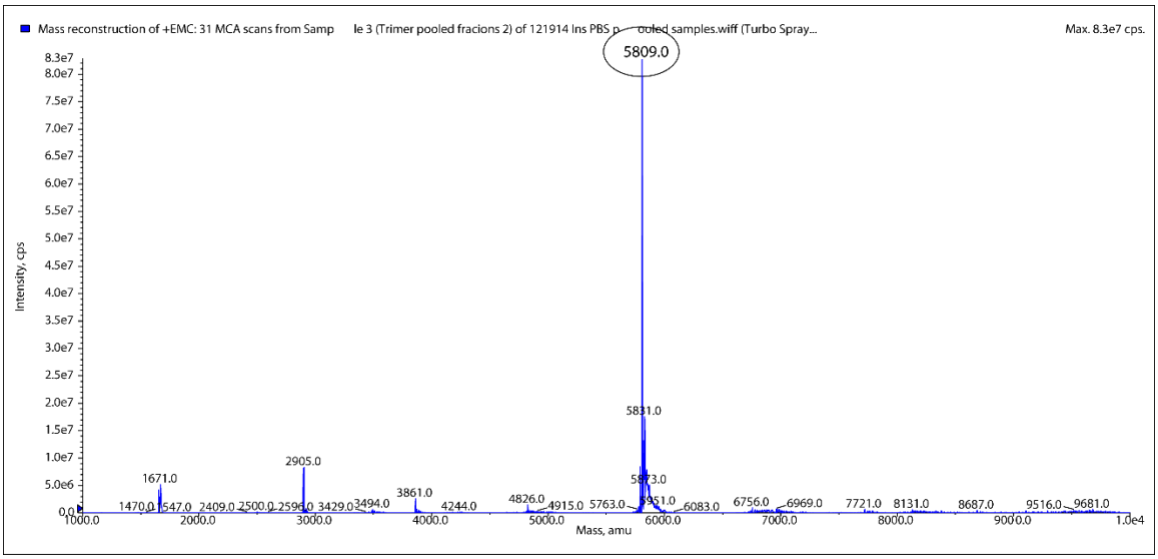

Figure 45: MS of insulin released from DMNPE insulin trimer (pooled samples). The product mass is seen at $[M]^{+}$=5809.0, calc. for 5808.0.

In the gel, all the time points from t=5 min showed a band which corresponds to insulin. In the later time points, other higher bands start appearing. It is probably because the portion of the material is slowly leaching into PBS. The heat generated from the LED might be accelerating this leaching process by heating the solvent and raising the overall temperature. The samples were all pooled together, and after spin filtration, showed a mass of insulin upon MS infusion. This gives additional confirmation that insulin is being released. We also performed ELISA on the samples. It was observed that insulin was being released steadily in the test (irradiated) sample but not in the control (unirradiated) sample. As the irradiation went on, the cumulative amount of insulin released also increased (Figure 47). The final yield of insulin release was 15.9% of the total. From these experiments, we demonstrated that trimer was synthesized, and it was behaving as expected; after that, the macropolymer was synthesized and characterized.

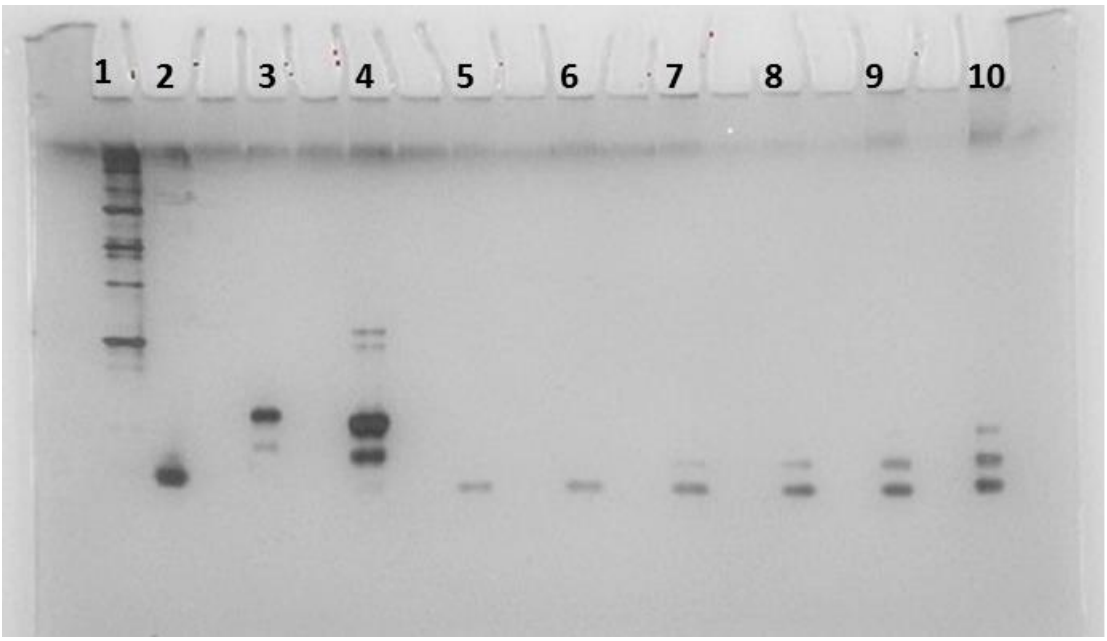

Figure 46: Characterization of photolysis of DMNPE insulin trimer in PBS using SDS-PAGE (silver staining). Lane 1-molecular weight ladder, lane 2-insulin std., lane 3-insulin trimer mixture in DMSO, lane 4-DMNPE insulin trimer crude mixture at t=0, lane 5-mixture at t=5 min, lane 6-mixture at t=15 min, lane 7-mixture at t=25 min, lane 8-mixture at t=35 min, lane 9-mixture at t=45, lane 10-mixture at t=55 min after photolysis in DMSO using the point source.

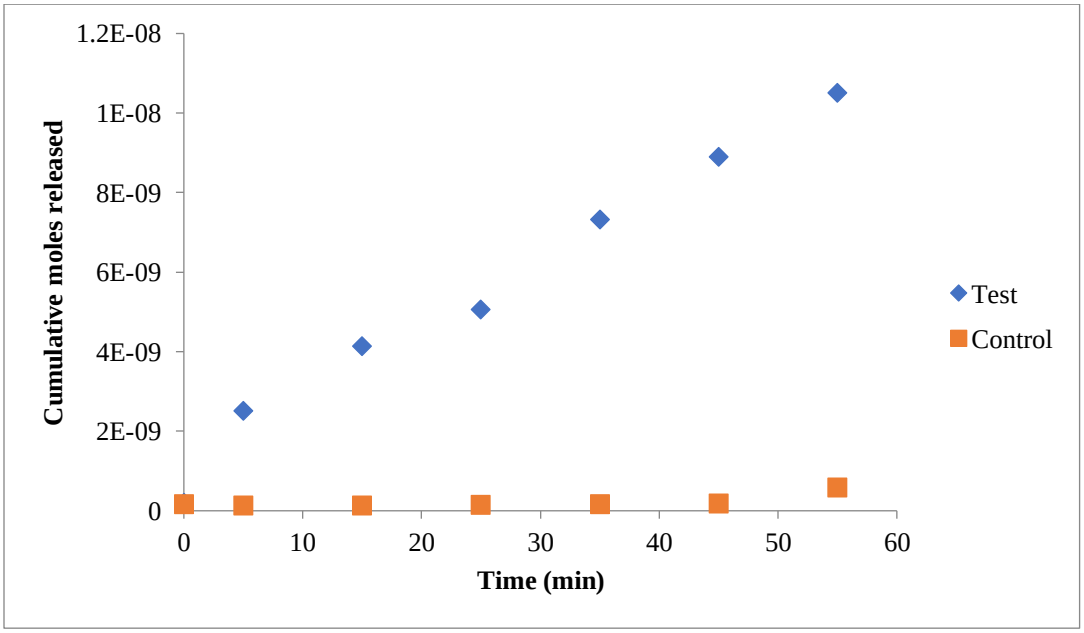

Figure 47: DMNPE insulin trimer was photolyzed in PBS as a suspension using 365 nm point source LED. Insulin release was measured using ELISA.

DMNPE insulin macropolymer synthesis and characterization

The approach to synthesize macropolymer from the components described above will be discussed here. DIMA, DIDA, and TDL2 if mixed in 1:1:1 proportion is expected to give multimers and insulin polymers of different lengths as shown in Figure 48.

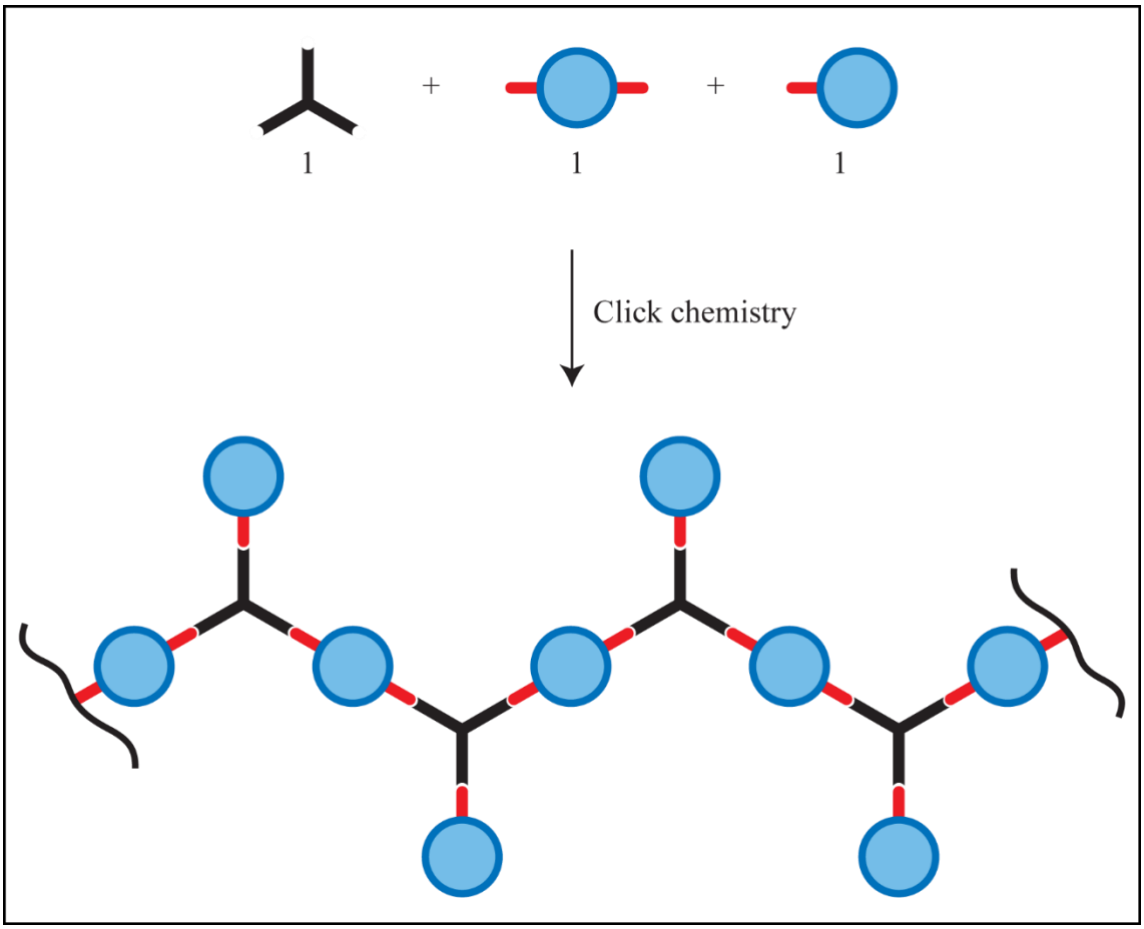

Figure 48: Synthesis of insulin macropolymer by mixing DIMA, DIDA and tris DBCO linker in 1:1:1 ratio.

Optimization of macropolymer synthesis

Attempt # 1 – Effect of changing ratio of DIMA: DIDA: TDL2

This was the very first attempt for the polymerization reaction. Theoretically, having DIMA: DIDA: TDL2 in 1:1:1 ratio is expected to yield higher MW polymeric

species. However, we anticipated that it would also result in a heterogeneous mixture of products and not a single product. Hence first we wanted to see what the effect is of changing the ratio of DIMA + DIDA to TD linker. The solutions of DIMA (15.7 mM), DIDA (3.9 mM) and TDL2 (7.76 mM) were prepared in DMSO and characterized by HPLC and MS to make sure they are pure. The overall insulin azide (both DIMA and DIDA) were used in 3.5 equivalents to TDL2. Both DIMA and DIDA were mixed in the desired proportion first and then added to TDL2 (Table 1).

Results

The very first reaction used a 100:0 ratio, it is the same ratio used in the synthesis of insulin trimer. In other reactions, a few higher MW bands were observed – specifically, 3-4 newer bands were observed on top of existing trimer band; however, the bottom three bands remained dark. We expected that the higher bands would be darker and lower MW bands would disappear as the reaction progressed. Here, although we varied the proportion of DIMA: DIDA from 0 to 100%, the pattern of bands looked very similar across all reactions (Figure 49) – this was rather unexpected. It suggested that the polymerization reaction was stopping at a certain threshold under all conditions. One possible reason is that there is overcrowding of insulin molecules and due to the steric hindrance, the reaction sites are inaccessible to each other. The stearic hindrance could be a reason for limited polymerization. The inherent tendency of insulin molecules to polymerize with each other non-covalently and form dimer, hexamers, and aggregates might make this issue even more challenging to resolve.[50] Another possibility is that during the reaction, the DBCO ring might be undergoing degradation as mentioned earlier, preventing the progress of the reaction.

Table 1: A set of reactions with different ratios of DIMA and DIDA to TDL2.

		Total insulin azide (3.5eq.) Proportion of DIMA: DIDA	
	TDL2 (nmol)	DIMA (%)	DIDA (%)
Reaction 1	1	100	0
Reaction 2	2	80	20
Reaction 3	3	60	40
Reaction 4	3	50	50
Reaction 5	3	40	60
Reaction 6	3	20	80
Reaction 7	3	0	100

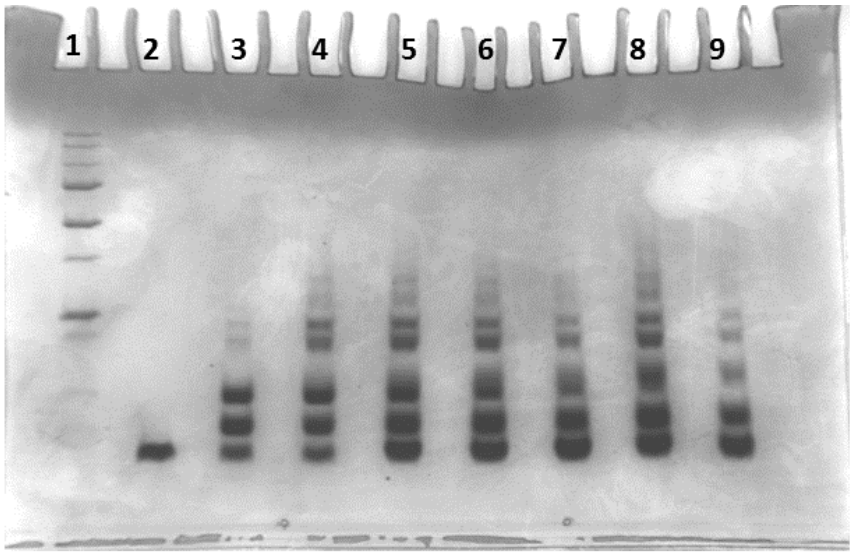

Figure 49: Characterization of the extent of polymerization of DMNPE insulin polymer using SDS-PAGE. Lane 1-molecular weight ladder, lane 2-insulin std., lane 3 to lane 9 – reaction 1 to 7 in order.

Attempt # 2- The effect of changing overall equivalents of insulin azides to TD linker keeping the ratio of DIMA: DIDA to 1:1 constant

In the previous experiment, we tested different ratios of DIMA: DIDA to TDL2. 1:1 ratio makes more sense theoretically, and also it was showing relatively better results. Here we thought of changing the overall equivalents of insulin azides to TD linker keeping the ratio (1:1) constant. The following conditions were used. The solutions of DIMA (15.7 mM), DIDA (3.9 mM) and TDL2 (7.76 mM) were prepared in DMSO. In each reaction, 2.5 nmol of TDL2 was used (Table 2). The effect of concentration on the reaction yields was tested by performing the reaction at a higher and lower concentration. The effect of other solvent systems was also investigated. We used PBS as well as water as solvents as the formed complexes might have different conformations in these solvents. The hypothesis was that using different solvents, the overcrowding could be prevented to improve the reaction efficiency.

Table 2: A set of reactions of TDL2 with DIMA: DIDA in 1:1 proportion varying equivalents, solvents, and concentrations, etc.

	Solvent	TDL2 (nmol)	Ins azide eq.	DIMA (nmol)	DIDA (nmol)	Vol. (µL)
1	DMSO	2.5	3.5	4.375	4.375	2.3
2	DMSO	2.5	3	3.75	3.75	2.0
3	DMSO	2.5	3	3.75	3.75	10.2
4	50%DMSO/water	2.5	3	3.75	3.75	4.1
5	20%DMSO/water	2.5	3	3.75	3.75	10.3
6	50%DMSO/PBS	2.5	3	3.75	3.75	4.1
7	DMSO	2.5	2.2	2.75	2.75	1.6
8	20% DMSO/water	2.5	2.2	2.75	2.75	8.2

Results

The results are as shown in Figure 50. The pattern of polymer formation was similar to the pattern observed in attempt #1. There were no additional or newer bands formed after changing the equivalents of insulin azides to TDL2.

The higher the concentration of insulin in the solution, the higher is its tendency to form multimers and aggregates.[51] This aggregation might sterically hinder sites from undergoing polymerization reactions. Because of this, we thought of reducing insulin concentration in the reaction, but it did not affect the extent of the polymerization reaction. Solvents other than DMSO for example water, PBS were also used hoping to observe if there is any change in the pattern of bands

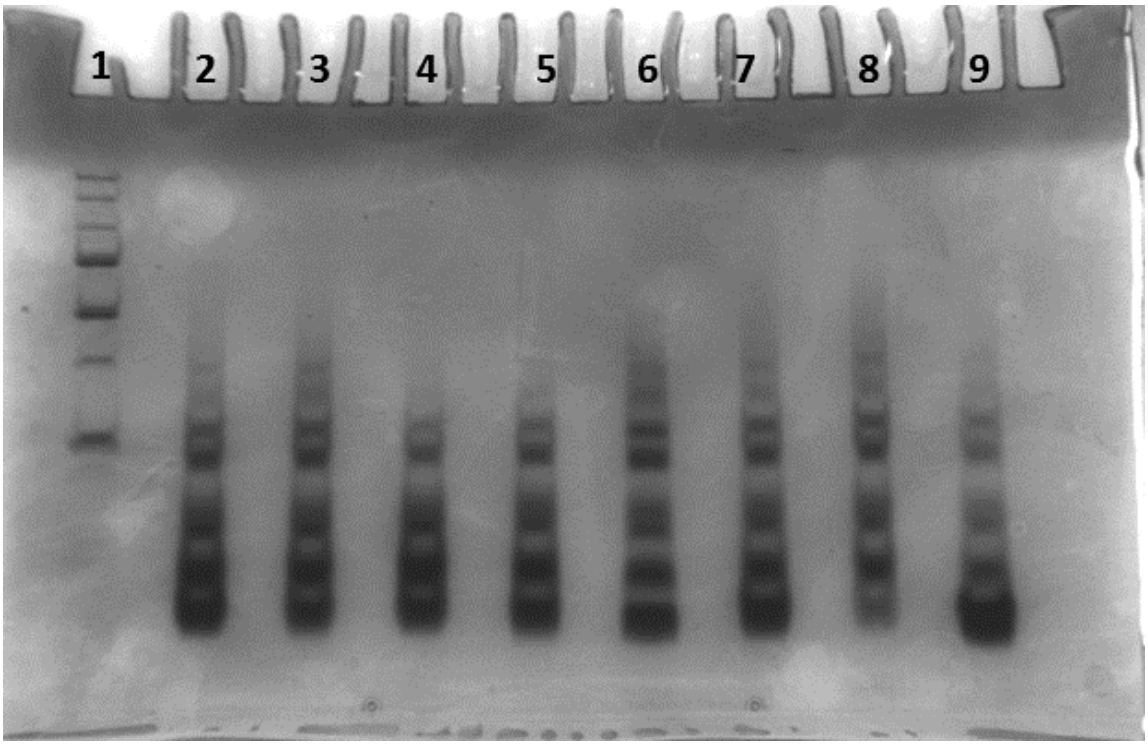

Figure 50: Characterization of the extent of polymerization of DMNPE insulin polymer using SDS-PAGE. Lane 1-molecular weight ladder, lane 2 to lane 9 – reaction # 1 to 8 in order.

Attempt # 3

In this attempt, the equivalents of insulin azide to TDL2 were varied over a wide range to see whether it helps in the improvements in synthesizing higher MW macropolymers (Table 3).

Results

As the equivalents of insulin azides increased to 3, gradually there was an improvement over the polymerization reaction, showing better reaction progression in a reaction where 3 eq. was used, as shown in Figure 51. This, however, didn't show any improvement over previous attempts.

Table 3: A set of reactions by varying the equivalents of insulin azides to TDL2.

	TDL2 (nmol)	Equivalents	DIMA (nmol)	DIDA (nmol)	Total vol. (µL)
1	3	1	1.5	1.5	1.2
2	2.5	1.3	1.625	1.625	1.2
3	2.5	1.7	2.125	2.125	1.4
4	2.5	2	2.5	2.5	1.7
5	2.5	2.3	2.875	2.875	1.8
6	2.5	2.7	3.375	3.375	2.1
7	2.5	3	3.75	3.75	2.3

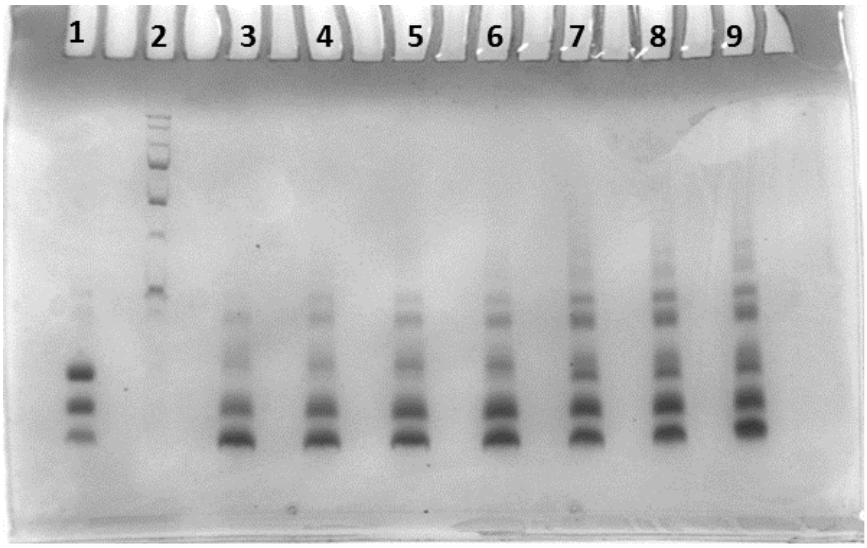

Figure 51: Characterization of the extent of polymerization of DMNPE insulin polymer using SDS-PAGE. Lane 2 – MW ladder, lane 3 to lane 9 – reaction # 1 to 7 in order.

At this point, different reaction conditions were manipulated, but there were no significant changes in the extent of the polymerization. Other things to promote the

polymerization reaction were tried as described below. None of it seemed to yield improved results though.

i. Along with PBS, water, 0.01N HCl, 20% acetic acid were used as solvents.

ii. Also, the reactions were also performed in the presence of chaotropic reagents like 6M urea, 1% Triton- 100x, 5 mM SDS to potentially break down non-covalent aggregates of insulin.

iii. The reactions were performed with or without sonication.

iv. The sequence of addition of DIMA or DIDA to TDL2 was also altered. Instead of mixing DIMA and DIDA together first and then adding to TDL2, either DIMA or DIDA were mixed with TDL2 first individually and allowed to react overnight, then remaining insulin azide was added.

After seeing no significant changes, we decided to change the arms length so that making these changes might improve the extent of the polymerization reaction.

Synthesis of a longer TD linker

Step 1 – Coupling of PEG boc linker to cyclohexane tricarboxylic acid followed by TFA cleavage

1,3,5-cyclohexanetricarboxylic acid (CTA) (Sigma-Aldrich, 344346-1G, 2.56 mg, 11.86 μmoles), O-(2-Aminoethyl)-O′-[2-(Boc-amino)ethyl]hexaethylene glycol (Sigma-Aldrich, 25 mg, 53.35 μmol), EDC (11.6 mg, 60.5 μmol) and HOBt hydrate (10.9 mg, 71.2 μmol) were mixed in 50 μL anhydrous DMF for 24 overnight (Figure 52). Here, we inserted a PEG-based arm between DBCO alkyne and central CTA molecule. This increased the length of each arm of TDL and we anticipated that the flexibility of TDL3 would overcome stearic restrictions potentially forming higher MW macropolymers.

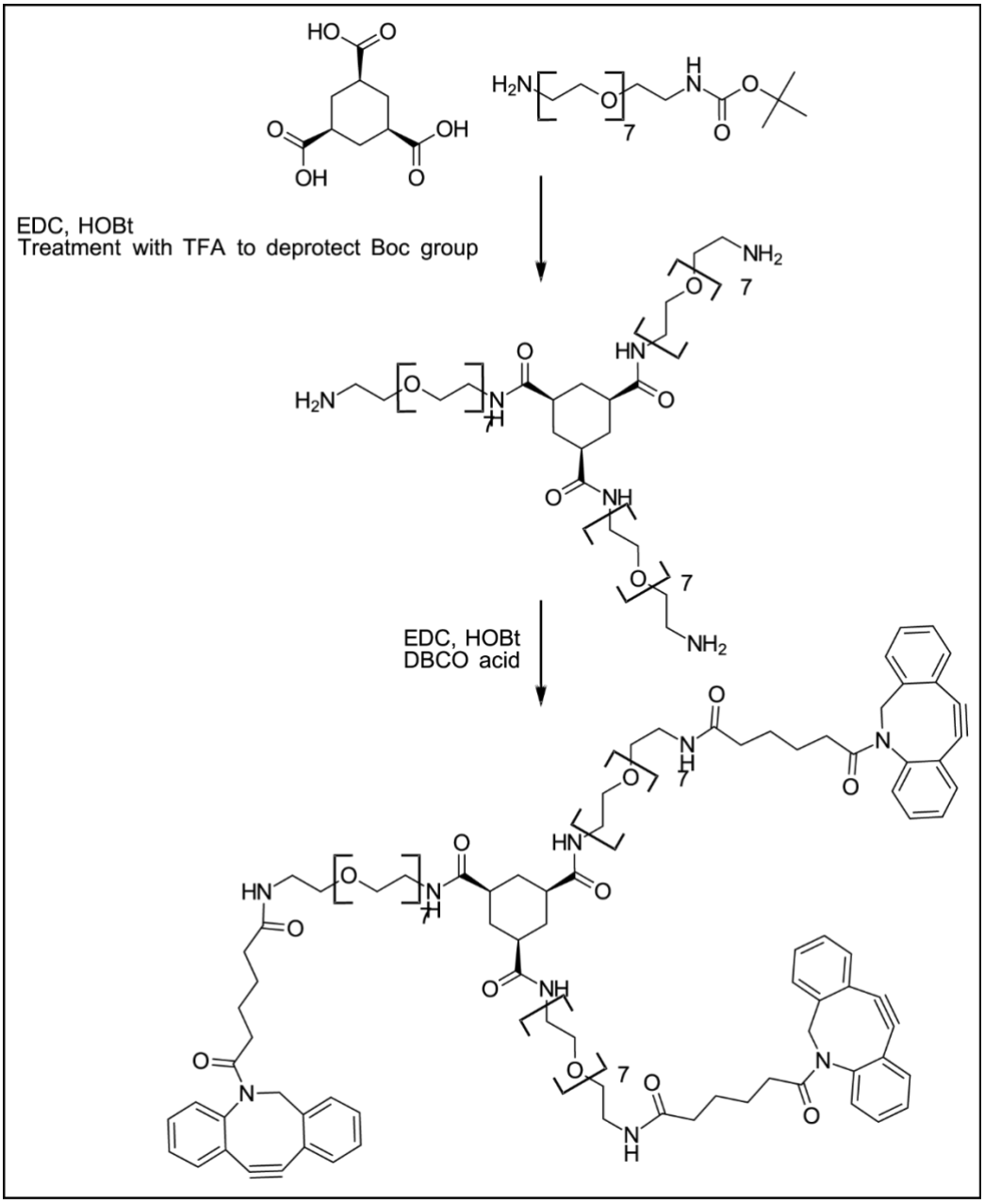

Figure 52: Synthesis of long arm TDL3.

The intermediate was attempted to be purified using flash chromatography. This purification was challenging because the product does not have any chromophore or ionizable group, the fractions from the flash column were difficult to analyze using TLC. On HPLC as well, the product had to be monitored at 205 nm where the baseline is often

noisy. Because the purification by flash chromatography was challenging, finally, it was purified using reversed phase semi-prep column. HPLC purification method – reversed-phase HPLC (flow rate 2 mL min^{-1}, runtime 30 min with 5 min post-run), solvent A (0.1% TFA in H_2O), solvent B (0.1% TFA in ACN), gradient 0% B to100 % B over 30 min, C18 Hypersil column (5 µm, 250 × 10 mm, Phenomenex), retention time: 33 min (Figure 54). The product purified was subjected to TFA cleavage in 10% DCM in TFA (0.5 mL) for 2 hours. Then TFA was evaporated, and the sample was dried. 1.8 mg of material was recovered. ESI-MS (m/z): $[M]^+$ calculated for, 1266.8; found, 1267.6 (Figure 53); analytical method – reversed-phase HPLC (flow rate 1 mL min^{-1}, runtime 30 min with 5 min post-run), solvent A (0.1% TFA in H_2O), solvent B (0.1% TFA in ACN), gradient 0% B to 100 % B over 30 min, C18 Hypersil column (5 µm, 250 × 4.6 mm, Phenomenex), retention time: 16-17 min (Figure 54).

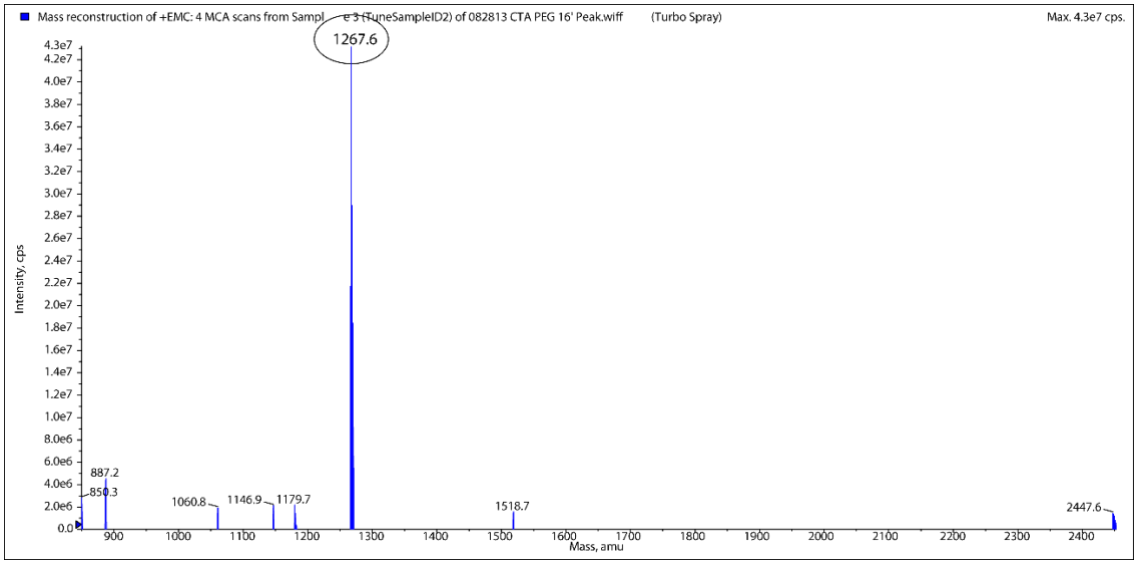

Figure 53: MS of purified TDL3 intermediate after TFA cleavage. The product is seen at $[MH]^+$=1267.6.

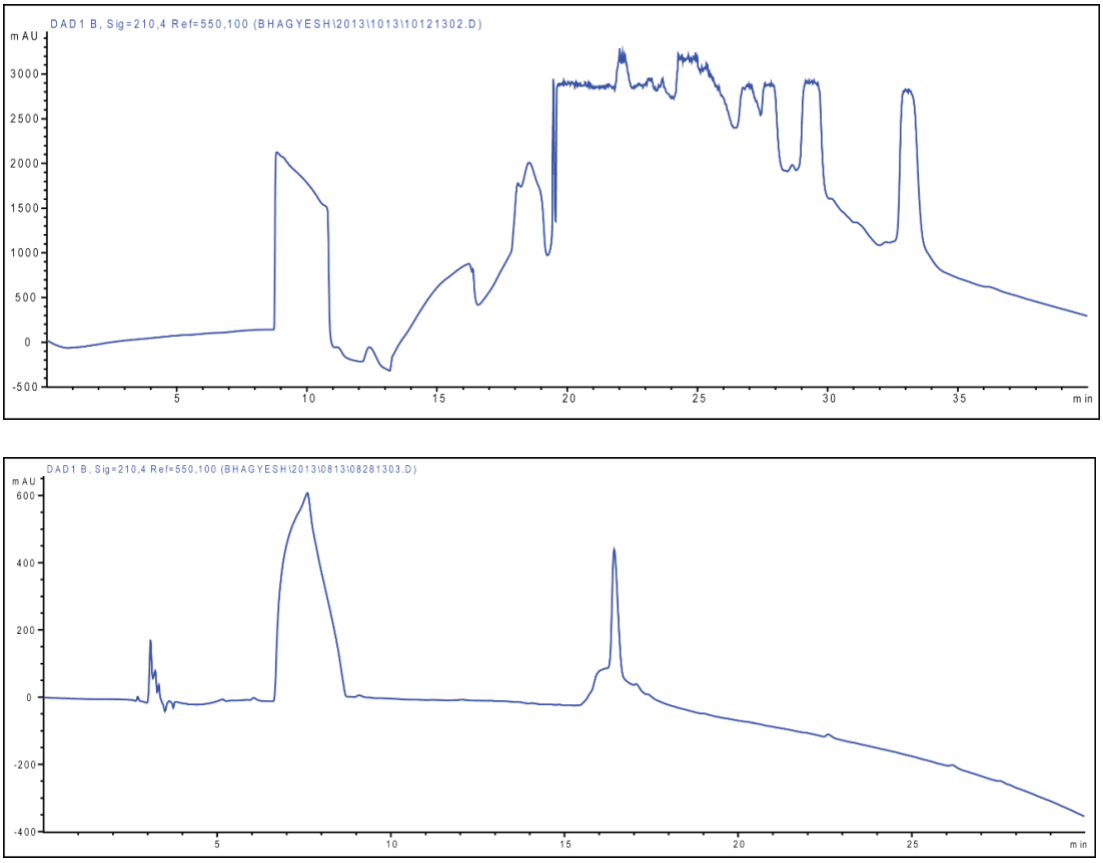

Figure 54: Upper chromatogram - Crude reaction mixture of the reaction, 33' peak was the product. After purification and TFA cleavage, it was analyzed by HPLC and is eluting at 17'(bottom). The peak between 6-9' in the bottom chromatogram is a solvent peak.

Step 2 – Coupling of DBCO acid to the intermediate to synthesize TD linker # 3

Once the TFA cleavage was performed, and the product was dried, and it was coupled to DBCO acid using HATU, DIEA conjugation chemistry. The intermediate (1.8 mg, 1.42 µmol), DBCO acid (3 mg, 9 µmol), HATU (Chem-Impex, 3.4 mg, 9 µmol) and DIEA (3.13 µL, 18 µmol) were mixed in 50 µL DMF. Then it was purified using normal phase HPLC (flow rate 2 mL min^{-1}, runtime 35 min with 5 min post-run), solvent A (H_2O (no TFA)), solvent B (ACN (no TFA)), gradient 100% B to 16.4 % B over 30 min, isocratic at 16.4% B for next 5 min, Silica Hypersil column (5 µm, 250 × 10 mm, Phenomenex), retention time ≈ 28 min (Figure 55); ESI-MS (m/z): $[M]^+$ calculated for, 2213.6; found,

2213.0 (Figure 56). Not all the crude mixture was purified, only a couple of rounds of HPLC were performed. About 20 nmol of TDL 3 were purified based on quantification using UV-vis spectrophotometry.

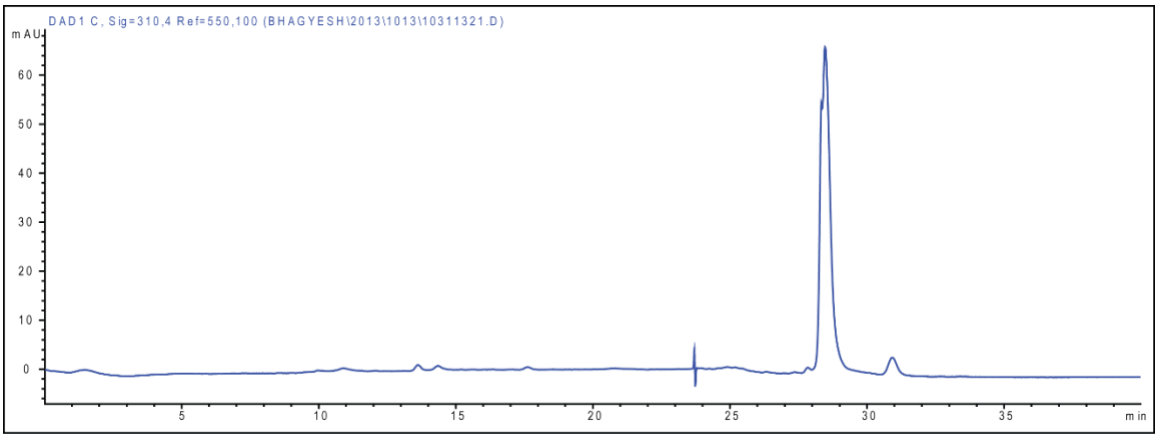

Figure 55: HPLC chromatogram of purified TDL3.

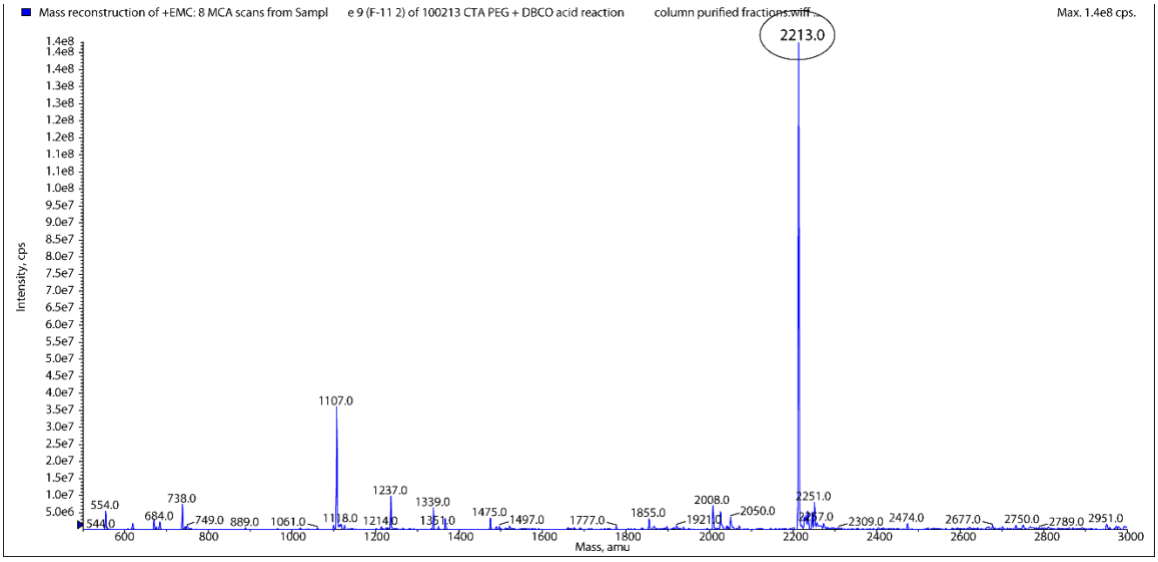

Figure 56: MS of purified TDL3. The product is seen at $[M]^+$=2213.0, calc. for 2213.6.

Polymerization attempt with long arm TDL3

The polymerization reactions were set up under similar conditions as performed earlier. The aim was to see if extending the length of arms of TD linker would affect the polymerization pattern and the extent of the polymerization reaction. For comparison, both TDL2 along with TDL3 was incorporated. The trimer reactions were also run in parallel. The stock solutions of each reagent were prepared in DMSO and analyzed by MS, HPLC and UV-vis spectroscopy. DIMA (25 mM), DIDA (5 mM), TDL2 (7.76 mM) and TDL3 (1.09 mM) (Table 4). The polymer reactions were diluted to 69.7 µL in 0.01 N HCl, and all reactions were performed overnight and analyzed using SDS-PAGE. The purpose of performing dilution using 0.01 N HCl was that diluting reduces the overall concentration of insulin and possibly helps to avoid aggregation. Extreme pH conditions may aid in this process too.

Table 4: A set of reactions of DMNPE insulin trimer and polymer using TDL2 and 3.

Reaction	TDL2 (nmol)	TDL3 (nmol)	Equivalents	DIMA (nmol)	DIDA (nmol)	Total vol. (µL)
Trimer – TDL2	1		3	3		1.2
Trimer – TDL3		1	3	3		
Polymer – TDL2	2		3	3	3	69.7
Polymer – TDL3		2	3	3	3	69.7

Results

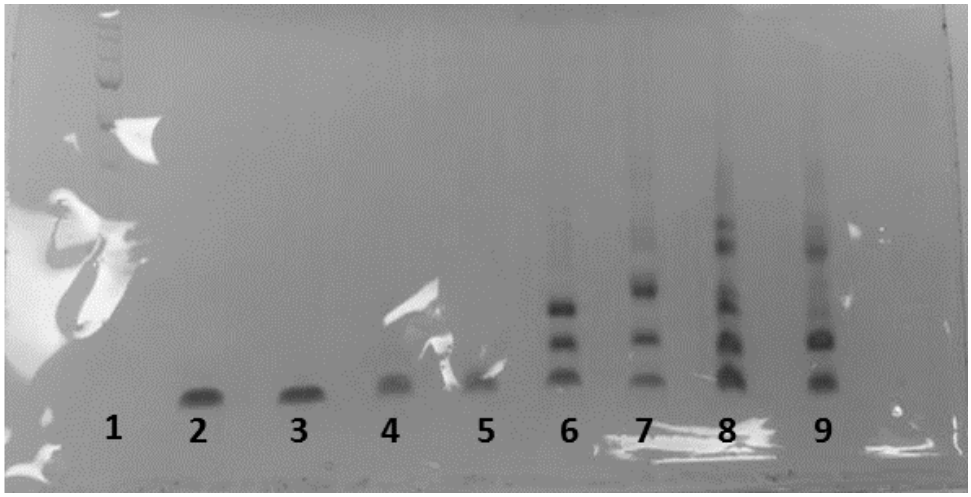

Figure 57: Characterization of the extent of polymerization of DMNPE insulin polymer using TDL2 and 3. Lane 1 – MW ladder, lane 2 – insulin std., lane 3 – insulin std. + TDL2, lane 4 – DIMA, lane 5 – DIDA, lane 6 – insulin trimer with TDL2, lane 7 – insulin trimer with TDL3, lane 8 – insulin polymer with TDL2, lane 9 – insulin polymer with TDL3.

In Figure 57, Lane 6 and 8 show insulin trimer and polymer respectively as demonstrated earlier using TDL2. Lane 7 shows insulin trimer using TDL3. Interestingly, it shows a very similar pattern as expected but the distance among bands is slightly larger, this makes sense as the MW of this linker is also larger compared to TDL2. However, the results were not so encouraging for polymerization reaction where the extent of polymerization is lesser than earlier polymer. Extending the length of TD arms had an unfavorable effect on the polymerization reaction. In fact, it predominantly stopped at the dimer stage. The quenching at the dimer stage was probably because of cross-linking occurring due to DIDA as explained in Figure 58. When one DIDA is conjugated on the TD linker, due to the increase in effective molarity, another end also reacts readily on an open alkyne of TD linker, effectively cross-linking intramolecularly and blocking a potential site of reaction as shown in Figure 58.

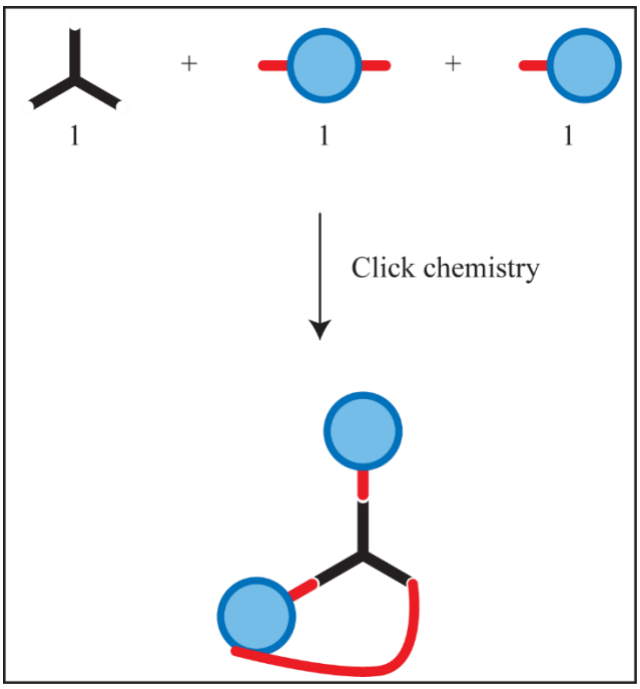

Figure 58: Cross-linking of TD linker caused by both azides of DIDA clicking on the same molecule of TD linker. A possible reason why polymerization stops at dimer step as shown here.

TD linker #4 – A short arm linker

Because we failed to see any effect after lengthening the arms of TD linker, for TDL3, in this approach, the length was reduced. We wanted to explore whether length might restrain the issue of intramolecular cross-linking by DIDA as shorter arms cannot undergo intramolecular cross-linking. The small linker chosen was 3-azido-1-propanamine (Sigma-Aldrich, 762016-100MG). Instead of incorporating it into TD linker; it was decided to incorporate it in DIMA and DIDA species. Using this linker, a new synthesis of insulin azide was designed. Newly synthesized DIMA and DIDA species were reacted with TDL2 to see how it works. The species were synthesized as shown in Figure 59 below and using newly synthesized DDA, insulin was caged.

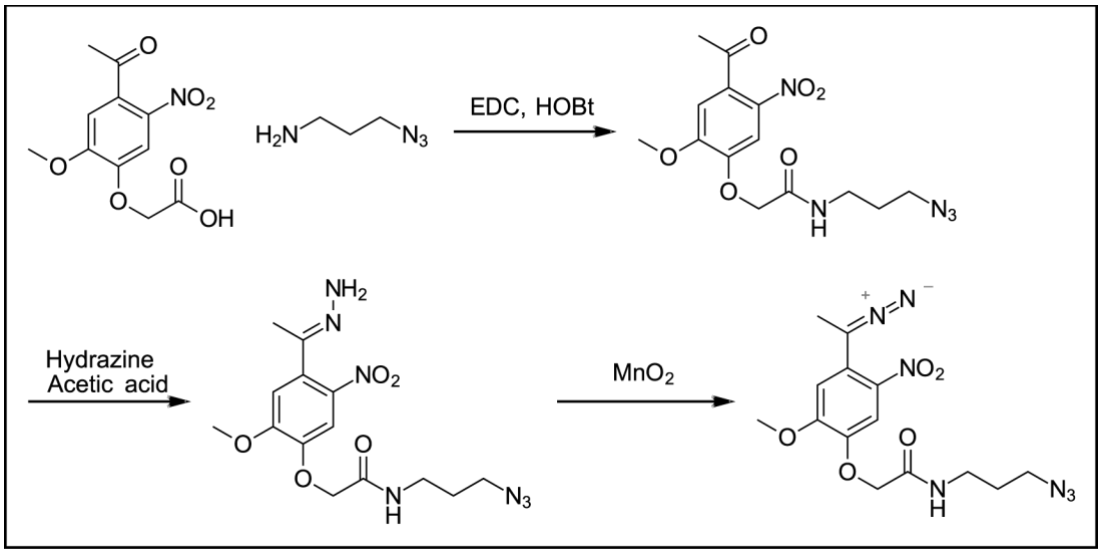

Figure 59: Synthesis of short length DDA by using 3-Azido-1-propanamine.

2-(4-Acetyl-2-methoxy-5-nitrophenoxy)-1-(3-azidopropylamino)-1-ethanone

NKA (100 mg, 371 µmol), 3-Azido-1-propanamine (39.1 µL, 380 µmol), HOBt hydrate (113.2 mg, 739.4 µmol) were dissolved in 1.3 mL DMF. Then EDC (123 mg, 640 µmol) was added and allowed to react overnight. The product was purified by partitioning the crude reaction mixture in water and EtOAc. The organic layer was first washed with 1N HCl, followed by saturated $NaHCO_3$, and finally with saturated NaCl. Then EtOAc layer was dried over $MgSO_4$ and filtered off. Yield = 121 mg (92.5%); ESI-MS (m/z): $[MH]^+$ calculated for $C_{14}H_{17}N_5O_6$, 352.1; found, 352.4 (Figure 60); analytical method – reversed-phase HPLC (flow rate 1 mL min^{-1}, runtime 30 min with 5 min post-run), solvent A (0.1% TFA in H_2O), solvent B (0.1% TFA in ACN), gradient 0% B to 100 % B over 30 min, C18 Hypersil column (5 µm, 250 × 4.6 mm, Agilent), retention time: 14.5-15 min (Figure 61).

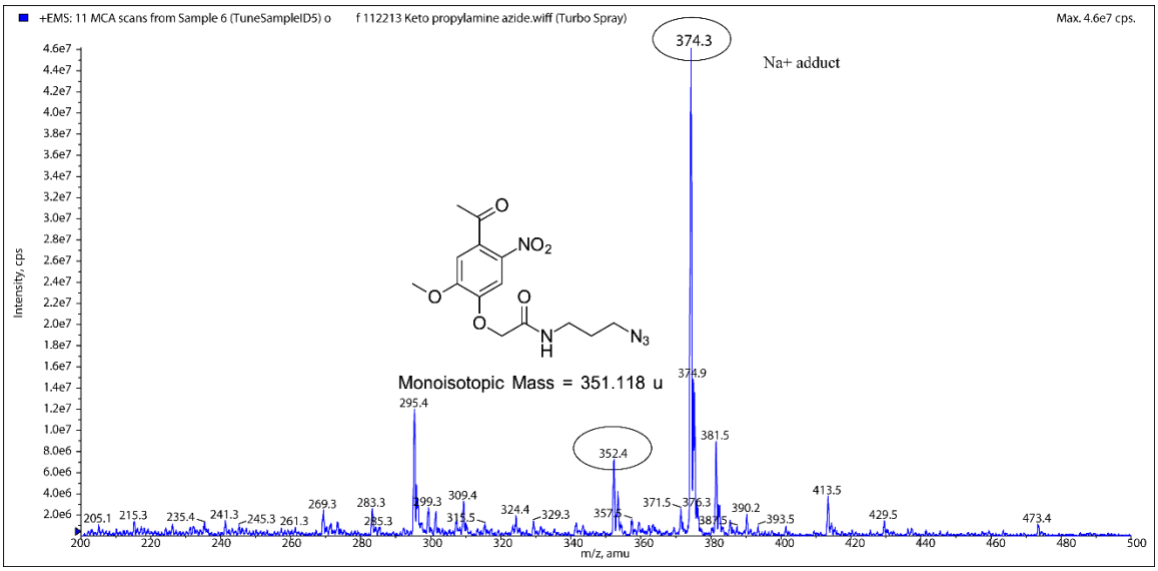

Figure 60: MS infusion of 2-(4-acetyl-2-methoxy-5-nitrophenoxy)-1-(3-azidopropylamino)-1-ethanone. The product mass is seen at $[MH]^+$=352.4.

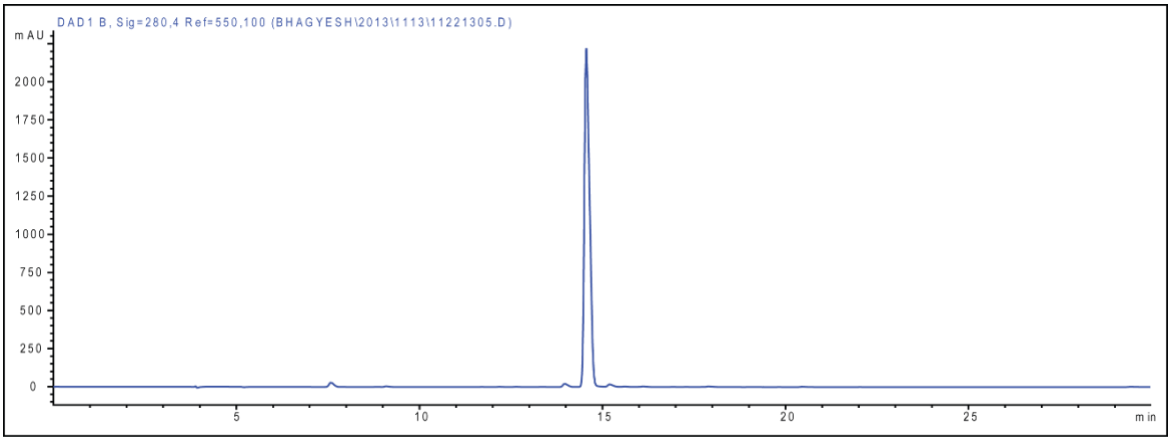

Figure 61: HPLC chromatogram of 2-(4-acetyl-2-methoxy-5-nitrophenoxy)-1-(3-azidopropylamino)-1-ethanone.

1-(3-Azidopropylamino)-2-{2-methoxy-4-[1-(methylimino)ethyl]-5-nitrophenoxy}-1-ethanone

(35.2 mg, 100 µmol) of 2-(4-Acetyl-2-methoxy-5-nitrophenoxy)-1-(3-azidopropylamino)-1-ethanone was dissolved in the 2.8 mL mixture of acetonitrile: ethanol (1:1). To this, glacial acetic acid (32.2 µL, 0.563 mmol) and hydrazine monohydrate

(Sigma-Aldrich, 64.6 µL, 1.33 mmol) were added. The reaction was performed in a closed sealed vial at 90 °C for 5 hours. After 5 hours, the reaction mixture was evaporated using rotavap. The crude mixture was dissolved in 5% methanol (MeOH) in dichloromethane (DCM) and purified using flash chromatography. Yield (17 mg, 46%); TLC (EtOAc/MeOH, 75:25 v/v): Rf = 0.33 and 0.46; LCMS method – reversed-phase HPLC-MS (flow rate 0.4 mL min^{-1}, runtime 30 min with 5 min post-run), solvent A (0.1% FA in H_2O), solvent B (0.1% FA in ACN), gradient 0% B to 50 % B over 5 min, gradient 50% B to 100 % B until 27, gradient 100% B to 0% B for next 2 min and isocratic 100% A for next 1 min; C18 Hypersil column (5 µm, 250 × 4.6 mm, Agilent), retention time: 15.04 min; ESI−MS (m/z): $[MH]^+$ calculated for, 366.1; found, 366.1 (Figure 62).

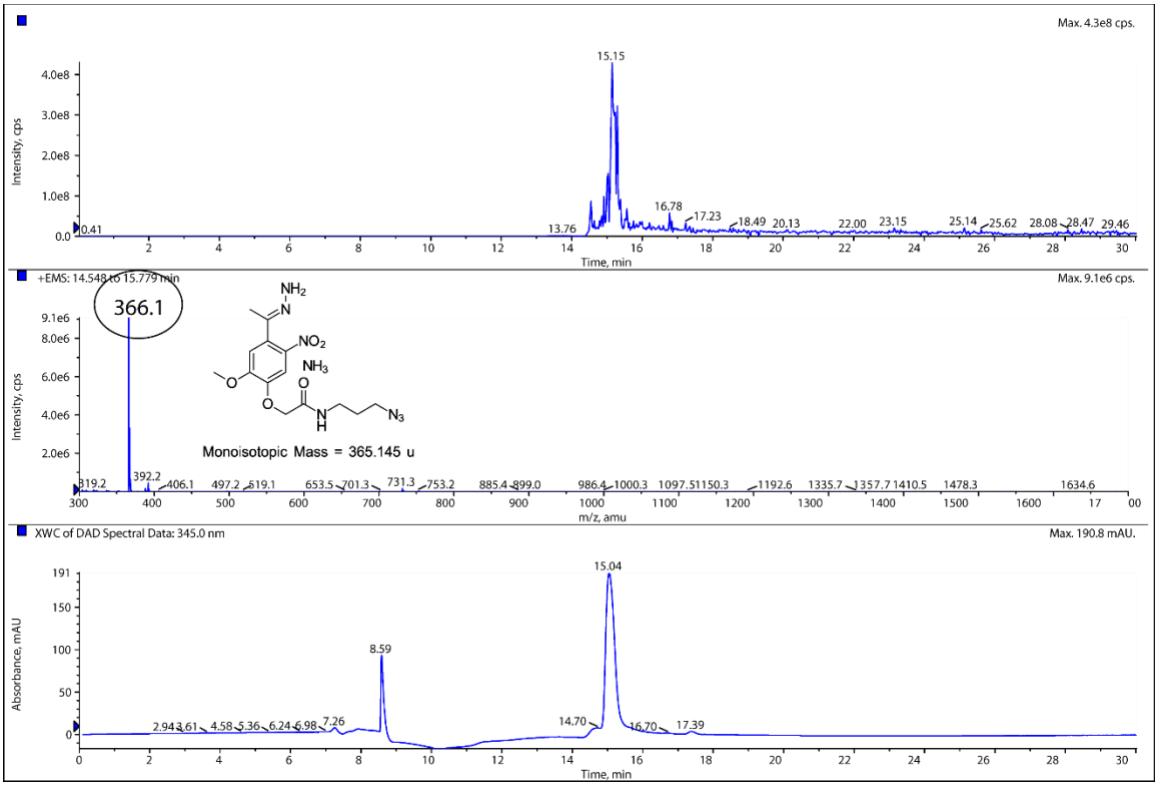

Figure 62: LCMS run of 1-(3-azidopropylamino)-2-{2-methoxy-4-[1-(methylimino)ethyl]-5-nitrophenoxy}-1-ethanone showing a single peak at 15' with a mass of 366.1.

Caging of insulin by shorter DDA

167 µL (70.0 mM solution in anhydrous DMSO, 11.7 µmol) of 1-(3-azidopropylamino)-2-{2-methoxy-4-[1-(methylimino)ethyl]-5-nitrophenoxy}-1-ethanone was mixed with 15 mg MnO_2 and allowed to vortex for 45 min in the dark. The red-black mixture was centrifuged, and the supernatant was filtered through Celite 545 using glass-wool/glass-pipette. The pipette was washed with anhydrous DMSO thrice to get final diazo solution of 800 µL. The successful diazo conversion was indicated by red color formation. In another tube, 25 mg (4.3 µmol, SAFC-91077C) of insulin was dissolved in 1 mL of anhydrous DMSO. The formed diazo solution was added to insulin. The volume was made up to 2.15 mL to make the concentration of insulin 2 mM by adding DMSO. The reaction was run for 24 hours in the dark. After 24 hours, DMSO was removed via freeze-drying. The dried residue was dissolved in 0.01N HCl and filtered through 5 kDa MWCO filters (Vivaspin®) and washed twice with 0.01N HCl. The fractions were collected from HPLC and DIMA, DIDA stock solutions in DMSO were prepared. Analytical method – reversed-phase HPLC (flow rate 1 mL min^{-1}, runtime 30 min with 5 min post-run), solvent A (0.1% TFA in H_2O), solvent B (0.1% TFA in ACN), gradient 0% B to 100 % B over 30 min, C18 Hypersil column (5 µm, 250 × 4.6 -mm, Agilent), retention time: DIMA-16-17 min, DIDA-17-18 min (Figure 63); ESI-MS (m/z) $[M]^+$ calculated for DIMA, 6144.0; found, 6143.0 (Figure 64); $[M]^+$ calculated for DIDA, 6478.0; found, 6476.0 (Figure 65).

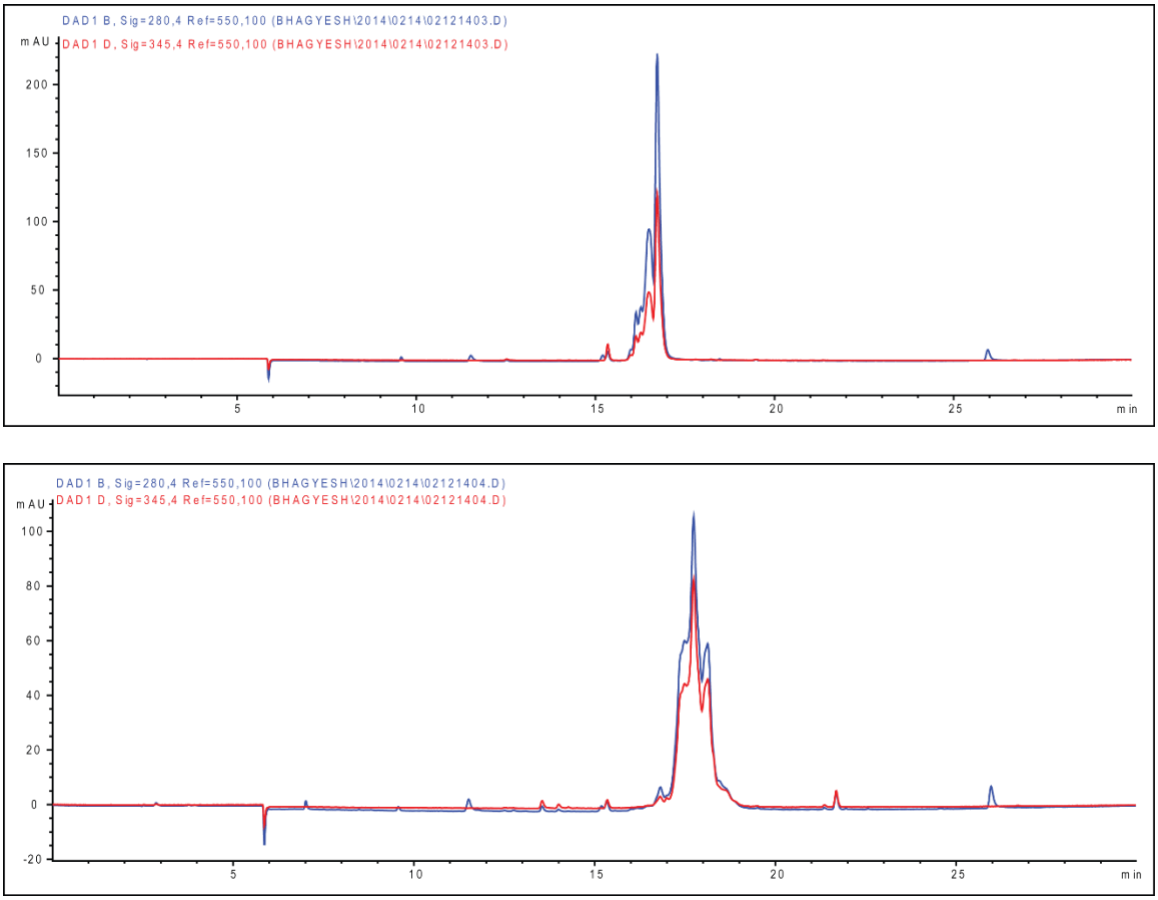

Figure 63: HPLC chromatograms of DIMA (top) and DIDA (bottom) with the short linker.

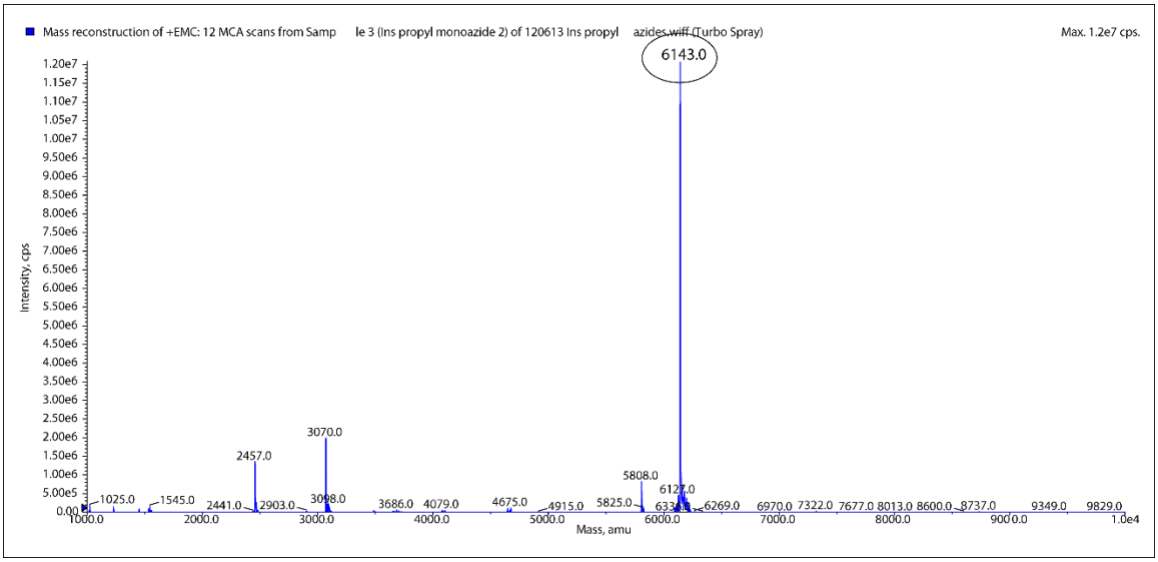

Figure 64: MS infusion of DIMA (top). The purified DIMA mass is seen at $[M]^{+}$=6143.0 (calc. 6144.0).

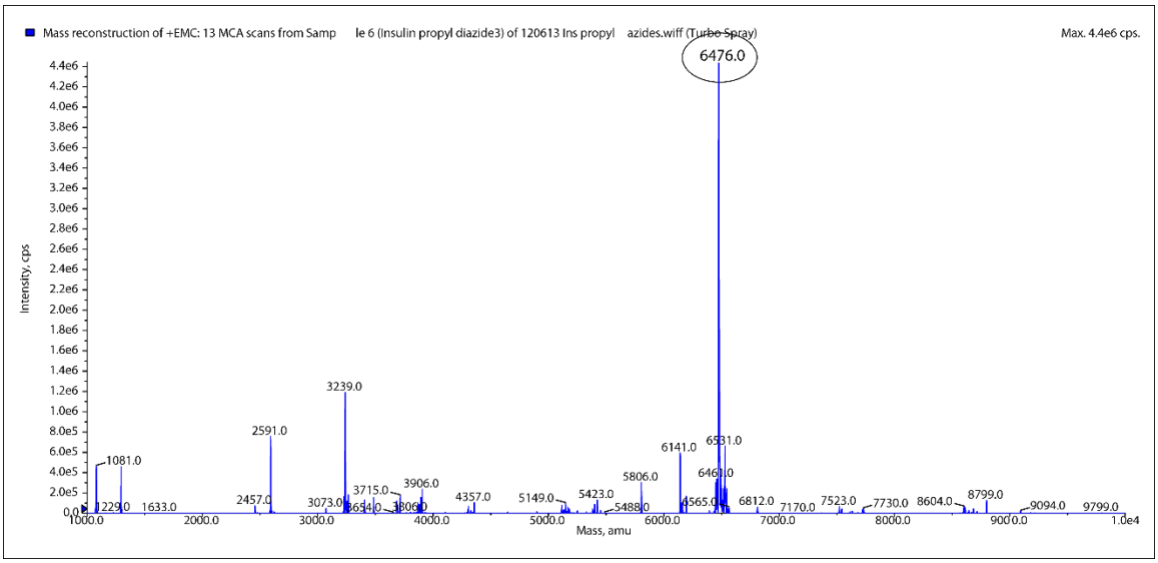

Figure 65: MS infusion of DIDA (bottom). The purified DIDA (bottom) is seen at $[M]^+$ =6476.0 (calc. 6478.0).

Macropolymerization attempt with short insulin azide linker and TDL2

The polymer reaction of this new insulin azide linker with TDL2 was tested and analyzed to see if there is any improvement over long-armed linker. Both trimer and polymer reactions were set up. For trimer reaction, DIMA (0.38 µL, 3 nmol) and TDL2 (1.52 µL, 9 nmol) were mixed and incubated at 37 °C overnight and analyzed by SDS-PAGE. Similarly, DIMA (0.68 µL, 4 nmol), DIDA (1.3 µL, 4 nmol) were mixed, and TDL2 (0.51 µL, 4 nmol) was added. The reaction was incubated overnight at 37 °C.

Results

The results are shown in Figure 66 were very similar to what was observed with old insulin azide linker. There was no improvement in the extent of polymerization.

Because all the other attempts to improve the polymerization have yielded no improvements over the very first attempts with original TD linker and insulin azides, it was decided to use the original reagents and perform polymerization reaction. Like the

photolysis of trimer, the photolysis of insulin macropolymer was conducted and analyzed.

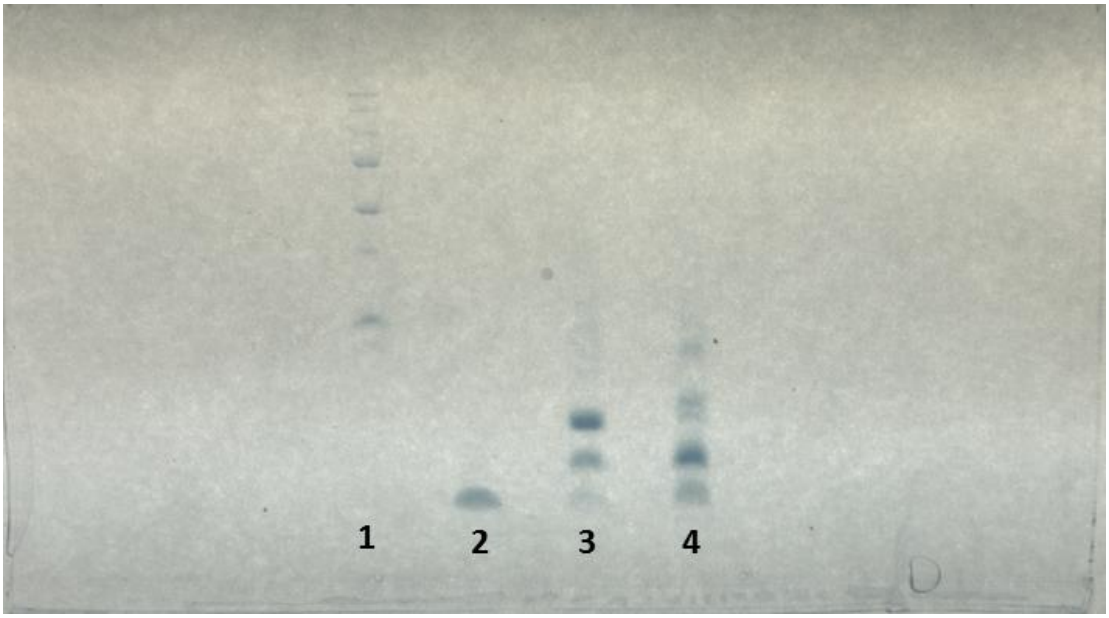

Figure 66: Characterization of the extent of polymerization of DMNPE insulin polymer using TDL2. Lane 1 – MW ladder, lane 2 – insulin std., lane 3 – insulin trimer, lane 4 – insulin polymer.

DMNPE insulin polymer photolysis in DMSO

Although we tried different tris-DBCO cross-linkers, they all seemed to give similar results – no linker was better than another. Since we had plenty of TDL2 synthesized, we decided to use it for macropolymerization and its subsequent characterization. DIMA (19.15 µL, 145 nmol), DIDA (16.86 µL, 145 nmol) were mixed, and to this mixture TDL2 (16.11 µL, 140 nmol) was added. All stock solutions were prepared in DMSO. The reaction was incubated for 48 hours at 37 °C. It was later analyzed by SDS-PAGE and photolysis.

The polymer sample prepared above was run on a gel (Criterion TGX Any Kd precast gel from Bio-rad) using Criterion vertical midi-format electrophoresis cell (Bio-rad) at 150V. Upon running on a gel, a few new bands were observed as before. The

samples in DMSO were withdrawn and mixed in 1:1 with sample loading buffer. This mixture was loaded into the gels. In parallel, the crude reaction mixture which is in DMSO was photolyzed using a Blak-Ray lamp (Model XX-15L, 30 watts) source. For photolysis, 6.26 µL of the reaction mixture was diluted to 45 µL in DMSO and aliquoted into a 96 well plate (BD Falcon). The mixture was irradiated from the top using the UV-vis lamp from 10 cm distance. 5 µL samples were withdrawn at 0, 1, 2, 4, 6, 8, 10, 20 min time points and run on SDS-PAGE. The final time point was also analyzed by MS infusion.

We saw 4-6 new higher bands (Figure 67). The upper band corresponded to higher MW species ranging from dimer to hexamers. The mixture was then photolyzed from the top using the blak-ray lamp at a 10-cm distance. As the sample was being irradiated, the higher bands are gradually disappeared and the bottom band which corresponded to insulin became darker. The pattern suggested that trimer was being photocleaved by light to give native insulin molecules. The bottom band was consistent with the mobility of insulin std. The final time point at t=20 min was also infused in MS to detect any mass of insulin. It only showed a single mass of insulin, $[M]^+$ calculated, 5808.0; found, 5807.0 (Figure 68).

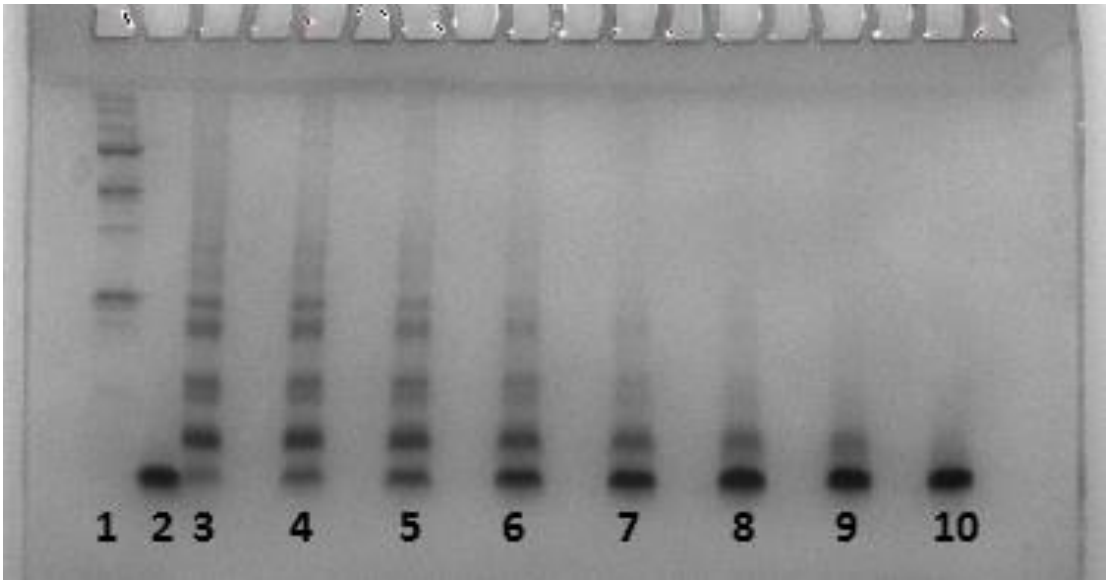

Figure 67: Characterization of DMNPE insulin polymer using SDS-PAGE. Lane 1-molecular weight ladder, lane 2-insulin std., lane 3-DIMA+DIDA mixed with TDL2 in 1:1:1 ratio at t=0 min, lane 4 – t=1 min, lane 5 – t=2 min, lane 6 – t=4 min, lane 7 – t=6 min, lane 8 – t=8 min, lane 9 – t=10 min and lane 10 – t=20 min of photolysis.

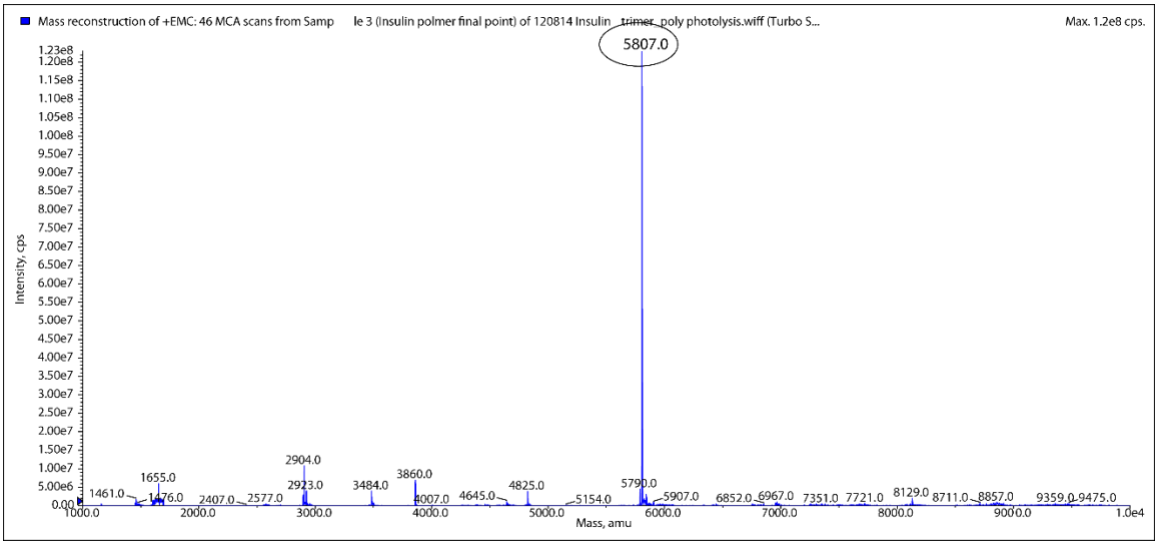

Figure 68: MS infusion of final time point from the photolysis of DMNPE insulin polymer. The $[M]^+$ of insulin at 5807.0 (calc. for 5808.0).

The above experiment was performed in DMSO where polymer species were soluble. However, in the real-world, DMSO will be replaced by bodily fluids. It is essential

that polymer material is insoluble in such aqueous solutions if we want to retain it at the site after injection. Otherwise, after injection, the material would diffuse away from the location and the depot no longer will exist. To test this hypothesis, the polymer material which was originally synthesized in DMSO was dried using a freeze dryer. PBS was added to the dried residue, the material precipitated out, and the solution became turbid. PBS was used because of its composition, osmolarity is closer to plasma, and the ways the material behaves here might give us some idea of how it would behave in a patient. The photocleavage of this material was tested using a 365 nm LED designed by Dr. Friedman in the same manner the trimer material was analyzed.

Photocleavage of DMNPE insulin polymer in PBS

The polymer crude mixture was added to two HPLC glass inserts (one for experimental and one for the control). HPLC glass vial insert (flat bottom glass vial inserts 100 µL, diameter 3.4 mm (inner), 4.5 mm (outer), height 30.5 mm (Agilent, 5183-2090) was used. The original reaction mixture which was in DMSO was added to these vials and freeze-dried overnight to get rid of all DMSO. Then 100 µL PBS was added to it, and the pellet which was at the bottom was scratched out using a needle to suspend the trimer material uniformly in PBS properly. For t=0, the sample in the insert was vortexed, centrifuged and half of it was withdrawn and replaced with fresh PBS. This procedure was repeated at the time of collection of each time point. The experimental samples were irradiated from the bottom by keeping the glass insert right on top of the LED. For the control samples, the volume was withdrawn at the time points after vortexing followed by centrifugation. The control samples were kept in the dark, not exposed to light.

HPLC was not used because the quantity that was released was too low to be detected by HPLC. Also, there was a concern whether other polymer components might get solubilized and elute at the same retention time as insulin, this would make the analysis challenging and complicated. The samples were analyzed by SDS-PAGE to confirm the presence of insulin in the supernatant. Because of small insulin quantity, it could not be detected using Coomassie blue staining. Hence, we used silver staining which is more sensitive (Thermo Fisher Scientific) as shown in Figure 69. The supernatant was also analyzed using MS. Because we were anticipating a much lower quantity of insulin in the material, we pooled all the supernatant solutions for MS analysis. This pooled solution was spin-filtered using 5000 Da MWCO filter to get rid of salt from PBS. The salt prevents ionization of insulin in MS. After spin filtration, the sample was dissolved in 0.01 N HCl and infused into the MS. [M] calculated 5808.0; found, 5808.0 (Figure 70). The release of insulin is seen in the experimental points (Figure 71) which were irradiated but not from the control samples which were kept in the dark. There was a brief lag period before insulin started appearing in the supernatant. The delay might be because, in the initial phases of photolysis, the macropolymer is just breaking apart into smaller MW constructs but not much insulin is being released. However, as the irradiation went on, newly formed smaller MW constructs underwent photolysis to give insulin. Hence it is not seen in the initial phases. The samples were also analyzed by ELISA to measure the concentration of insulin present in the supernatant.

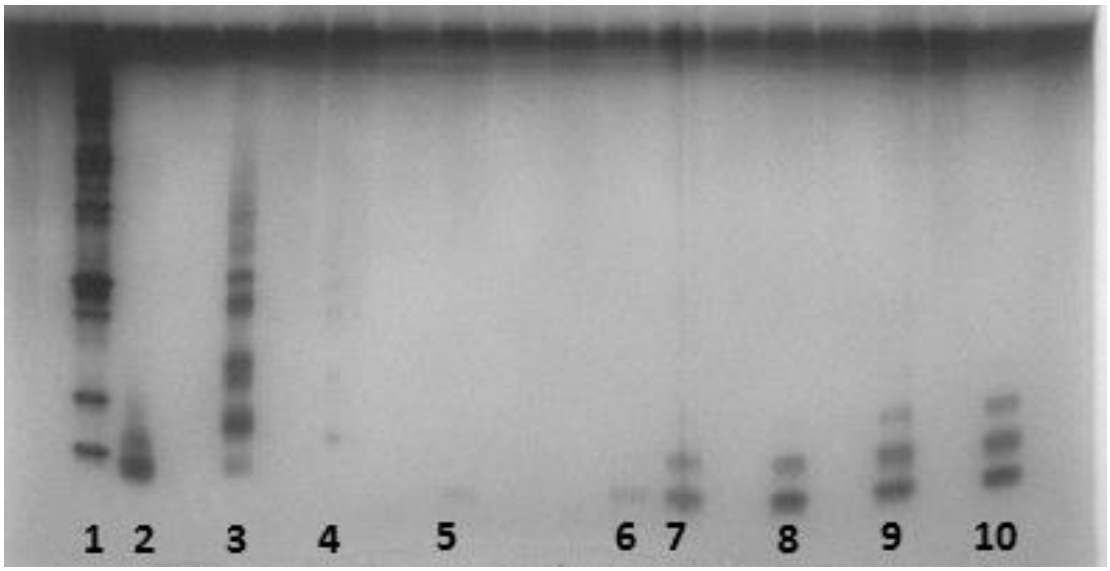

Figure 69: Characterization of photolysis of DMNPE insulin polymer in PBS using SDS-PAGE (silver staining). Lane 1-molecular weight ladder, lane 2-insulin std., lane 3-insulin trimer mixture in DMSO, lane 4-DMNPE insulin trimer crude mixture at t=0, lane 5-mixture at t=5 min, lane 6-mixture at t=15 min, lane 7-mixture at t=25 min, lane 8-mixture at t=35 min, lane 9-mixture at t=45, lane 10-mixture at t=55 min after photolysis is DMSO using the point source.

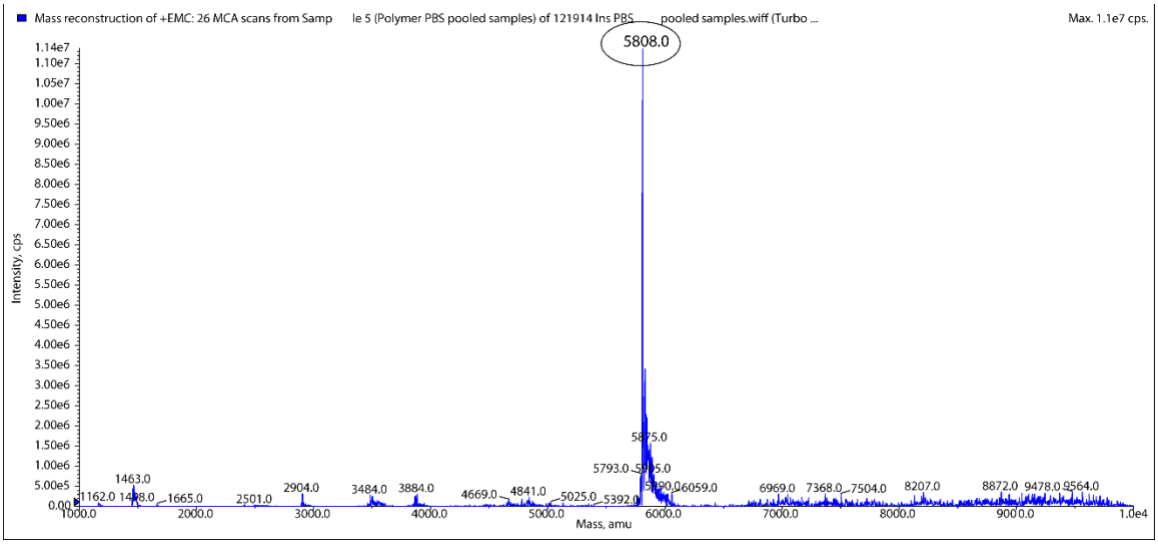

Figure 70: MS infusion of DMNPE insulin polymer samples photolyzed in PBS. The samples were pooled, combined and infused in MS. The mass $[M]^+$ is seen at 5808.0.

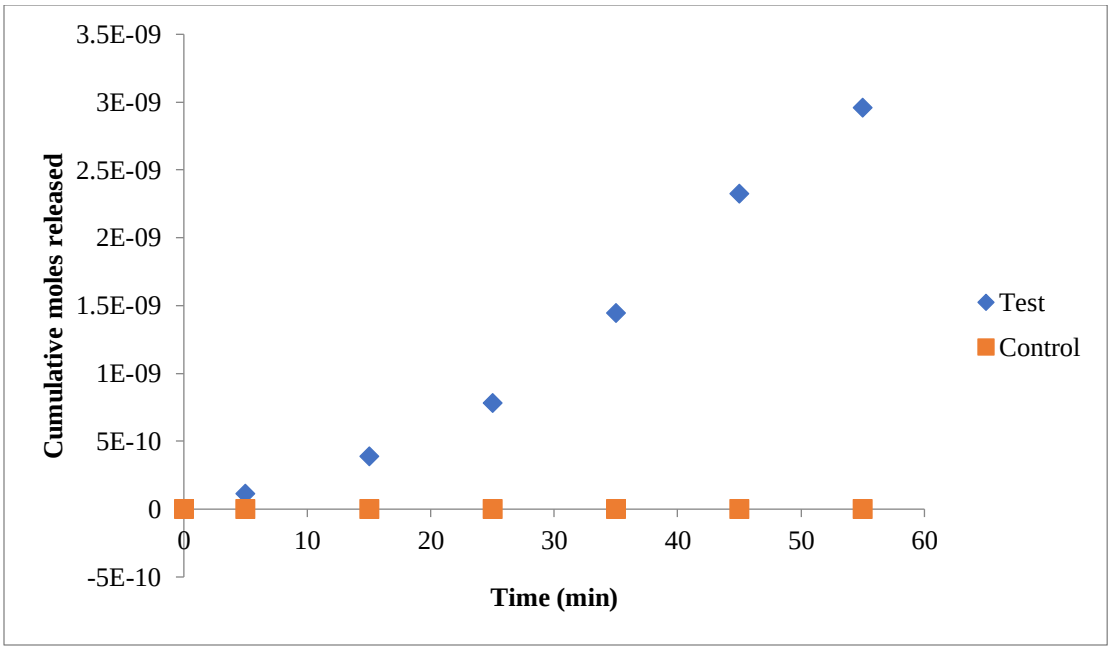

Figure 71: Insulin release as measured using ELISA from DMNPE insulin macropolymer photolysis in PBS using the LED point source.

Macropolymer synthesis using insulin lispro

Insulin lispro is a fast-acting insulin analog. In lispro, lysine and proline residues on B chain are reversed by using recombinant DNA technology. This change prevents the dimer and hexamer formation in insulin lispro. Thus, lispro stays predominantly in the monomer form and hence it has faster absorption kinetics into the systemic circulation.[52] This is shown in Figure 72 comparing its absorption with human regular insulin. It has a rapid onset of action.

Insulin monomers have an inherent tendency to undergo self-association to form higher order aggregates such as dimers, tetramers, hexamers, and polymers of hexamers.[53] In the pancreas, proinsulin hexamer aggregates are soluble but once converted to insulin hexamers, the hexamers precipitate out as microcrystals. Zn^{2+} ions or other divalent cations

are known to stabilize the hexamers by complexing with histidine residues. It is known that hexamer formation stores, protects, and stabilizes insulin in the pancreas.[54] When insulin is required, it is secreted from the beta cells in response to rising blood sugar levels. In the bloodstream, the hexamers dissociate into monomers due to a reduced concentration of zinc in the blood compared to beta cells and slightly higher pH which favors the dissociation. The monomer is active form and binds to the receptors to promote the uptake of glucose. The rate of dissociation has a crucial effect on the rate of absorption of insulin and the pharmacokinetic properties. The faster the hexamers dissociate to form monomers, the faster is its absorption and quicker therapeutic effect. The fast-acting insulin analogs are designed such that there will be minimum aggregation and hexamer formation. While the delayed acting insulin analogs are prepared by complexing insulin hexamers with zinc to increase circulation time and prolong the response.[55]

One of the hypotheses why the polymerization reaction of insulin is being quenched at certain stage might be because of overcrowding and steric hindrance. The inherent tendency of insulin to multimerize and self-aggregate might be making the reaction even more challenging. The overcrowding might render the reaction sites inaccessible hindering the progress of reactions. To prevent this issue, we thought of using insulin lispro as it has a reduced tendency to aggregate and form multimers. It might potentially allow the reactions to move forward and we can synthesize higher MW insulin macropolymers. To test this hypothesis, similar reactions were performed and repeated except regular insulin was replaced with insulin lispro analog (Sigma Aldrich, catalog # Y0000348).

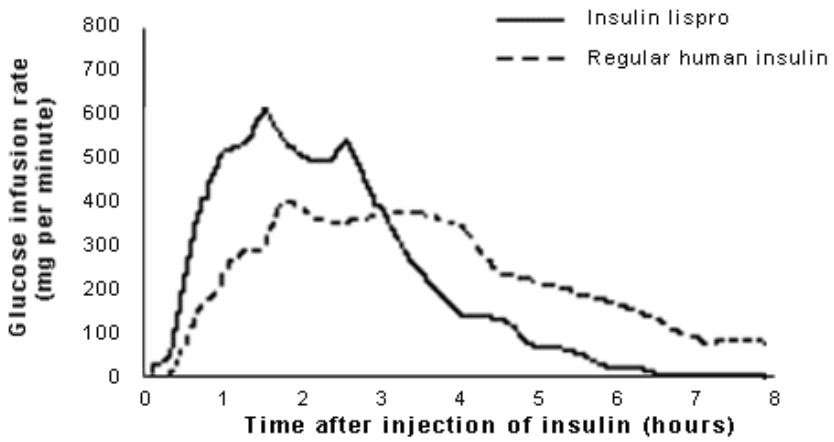

Figure 72: Absorption profile of insulin lispro vs regular human insulin.[56]

Caging of insulin lispro

Aliquot (112 µL, 86.1 mM solution in anhydrous DMSO, 9.67 µmol) of N-(2-{2-[2-(2-azido-ethoxy)-ethoxy]-ethoxy}-ethyl)-2-[4-(1-hydrazono-ethyl)-2-methoxy-5-nitro-phenoxy]-acetamide was mixed with 23.35 mg MnO_2 and vortexed for 45 min in the dark. The red-black mixture was centrifuged, and the supernatant was filtered through Celite 545 using glass-wool/glass-pipette. The pipette was washed with anhydrous DMSO thrice to get a final diazo solution of 576 µL. Successful diazo conversion is indicated by red color formation. In another tube, 21.4 mg (3.68 µmol, Sigma-Aldrich, catalog # Y0000348) of insulin was dissolved in 0.8 mL anhydrous DMSO. The formed diazo solution was added to insulin. The volume was made up to 1.84 mL using DMSO to make the final concentration of insulin 2 mM. The reaction was performed for 24 hours in the dark. After 24 hours, DMSO was evaporated using freeze-drying. The dried residue was dissolved in 0.01N HCl and filtered through 5 kDa MWCO filters (Vivaspin) and washed twice with 0.01N HCl. Caged insulin species were purified using the semi-prep column on HPLC. Purification method – reversed-phase HPLC (flow rate 2 mL min^{-1}, runtime 45 min with

5 min post-run), solvent A (0.1% TFA in H_2O), solvent B (0.1% TFA in ACN), gradient 0% B to 75 % B over 45 min, C18 Hypersil column (5 µm, 250 × 10 mm, Phenomenex).

DMNPE insulin lispro mono-azide (DILMA)

ESI-MS (m/z): $[M]^+$ calculated for, 6267.0; found, 6264.0 (Figure 73); Analytical method – reversed-phase HPLC (flow rate 1 mL min^{-1}, runtime 30 min with 5 min post-run), solvent A (0.1% TFA in H_2O), solvent B (0.1% TFA in ACN), gradient 0% B to 100 % B over 30 min, C18 Hypersil column (5 µm, 250 × 4.6 mm), retention time: 16-17 min (Figure 74).

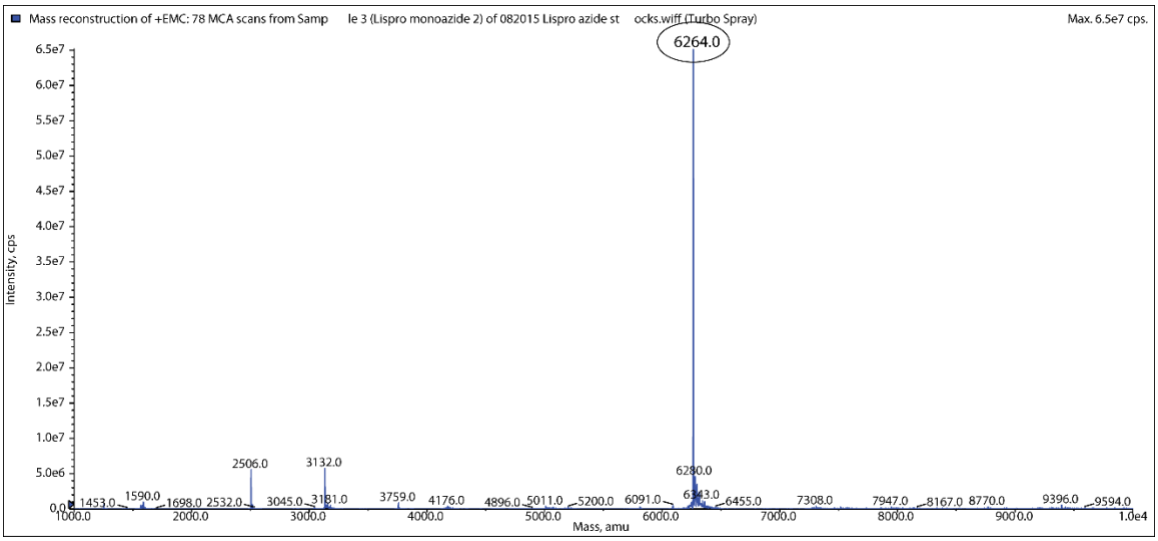

Figure 73: MS of purified DILMA. The product is seen at $[M]^+$=6264.0; calc. 6267.0.

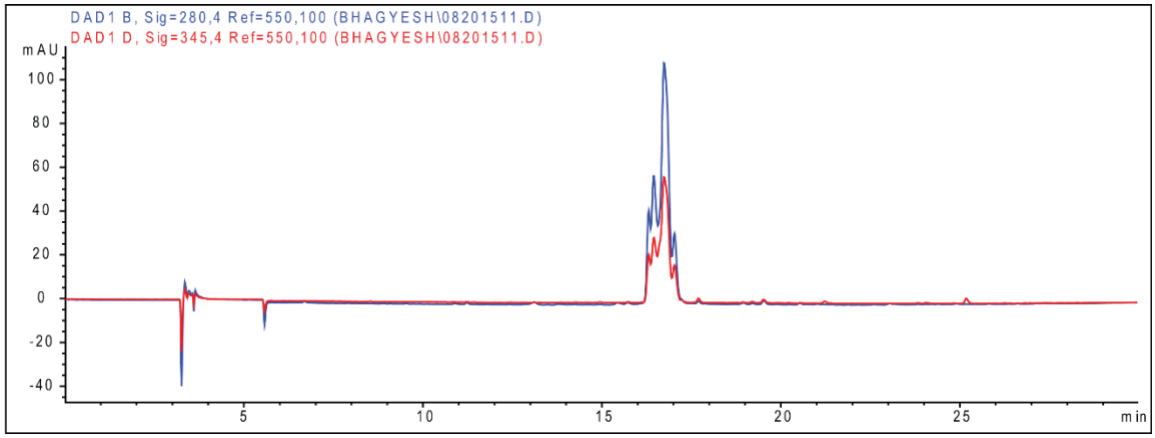

Figure 74: HPLC chromatogram of DILMA.

DMNPE insulin lispro di-azide (DILDA)

ESI-MS (m/z): $[M]^+$ calculated for, 6719.0; found, 6717.0 (Figure 75); Analytical method – reversed-phase HPLC (flow rate 1 mL min^{-1}, runtime 30 min with 5 min post-run), solvent A (0.1% TFA in H_2O), solvent B (0.1% TFA in ACN), gradient 0% B to 100 % B over 30 min, C18 Hypersil column (5 µm, 250 × 4.6 mm), retention time: 17-19 min (Figure 76).

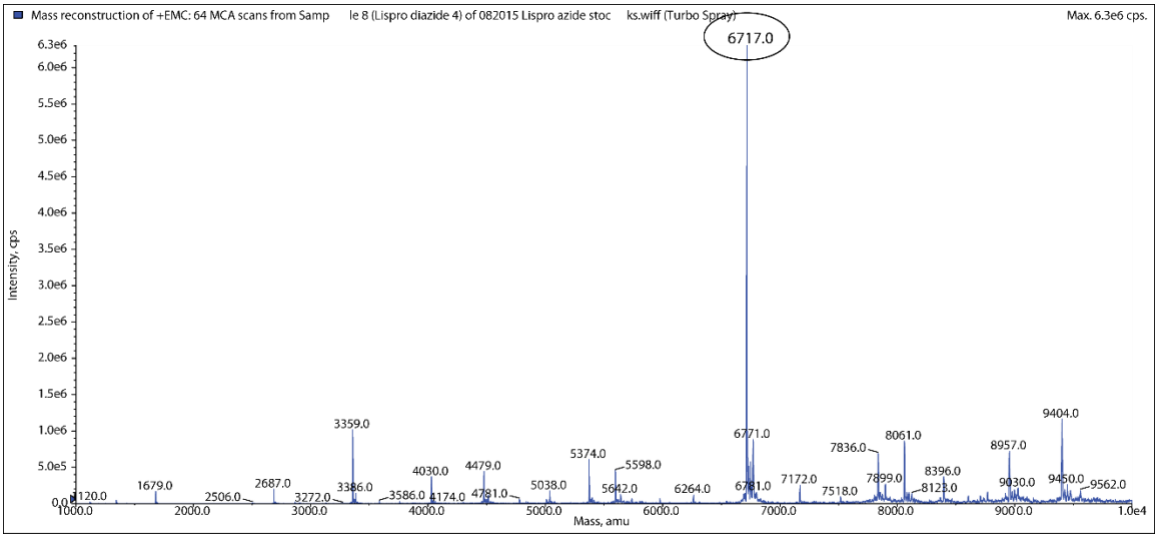

Figure 75: MS of purified DILDA. The product is seen at $[M]^+$=6717.0, calc; for 6719.0.

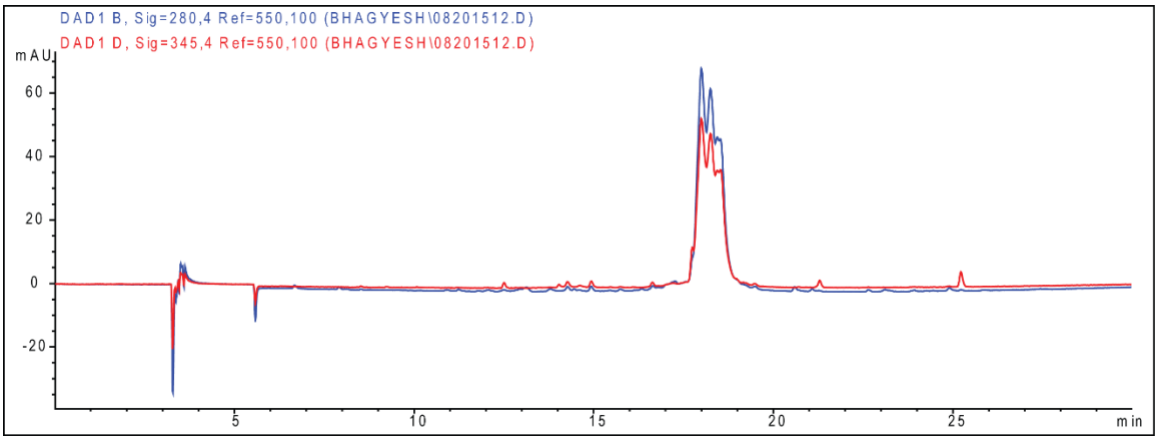

Figure 76: HPLC chromatogram of purified DILDA.

The stock solutions were prepared in DMSO of DILMA, DILDA and TDL 2. The concentrations were as follows; DILMA (11.95 mM), DILDA (7.42 mM) and TDL2 (8.69 mM). For the preparation of trimer, TDL2 (6 nmol, 0.69 µL) and DILMA (19.8 nmol, 1.65 µL) were mixed and incubated at 37 °C overnight. For the synthesis of the polymer, DILMA (5.175 nmol, 0.43 µL) and DILDA (5.175 nmol, 0.69 µL) were premixed and then combined with TDL2 (5 nmol, 0.575 µL) and incubated at 37 °C overnight. The mixtures were then analyzed by running on a gel. A part of the mixture was also photolyzed using 365 nm lamp to confirm that formed material is undergoing photolysis to release the native insulin.

The results of polymerization as shown in Figure 77 using insulin lispro were not different from what we have observed with regular human insulin. There were 3-4 prominent new bands observed but not more than. It suggested that even with non-aggregating insulin, the reactions are being quenched. Perhaps aggregation is not the issue but rather something else which is causing the quenching. It will be worth investigating the effect of concentration, pH, solvent, and using a different length of TD linker with insulin lispro.

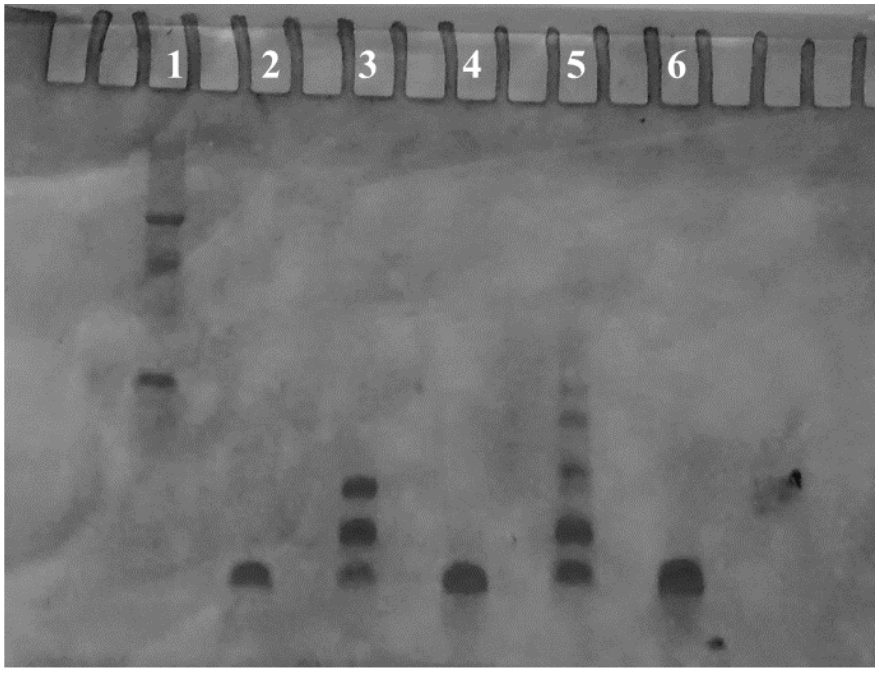

Figure 77: Characterization of the extent of polymerization of DMNPE insulin lispro trimer and polymer using SDS-PAGE. Lane 1-molecular weight ladder, lane 2-insulin std., lane 3 – Insulin lispro trimer, lane 4 – insulin lispro trimer photolyzed for 10 min, lane 5 – insulin lispro polymer, lane 6 – insulin lispro polymer photolyzed for 10 min.

Chapter 3

IN-VIVO TESTING OF FIRST-GENERATION PAD MATERIAL

Rationale and hypothesis

The synthesis of first-generation material was reported earlier in the lab and described in Chapter 1. The study demonstrated that insulin could be covalently conjugated to an insoluble polymer via a photocleavable linker. Irradiating this material with the light at 365 nm wavelength releases insulin in a predictable manner, i.e., the amount of insulin released can be controlled by controlling the duration and intensity of irradiation. Insulin release was observed only in the presence of light. In the absence of light, no insulin release was observed. This release pattern suggested that insulin release is happening solely due to photolytic processes and not due to leaching. This study demonstrated a proof of concept of light triggered insulin release *in-vitro*. However, there were several questions needed to be answered to show successful demonstration *in-vivo* in an animal model. We asked the following questions before initiating the studies –

i. First question – whether insulin is still bioactive after release as it is exposed to organic solvents and extreme pH during and after reactions? Insulin was exposed to 100% DMSO during the caging reaction by DDA. DMSO was used because insulin has a very high solubility in DMSO. Water is not an ideal solvent for the diazotization reaction as diazo is unstable and gets hydrolyzed quickly. Hence, the caging reaction has poor yields in water. Also, during the spin-filtration step, insulin azide mixture is typically dissolved in 0.01 N HCl as insulin has higher solubility at low pH. Despite harsh conditions, in the end, photoreleased insulin shows a correct mass in MS and the same retention time on HPLC as native insulin.

However, based on this evidence, we cannot conclude if it is still bioactive. The bioactivity here refers to the efficacy of insulin to bring down blood glucose (BG) in an animal. Bioactivity is yet required to be tested experimentally.

ii. Second question – how fast is the diffusion of insulin from the intradermal depot site once it is photoreleased – is it fast enough to be useful in a clinical sense? Insulin is typically administered via subcutaneous injection clinically. The reason is that insulin is released in a sustained manner from subcutaneous tissue. This tissue layer has a lower blood flow rate and hence slower, but steadier absorption of insulin occurs from the site. However, the depot here is supposed to be injected intradermally so that the depot material will be held at the injection site. If it is injected subcutaneously, it might move and diffuse away from the location which is undesirable, and the PAD approach would not work. Also, light penetration would be very limited to deeper subcutaneous tissue than a shallower intradermal layer. Intradermal administration as intended in our case is not practiced clinically. As a result, there is very little literature about the kinetics of insulin absorption from the intradermal layer. We do not know how fast or slow the absorption will be from this layer and it must be determined experimentally. If there is very slow diffusion from this site, insulin that is released due to photolysis will take longer to go into the systemic circulation, and the response would be delayed.

iii. Third question – what is the extent of light penetration into the skin? In our approach, 365 nm light is being utilized to trigger insulin release from the depot material. The question is whether this 365 nm light has enough penetrating power to penetrate the dermal layer. There are not many studies investigating the depth of

penetration of light in the skin. Moreover, it is critical whether the quantity of insulin that is released would be physiologically relevant to cause a significant change in the blood glucose levels.

Development of a cell culture-based assay for insulin bioactivity confirmation

The assay was performed to confirm the bioactivity of insulin. The steps are outlined in Figure 78. It is an *in-vitro* assay using adipocytes as these cells express high levels of GLUT transporters which facilitate glucose uptake. Insulin promotes the uptake of glucose into the adipocytes even at lower concentrations. The glucose is radiolabeled. The uptake effect thus can be measured using scintillation counting to determine the extent of insulin-stimulated glucose uptake upon addition of insulin in the cell culture. The response can be compared when the cells are treated with native insulin vs photoreleased insulin. The assay would confirm if the released insulin has retained its bioactivity. The protocol was taken from the literature and is described below.[57–63]

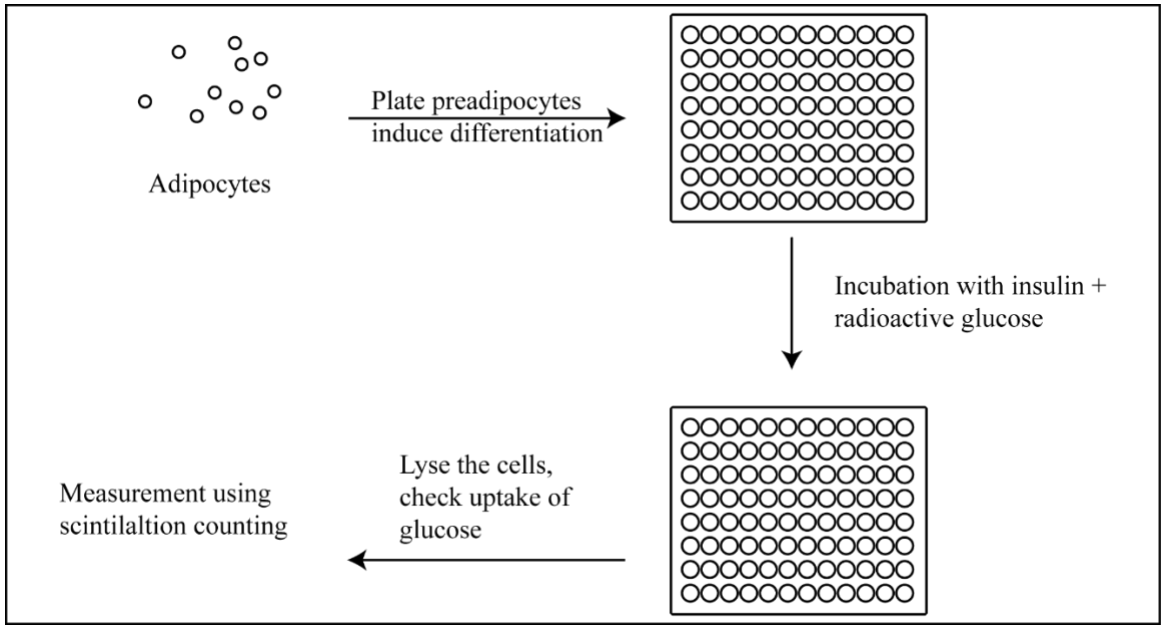

Figure 78: The assay for testing bioactivity of insulin using adipocytes.

Glucose uptake assay

Glucose gets metabolized into the cells upon uptake, hence 2-deoxy-D-glucose (2-DODG) is used instead which gets trapped inside the cells once internalized and doesn't undergo metabolism. Radiolabeled 2-deoxy-D-glucose was purchased from Moravek Biochemicals with 25 Ci/ mmol with a concentration of 1 mCi/ mL. Non-radioactive (cold) 2-DODG was also used (Sigma-Aldrich D3179).

Adipocytes ATCC CL-173 (3T3-L1) were obtained from ATCC. To culture and differentiate adipocytes, three different culture media were recommended. They were prepared as reported using the following reagents. Pre-adipocytes are required to undergo differentiation before being utilized for this assay. To grow pre-adipocytes, 90% DMEM (ATCC-30-2002) with 10 % fetal calf serum (FCS) (SH3040101) was prepared and used. Adipocytes differentiation media was used containing 90% DMEM with 10% FCS, 1 µM dexamethasone Sigma-Aldrich, D4902), 0.5 mM methylisobutylxanthine (IBMX, Sigma-Aldrich, I5879) and 1 µg/ mL bovine insulin (Sigma-Aldrich I0516) to induce differentiation. Once adipocytes were differentiated, adipocyte maintenance media was prepared to passage and maintain them. It was prepared by adding 1 µg/mL bovine insulin, 90% DMEM and 10% FCS. The cells were plated at the density of 2000 cells/well in a 96 well-plate in preadipocytes expansion medium. Typically, the cells were grown until they are 70% confluent and passaged unless we needed to perform differentiation. Cells must reach 100% confluency and allowed to stay confluent for the next 48 hours before inducing differentiation. Then, the preadipocyte expansion medium was replaced with adipocytes differentiation medium and incubated for the next 48 hours. After 48 hours, this medium was replaced with adipocytes expansion medium, and the assay was performed after about

12 days after inducing differentiation. The preadipocytes expansion medium was changed every 2-3 days while adipocytes expansion medium was changed every 2 days. The cell images were taken after performing calcein treatment so that it can be visualized using green fluorescence (Figure 79).

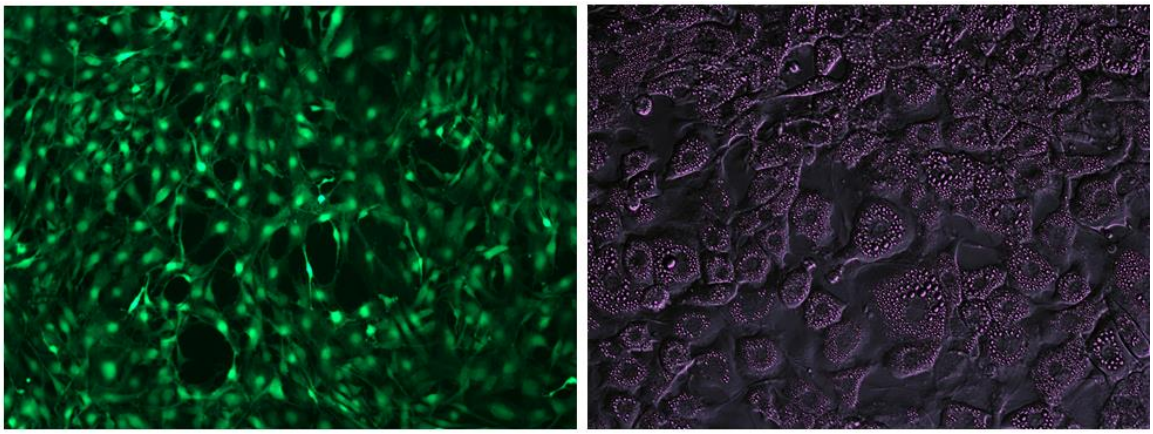

Figure 79: The pictures of pre-adipocytes before differentiation treated with calcein (left) and differentiated adipocytes with visible lipid globules (right).

Protocol for the glucose uptake assay -

i. The night before the assay, adipocyte expansion medium was replaced with DMEM containing 0.1 % bovine serum albumin (BSA) without any serum.

ii. On the day of the assay, the cells were washed with glucose-free, serum-free DMEM, 0.1 % BSA and incubated in it for 2 hours.

iii. The well plate was brought to the lab from the incubator after 2 hours of incubation.

iv. The cells were washed twice with Krebs-Ringer phosphate (KRPH) buffer (140 mM NaCl, 4.7 mM KCl, 1 mM $CaCl_2$, 5 mM KH_2PO_4, 1 mM $MgSO_4$, 20 mM HEPES and 0.1 BSA, pH 7.4).

v. KRPH buffer containing insulin was incubated with cells for 30 min to stimulate glucose uptake. Then the cells were washed twice with KRPH buffer.

vi. 0.2 µCi/well of [^{3}H]-2-deoxy-D-glucose (2-DOG) in KRPH buffer supplemented with 100 µM 2-deoxy-D-glucose was added and incubated for 20-30 min at 37 ºC. The supernatant was removed and discarded.

vii. The wells were rinsed carefully four times with ice-cold PBS to stop the uptake process. The cell lysis was performed by treating them with 1N NaOH for 60 min with shaking and transferred the whole-cell lysate in a scintillation vial containing 6 mL scintillation fluid. The readings were taken after 3 hours.

Experiment # 1

In this experiment, cells were treated with various amounts of radiolabeled glucose to determine their optimum concentration. In the first two sets, 0.2 µCi and 0.1 µCi of radiolabeled 2-DODG was used respectively and the total concentration was maintained by supplementing with 100 µM with cold 2-DODG. While in the third case, only radiolabeled glucose was used, hence the concentration was much lower (Table 5). The cells were treated with varying concentrations of insulin to see if there is insulin-dependent glucose uptake.

Table 5: Sets of samples with varying amounts of 2-DODG and radioactivity and insulin.

	0.2 µCi of 2-DODG				0.1 µCi of 2-DODG		0.2µCi of 2-DODG only	
Insulin concentration (nM)	0	4	8	32	0	16	0	16
Replicates	9	4	3	5	5	5	2	2

Results

There was no trend observed in response to a varying amount of radiolabeled 2-DODG or different insulin concentrations (Figure 80). The 2-DODG uptake seemed unaffected by changing concentrations of insulin. Although in set 1, there was a very minor effect, it wasn't significant between insulin versus non-insulin samples.

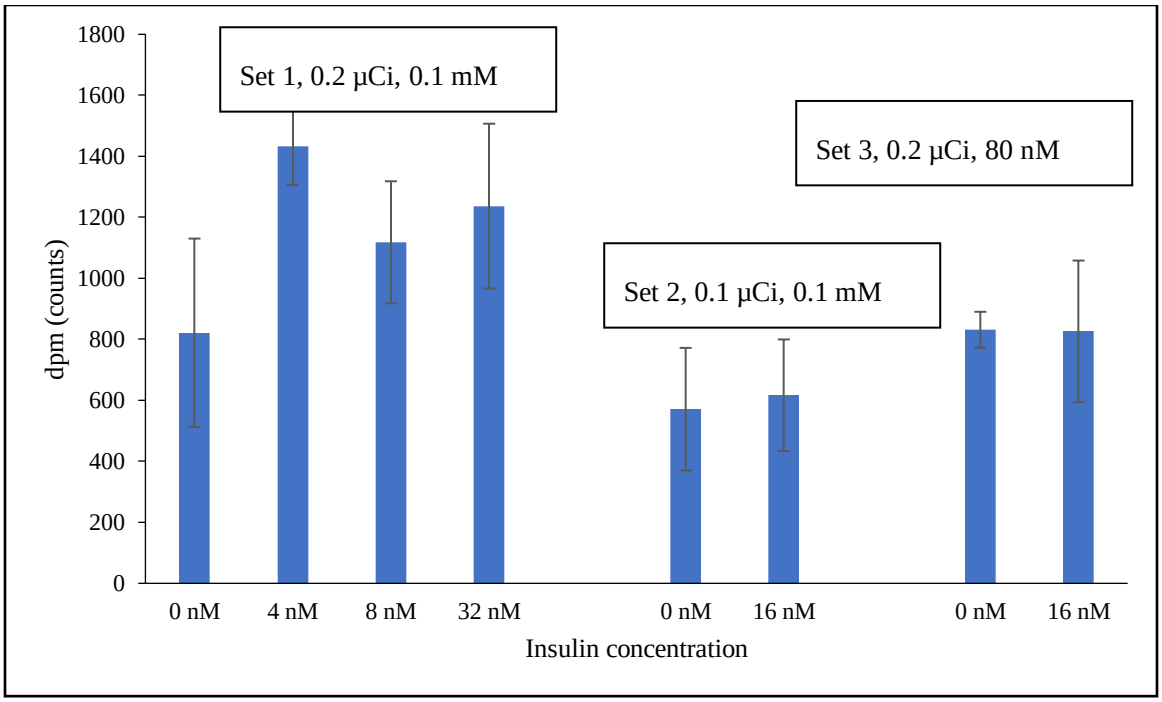

Figure 80: 2-DODG uptake measured in adipocytes in three sets with different concentrations of 2-DODG and different amounts of radioactivity.

Experiment # 2

In experiment # 1, we did not observe any specific trend in 2-DODG uptake after increasing insulin concentrations. In this experiment # 2, insulin concentration range was increased to 100 nM from 32 nM hoping to see whether higher insulin concentrations promote higher glucose uptake by the cells. We didn't see any difference between 0.1 µCi/well and 0.2 µCi/well, hence, we decided to keep 2-DODG radioactivity at 0.2 µCi/well (Table 6).

Table 6: 2 sets of samples with a varying concentration of native insulin and photoreleased insulin at 100 nM.

	Insulin std.			Photoreleased insulin
Insulin concentration (nM)	0	17	100	100
Number of replicates	8	8	4	3

Uptake at 100 nM concentration was higher than at zero concentration as shown in Figure 81. However, the observed standard deviations were too high rendering the data difficult to interpret.

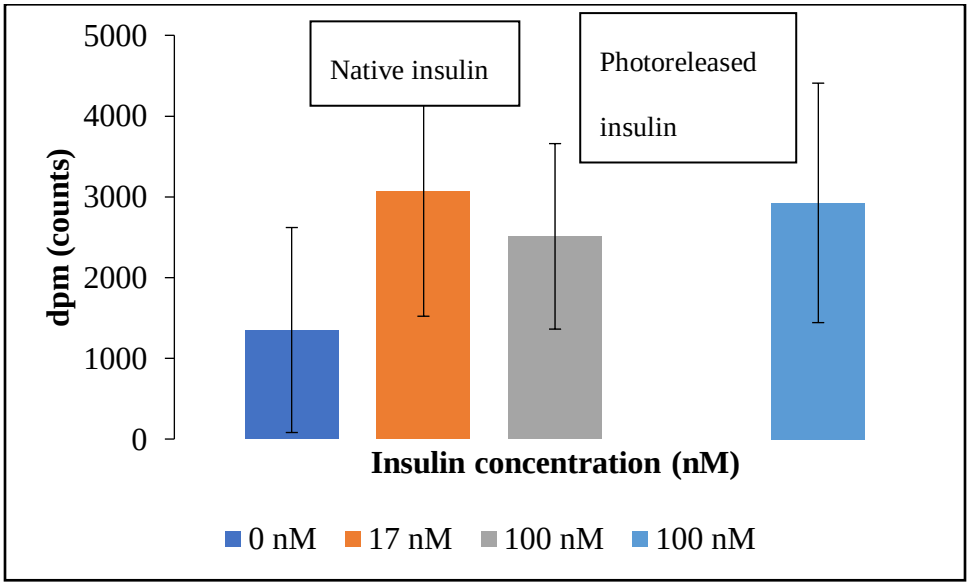

Figure 81: 2-DODG uptake measured in adipocytes with varying concentrations of native insulin and photoreleased insulin.

Experiment # 3

In this attempt, the following changes were made in the protocol. During many washing steps, the number of cells left behind may vary and non-uniform lysis of cells might have resulted in larger standard errors. Hence, the samples were also analyzed by BCA protein assay kit (Thermo Fisher Scientific) to minimize sample to sample variation in uptake. Final radioactivity values were normalized to protein content to get results in counts/µg/mL. Other lysed samples were added to the scintillation cocktail and counts were measured after 24 and 48 hours. This time, 2% Triton X-100 was added to lyse solution along with NaOH to help cell lysis effectively. Here there were only two concentrations of insulin 0, 100 nM used.

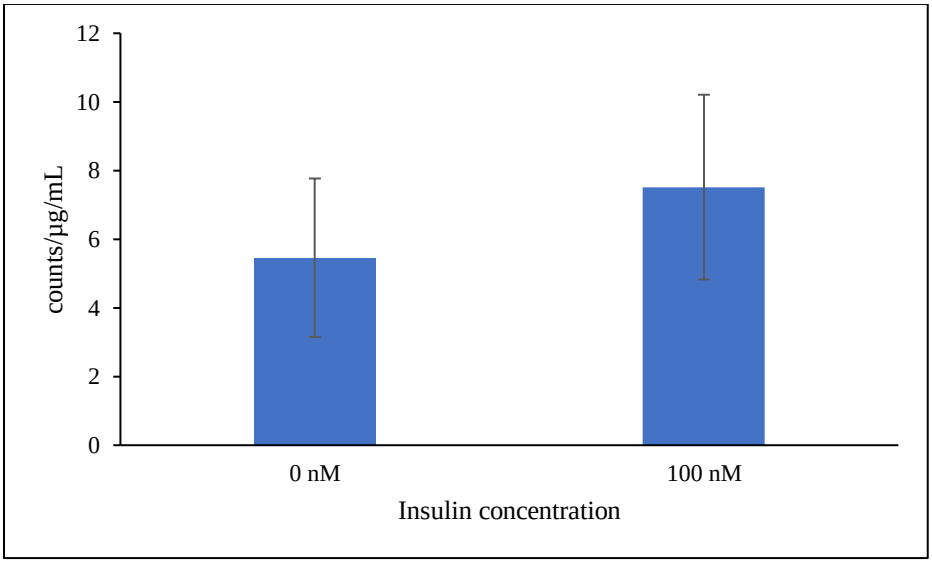

Figure 82: 2-DODG uptake as measured in adipocytes in with 0, 100 nM insulin concentration normalizing it to BCA protein assay.

Results

The data is shown in Figure 82, there was 1.37 times higher 2-DODG uptake in 100 nM insulin samples versus control samples where there was no insulin. However,

normalizing the counts to the amount of protein present did not help amplify the uptake percentage. 1.37 is not statistically significant given with % std. dev. was approximately 40% in both samples. The results were suboptimal when compared to results reported in the literature. At this point, we discontinued this cell culture assay because it could not be established and planned to test the bioactivity in the animal models instead.

Testing for insulin bioactivity *in-vivo*

We attempted to confirm insulin bioactivity using adipocytes-based *in-vitro* assay, but we could not establish the assay properly. Hence, to move the project forward, we decided to use *in-vivo* models. For these studies, male Sprague-Dawley (Harlan Laboratories) rats were chosen. These animal models are used for performing studies related to diabetes or insulin delivery. The protocol was approved by the University of Missouri-Kansas City Institutional Animal Care Use Committee protocol #1401.

First, we generated diabetic models by inducing diabetes chemically. Diabetogenic chemicals such as alloxan or streptozotocin which affect β cells functionality or structural integrity are used.[64] Both the structures are shown in Figure 83. Both work by different pathways but selectively destroy β-cells. These chemicals selectively enter β-cells via GLUT 2 transporter due to their structural similarities with glucose. When insulin-producing cells are destroyed, insulin is no longer produced, and the condition mimics type 1 diabetes mellitus. Alloxan generates reactive oxygen species (ROS) intracellularly in the presence of intracellular thiols and produces dialuric acid. Oxidation of dialuric acid generates superoxide radicals, hydroxyl radicals, and hydrogen peroxide. These species cause β-cell death and diabetes. Streptozotocin has a different mechanism of action than that of alloxan. When it gets internalized by cells, it breaks down into glucose +

methylnitrosourea. Methylnitrosourea is an alkylating agent, and once inside the β-cells alkylates DNA and causes cell death.[65]

For our experiments, streptozotocin was chosen for inducing diabetes. It was injected intraperitoneally to rats at 65 mg/kg dose. To measure glucose, blood was collected from the tail vein, and a drop of blood was collected on a glucose strip and One Touch® glucose meter. Blood glucose was monitored every day to confirm that the rats were diabetic after administration of streptozotocin. Rats were defined as diabetic if blood glucose was above 250 mg/dL for three consecutive days.

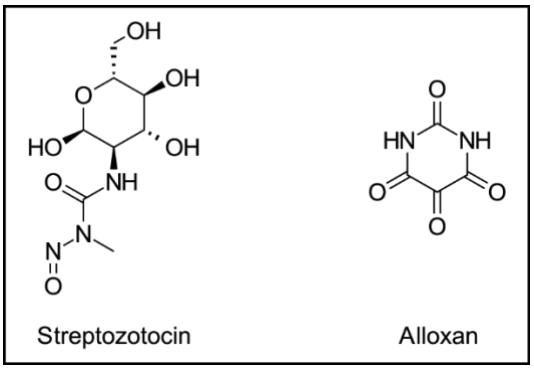

Figure 83: Structure of streptozotocin and alloxan, chemicals used for inducing diabetes in animal models.

Preparation of photoreleased insulin

First-generation material with insulin was synthesized to evaluate the bioactivity of photoreleased insulin. It was then subjected to the photolysis as shown in Figure 84. Insulin that was released upon light excitation was collected in a tube. To determine its bioactivity, it was injected in the rat via an intradermal route. If insulin has retained its bioactivity, it would exert a physiological effect, and we expected to see a drop in the blood glucose (BG). Simultaneously, insulin concentration in the blood was measured using ELISA as per the instructions provided with the kit. This activity was compared to commercially purchased insulin which was administered in the same manner at the same dose.

To prepare first-generation material, caged insulin (DIMA) was immobilized on the resin. Briefly, freshly prepared DDA (approx. 43 µmol) in DMSO (1.16 mL) was added to a solution of human recombinant insulin (0.20 g, 34.4 µmol) in DMSO (16.04 mL). The mixture was gently shaken for 24 h, protected from light. The mixture was freeze-dried and reconstituted in 0.01 N HCl. The sample was then filtered and washed twice with 0.01 N HCl using spin filters 5 kDa MWCO filters). The spin filtration was performed to remove small molecules while retaining the > 5000 MW insulin conjugates.

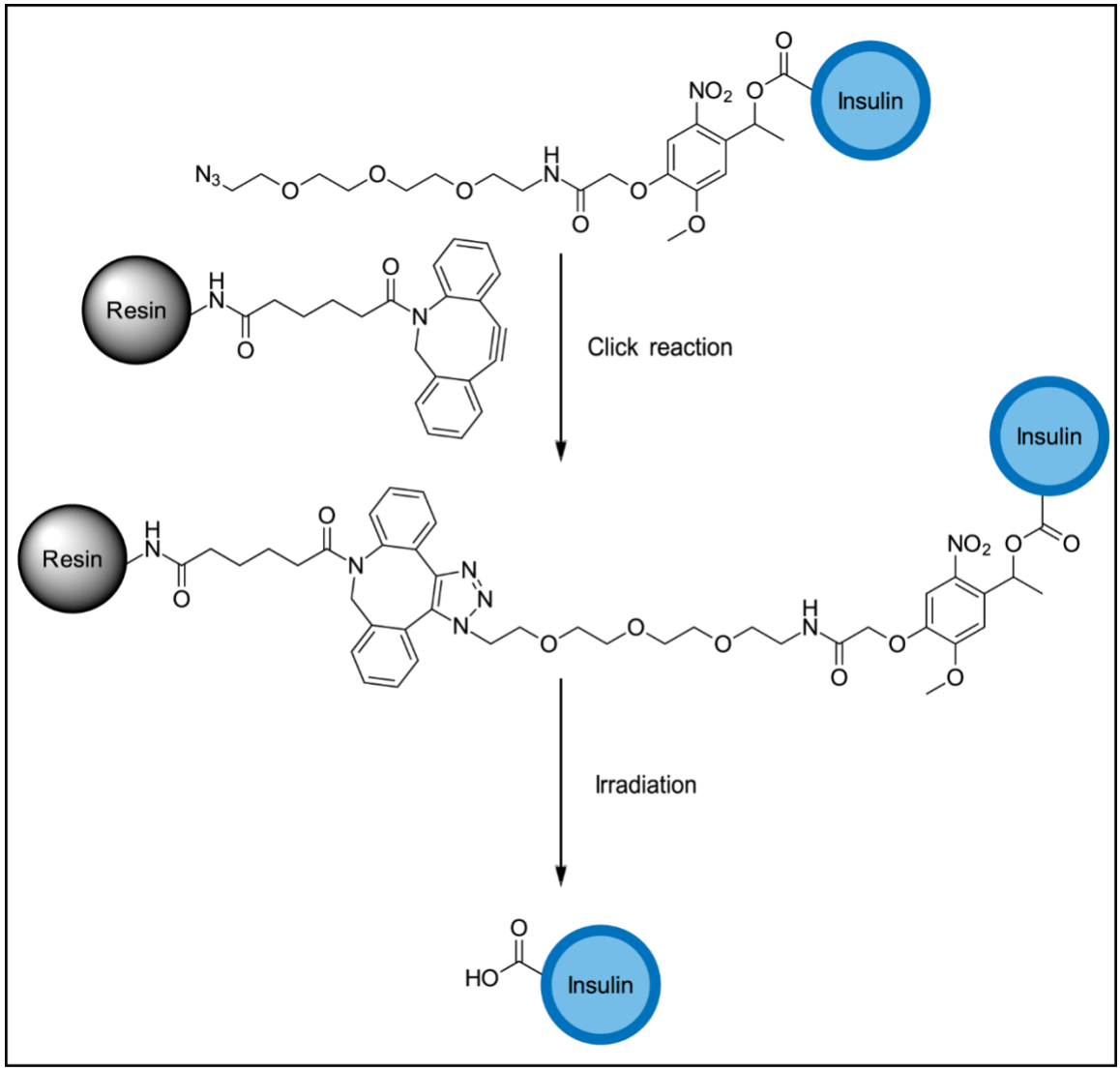

Figure 84: Synthesis of first-generation PAD material. Irradiating the construct yields insulin.

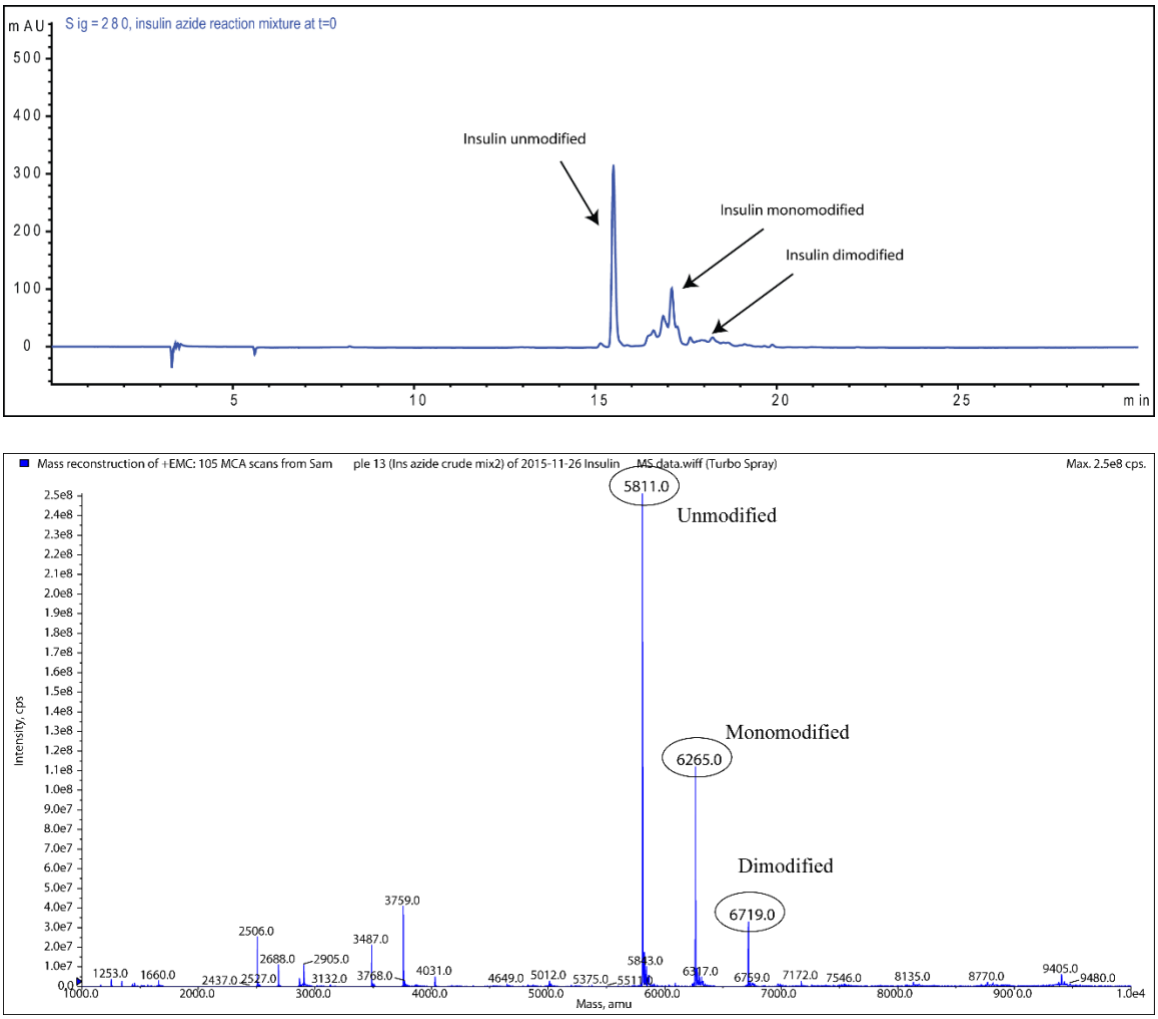

Figure 85: HPLC (top) and MS infusion (bottom) of insulin azide mixture after spin filtration.

The concentrate was then reconstituted in 0.01 N HCl and freeze-dried to remove the solvent. Insulin, insulin mono-azide and insulin di-azide were analyzed using reversed-phase HPLC. Reversed-phase HPLC (flow rate 1 mL/min, runtime 30 min), solvent A (0.1% TFA in H_2O), solvent B (0.1% TFA in ACN), gradient 0% B to 100% B over 30 minutes, post-run 0% B for 5 minutes, C18 Hypersil column (5 µm, 250 × 4.6 mm, Varian), retention time (min), relative yields (%); insulin (15.9 min, 62.9%) insulin monoazide (17.2-18.4 min, 33.1%); insulin di-azide (18.7-19.7 min, 3.9%) (Figure 85). The crude

insulin-azide mixture was analyzed using direct infusion ESI-MS in 0.01 N HCl. Individual species i.e. insulin, insulin mono-azide, and insulin diazide were purified using the HPLC and analyzed using direct infusion in ESI-MS for MS characterization. For direct infusion ESI−MS (m/z): $[M]^+$ calculated for insulin, 5808.0; found, 5811.0; $[M]^+$ calculated for insulin mono-azide, 6262.2; found, 6265.0; $[M]^+$ calculated for insulin di-azide, 6716.4; found, 6719.0; Extinction coefficient calculated ($\varepsilon_{280\ nm}$): insulin (5130 $M^{-1}\ cm^{-1}$), mono-azide (8400 $M^{-1}\ cm^{-1}$), di-azide (11700 $M^{-1}\ cm^{-1}$).

Insulin azide was immobilized on the resin (10 μm Tentagel M-RAM (M30123, Rapp Polymere) via click reaction. The copper-free click reaction was selected because copper assisted click reaction did not work. The copper-free reaction was efficiently carried out using an azide and a strained alkyne like dibenzocyclooctyne (DBCO) in this case. It does not require any other catalyst, biorthogonal in nature and hence compatible with biomolecules.[66–69]

For conjugating DBCO on the resin, 10 μm Tentalgel R-RAM resin (85 mg, 17 μmols of amino groups) was washed thrice with DMF (600 μL). A solution of DBCO acid (6 mg, 18 μmols, 250 mM), HATU (6.84 mg, 18 μmols, 250 mM) and N, N-diisopropylethylamine (6.25 μL, 36 μmols, 500 mM) in DMF (72 μL) was shaken for 15 min. This activated solution was then added to the washed resin and was gently stirred for 20 h. This resin was washed several times with DMF, methanol after the reaction. Then it was dried under vacuum. A small amount was treated with 95% TFA (500 μL) for 90 minutes. The purple-colored cleaved DBCO amide was recovered by removing TFA under vacuum and then reconstituted in methanol. This product was analyzed by reversed-phase HPLC-MS (flow rate 0.4 mL/min, runtime 30 minutes), solvent A (0.1% FA in H_2O),

solvent B (0.1% FA in ACN), gradient 0% B to 50% B over 5 minutes, gradient 50% B to 100% B for from 5 to 27 minutes, Isocratic 100% B over next 2 minutes, gradient 100% B to 0% B for 1 minutes, C18 Hypersil column (5 µm, 250 × 4.6 mm, Varian), retention time: 17.8 min; ESI−MS (m/z): $[MH]^+$ calculated for $C_{19}H_{27}N_5O_9$, 333.1; found, 333.1 (Figure 86).

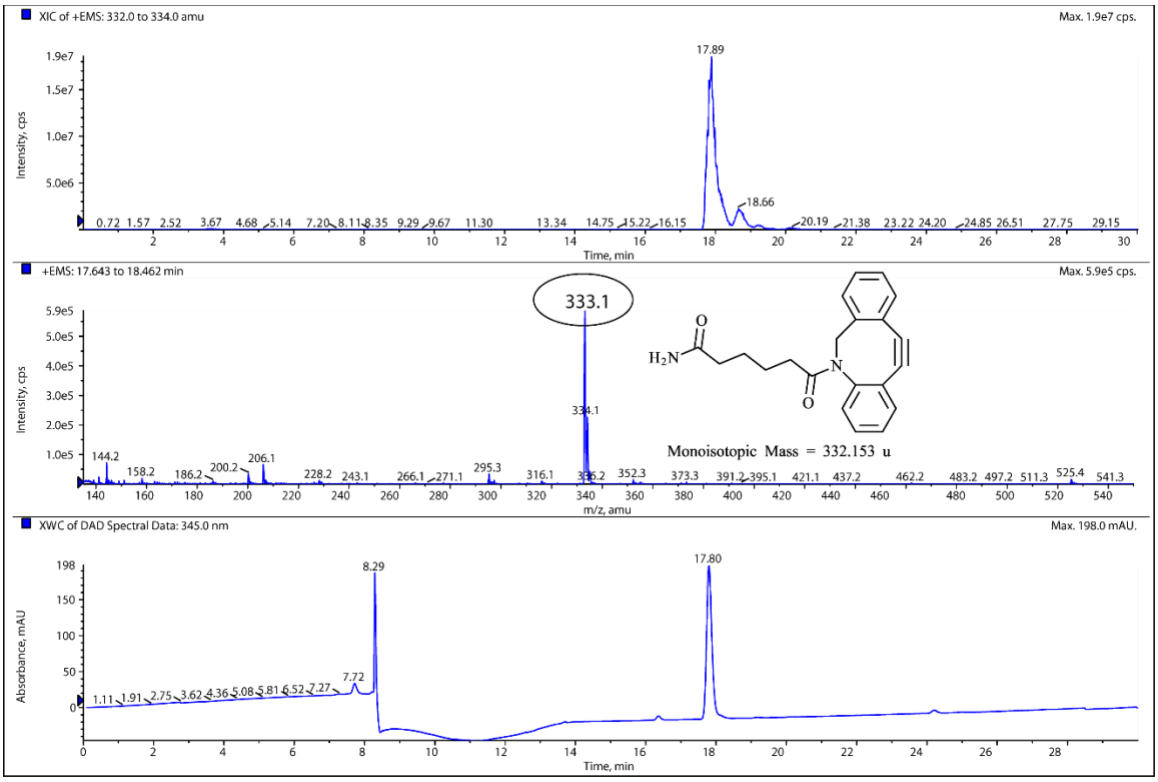

Figure 86: HPLC-MS of TFA cleavage of DBCO acid coupled to the resin. The product mass is seen at $[MH]^+$=333.1 eluting at 17.8 minutes.

Once insulin azide and DBCO modified resin were synthesized, they were mixed to immobilize caged insulin onto the resin. 25 mg DBCO conjugated resin was washed three times with 500 µL DMF and five times with 500 µL MilliQ water. In another tube, 11.2 mg of insulin azide mixture was dissolved in 200 µL of 0.01 N HCl, and the pH was brought to 7.5 using 1 N NaOH until it became a clear solution. Insulin azide solution was

then mixed with the DBCO conjugated resin and stirred at 550 rpm at 37 °C for 48 hours. After the reaction, it was washed multiple times with PBS to wash off any unbound insulin. The supernatant analysis (before and after the reaction) was performed using reversed-phase HPLC. The disappearance of insulin azide relative to insulin from the supernatant was measured to calculate the amount immobilized on the resin. Both the chromatograms are shown in Figure 87. The integration area of insulin and insulin azide at 280 nm on HPLC chromatogram was normalized with its extinction coefficient to quantify the amount disappeared. This reaction was performed in multiple replicates on this scale. Insulin immobilization was also confirmed by performing TFA cleavage of a small amount of resin. ESI−MS (m/z): $[MH]^+$ calculated for, 6594.0; found, 6597.0 (Figure 88).

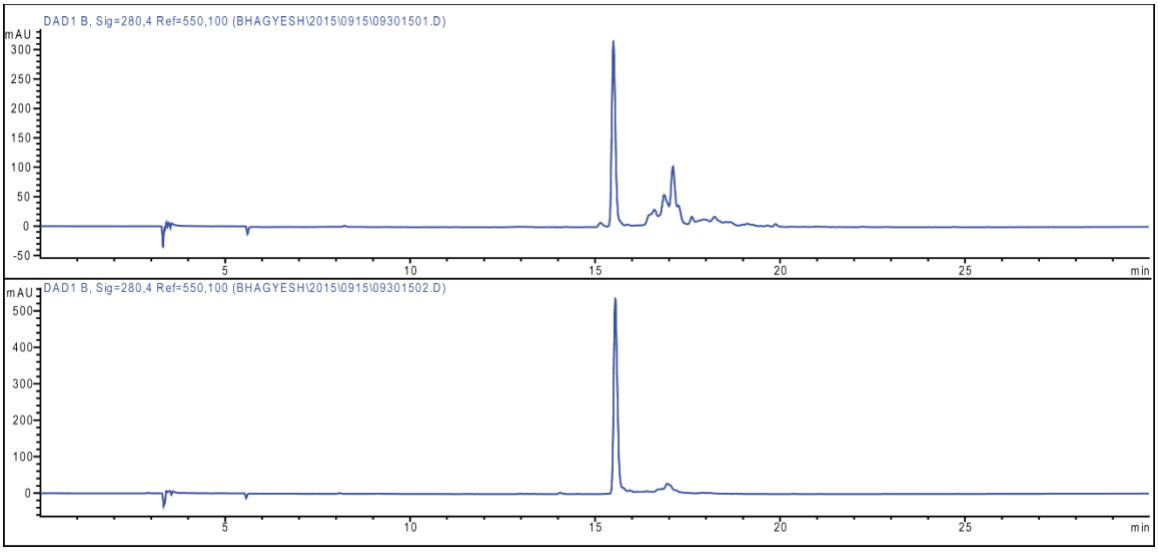

Figure 87: Supernatant analysis of insulin azide mixture from click reaction. The top chromatogram is insulin azide at t=0, and the bottom chromatogram is at at=48 hours. Insulin azide mixture peaks disappear, but insulin is not consumed.

Insulin conjugated resin (20 mg, 356 nmol insulin) was washed several times with PBS. The final wash was run on HPLC to confirm that there is no unbound insulin leaching from the resin. The resin was suspended in 110 μL of PBS in a flat-bottom glass tube. A

200 mW Nichia® 365 nm LED was used to irradiate the sample for 20 min. The suspension was vortexed briefly, and the supernatant was collected. 2 µL of it was diluted to 20 µL and injected in HPLC to confirm insulin release (Figure 89 and Figure 90). 10 µL of this supernatant was desalted using 5 kDa MWCO spin filter and reconstituted in 0.01 N HCl for direct infusion for ESI-MS characterization (Figure 91).

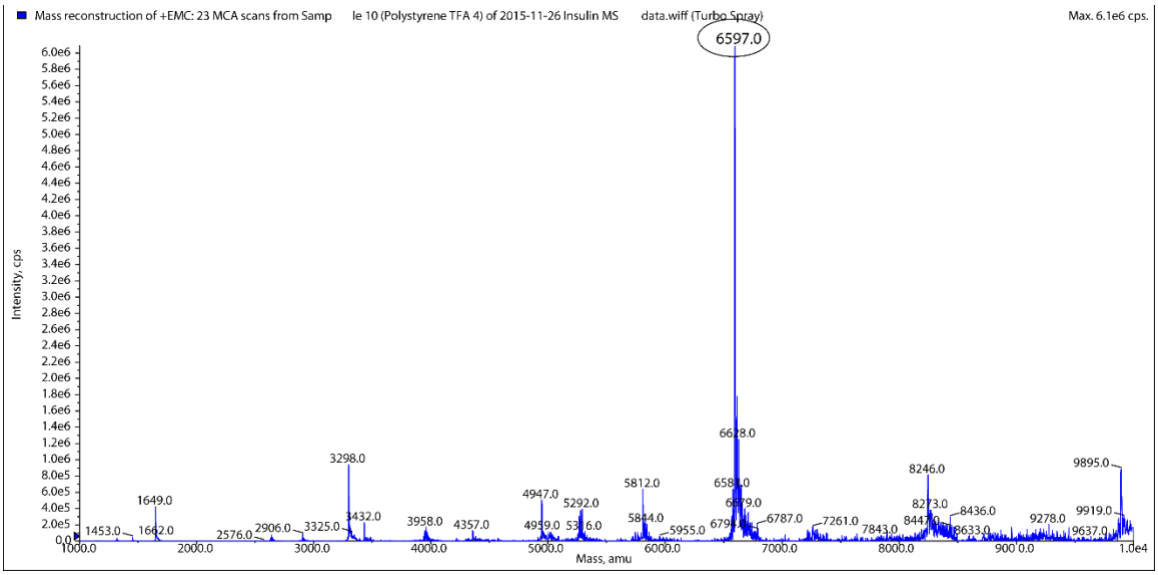

Figure 88: Insulin construct immobilized onto the resin was cleaved using TFA and infused in MS. The mass of the product is seen at $[M]^+$=6597.0 (calc. for 6594.0)

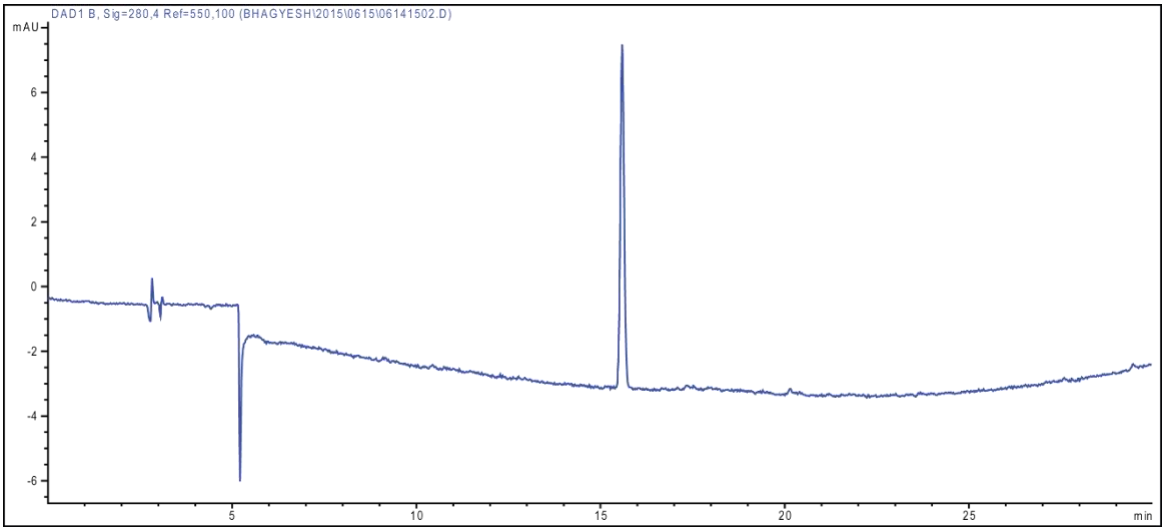

Figure 89: HPLC chromatogram of insulin standard.

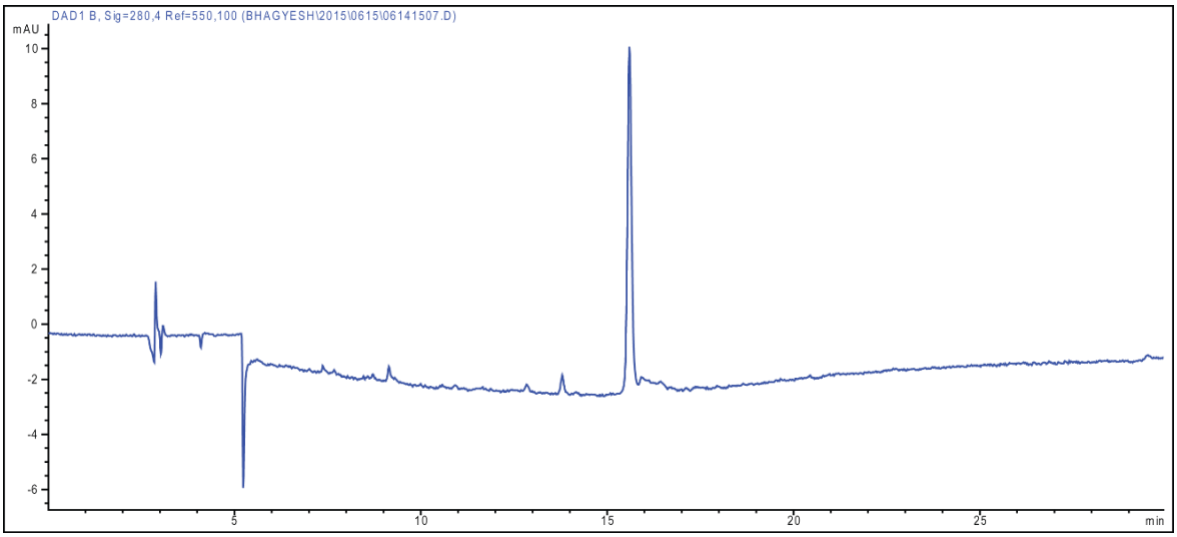

Figure 90: Photoreleased insulin from the resin.

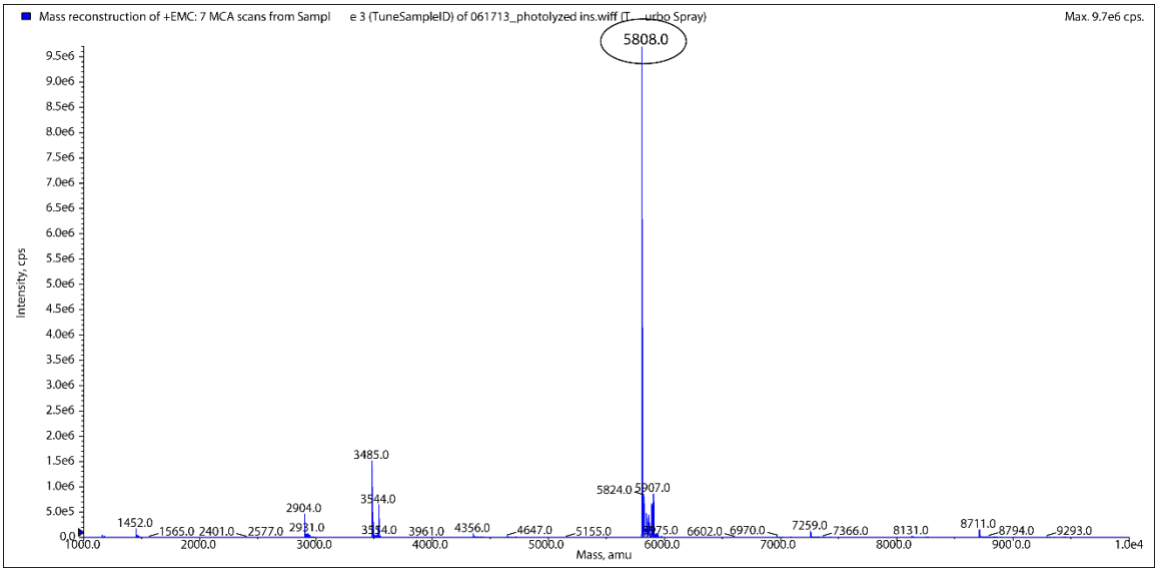

Figure 91: Photoreleased insulin from the resin upon light irradiation infused into MS. The mass of insulin is seen at $[M]^+$ 5808.0.

To prepare samples of testing the bioactivity of insulin, the concentration of photoreleased insulin in the supernatant (PBS) was 150 µM (determined using UV-vis spectroscopy). Initially, we planned to filter this solution using a 5 µm sterile syringe filter. However, it was observed that insulin was binding to the filter surface hence there was a

significant loss of insulin after syringe filtration.

Male Sprague-Dawley rats were used for the studies. Diabetes was induced by injecting 65 mg/kg of streptozotocin intraperitoneally. 14.2 nmol/kg of insulin dose was selected for these studies. The rats were first anesthetized using isoflurane in a chamber. Insulin was injected intradermally on the back using a 31G needle. BG levels and insulin concentration were measured over a period of 2 hours. Blood samples were collected in Microvette 100 µL Li-HEP tubes (Sarstedt) from the tail-vein using a glass capillary. After collecting all time points from an experiment, the samples were centrifuged at 5000 rpm for 2 minutes. The supernatant was removed and stored at -20 °C until the ELISA analysis was performed. The ultrasensitive human insulin ELISA kit (Alpco, Salem, NH) was used following the manufacturer's instructions. The experiment was carried out in triplicate (n=3) and the results are shown in Figure 92.

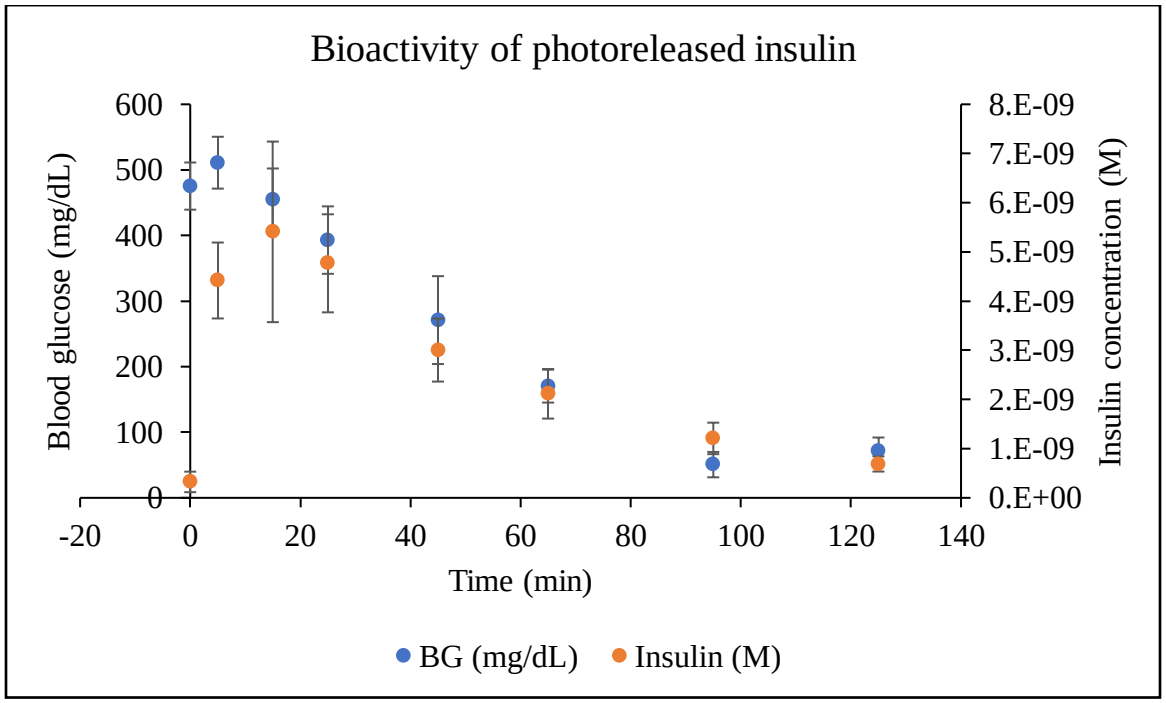

Figure 92: BG and insulin values after photoreleased insulin was injected into the rats.

The response after injecting photoreleased insulin suggested that insulin is still bioactive. Insulin was detected using ELISA; this suggested that it still has retained its native 3D conformation because the antibodies which are very specific were recognizing it. Simultaneously it also reduced the BG level significantly, and BG dropped very low by the end of the experiments. These results confirmed that insulin has still retained its bioactivity. We performed a similar experiment using native insulin obtained commercially and injected it in the same manner. It yielded a similar response. Typically, as reported elsewhere, 2-3 IU/kg dose of human insulin causes approximately 70% reduction in glucose levels in Sprague-Dawley rats when injected subcutaneously post 2-hour period.[70–72] We injected 2.36 IU/kg (14.2 nmol/kg) of dose here and observed similar result even when injected intradermally. This study was critical and answered two of our questions; 1) Insulin has still retained its bioactivity after photorelease. 2) Insulin can be absorbed from the dermal layer after intradermal injection.

Testing light triggered insulin release *in-vivo*

Experimental setup

Here we investigated our central hypothesis whether light can be used to trigger the release of insulin from a transcutaneous depot. Dr. Friedman designed a light source to irradiate on an injected sample from the top of the skin. It is shown in Figure 93 and Figure 94. The light source has three components. The first element is an on/off switch for LED. The actual light source has two additional parts; a top disc with 365 nm LED with four magnets and a bottom disc with a hole in the center with four magnets. A shallow depot was injected intradermally. Such intradermal injection appeared as a bleb on the skin. The bottom disc was placed on this, centering the hole on the bleb using superglue. Then top

disc aligns itself directly on the bottom plate with the help of magnets. Such design allowed the LED light to fall directly onto the injected depot. This assembly also makes sure that the LED is affixed securely over the depot site.

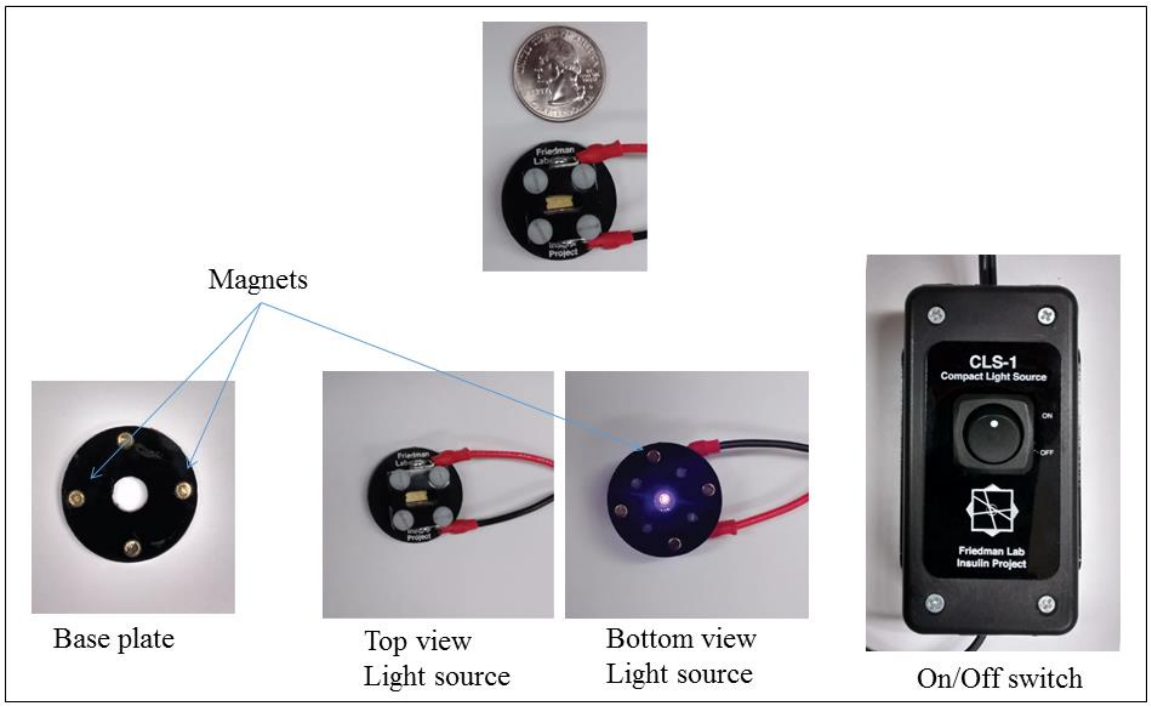

Figure 93: Design of the compact light source.

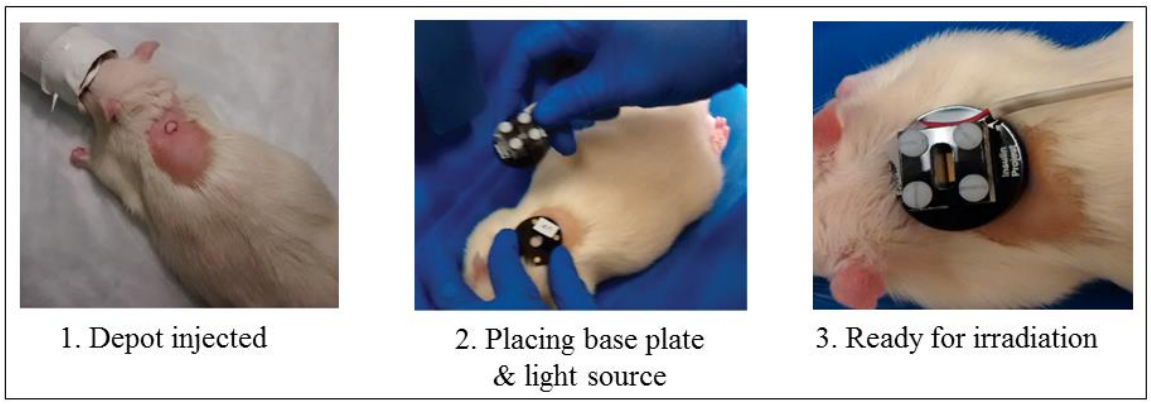

Figure 94: How light source was placed over the intradermal PAD (bottom) in a rat.

The light source was constructed using Nichia NCSU033B LED with a 365 nm

peak irradiation. The LED was driven by a 6.5 V power supply using a current limiting power resistor. The light source holds the LED ~0.32 cm from the skin surface, and the absolute irradiance at the skin was estimated to be 0.71 W/cm^2. The absolute irradiance of the light source was determined using a calibrated USB2000 spectrophotometer (Ocean Optics) and a CC-3-UV-S cosine corrector via an optic fiber. The Spectrasuite® software was used to analyze absolute irradiance in the range of 350-400 nm that brackets the LED output.

The time points were kept like that of photoreleased insulin bioactivity studies. Except, here instead of photoreleased insulin, first-generation PAD material was injected and then irradiated using the compact light source. The aim was to see if insulin can be detected in blood and if it causes any changes in BG levels after irradiation. Original ChemMatrix® resin described earlier could have been used here because it is completely made up of biocompatible PEG and has very high loading density. However, the resin size was too large to be injected through a 23G needle. At this point, we started looking for smaller sized biocompatible resins, we requested a smaller sized resin from PCAS for these studies however they provided us with a limited quantity sample which was not a catalog item. The PAD material could be synthesized using smaller sized resin, but because it was not a catalog item, we decided not to use it. So, we started searching for different smaller sized resins, there were three main criteria - i) the resin should be smaller in size so that it can be injected easily in a pain-free manner, ii) it should have a high loading capacity, iii) it is made up of biocompatible or preferably biodegradable material. We found a company which sold similar products and tested these items, 5 µm polystyrene resin (HM1523, loading density 0.62 mmol/g) and 10 µm Tentagel M-RAM (M30123, loading density 0.2-

0.22 mmol/g). In Tentagel®, polystyrene core is grafted with PEG polymers. The immobilization of insulin was performed in the same exact manner as performed on ChemMatrix resin.

17.7 mg (11 µmol) of 5 µm polystyrene resin and 55 mg (11 µmol) of 10 µm Tentagel resin were washed in 0.5 mL DMF thrice. Then it was treated three times with 0.5 mL of 20% piperidine in DMF to remove Fmoc. A common DBCO acid activating mixture was prepared by mixing 7.5 mg DBCO acid (22.5 µmol), 10 mg HATU (26.3 µmol) and 7.6 µL DIEA (44 µmol) in 146 µL DMF. The activating reaction was performed for 15 minutes at room temperature (RT). Then the volume was split into two equal parts and added to each 5 µm and 10 µm resin. The reactions were run for 18 hours, and then the resin was washed 5 times with 0.5 mL DMF, methanol and dried thoroughly. A small portion of it was treated with 0.3 mL of 95 % TFA in water for 1 hour and ran LCMS to confirm DBCO acid coupling. LCMS analysis – reversed-phase HPLC-MS (flow rate 0.4 mL min^{-1}, runtime 30 min with 5 min post-run), solvent A (0.1% FA in H_2O), solvent B (0.1% FA in ACN), gradient 0% B to 50 % B over 5 min, gradient 50% B to 100 % B until 27, gradient 100% B to 0% B for next 2 min and isocratic 100% B for next 1 min; C18 Hypersil column (5 µm, 150 × 3.2 mm, Agilent), retention time: 18.2 min; ESI−MS (m/z): $[MH]^+$ calculated for, 333.1; found, 333.2 (Figure 95).

The click reactions of caged insulin azide with each of these resins were carried out in DMSO as well as in water to see which solvent gives the best yield. Thus, four reactions were set up. First, 2 mg (1.2 µmol) of 5 µm resin were treated with 2.5 mg insulin azide mixture in 16 µL DMSO in reaction # 1. Then, 6 mg (1.2 µmol) of 10 µm resin was treated with 2.5 mg insulin azide mixture in 16 µL DMSO in reaction # 2. For reaction # 3 and #

4, 2 mg of 5 µm resin and 6 mg of 10 µm resin were treated with 2.5 mg insulin azide in 0.1 mL water respectively. Insulin azide is not soluble in neutral water, it was first dissolved in 0.01 N HCl, and the pH was brought to 7.4 to make it neutral. The disappearance of insulin azide from the supernatant was measured to determine the extent of click reaction. The reactions were run for 48 hours with shaking. After 48 hours, it was washed with PBS multiple times.

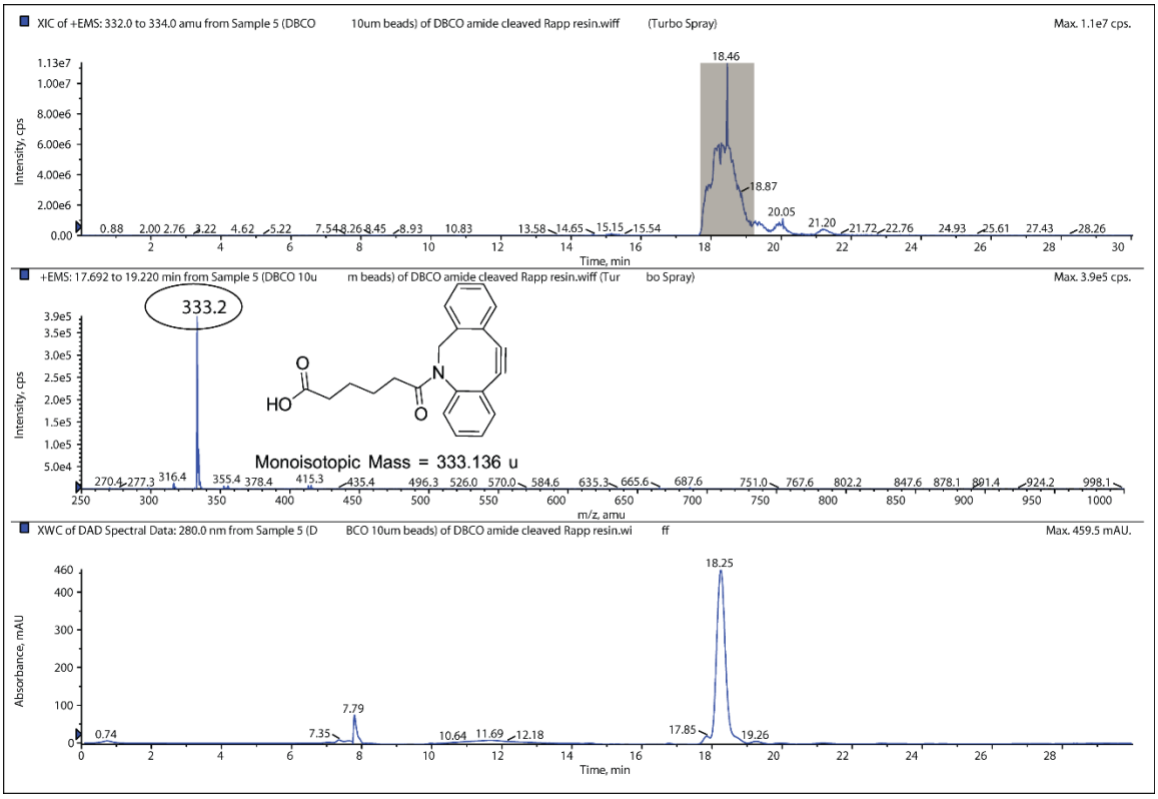

Figure 95: LCMS of cleaved DBCO amide. The product is seen at $[MH]^+$=333.2 eluting at 18.25 min.

Based on the results from the chromatograms (not shown here), it was observed that the yield was very poor with 5 µm resin in both solvents. In the case of 10 µm resin, the yield was better in water than in DMSO (Figure 96). Both the resins clumped together in DMSO but not in water. Hence, it was decided to use 10 µm resin for future studies and

water as a solvent for click reactions. Initially, DMSO was intended to be used but significant clumping of resin was observed in DMSO, hence water was used.

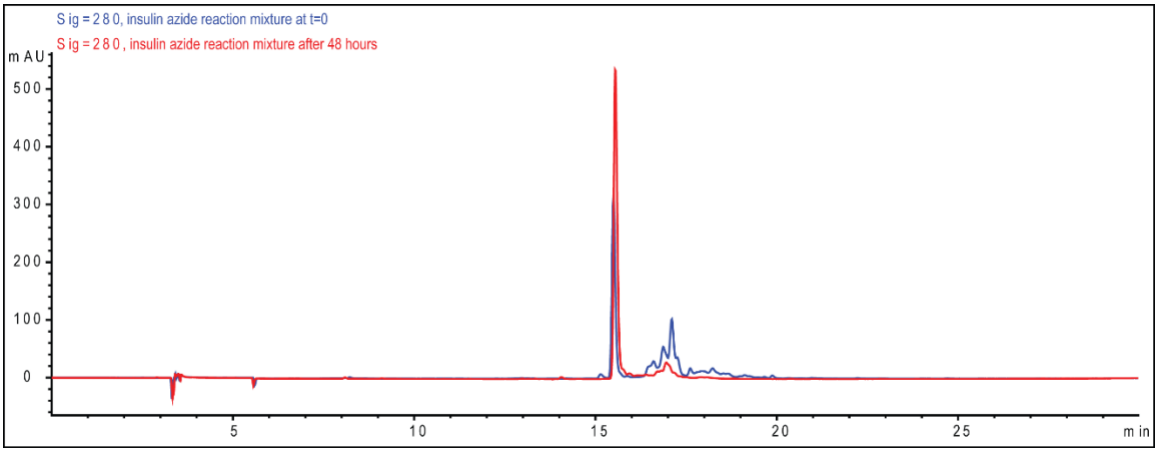

Figure 96: HPLC chromatograms of insulin azide mixture before (blue) and after (red) the click reaction.

In-vitro photolysis experiments

The *in-vitro* photolysis experiments were already performed using ChemMatrix® resin in the lab showing the ability of light to trigger and control insulin release. However, because we switched from ChemMatrix to Tentagel, we performed it again to confirm that the system is behaving as expected. For obtaining photoreleased insulin (described earlier in this chapter), this 10 µm resin was used. The procedure is already outlined earlier.

Insulin, 140 nmol conjugated on the resin was washed with PBS multiple times. For the photolysis studies, it was suspended in 100 µL PBS. The photolysis was performed in Agilent glass vial inserts (catalog # 5183-2090). The irradiation was carried out by placing the glass vial insert directly above 365 nm Nichia LED as shown in Figure 97. The irradiation was performed twice (for two minutes each) from t=0 to t=2 min and t=65 to t=67 min. The sample was vortexed for 5 min and centrifuged before collecting samples

for each time point. A 25 µL volume was removed and replaced with the same volume of fresh PBS. The amount of insulin released was quantitated using HPLC using an insulin standard curve. The solution of the final time point was desalted with 5 kDa MWCO centrifugal spin filter and infused into MS to get molecular weight. The control sample was treated identically except the light was blocked by an aluminum foil from reaching the sample. Reversed-phase HPLC (flow rate 1 mL min^{-1}, runtime 30 min with 5 min post-run), solvent A (0.1% TFA in H_2O), solvent B (0.1% TFA in ACN), gradient 0% B to 100 % B over 30 min; C18 Hypersil column (5 µm, 250 × 4.6 mm, Agilent), retention time: 16 min (Figure 98); ESI−MS (m/z): $[M]^+$ calculated for, 5808.0; found, 5809.0 (Figure 99).

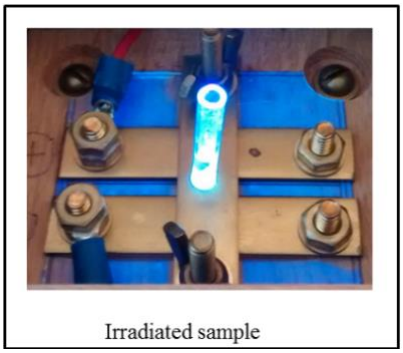

Figure 97: For *in-vitro* photolysis, the resin material was suspended into a glass vial which then was mounted on top of a 365 nm LED.

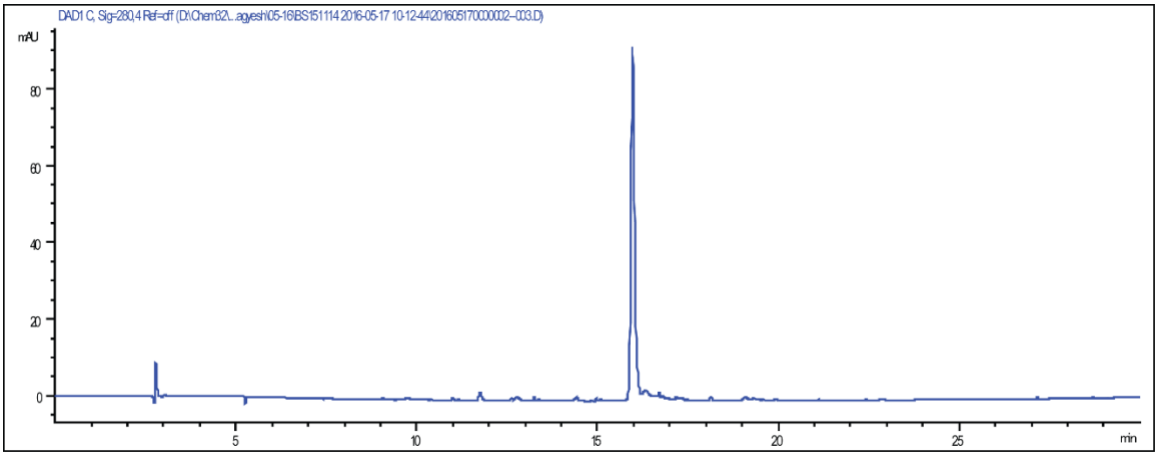

Figure 98: HPLC chromatogram of photoreleased insulin.

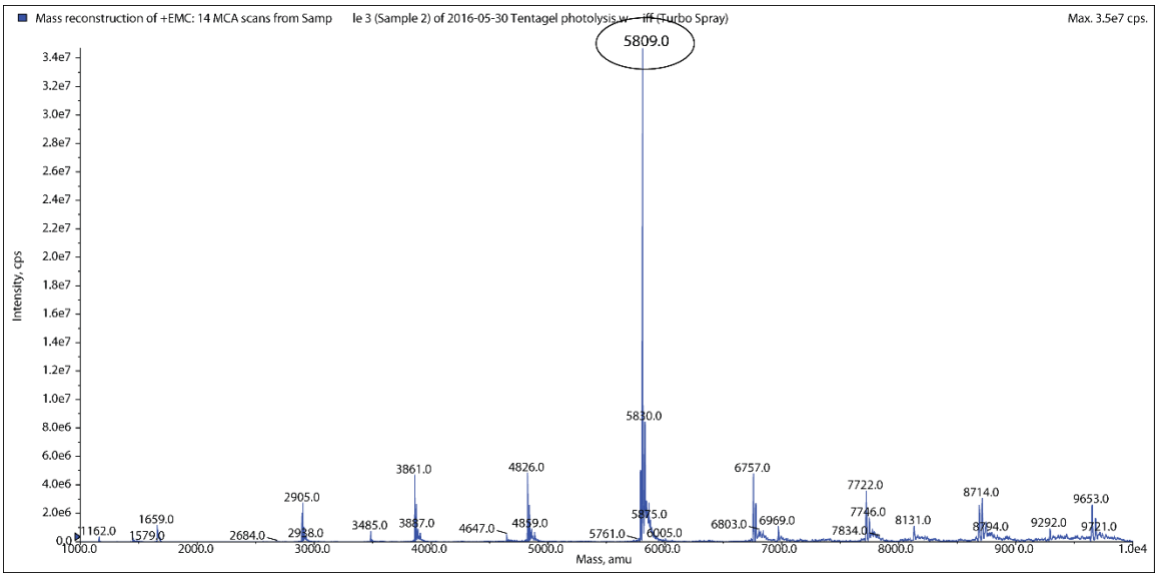

Figure 99: Characterization of photoreleased insulin from Tentagel resin. MS infusion showing insulin at $[M]^{+}$=5809.0.

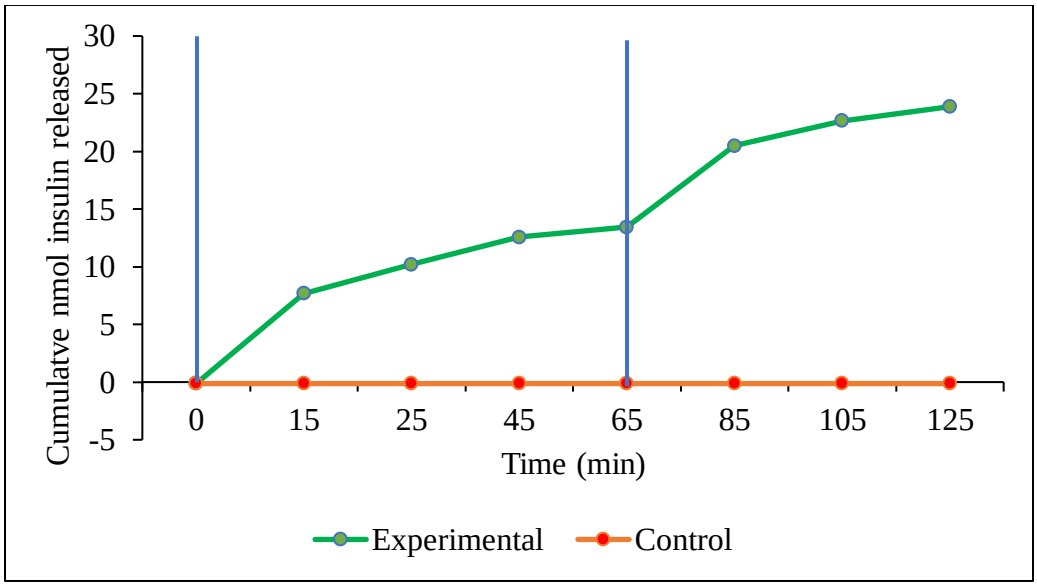

Figure 100: *In-vitro* release study from insulin conjugated Tentagel resin. The irradiation was performed for 2 min at t=0 and t=65 min each (as represented by 2 vertical blue lines).

The release pattern for the Tentagel resin was much different from ChemMatrix resin used earlier.[29] Even though the irradiation was performed only for 2 min at t=0 and

t=65, we observed that insulin was still coming off from the resin after that. It is maybe because insulin which was released due to light remained bound to the resin non-covalently and slowly leached out from the resin attaining a plateau after about an hour (Figure 100). This binding issue was not observed with ChemMatrix resin, all the insulin which was released immediately came off in the supernatant. In this study, just with 4 minutes of irradiation, approximately 18% of insulin was released.

In-vivo experiments

For performing the *in-vivo* studies, this scale of synthesis was insufficient. This material once made had storage issues, and the frequency of animal studies was low (1-2 replicates/ week) – we couldn't finish all replicates in one or two days. Due to these challenges, it was decided to perform the final step i.e. click reaction just one day before the scheduled animal studies to use the material immediately after it was synthesized. The DBCO conjugated 10 µm resin, as well as insulin azide, were stored in -20 °C for a longer period, and they were mixed to immobilize caged insulin on resin just before the studies. The amount of insulin-immobilized was calculated, and the studies were performed.

Rats were first anesthetized with isoflurane using a precision vaporizer. The upper backs of rats were shaved before injection of the PAD materials. Injections of ~80 µL of PAD material were made using a 0.5 cc syringe attached to a 27-G needle. Due to the limitations of the volume that can be injected into the dermal layer of skin at one time, two injections (of 40 µL each) of PAD materials were made side by side. The compact LED light source was anchored to the skin over the injection sites using superglue. The body temperature and hydration were maintained throughout the experiment. For the experiment, the depot was injected first and allowed to stay there for 20 minutes before

irradiation. It was to observe if there is any unwanted leaching from the site before irradiation. This time point was annotated as t = -20 minutes. Twenty min post-injection, the depot was irradiated for 2 minutes. The irradiation was between t=0 to t=2 minutes. There was a reason for limiting the irradiation duration to two minutes. The heat generated from the light source appeared to cause skin damage, and scab formation was observed after 5 minutes of irradiation. 2 minutes of irradiation did not show such toxicity. Hence it was selected rather than irradiating for a longer duration.

The results were encouraging as shown in Figure 101 for insulin release. For the first 20 min before irradiation, we did not see any change in insulin levels suggesting there was no leaching from the depot. As soon as we irradiated for 2 minutes, insulin levels jumped quickly from baseline levels and peaked at 45 min then slowly dropped down. This release profile was comparable to what we saw with injected photoreleased insulin (Figure 92). In the control samples, where the light was blocked using an aluminum foil, there was no change in insulin as expected. In irradiated animals higher insulin levels were measured and resultantly, BG levels dropped, and the physiological effect of the released insulin was seen (Figure 102). The released insulin caused BG drop which lasted for the first 60 min and then it started going up suggesting that the effect of insulin was over by the end of the hour.

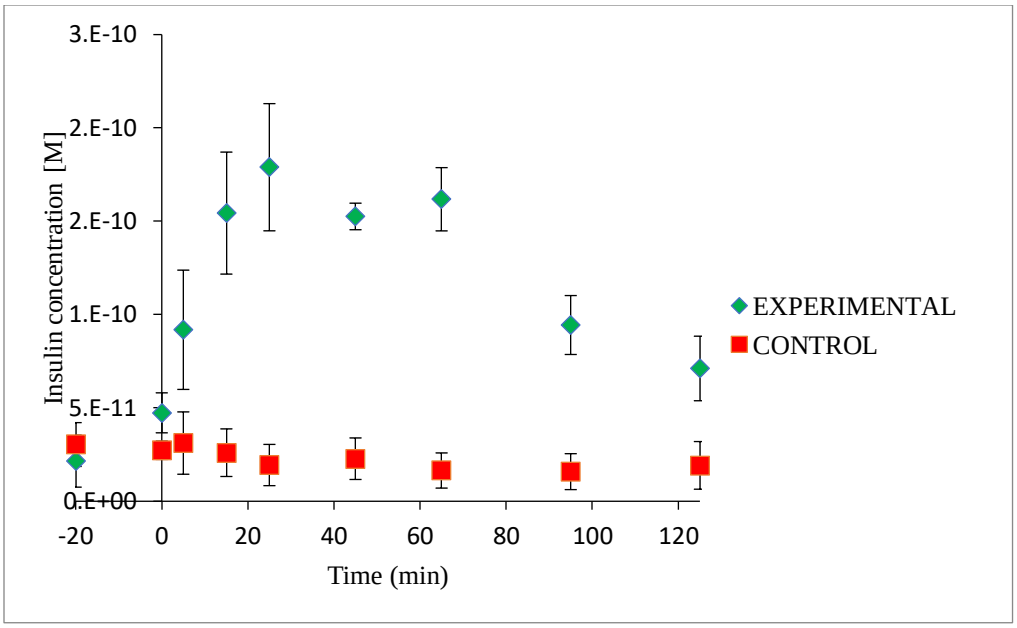

Figure 101: Results of irradiation of PAD material in animals in triplicates. The irradiation was performed between t=0 to t=2 min. The plot shows insulin concentration in the blood.

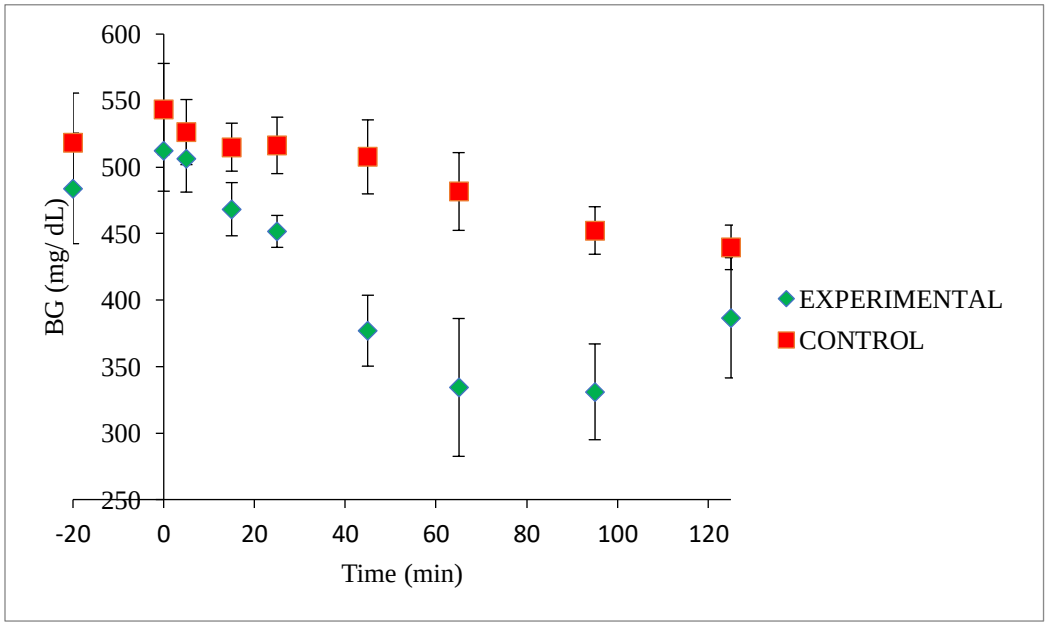

Figure 102: Results of irradiation of PAD material in animals in triplicates. The irradiation was performed between t=0 to t=2 min. The plot shows BG levels.

This experiment answered three questions that -

i. Light has sufficient penetrating power in the skin to hit the PAD material and release insulin,

ii. Once insulin is released from the site, it quickly gets into the systemic circulation as it was detected in the bloodstream just within 5 min and peaked at around 25 min after the irradiation,

iii. The amount of insulin that was released due to 2 min irradiation was enough to reduce BG. Although the effect was not very significant and lasted only for 60 minutes, it could be increased by increasing the duration of irradiation.

The next question we wanted to ask was whether additional pulses of light in discrete intervals irradiation would release more amount of insulin from the depot. How would this affect the BG levels? To test this, as performed earlier, we injected PAD material holding 140 nmol of insulin on the resin. There was a brief interval of 20 minutes between the time of injection and the time of irradiation. The first irradiation was performed between t=0 to t=2. The next irradiation was performed approximately after an hour later between t=65 to t=67 minutes. We expected that we should see a spike in insulin concentration after each irradiation. For the control samples, the LED was switched on, but the light was blocked using an aluminum foil.

Looking at the results (Figure 103 and Figure 104), as expected, we saw an increase in insulin concentrations after both irradiations. Due to additional insulin being released due to additional pulses of light, there was a robust drop in BG. By the end of 2 hours, it was still going down, and it was statistically significant. The duration of study for this experiment was very short. However, it verified the concept that insulin release could be

triggered using light in a live animal using PAD.

In these experiments, the hypothesis that insulin could be delivered in a live animal using light and PAD was demonstrated for the first time.[73] Though it also helped reduce BG in rats, it is still in the very early stages of development. There are still concerns that need attention –

i. The risk of toxicity due to light – in this case, we used 365 nm wavelength. However, longer repetitive exposure will be harmful to the skin. The risks need to be assessed, and if it is harmful, strategies to overcome these issues should be sought.

ii. Assessing the potential of an immune reaction to the injected material. The body's immune system can attack material because it may find it foreign in nature.

iii. What is the lifetime of the depot? How long would it last and predictably release insulin after an injection? How would we know how much insulin is left in the depot and when is the time to re-inject?

iv. In the long term, we need to automate insulin delivery system and link it to a glucose monitoring system. In doing so, the fluctuation in the BG levels would trigger the LED which would result in insulin being released, and hence lowering of BG.

v. Designing material in such a way that would introduce a minimum number of foreign elements in the body. Such a system would result in a reduction of the body's reaction to the material, reduced synthetic steps, and toxicity, etc.

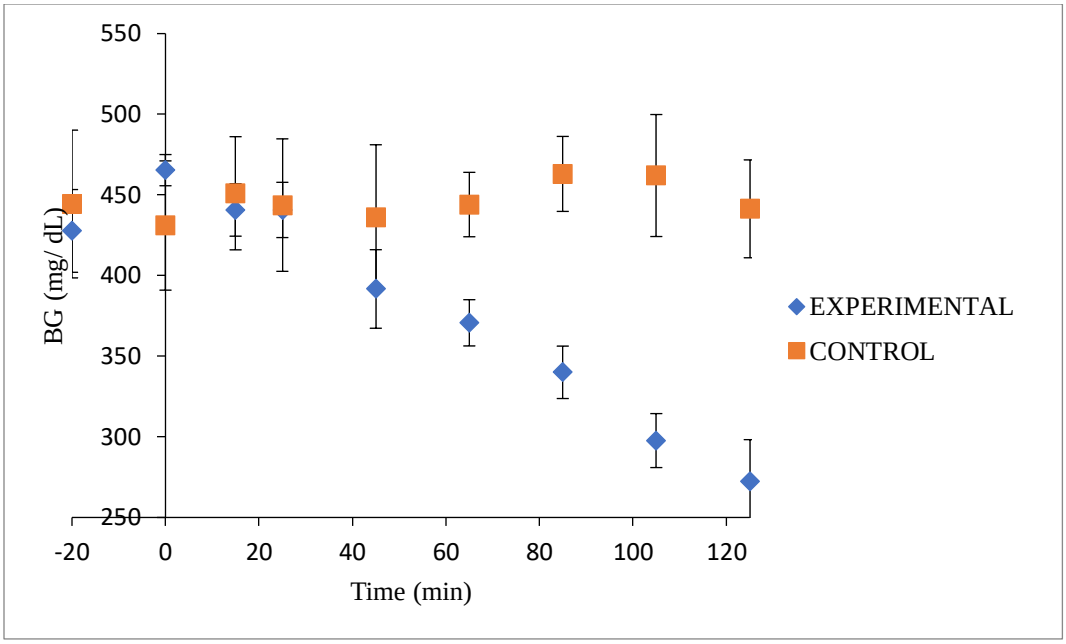

Figure 103: Results of irradiation of PAD material twice in animals in triplicates. The irradiation was performed between t=0 to t=2 min and t=65 to t=67 minutes. BG levels are shown here.

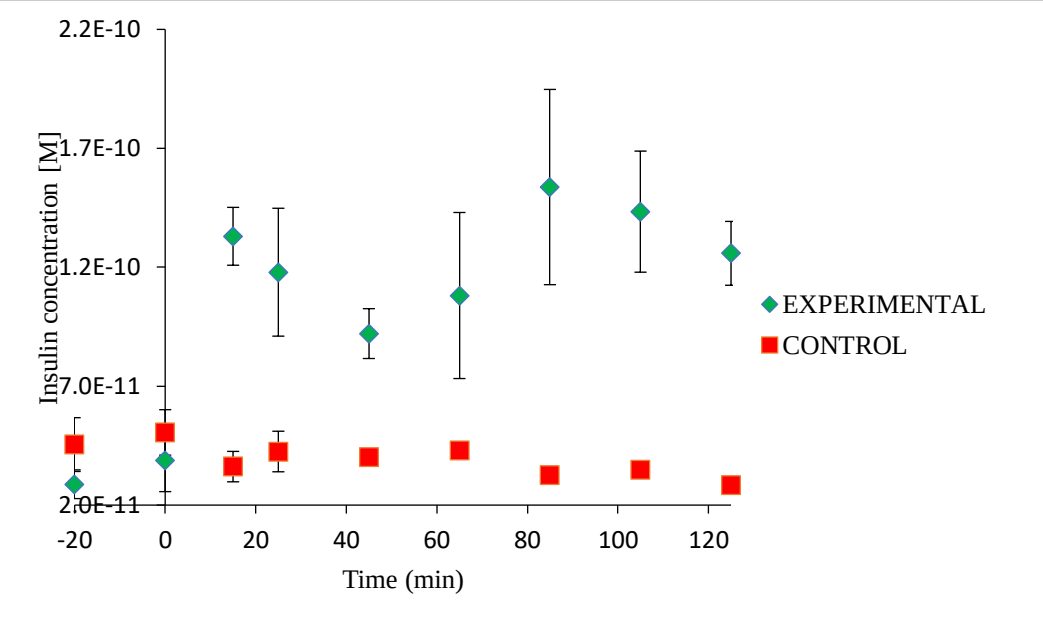

Figure 104: Results of irradiation of PAD material twice in animals in triplicates. The irradiation was performed between t=0 to t=2 min and t=65 to t=67 minutes. Insulin measured is shown in the figure.

Chapter 4

SYNTHESIS AND TESTING OF ADVANCED SECOND-GENERATION MATERIAL

Visible light-activated photolabile group

In the lab, DMNPE has been used as the photolabile group for various projects as described in earlier chapters. DMNPE was used because of its higher quantum yields, clean photorelease reactions and due to our experience working with it.[30] The quantum yield is defined as the number of moles of substrate released from the caged compound divided by the number of photons absorbed at an irradiated wavelength by the caged compound. A photolabile group having higher quantum yield is desirable, especially for biological and *in-vivo* medical applications. Another critical criterion to evaluate the efficiency of a photolabile group is the product of multiplication of quantum yield and its molar extinction coefficient (ε). Although DMNPE group works well and we are continuously using it for a variety of projects, it is not ideal for insulin project. To deliver insulin continuously, multiple irradiations would be needed throughout the day for a lifetime and 365 nm wavelength is categorized as near UV radiation which has the potential for toxicity. The energy contained in the radiations generate singlet oxygen species which do oxidative damage to fibroblasts cells when studied.[74–76] The link between UV exposure and cancer is well established.[77–79] Furthermore, DMNPE after photolysis generates a nitroso group,[80,81] N-nitroso compounds are known to be carcinogenic.[82,83] Because of the risk of both chemical and phototoxicity and potential for carcinogenicity, DMNPE usage in the long term will not be feasible. To avoid these issue, longer wavelengths in the visible light range or infrared range would be a much safer option. Longer wavelength radiation has

less, or no potential of toxicity compared to that of 365 nm light. Hence, we started looking for different photolabile groups which could be photocleaved using visible light.

Coumarin is a suitable alternative DMNPE and provides following advantages over DMNPE that –

1. Coumarin could be activated by visible light wavelengths, two-photon excitation or infrared irradiations.[84–90]
2. Longer wavelengths have a deeper penetration into the skin which provides advantages over shorter wavelengths as more photons would be able to hit PAD material in the dermal layer.[91]

Considering these advantages provided by coumarin, we pursued designing coumarin-based photolabile group which could be used for PAD material synthesis. The structures of coumarin and DMNPE are shown in Figure 105.

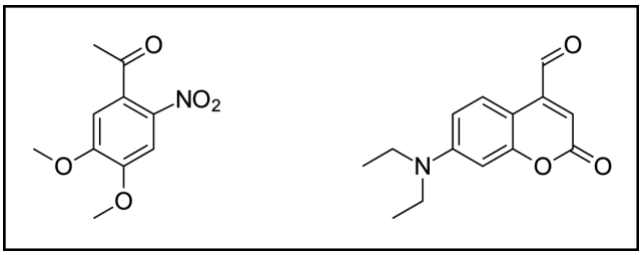

Figure 105: Structure of DMNPE ketone (left) and DEACM aldehyde (right).

In the figure above, DMNPE ketone is shown which was used in all earlier studies, for insulin macropolymer synthesis and first-generation *in-vivo* studies. 7-Diethylaminocoumarin-4-yl (DEACM) is commercially available, which has been used as a photocleavable group in the past.[92–94] It can be modified further to introduce an aldehyde and subsequently a hydrazone functionality similar to DMNPE hydrazone. We decided to continue using alkyne-azide based click chemistry here for conjugation but introducing

azide functionality was a bit challenging for a variety of reasons. Below all the synthetic routes that were pursued and problems encountered are reported and described.

Synthesis of coumarin caged insulin

Multiple synthetic routes were explored to synthesize coumarin ring containing a handle for caging insulin and another handle for performing click reaction. The unsuccessful routes are described in the beginning. Route # 4 was the easiest and hence used for caging insulin.

Route 1: Synthesis using 7-amino-4-methyl coumarin

The initial steps were adapted from Hagen, et al., where dialkylation of 7-amino-4-methyl coumarin (7-AMC) was performed.[86] The synthesis scheme is shown in Figure 106. The alkylation was followed by oxidation by selenium dioxide to introduce aldehyde functionality. After this, Hagen, et al., further converted it to hydrazone, hydrazone was later converted to diazo to cage carboxylic acid. However, we decided to cage the amino group on insulin rather than carboxylic acid this time. It was decided because - i) We wanted to explore if amino groups on proteins can be caged and whether it can be utilized for such applications. Insulin has six carboxylic acid groups. Earlier after caging insulin to synthesize DIMA we used to get a mixture of isomers. We postulated that since insulin has only three amino groups and only one of it is a B29 lysine which might react preferentially yielding only single isomer.[38] ii) It might have implications in insulin hexamer formation and its onset of action. Hence after oxidation by selenium dioxide oxidation, we reduced aldehyde using $NaBH_4$ to give alcohol functionality. Two t-butyl esters were then cleaved using trifluoroacetic acid (TFA) to yield free carboxylic acids. Here multiple functionalities like azide could be coupled to alter the properties of caged insulin.

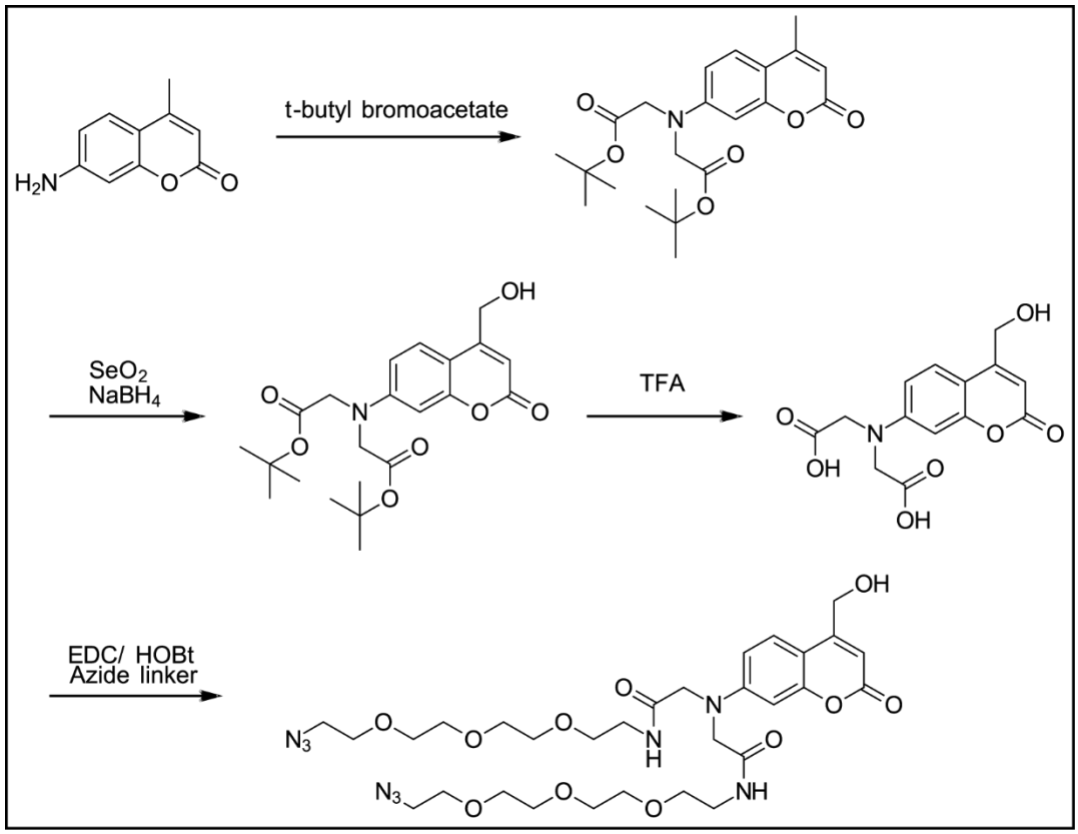

Figure 106: Synthesis Scheme 1 for coumarin azido alcohol (CAA)

Originally, we planned on conjugating mono-alkylation on 7th position amine but in that case, the SeO_2 oxidation step was problematic and resulted in many side products. However, when we alkylated twice forming a 3º amine, the yield improved significantly. Hence it was performed in this manner.

tert-Butyl [(*tert*-butoxycarbonylmethyl)(4-methyl-7-coumarinyl)amino]acetate

AMC (5.26 g, 30 mmol, Chem-Impex), t-butyl bromoacetate (30 mL, 200 mmol, Fisher Sci.), DIEA (20.5 mL, 117.7 mmol, Fisher Sci.) and sodium iodide (4.5 g, 30 mmol) were mixed in 90 mL acetonitrile. The reaction was refluxed for five days. The crude reaction mixture was cooled to room temp., filtered and dried using rotary

evaporator. This reaction yielded a 30:70 ratio of monoalkylated to the dialkylated product. The reaction never went to completion to give the only dialkylated product. The product was purified by using flash chromatography using DCM: EtOAc (4:1) as the solvent system. Yield (1.55 g, 12.8%); analytical HPLC – reversed-phase HPLC-MS (flow rate 0.4 mL min^{-1}, runtime 15 min with 5 min post-run), solvent A (0.1% FA in H_2O), solvent B (0.1% FA in ACN), gradient 60 % B isocratic over 15 min, C18 Hypersil column (5 µm, 150 × 3.2 mm, Agilent), retention time: 11.15 min; ESI-MS (m/z) $[MH]^+$ calculated for $C_{22}H_{29}NO_6$, 404.2; found, 404.2 (Figure 107).

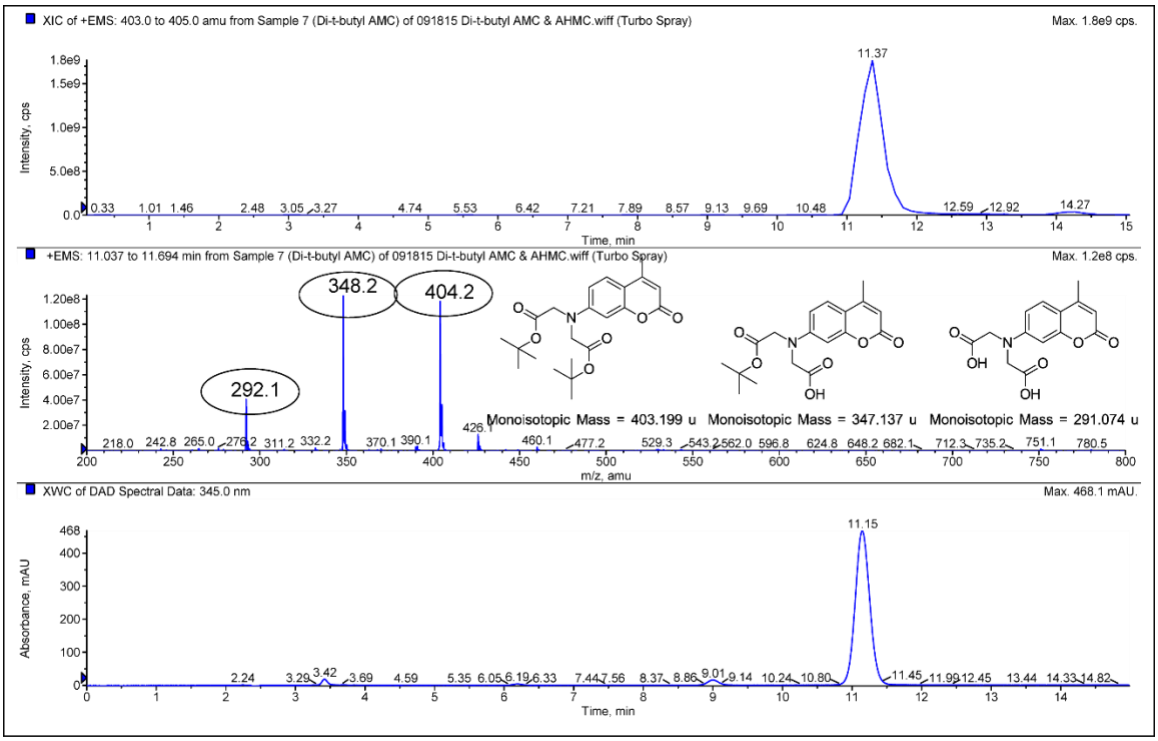

Figure 107: LCMS of tert-butyl [(tert-butoxycarbonylmethyl)(4-methyl-7-coumarinyl)amino]acetate. The peaks of 292.1 and 348.2 were due to the subsequent fragmentations of the ester bond and cleavage of the t-butyl group while flying in the MS.

tert-butyl{(*tert*-butoxycarbonylmethyl)[4-(hydroxymethyl)-7-coumarinyl]amino}acetate

tert-Butyl [(tert-butoxycarbonylmethyl)(4-methyl-7-coumarinyl)amino]acetate purified earlier (0.342 mg, 0.850 mmol), SeO_2 (0.215 g, 1.40 mmol) were mixed in 25 mL *p*-xylene and refluxed for 24 hours. It was filtered hot to get rid of SeO_2 and dried using rotavap. 50 mL of anhydrous MeOH added and stirred for 30 min, and $NaBH_4$ (0.1 g) was added, the reaction was run for 2 hours. It was filtered and dried on rotavap. The crude mixture was then partitioned between DCM and water. DCM layer was washed thrice with water, then with brine and dried finally. Yield (215 mg, 60.1%); analytical method – reversed-phase HPLC-MS (flow rate 0.4 mL min^{-1}, runtime 15 min with 5 min post-run), solvent A (0.1% FA in H_2O), solvent B (0.1% FA in ACN), gradient 60 % B isocratic over 15 min, C18 Hypersil column (5 μm, 150 × 3.2 mm, Agilent), retention time: 5.81 min; ESI-MS (m/z): $[MH]^+$ calculated for $C_{22}H_{29}NO_7$, 420.2; found, 420.2 (Figure 108).

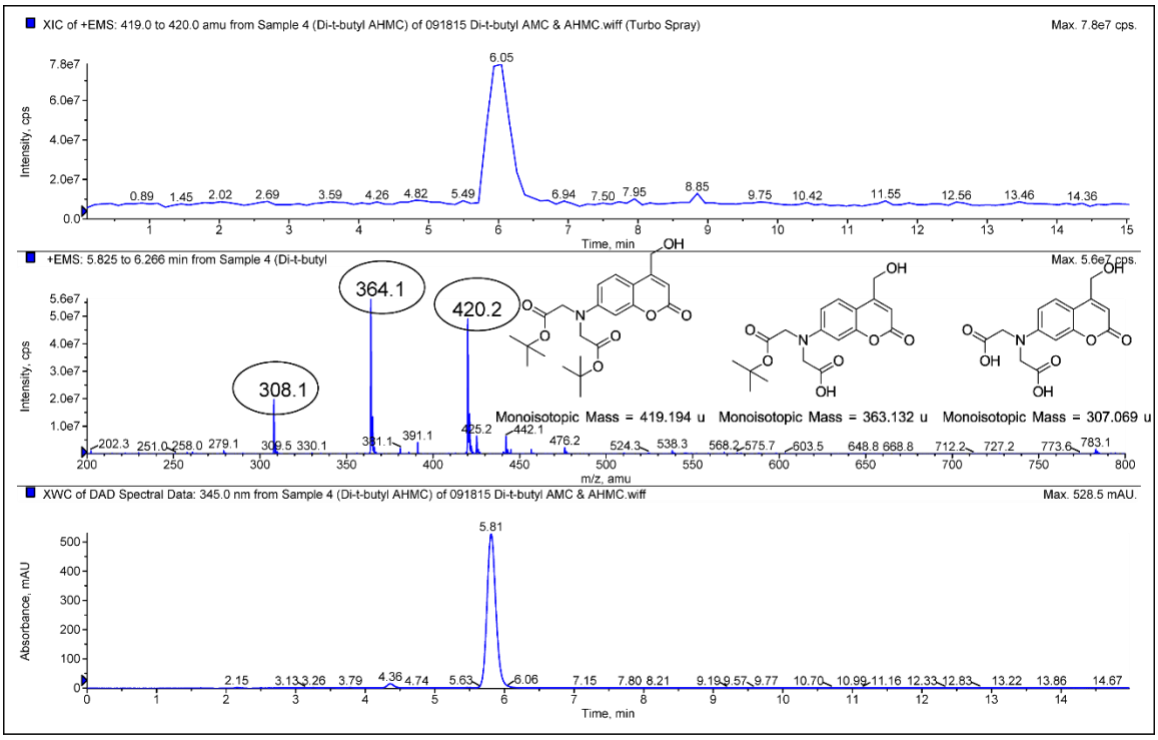

Figure 108: LCMS of tert-butyl{(tert-butoxycarbonylmethyl)[4-(hydroxymethyl)-7-coumarinyl]amino}acetate. The peaks of 308.1 and 364.1 were due to the subsequent fragmentations of the ester bond and cleavage of the t-butyl group while flying in the MS.

{(Carboxymethyl)[4-(hydroxymethyl)-7-coumarinyl]amino}acetic acid

The product purified above (42.8 mg, 0.10 mmol) was mixed in 4 mL cocktail containing 75% TFA: 1% water and 24% DCM. The reaction was run for 1 hour and dried using rotavap. Analytical method – reversed-phase HPLC (flow rate 1 mL min^{-1}, runtime 30 min with 5 min post-run), solvent A (0.1% TFA in H_2O), solvent B (0.1% TFA in ACN), gradient 0 % B to 100% B over 30 min, C18 Hypersil column (5 µm, 250 × 4.6 mm, Agilent), retention time: 8.8 min. (Figure 110). The ^1H NMR for the hydrolyzed product is shown in Figure 109.

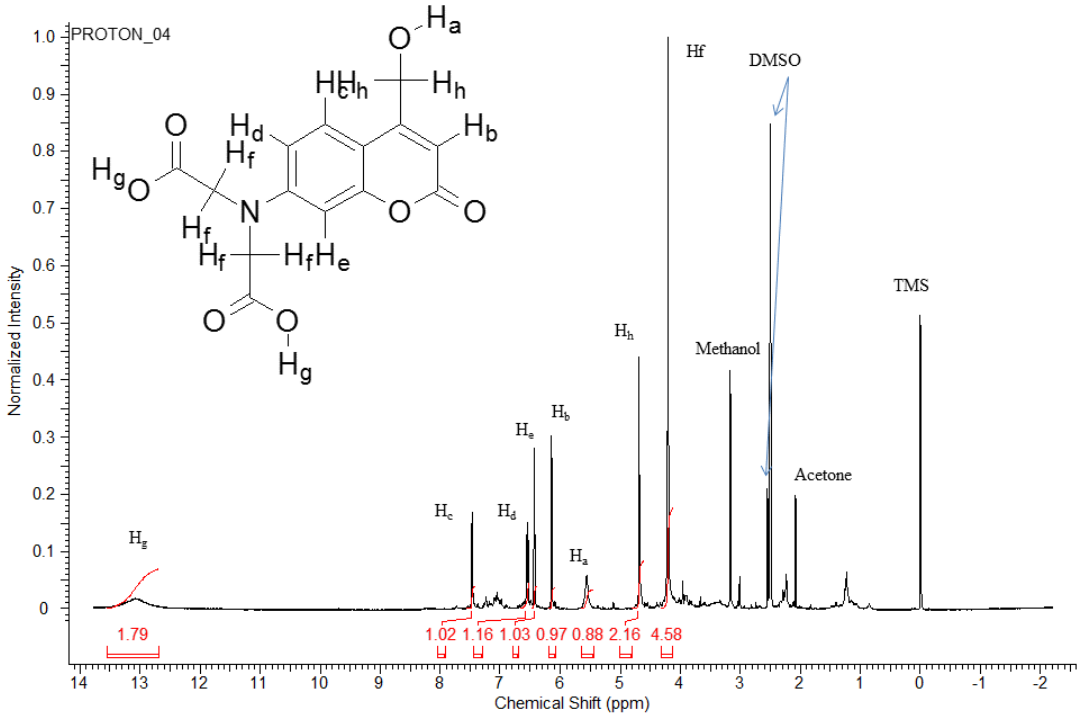

Figure 109: NMR of {(carboxymethyl)[4-(hydroxymethyl)-7-coumarinyl]amino}acetic acid.

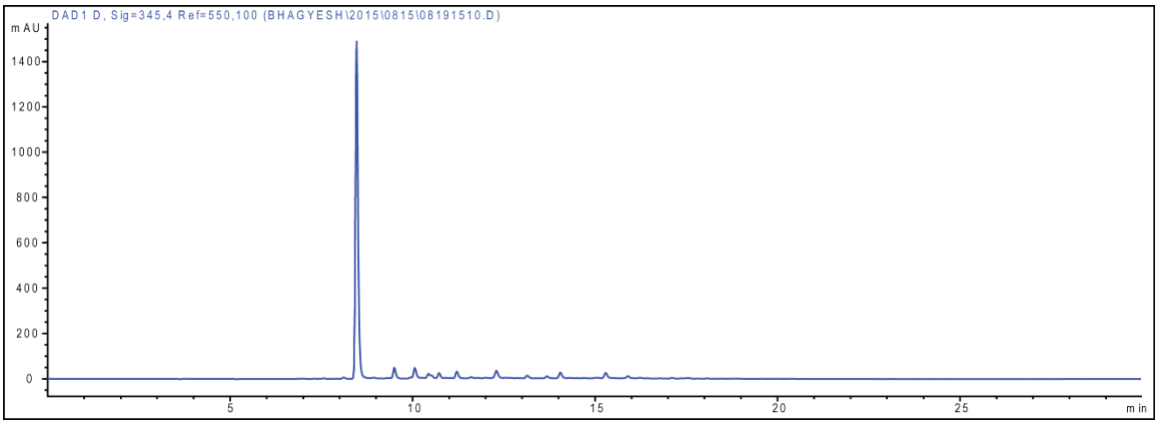

Figure 110: HPLC chromatogram of {(carboxymethyl)[4-(hydroxymethyl)-7-coumarinyl]amino}acetic acid.

1-(2-{2-[2-(2-azidoethoxy)ethoxy]ethoxy}ethylamino)-2-{[2-(2-{2-[2-(2-azidoethoxy)ethoxy]ethoxy}ethylamino)-2-oxoethyl][4-(hydroxymethyl)-7-coumarinyl]amino}-1-ethanone

After Boc deprotection, the free carboxylic acid containing product (45.3 mg, 147 µmol), 11-azido-3,6,9-trioxaundecan-1-amine (62 µL, 310 µmol), HOBt hydrate (90.3 mg, 590 µmol) were dissolved in 0.6 mL of anhydrous DMF. Then EDC (79.2 mg, 501 µmol) was added to the mixture. However, it was not clean. Hence it was purified using flash chromatography using DCM as a solvent. Yield (8.6 mg, 8.2%); analytical method – reversed-phase HPLC-MS (flow rate 0.4 mL min^{-1}, runtime 15 min with 5 min post-run), solvent A (0.1% FA in H_2O), solvent B (0.1% FA in ACN), gradient 60 % B isocratic over 15 min, C18 Hypersil column (5 µm, 150 × 3.2 mm, Agilent), retention time: 3.25 min; ESI-MS (m/z): $[MH]^+$ calculated for $C_{30}H_{45}N_9O_{11}$, 708.3; found, 708.2 (Figure 111); reversed-phase HPLC (flow rate 1 mL min^{-1}, runtime 30 min with 5 min post-run), solvent A (0.1% TFA in H_2O), solvent B (0.1% TFA in ACN), gradient 0 % B to 100% B over 30

min, C18 Hypersil column (5 µm, 250 × 4.6 mm, Agilent), retention time: 16 min (Figure 112).

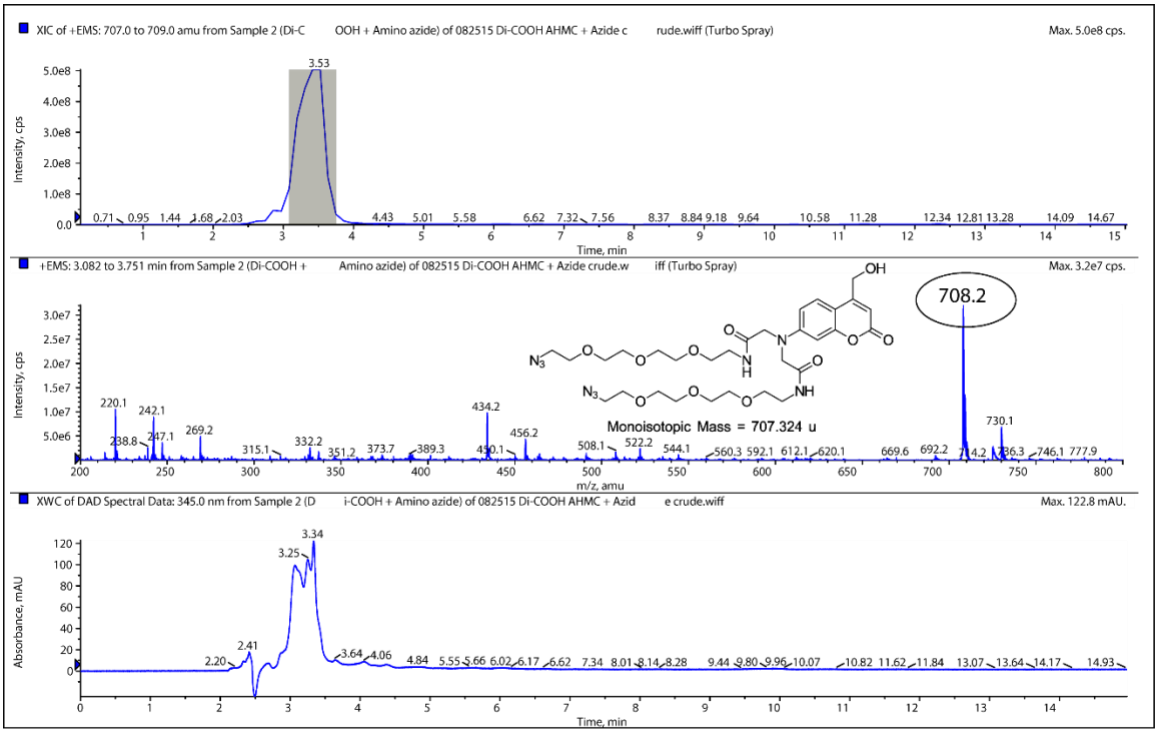

Figure 111: LCMS of the product. The product mass is seen at $[MH]^+$=708.2 eluting at 3.25-3.34 minutes.

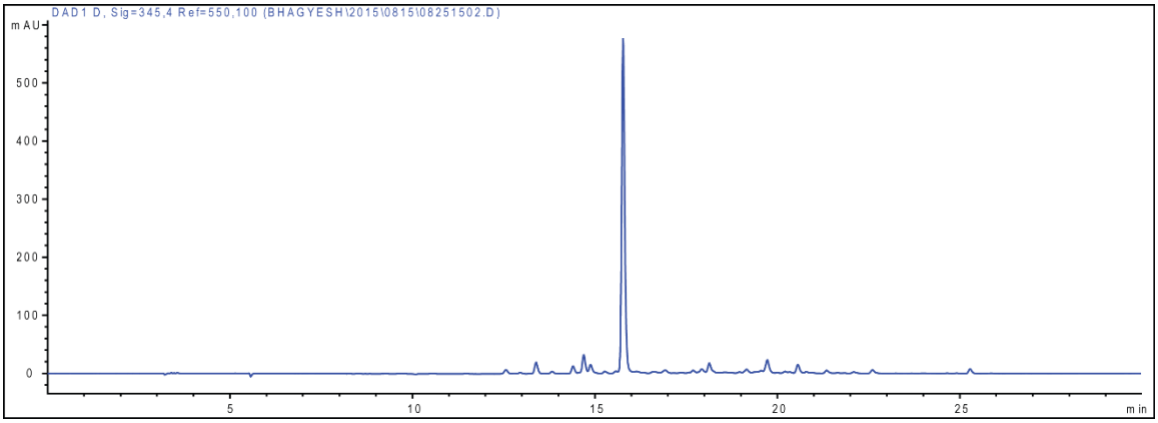

Figure 112: HPLC chromatogram of the product.

Purified coumarin alcohol azide (CAA) (8.6 mg) was conjugated to insulin using CDI/DMAP as coupling reagents. Insulin could be caged successfully but at much lower yields. Large quantities of the caged material will be required for performing *in-vivo* studies, scale-up would be a problem if this route is followed. Also, the percent yield of the first step is close to 10% which is low. Moreover, given that 7-AMC is an expensive chemical, we started looking for more feasible and convenient synthetic routes.

Route 2: Synthesis of 7-azido-4-methyl coumarin from 7-amino-4-methyl coumarin

Here, the original reaction conditions were taken from literature reported earlier.[95–98] The advantage here is that instead of alkylating 7-position amine with an ester, then hydrolyzing and subsequent coupling using an azide-containing linker (as shown in the route # 1), 7-position amino group could be converted to an azide moiety directly as shown in Figure 113. This reduces the number of steps from three to one and the reported yield in the literature is over 90%. Once the azide group is synthesized, 4'-methyl group could be oxidized by SeO_2 to introduce aldehyde group. Thus, CAA could be synthesized in only two steps rather than four.

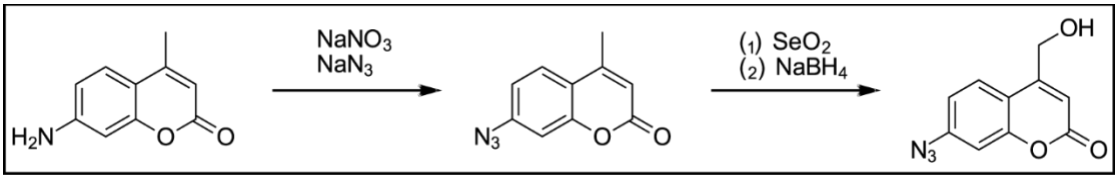

Figure 113: Route # 2: Synthesis of CAA through 7-azido-4-methyl coumarin route.

7-azido-4-methylcoumarin synthesis

7-AMC (3.000 g, 17.14 mmol, Chem-Impex®) was suspended in 66 mL DI water in a 3-necked flask in an ice bath. After 10 min, H_2SO_4 (18 mL) was added in a dropwise manner maintaining the temperature. Meanwhile, in separate flasks, sodium nitrite (1.500

g, 21.74 mmol) and sodium azide (1.98 g, 30.5 mmol) were dissolved in 20.4 mL and 12 mL volume of water, respectively, and chilled in ice to 0 °C. Once H_2SO_4 addition was finished, sodium nitrite was added in a dropwise manner followed by sodium azide in the same fashion. A precipitate was observed immediately after sodium azide addition. It was stirred overnight, filtered and washed with 50 mL cold water. The precipitate was dissolved in DCM and washed DCM layer with saturated $NaHCO_3$, followed by saturated NaCl, dried over $MgSO_4$ and dried using rotavap. Yield (3.079 g, 89.3%); ESI-MS (m/z): $[MH]^+$ calculated for $C_{10}H_7N_3O_2$, 202.1; found, 202.1 (Figure 115); analytical method – reversed-phase HPLC (flow rate 1 mL min^{-1}, runtime 30 min with 5 min post-run), solvent A (0.1% TFA in H_2O), solvent B (0.1% TFA in ACN), gradient 0 % B to 100% B over 30 min, C18 Hypersil column (5 µm, 250 × 4.6 mm, Agilent), retention time: 19.5 min (Figure 114); reversed-phase HPLC-MS (flow rate 0.4 mL min^{-1}, runtime 15 min with 5 min post-run), solvent A (0.1% FA in H_2O), solvent B (0.1% FA in ACN), gradient 60 % B isocratic over 15 min, C18 Hypersil column (5 µm, 150 × 3.2 mm, Agilent), retention time: 5.36 min (Figure 115).

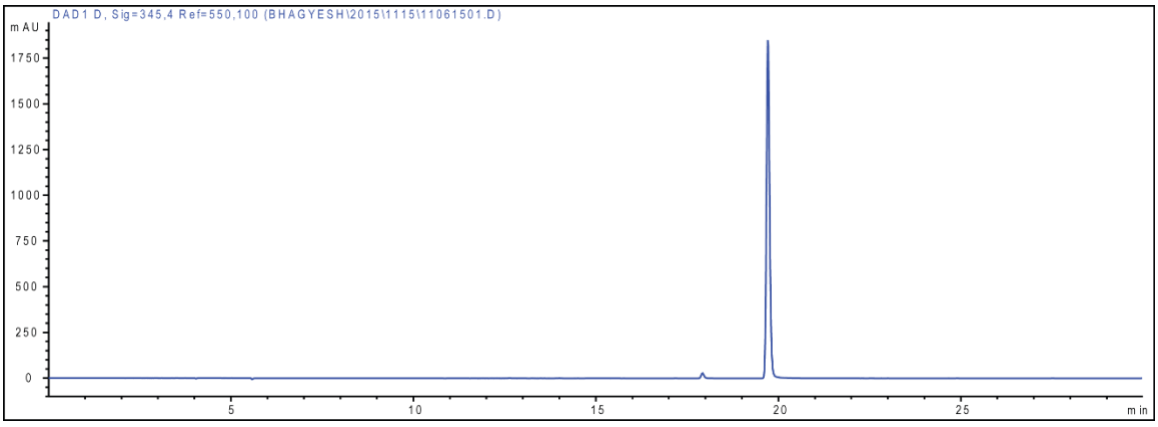

Figure 114: HPLC chromatogram of 7-azido-4-methylcoumarin.

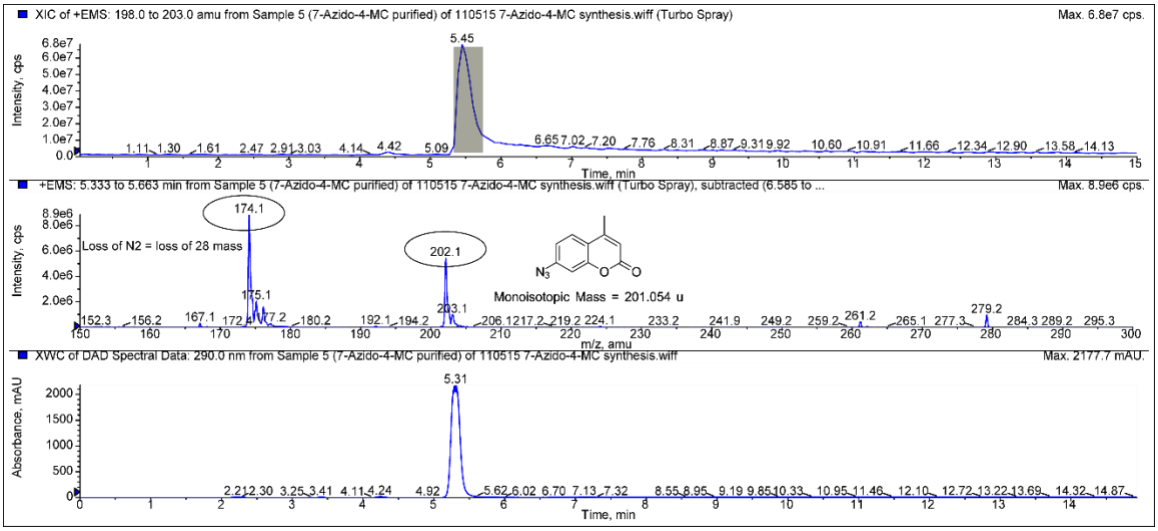

Figure 115: LCMS of 7-azido-4-methylcoumarin. The product mass is seen at $[MH]^+$=202.2 eluting at 5.45 min.

A test click reaction on 7-azido-4-methyl coumarin (7-AzMC)

At this point, we wanted to run a test click reaction on 7-AzMC to see if azide is still reactive towards the strained alkyne and how much change in UV-vis spectrum occurs after the reaction, refer to the Figure 116. We suspected whether having an azide on the conjugated ring system would affect its reactivity or not. We wanted to test how this would affect the UV-vis spectrum of 7-AzMC. Hence, we set up a reaction between 7-AzMC and DBCO conjugated ChemMatrix resin (synthesis is described above in Chapter 3). If the click reaction is successful, 7-AzMC will get clicked onto the resin, which could be analyzed by performing TFA cleavage easily.

7-Azido-4-methyl coumarin (0.6 mg, 3 µmol) was added to pre-swollen DBCO conjugated ChemMatrix resin in 20 µL DMSO. The mixture was shaken at 40 °C at 600 rpm for 24 hours. After 24 hours, the resin was washed five times using 0.3 mL DMSO, then DCM and dried. TFA cleavage was performed to analyze the reaction.

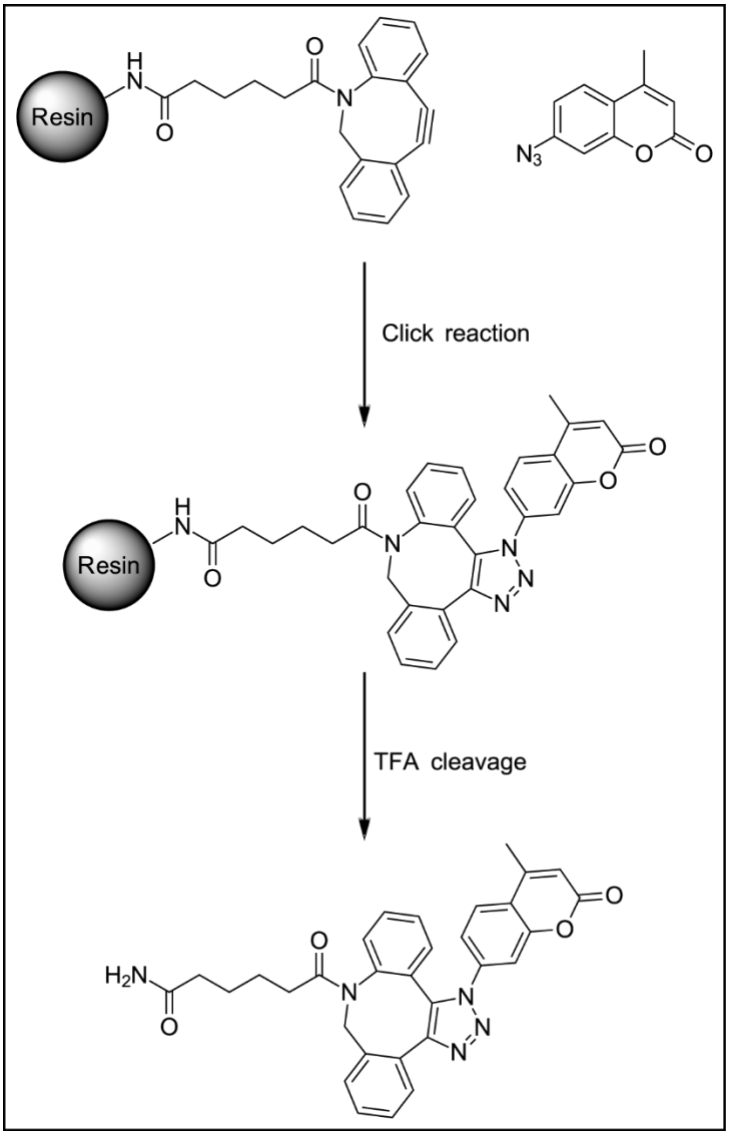

Figure 116: Click reaction between DBCO conjugated resin and 7-azido-4-methyl coumarin.

LCMS analytical method – reversed-phase HPLC-MS (flow rate 0.4 mL min^{-1}, runtime 15 min with 5 min post-run), solvent A (0.1% FA in H_2O), solvent B (0.1% FA in ACN), gradient 50 %B isocratic over 15 min, C18 Hypersil column (5 µm, 150 × 3.2 mm, Agilent), retention time: 7.59 min; ESI-MS (m/z): $[MH]^+$ calculated, 534.2; found, 534.4 (Figure 117).

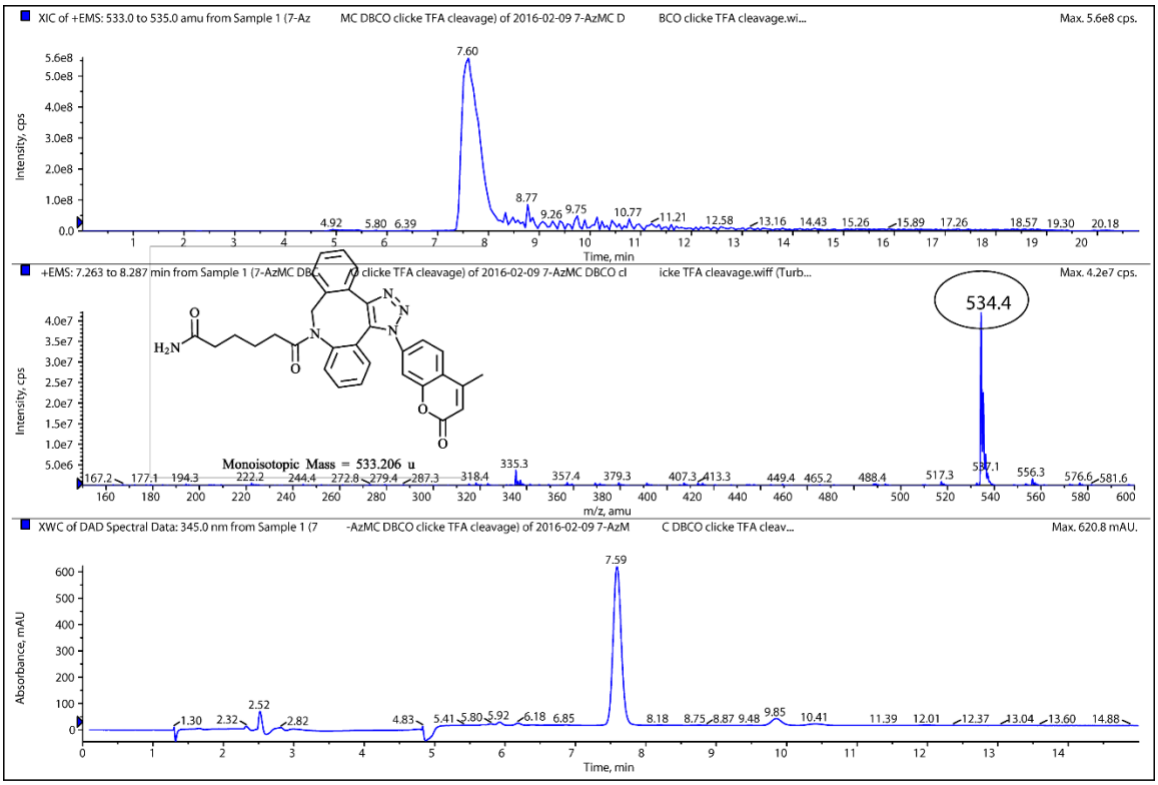

Figure 117: LCMS of the clicked product. It is seen at $[MH]^+$=534.4 eluting at 7.59 min.

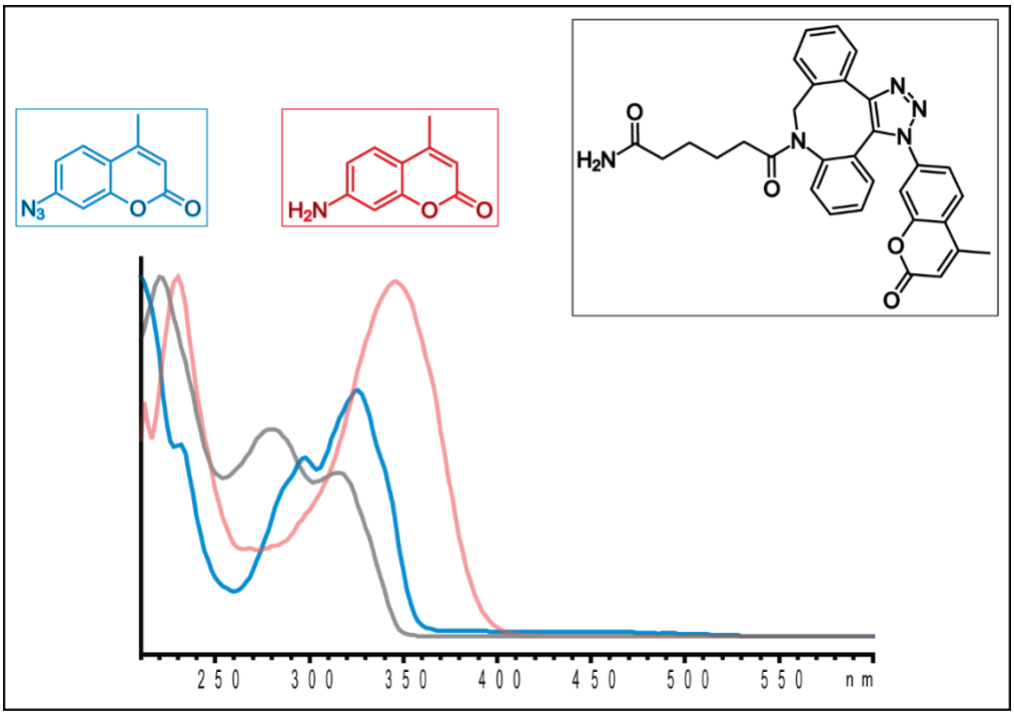

Figure 118: UV-vis spectrum of the coumarin species synthesized in the above reaction.

The click reaction worked, and we could see the product as a single peak with the correct mass on LCMS. So, the reactivity of azide is retained despite it being conjugated on the ring. However, the spectra of both 7-AzMC and clicked product are very different from 7-AMC, refer to Figure 118. We want to photocleave coumarin at >400 nm wavelength i.e. visible light range. Both UV-vis spectra do not have any absorbance at that wavelength. Hence, we did not move forward with this approach.

Route 3 – Synthesis using 7-hydroxy-4-methyl coumarin

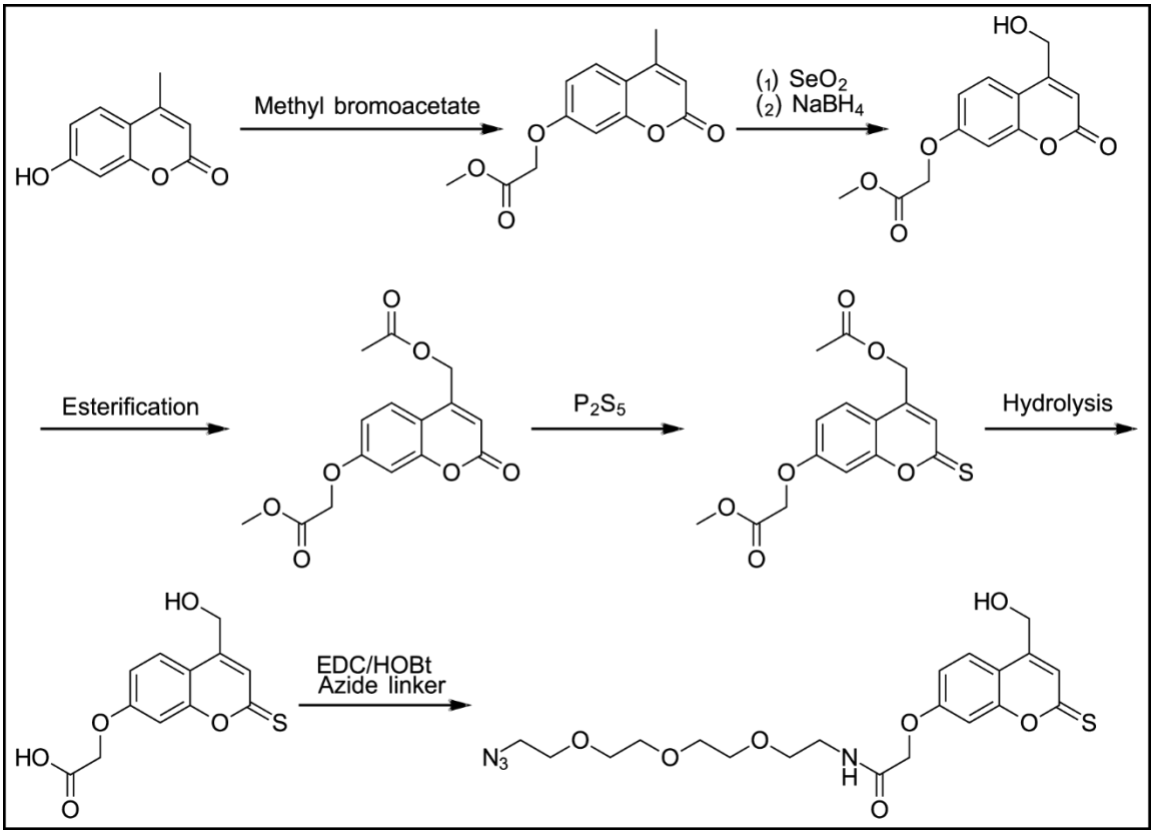

Figure 119: Synthesis using 7-hydroxy-4-methyl coumarin.

The route # 1 was challenging mainly because of the first alkylation of 7-position amine. Just monoalkyating that amine was not working because in that case, SeO_2 step generated many side products with a minimum yield of the desired product. Instead, the

SeO_2 reaction proceeds well only with 3° amine and does not work with 2° amines. The dialkylation reaction was often incomplete, and the yield was close 10%. Hence to avoid these issues, we thought of utilizing 7-hydroxy-4-methyl coumarin (7-HMC) instead of 7-amino-4-methyl coumarin. Here single alkylation could be performed easily in quantitative yield instead of worrying about mono versus dialkylation. The disadvantage, however, is that 7-AMC absorbs at longer wavelength compared to 7-HMC which is desirable. The 7-AMC has λ_{max} at 345 nm whereas 7-HMC has λ_{max} at 325 nm. We could, however, modify the ring so that it would absorb higher wavelength light. For example, by replacing oxygen from second position carbonyl group with sulfur.[90] The synthesis route is described in Figure 119.

Methyl (4-methyl-7-coumarinyloxy)acetate

7-HMC (11.44 g, 65.00 mmol) and K_2CO_3 (18 g, 65 mmol) were added in 80 mL DMF at 50 °C under reflux and stirred for 10 minutes. Then methyl bromoacetate (6.4 mL, 67 mmol, Fisher Sci.) was added dropwise. It was run for 21 hours, and the solvent was evaporated using rotavap. The dried residue was partitioned in DCM and water. DCM layer was then washed with saturated NaCl, dried over $MgSO_4$, filtered. Yield (13.28 g, 82.3%); LCMS method – reversed-phase HPLC-MS (flow rate 0.4 mL min^{-1}, runtime 15 min with 5 min post-run), solvent A (0.1% FA in H_2O), solvent B (0.1% FA in ACN), gradient 50 % B isocratic over 15 min, C18 Hypersil column (5 μm, 150 × 3.2 mm, Agilent), retention time: 5.35 min; ESI-MS (m/z): $[MH]^+$ calculated for $C_{13}H_{12}O_5$, 249.1; found, 249.2 (Figure 120).

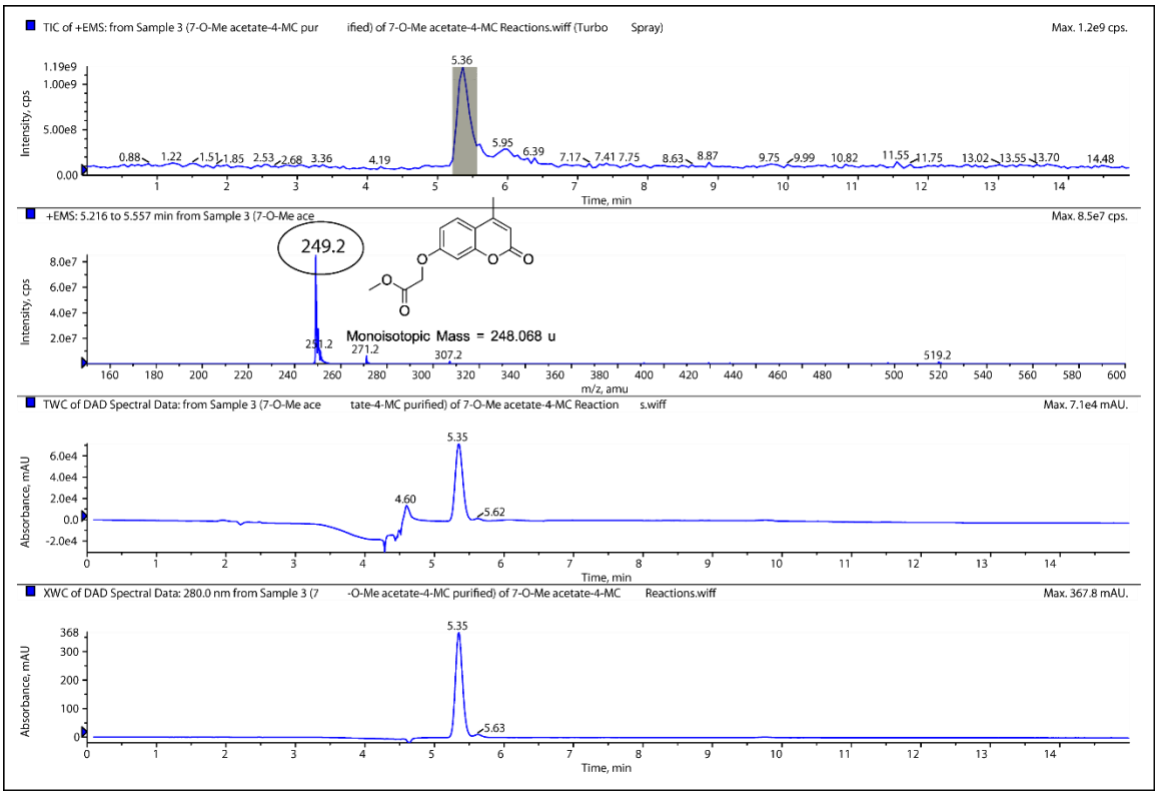

Figure 120: LCMS of methyl (4-methyl-7-coumarinyloxy)acetate. The product mass is seen at $[MH]^+$=249.2 eluting at 5.35 minutes.

Methyl [4-(hydroxymethyl)-7-coumarinyloxy]acetate

Methyl (4-methyl-7-coumarinyloxy)acetate (1.02 g, 4.10 mmol) and finely crushed SeO_2 (1.00 g, 9.02 mmol) was suspended in 46 mL *p*-xylene. The mixture was stirred under reflux for 20 hours. The mixture was filtered when hot, and the filtrate was dried on rotavap. To the dried residue, 80 mL methanol was added and stirred for 20 minutes. To this, $NaBH_4$ (0.170 g, 4.51 mmol) was added. After 40 minutes, it was filtered and dried. The dried residue was partitioned between DCM, water. DCM layer was washed with saturated NaCl, dried over $MgSO_4$, filtered, dried. Yield (0.37 g, 34 %); LCMS method – reversed-phase HPLC-MS (flow rate 0.4 mL min^{-1}, runtime 15 min with 5 min post-run), solvent A (0.1% FA in H_2O), solvent B (0.1% FA in ACN), gradient 50 % B isocratic over

15 min, C18 Hypersil column (5 µm, 150 × 3.2 mm, Agilent), retention time: 3.06 min; ESI-MS (m/z): $[MH]^+$ calculated for $C_{13}H_{12}O_6$, 265.1; found, 265.2 (Figure 121).

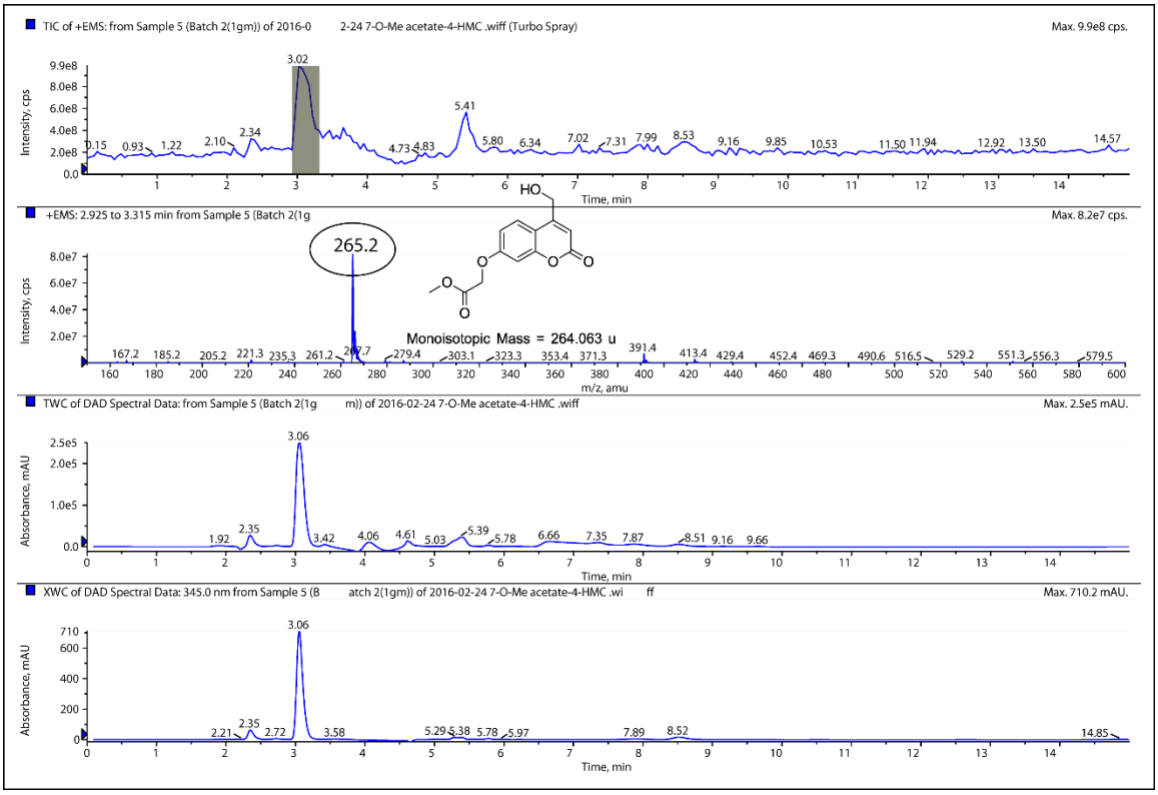

Figure 121: LCMS of methyl [4-(hydroxymethyl)-7-coumarinyloxy]acetate. The mass is seen at $[MH]^+$=265.2 eluting at 3.06 minute.

Methyl [4-(acetoxymethyl)-7-coumarinyloxy]acetate

Methyl [4-(hydroxymethyl)-7-coumarinyloxy]acetate (0.20 g, 0.75 mmol), DMAP (0.230 g, 1.91 mmol), acetic acid (109 µL, 1.91 mmol) were added in mixture of 40 mL DCM+5 mL DMF cooled to 0 ºC. The mixture was stirred on ice for 10 min, and then EDC (295 mg, 1.90 mmol) was added. The ice bath was then removed and allowed to stir overnight. The product was purified by washing DCM first with water, 1 N HCl and saturated NaCl. DCM layer was dried over $MgSO_4$, filtered and dried. Yield (0.183 g, 79.4%); Reversed-phase HPLC-MS (flow rate 0.4 mL min^{-1}, runtime 21 min with 5 min

post-run), solvent A (0.1% FA in H_2O), solvent B (0.1% FA in ACN), gradient 50 % B isocratic over 21 min, C18 Hypersil column (5 µm, 150 × 3.2 mm, Agilent), retention time: 5.48 min; ESI-MS (m/z): $[MH]^+$ calculated for $C_{15}H_{14}O_7$, 307.1; found, 307.2 (Figure 122).

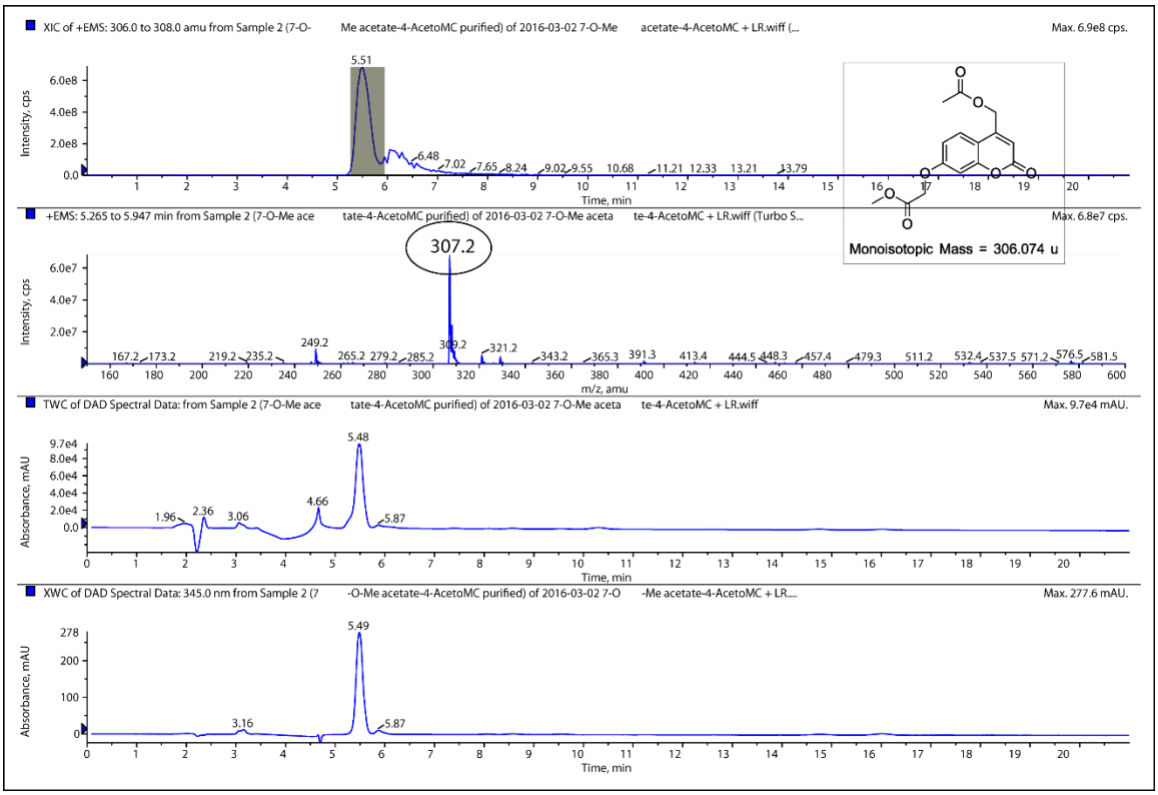

Figure 122: LCMS of methyl [4-(acetoxymethyl)-7-coumarinyloxy]acetate. The product is seen at $[MH]^+$=307.2 eluting at 5.49 minutes.

Methyl [4-(acetoxymethyl)-2-thioxo-7-chromenyloxy]acetate

Methyl [4-(acetoxymethyl)-7-coumarinyloxy]acetate (50.8 g, 0.166 mmol) and P_2S_5 (35.0 mg, 0.157 mmol) were refluxed in 5 mL toluene overnight. The reaction completion was monitored using HPLC. When a complete conversion was seen, toluene was removed using rotavap. The crude mixture was partitioned between DCM and water. DCM layer was washed with water, then with saturated NaCl. DCM layer dried over $MgSO_4$, dried. The product could be easily identified because of a redshift in the UV-vis

spectrum. Yield (43 mg, 80%); analytical method – reversed-phase HPLC (flow rate 0.4 mL min^{-1}, runtime 15 min with 5 min post-run), solvent A (0.1% TFA in H_2O), solvent B (0.1% TFA in ACN), gradient 60 % B isocratic over 15 min, C18 Hypersil column (5 µm, 150 × 3.2 mm, Agilent), retention time: 4.5-5.5 min (Figure 123).

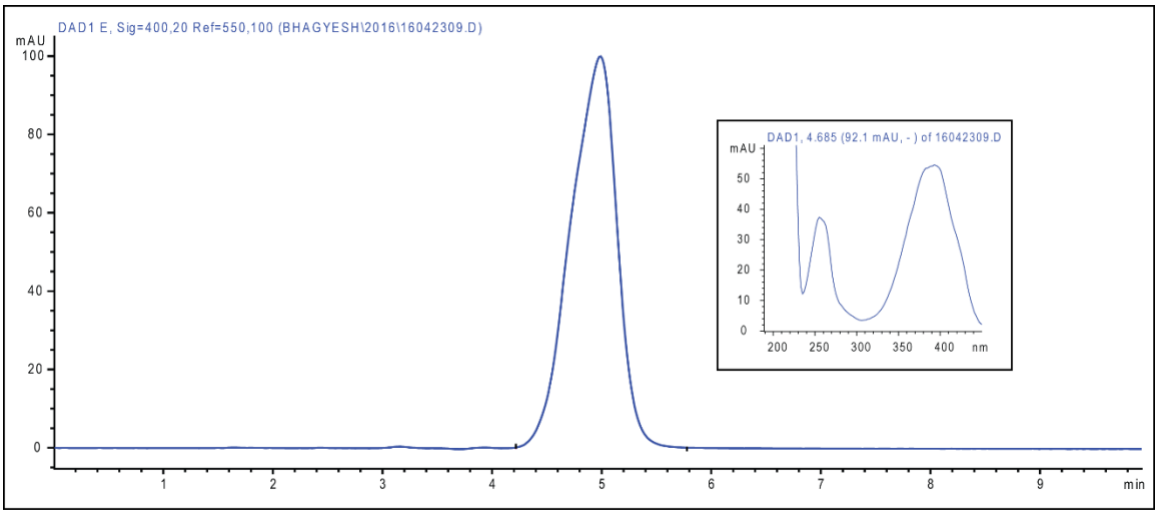

Figure 123: HPLC chromatogram of methyl [4-(acetoxymethyl)-2-thioxo-7-chromenyloxy]acetate.

[4-(Hydroxymethyl)-2-thioxo-7-chromenyloxy]acetic acid

Here for hydrolysis, first we tried NaOH but it was not used because it was too harsh and hydrolysis of lactone was always observed (Figure 124). Hence mild acidic conditions were used. Typically, water: ethanol mixture is used for hydrolysis in acidic conditions. However, this caused transesterification and hence couldn't be used (Figure 125). A mix of water: dioxane (1:1) was also used as a solvent for hydrolysis. The reaction was not clean, and several side products were observed (Figure 126). Upon MS analysis, it appeared that sulfur atom was being replaced by oxygen from thiolactone moiety during the hydrolysis reaction. Replacing the sulfur atom reversed the redshifted spectrum. We were not able to get the desired product cleanly despite several attempts. Hence, we

abandoned the thiol modification approach. Without thiol modification, this 7-HMC group has no absorption in the visible light range. Analytical method – reversed-phase HPLC (flow rate 0.4 mL min^{-1}, runtime 15 min with 5 min post-run), solvent A (0.1% TFA in H_2O), solvent B (0.1% TFA in ACN), gradient 50 % B isocratic over 15 min, C18 Hypersil column (5 µm, 150 × 3.2 mm, Agilent).

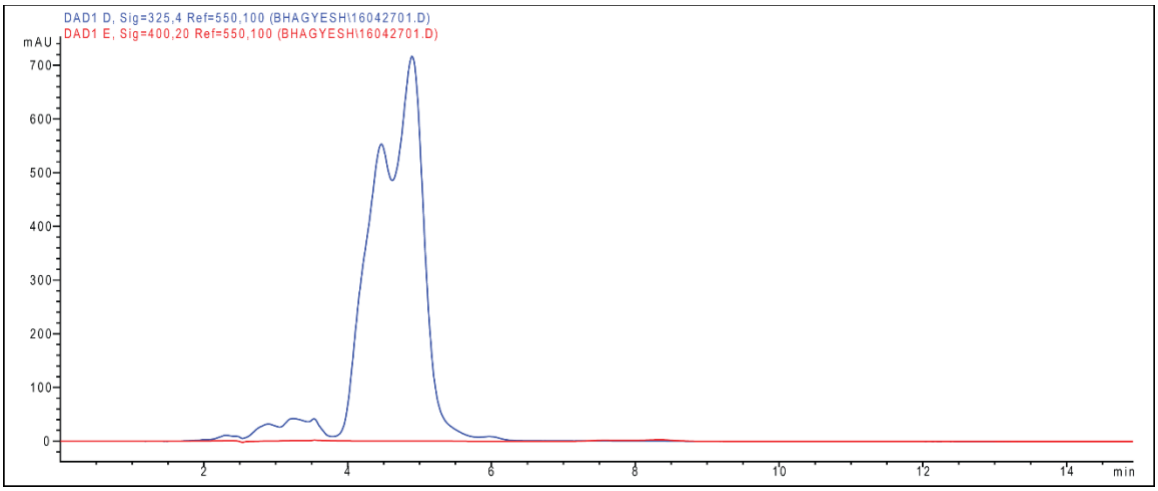

Figure 124: Hydrolysis of [4-(hydroxymethyl)-2-thioxo-7-chromenyloxy]acetic acid using NaOH.

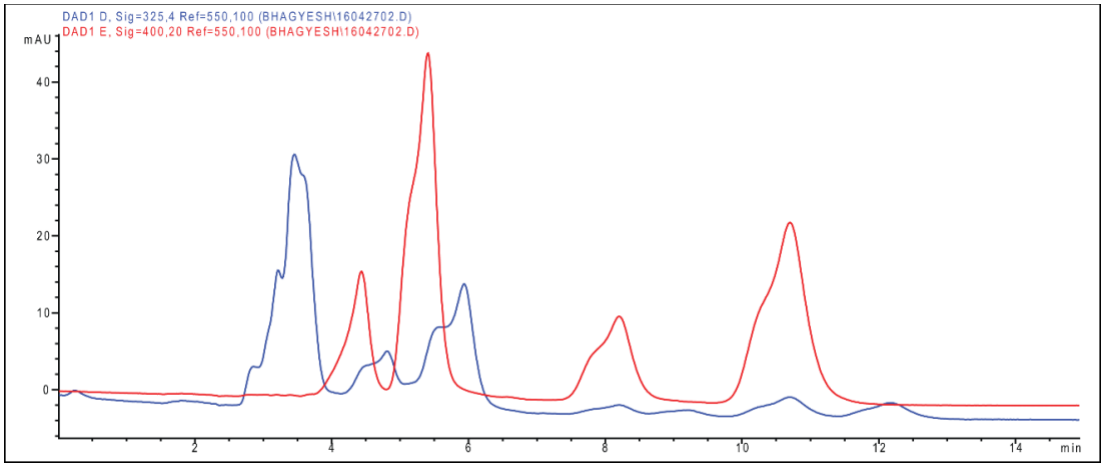

Figure 125: HPLC chromatogram of hydrolysis of [4-(hydroxymethyl)-2-thioxo-7-chromenyloxy]acetic acid using water: ethanol under acidic conditions.

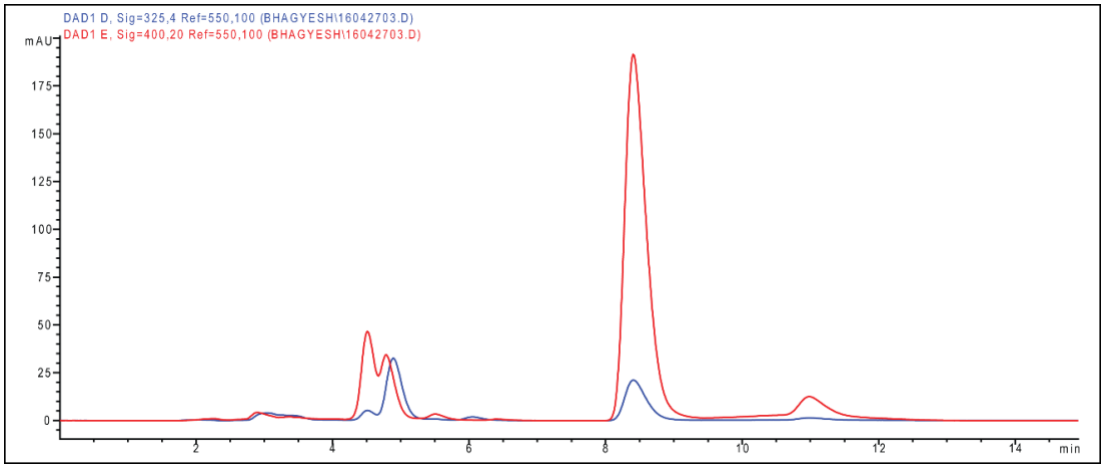

Figure 126: HPLC chromatogram of hydrolysis of [4-(hydroxymethyl)-2-thioxo-7-chromenyloxy]acetic acid using water: dioxane under acidic conditions.

Route 4: Synthesis using 7-amino-4-methyl coumarin (modification of route 1)

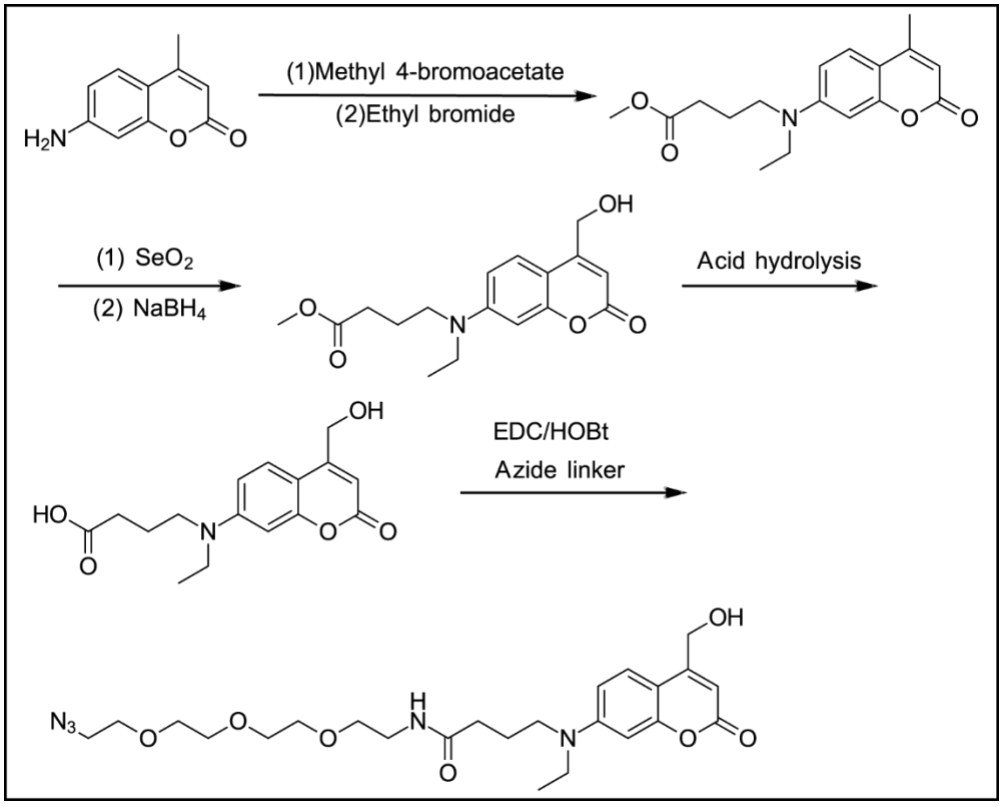

Figure 127: Route 4 of coumarin synthesis.

In this synthetic route (Figure 127), which is similar to route # 1, the second

alkylation was performed using ethyl bromide to introduce an ethyl group. The described synthesis is analogous to the one reported earlier. The substitutions of electron donating groups on seventh position amino group enhance redshift in its absorption spectrum. The addition of the ethyl group promotes redshift absorption as seen from the data here. Also, we utilized methyl-4-bromobutyrate where the carbonyl group is at δ position. Carbonyl group is an electron withdrawing group which prevents redshift absorption, putting it away from amino nitrogen gets rid of this effect. The effect is shown in Figure 128.

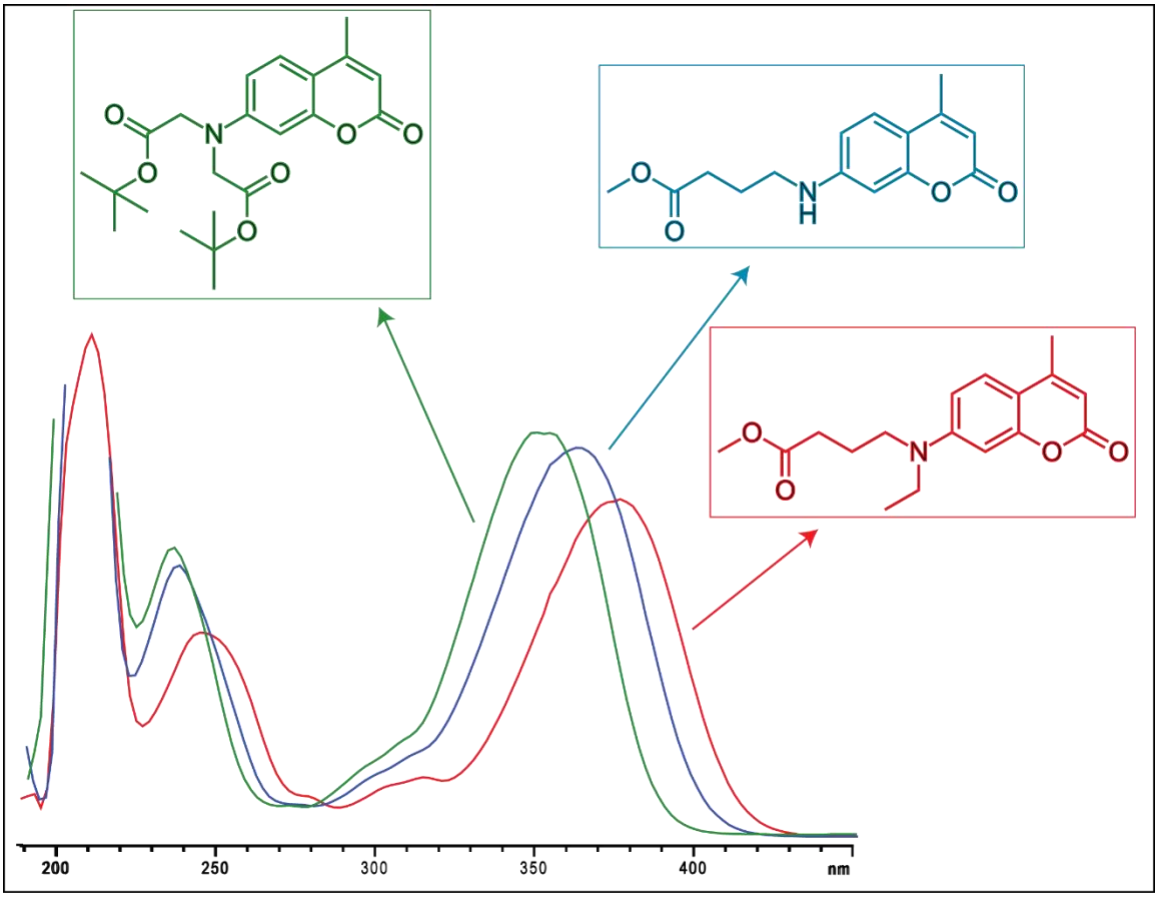

Figure 128: The effect of substitution on the UV-vis absorption spectrum of the coumarin ring. N-alkylation has an electron donating effect which redshifts the absorption but having an electron withdrawing carbonyl group at the β position nullifies that effect.

Methyl 4-[N-ethyl(4-methyl-7-coumarinyl)amino]butyrate

7-amino-4-methylcoumarin (8.89 g, 50.0 mmol), sodium iodide (7.5 g, 50 mmol), methyl-4-bromobutyrate (14.3 mL, 100 mmol) and DIPEA (35 mL, 200 mmol) were mixed in 170 mL acetonitrile and stirred for 48 hours under reflux. It was filtered and dried under vacuum. The dried residue was partitioned between DCM and 1N HCl, the DCM layer was subsequently washed 4-5 times with 1N HCl. Finally, it was partitioned between saturated $NaHCO_3$ and DCM. DCM solvent then was evaporated under vacuum. The remaining residue was scraped off and added to a 20 mL pressure vessels (Ace Glass). To the pressure vessel, sodium iodide (2.1 g, 14 mmol), DIPEA (9.8 mL, 56 mmol) and ethyl bromide x (12.0 mL, 160 mmol) were added and sealed tightly. The reaction was performed at 150 ^{o}C and the reaction progress was followed on HPLC till the intermediate was consumed. After the complete conversion of the intermediate, it was dried and partitioned again between DCM, water. The water layer was discarded, the DCM layer was dried. It was purified using 5% ethyl acetate in DCM. The crude mixture was not purified all at once, rather it was divided into 3 parts and purified via flash chromatography. Yield (2.20 g, 14.5%); LCMS analysis – reversed-phase HPLC (flow rate 0.4 mL min^{-1}, runtime 15 min with 5 min post-run), solvent A (0.1% FA in H_2O), solvent B (0.1% FA in ACN), gradient 50 %B isocratic over 15 min, C18 Hypersil column (5 μm, 150 × 3.2 mm, Agilent), retention time: 11 min; ESI-MS (m/z): $[MH]^+$ calculated for molecular formula = $C_{17}H_{21}NO_4$, 304.15; found, 304.30 (Figure 129); on HPLC the retention time: 10 min (Figure 130); ^{1}H NMR (DMSO-d_6 ,400MHz): δ = 7.50 (d, *J*=9.0 Hz, 1 H), 6.73 (dd, *J*=9.0, 2.3 Hz, 1 H), 6.58 (d, *J*=2.7 Hz, 1 H), 5.94 (d, *J*=1.2 Hz, 1 H), 3.62 (s, 3 H), 3.43 (q, *J*=7.0 Hz, 2 H), 3.36 (t, 2 H), 2.41 (t, *J*=7.2 Hz, 2 H), 2.33 (d, *J*=1.2 Hz, 3 H), 1.80 (quin, 2 H),

1.11 ppm (t, *J*=6.8 Hz, 3 H) (Figure 131); ^{13}C NMR (100 MHz, DMSO-d6): δ 173.17, 160.73, 155.54, 153.49, 150.53, 126.16, 108.60, 108.37, 107.74, 96.84, 51.35, 48.73, 44.40, 30.25, 22.05, 17.92, 12.06 (Figure 131).

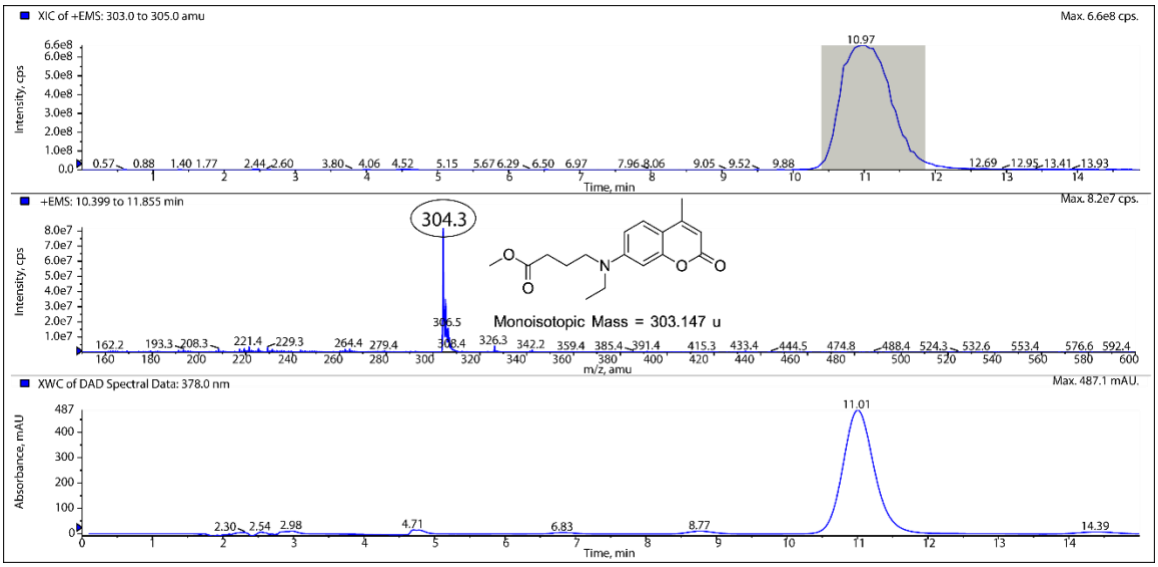

Figure 129: LCMS analysis of methyl 4-[N-ethyl(4-methyl-7-coumarinyl)amino]butyrate. The product mass is seen at $[MH]^+$=304.3 eluting at 11 min.

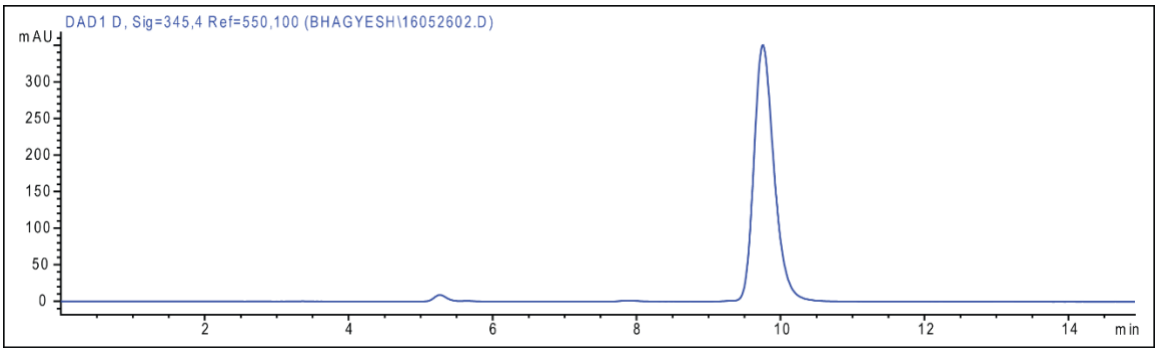

Figure 130: HPLC of methyl 4-[N-ethyl(4-methyl-7-coumarinyl)amino]butyrate.

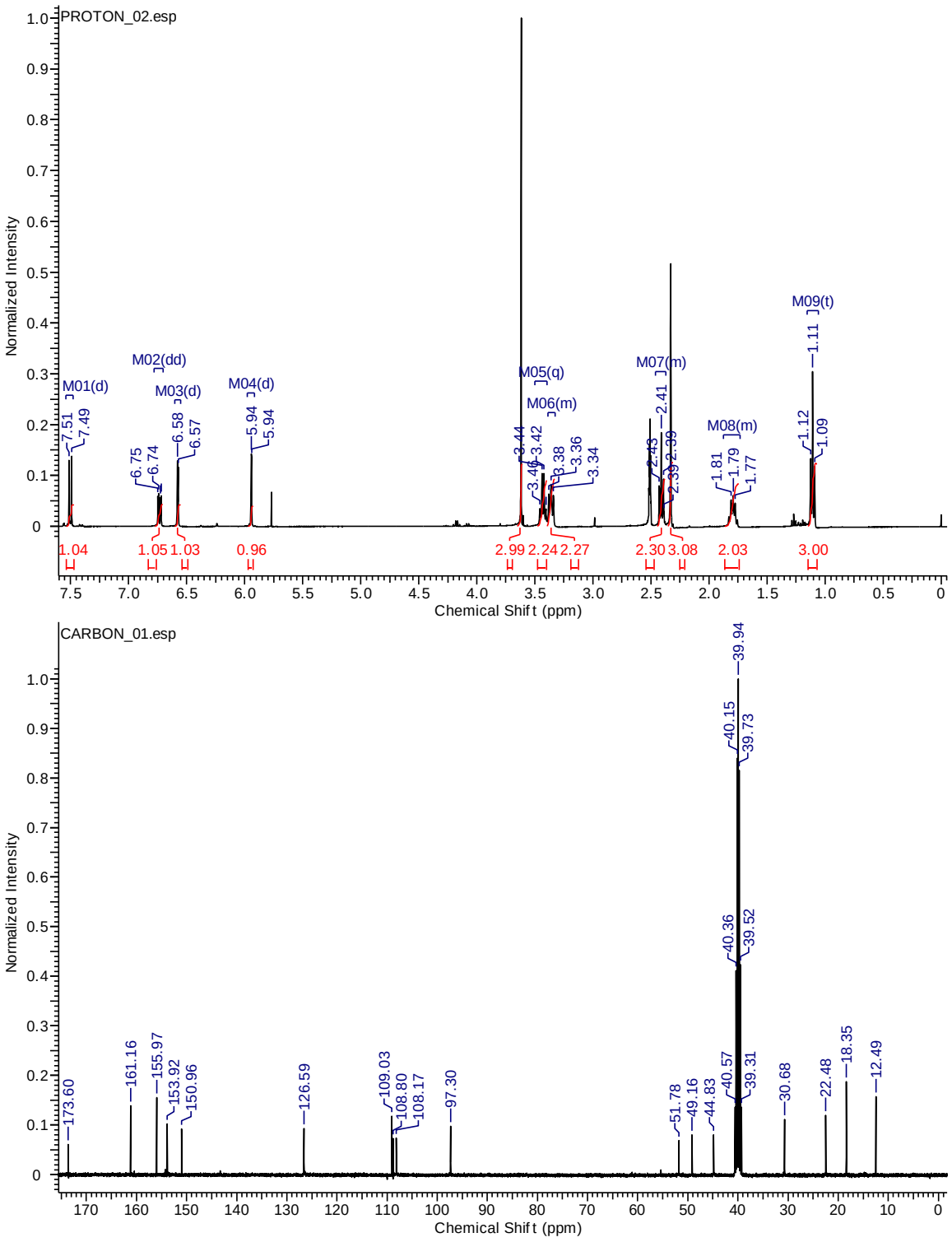

Figure 131: ^{1}H Proton NMR (top) and ^{13}C NMR of methyl 4-[N-ethyl(4-methyl-7-coumarinyl)amino]butyrate.

Methyl 4-{*N*-ethyl[4-(hydroxymethyl)-7-coumarinyl]amino}butyrate

Methyl 4-[N-ethyl(4-methyl-7-coumarinyl)amino]butyrate (1.43 g, 4.70 mmol) and SeO_2 (1.04 g, 9.80 mmol) were suspended in 40 mL *p*-xylene. It was refluxed overnight, filtered hot and dried under vacuum. After drying, 400 mL methanol was added to it and stirred for 20 min. Then $NaBH_4$ (0.20 g, 5.3 mmol) was added and allowed to go for 10 minutes. It was filtered and methanol was dried under vacuum. The crude was purified using 5% methanol in DCM using flash chromatography. Yield (0.5 g, 33.3%); LCMS analysis – reversed-phase HPLC (flow rate 0.4 mL min^{-1}, runtime 15 min with 5 min post-run), solvent A (0.1% FA in H_2O), solvent B (0.1% FA in ACN), gradient 50 % B isocratic over 15 min, C18 Hypersil column (5 μm, 150 × 3.2 mm, Agilent), retention time: 5.61 min; ESI-MS (m/z): $[MH]^+$ calculated for molecular formula = $C_{17}H_{21}NO_5$, 320.14; found, 320.30 (Figure 132); on HPLC the retention time = 5 min (Figure 133); ^{1}H NMR (DMSO-d_6 ,400MHz): δ = 7.44 (d, *J*=9.0 Hz, 1 H), 6.70 (dd, *J*=9.2, 2.5 Hz, 1 H), 6.59 (d, *J*=2.7 Hz, 1 H), 6.08 (t, *J*=1.4 Hz, 1 H), 5.52 (t, *J*=5.7 Hz, 1 H), 4.67 (dd, *J*=5.5, 1.2 Hz, 2 H), 3.61 (s, 3 H), 3.42 (q, *J*=6.9 Hz, 2 H), 3.36 (t, 2 H), 2.41 (t, *J*=7.0 Hz, 2 H), 1.79 (quin, 2 H), 1.10 ppm (t, *J*=7.0 Hz, 3 H) (Figure 134); ^{13}C NMR (100 MHz, DMSO-d6):173.2, 161.1, 158.8, 155.5, 150.3, 125.0, 108.8, 105.8, 104.4, 97.10, 59.0, 51.3, 48.7, 44.4, 30.2, 22.0, 12.1 (Figure 134).

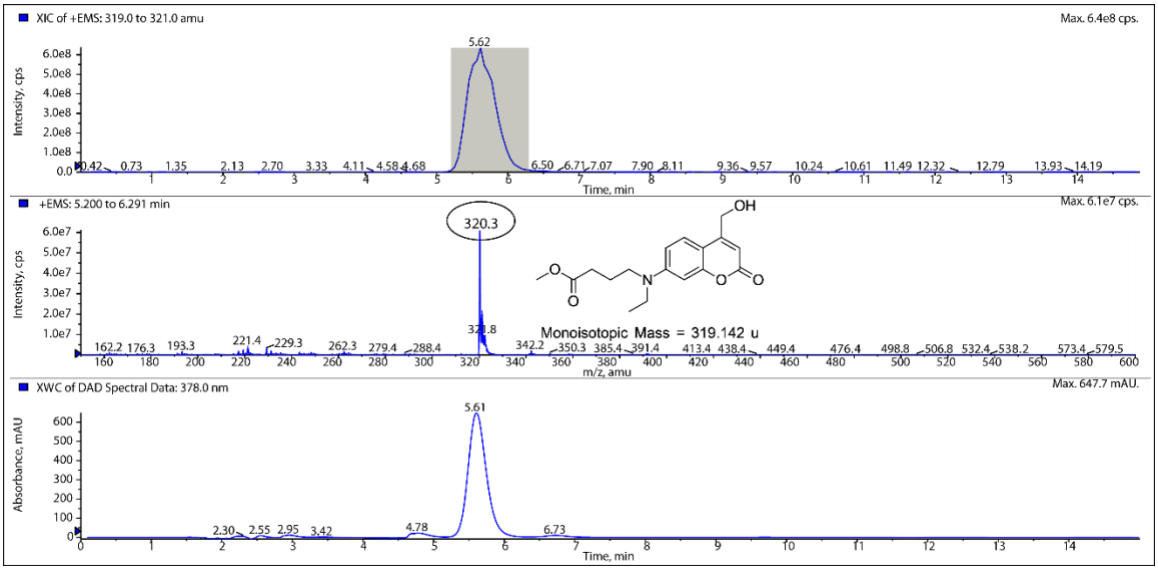

Figure 132: LCMS of methyl 4-{N-ethyl[4-(hydroxymethyl)-7-coumarinyl]amino}butyrate.

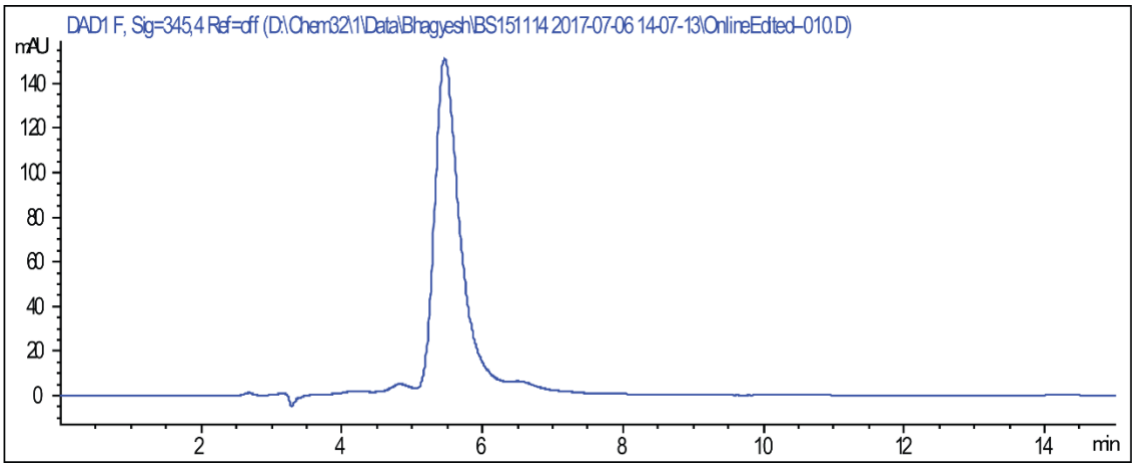

Figure 133: HPLC of methyl 4-{N-ethyl[4-(hydroxymethyl)-7-coumarinyl]amino}butyrate.

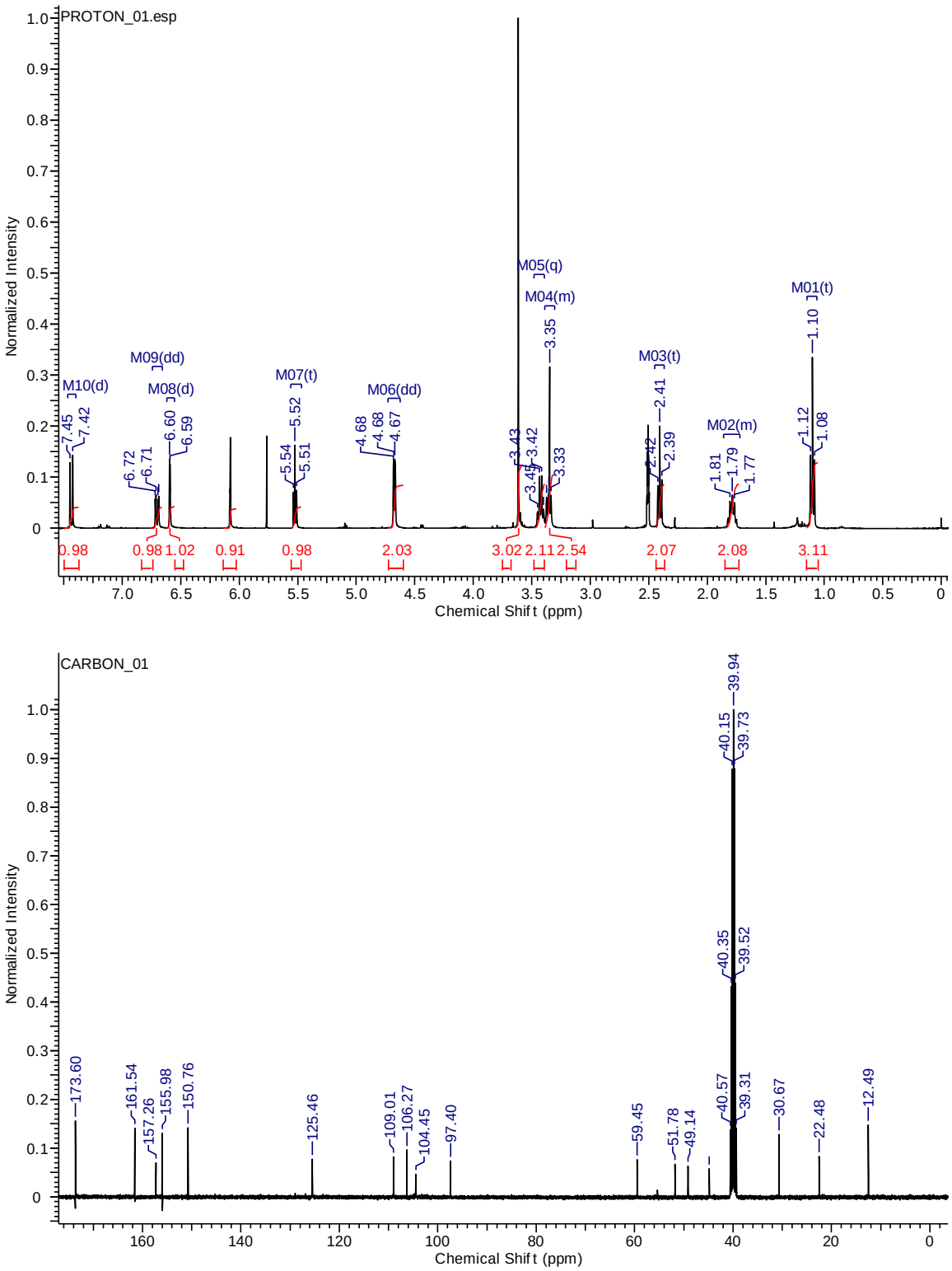

Figure 134: Proton NMR (top) and ^{13}C NMR (bottom) of methyl 4-{N-ethyl[4-(hydroxymethyl)-7-coumarinyl]amino}butyrate.

4-{*N*-ethyl[4-(hydroxymethyl)-7-coumarinyl]amino}butyric acid

Methyl 4-{N-ethyl[4-(hydroxymethyl)-7-coumarinyl]amino}butyrate (0.39 g, 1.24 mmol) was added to 40 mL mixture of water:THF in 1:1 ratio. HCl was added into it in 50x molar excess to that of the substrate. The reaction was run for 2 hours and then neutralized with NaOH to bring pH to 7. Then the crude mixture was dried using a vacuum. The material was extracted from the dried residue by washing with a 10-15 mL mixture of acetone+ethanol three times. The yield was quantitative. LCMS analysis – reversed-phase HPLC (flow rate 0.4 mL min^{-1}, runtime 15 min with 5 min post-run), solvent A (0.1% FA in H_2O), solvent B (0.1% FA in ACN), gradient 50 % B isocratic over 15 min, C18 Hypersil column (5 μm, 150 × 3.2 mm, Agilent), retention time: 3.17 min; ESI-MS (m/z): $[MH]^+$ calculated for molecular formula = $C_{16}H_{19}NO_5$, 306.12; found, 306.20 (Figure 135); retention time on HPLC: 3 min (Figure 136); ^{1}H NMR (DMSO-d_6 ,400MHz): δ = 11.81 - 12.71 (m, 1 H), 7.43 (d, *J*=9.0 Hz, 1 H), 6.71 (dd, *J*=9.2, 2.5 Hz, 1 H), 6.59 (d, *J*=2.3 Hz, 1 H), 6.08 (s, 1 H), 4.67 (d, *J*=1.2 Hz, 2 H), 3.43 (q, *J*=6.8 Hz, 2 H), 3.35 (t, 2 H), 2.31 (t, *J*=7.0 Hz, 2 H), 1.75 (quin, *J*=7.4 Hz, 2 H), 1.23 (s, 1 H), 1.10 ppm (t, *J*=7.0 Hz, 3 H) (Figure 137); ^{13}C NMR (100 MHz, DMSO-d_6): 174.2, 161.2, 159.9, 155.6, 150.4, 125.0, 108.6, 105.8, 104.0, 96.9, 59.0, 48.9, 47.1, 44.4, 30.6, 22.1, 12.1 (Figure 137, ^{13}C not shown).

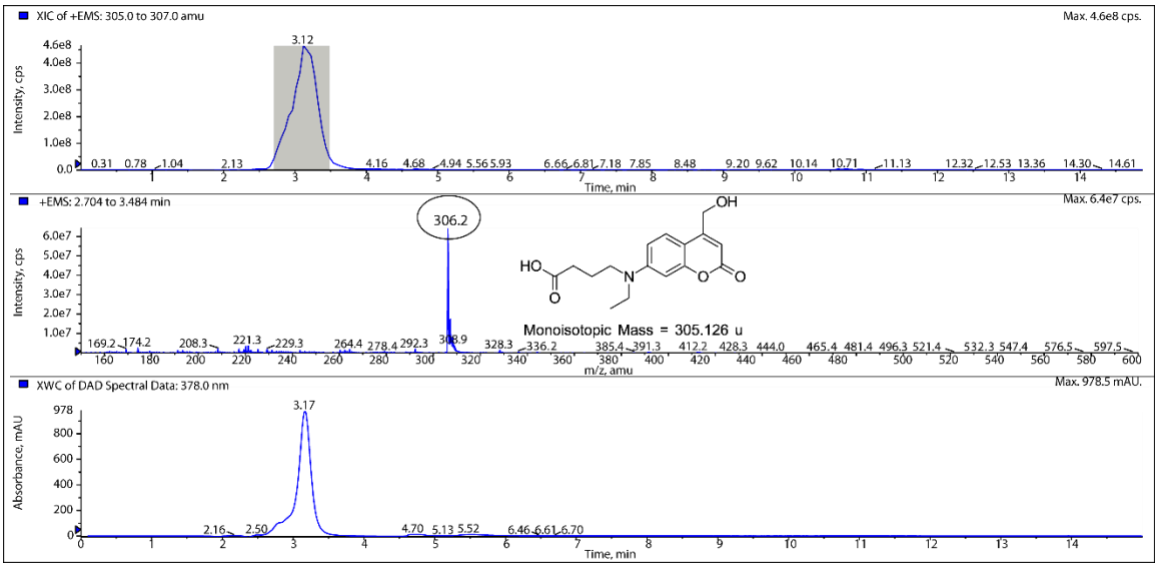

Figure 135: LCMS of 4-{N-ethyl[4-(hydroxymethyl)-7-coumarinyl]amino}butyric acid.

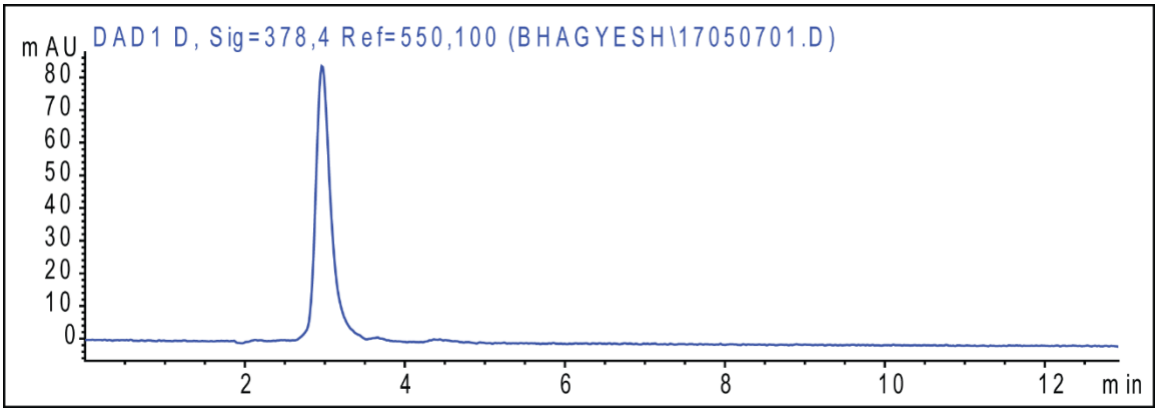

Figure 136: HPLC of 4-{N-ethyl[4-(hydroxymethyl)-7-coumarinyl]amino}butyric acid.

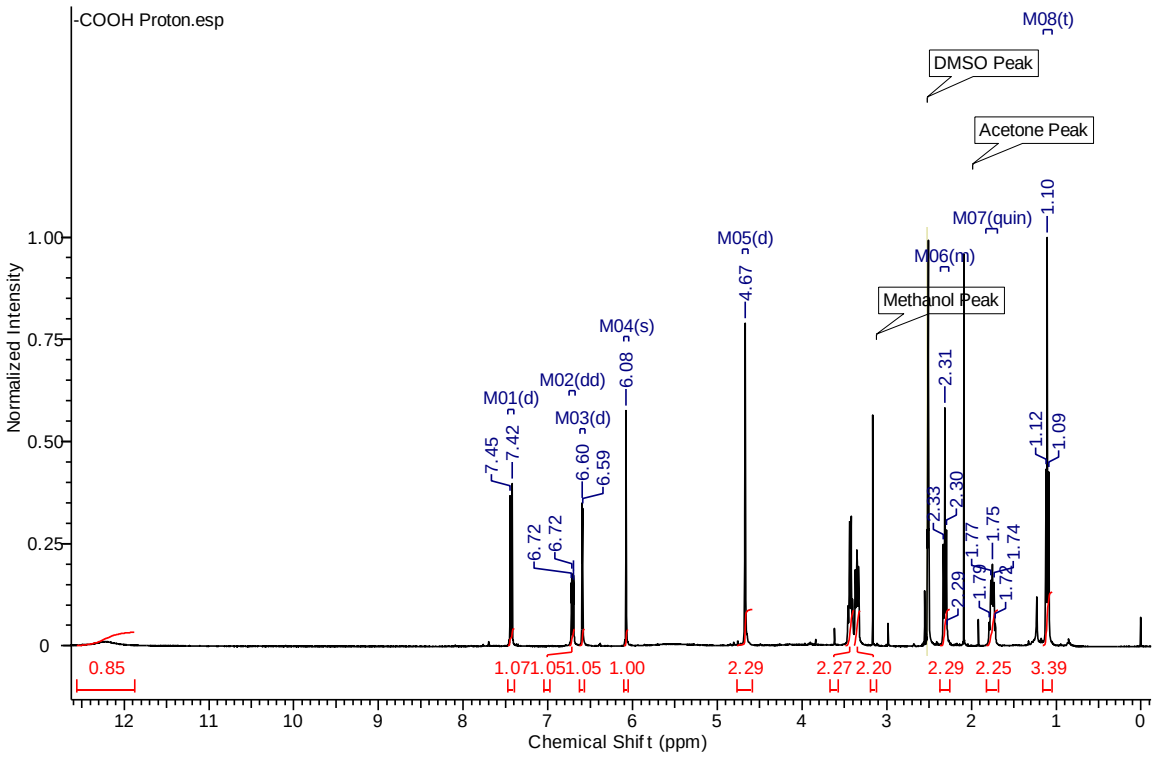

Figure 137: NMR of 4-{N-ethyl[4-(hydroxymethyl)-7-coumarinyl]amino}butyric acid.

4-{*N*-Ethyl[4-(hydroxymethyl)-7-coumarinyl]amino}-1-(2-{2-[2-(2-azidoethoxy)ethoxy]ethoxy}ethylamino)-1-butanone

The dried residue of 4-{N-Ethyl[4-(hydroxymethyl)-7-coumarinyl]amino}butyric acid (1.24 mmol), EDC (0.4 g, 1.24 mmol), HOBt hydrate (0.380 g, 1.24 mmol) and 11-azido-3,6,9-trioxaundecan-1-amine (0.270 mL, 1.364 mmol) were mixed with 25 mL DMF. It was stirred overnight. DMF was evaporated under vacuum. The dry crude reaction mixture was partitioned between EtOAc and water. EtOAc was then washed with saturated NaCl and dried over $MgSO_4$. EtOAc was further filtered and dried under vacuum. Yield (0.574 g, 91.6%); LCMS analysis – reversed-phase HPLC (flow rate 0.4 mL min^{-1}, runtime 15 min with 5 min post-run), solvent A (0.1% FA in H_2O), solvent B (0.1% FA in ACN), gradient 50 % B isocratic over 15 min, C18 Hypersil column (5 µm, 150 × 3.2 mm,

Agilent), retention time: 3.89 min; ESI-MS (m/z): $[MH]^+$ calculated for molecular formula = $C_{24}H_{35}N_5O_7$, 506.25; found, 506.30 (Figure 138); ^1H NMR (DMSO-d_6 ,400MHz): δ = 7.93 (s, 1 H), 7.43 (d, *J*=9.0 Hz, 1 H), 6.70 (dd, *J*=9.2, 2.5 Hz, 1 H), 6.57 (d, *J*=2.3 Hz, 1 H), 6.07 (s, 1 H), 5.49 - 5.54 (m, 1 H), 4.67 (dd, *J*=5.5, 1.2 Hz, 2 H), 3.50 - 3.62 (m, 13 H), 3.40 (dt, *J*=15.0, 5.6 Hz, 7 H), 3.29 - 3.35 (m, 3 H), 3.22 (q, *J*=5.7 Hz, 2 H), 2.54 (s, 4 H), 2.16 (t, *J*=7.0 Hz, 2 H), 1.69 - 1.81 (m, 2 H), 1.10 ppm (t, *J*=6.8 Hz, 3 H) (Figure 139); ^{13}C NMR (100 MHz, DMSO-d6): 171.7, 161.1, 156.8, 155.6, 150.4, 125.0., 108.6, 105.7, 103.9, 96.9, 72.3, 69.8, 69.7, 69.7, 69.5, 69.2, 60.2, 59.0, 50.0, 49.1, 44.4, 32.0, 22.7, 12.07 (Figure 139); retention time on HPLC: 4 min (Figure 140).

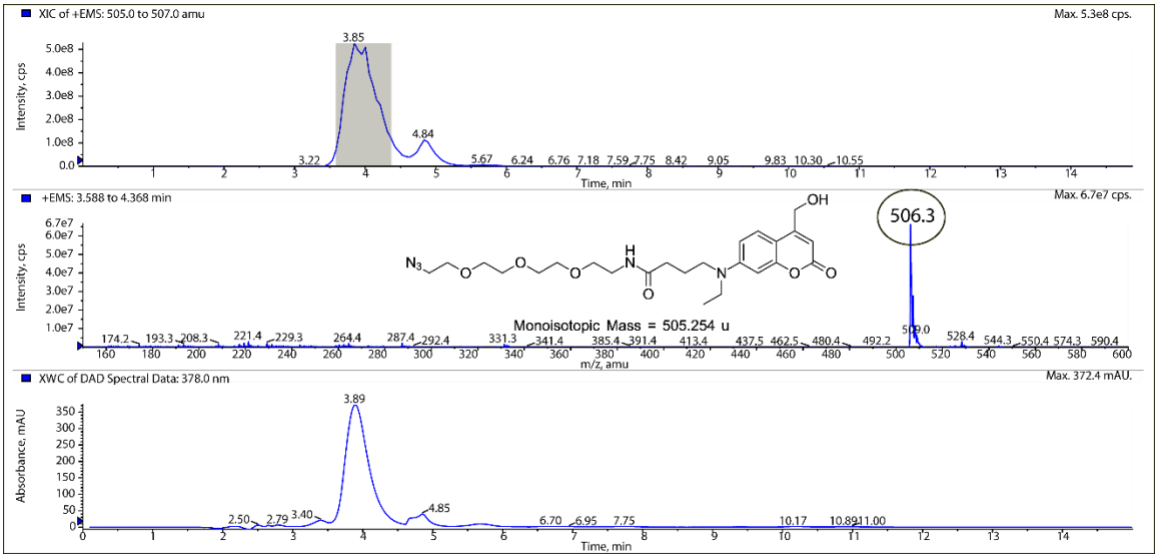

Figure 138: LCMS of 4-{N-ethyl[4-(hydroxymethyl)-7-coumarinyl]amino}-1-(2-{2-[2-(2-azidoethoxy)ethoxy]ethoxy}ethylamino)-1-butanone.

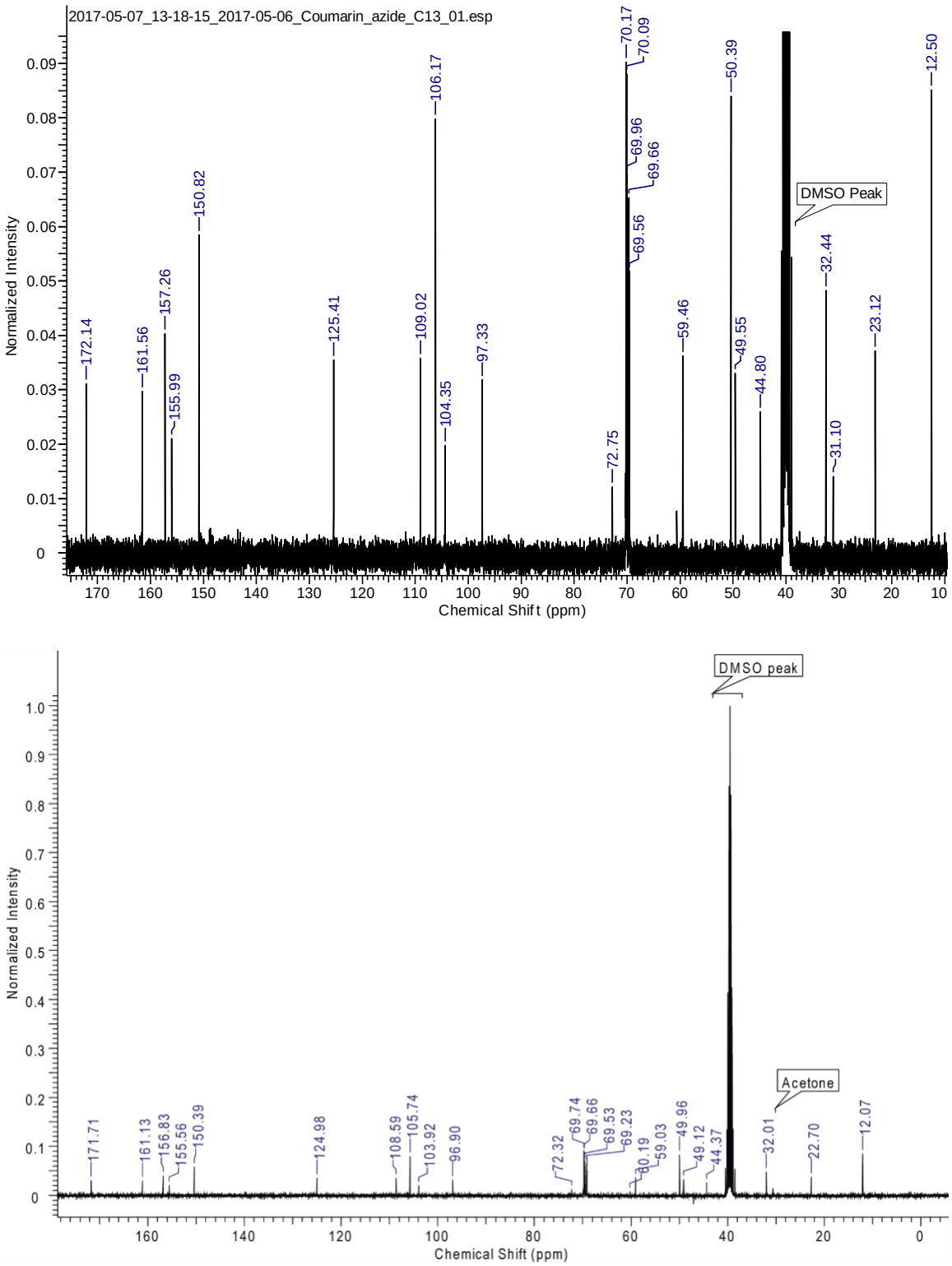

Figure 139: NMR of 4-{N-ethyl[4-(hydroxymethyl)-7-coumarinyl]amino}-1-(2-{2-[2-(2-azidoethoxy)ethoxy]ethoxy}ethylamino)-1-butanone.

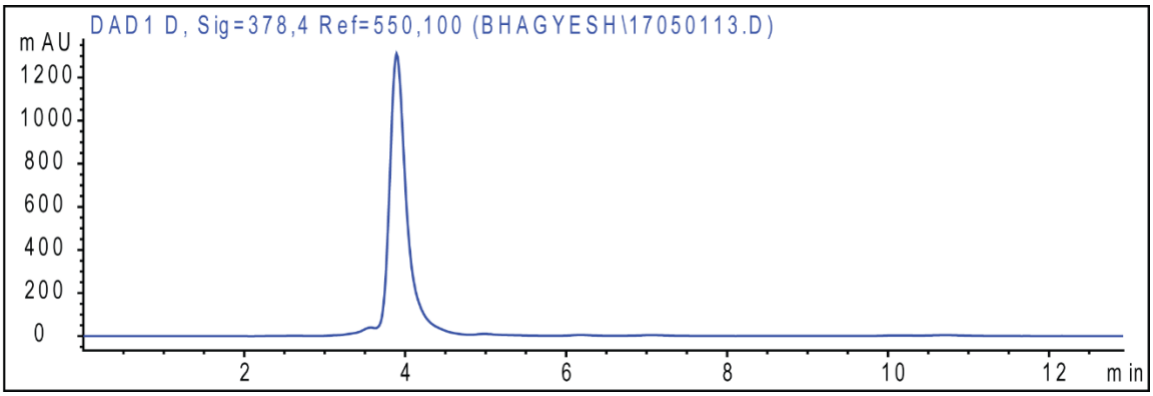

Figure 140: HPLC of 4-{N-ethyl[4-(hydroxymethyl)-7-coumarinyl]amino}-1-(2-{2-[2-(2-azidoethoxy)ethoxy]ethoxy}ethylamino)-1-butanone

Caging insulin using coumarin azide

4-{*N*-Ethyl[4-(hydroxymethyl)-7-coumarinyl]amino}-1-(2-{2-[2-(2-azidoethoxy)ethoxy]ethoxy}ethylamino)-1-butanone (89.9 mg, 178 µmol), carbonyldiimidazole (CDI) (28.8 mg, 178 µmol) and 4-Dimethylaminopyridine (DMAP) (21.75 mg, 178 µmol) were mixed in 0.3 mL of anhydrous DMSO. Moisture from DMSO was removed by the following procedure – the molecular sieves were kept under vacuum in a 100 ºC heated chamber overnight. Then molecular sieves were suspended in DMSO to dry it. The activation reaction was kept at 40 ºC for 70 minutes. Then this mixture was added to insulin (1.2 g, 0.206 mmol) dissolved in 90 mL of anhydrous DMSO. The caging reaction was quenched by adding 5 mL of water after running it for 24 hours at 40 ºC. This reaction was performed multiple times on this scale to obtain caged insulin. ESI−MS (m/z): $[M]^+$ calculated for, 6339.2; found, 6344.0 (Figure 141); analytical method – reversed-phase HPLC-MS (flow rate 0.4 mL min^{-1}, runtime 30 min with 5 min post-run), solvent A (0.1% TFA in H_2O), solvent B (0.1% TFA in ACN), gradient 0% B to 100 % B over 28 min, gradient 100% B to 0 % B until 30 min, C18 Hypersil column (5 µm, 150 × 3.2 mm, Agilent), retention time: 15.7-16.8 min (Figure 142).

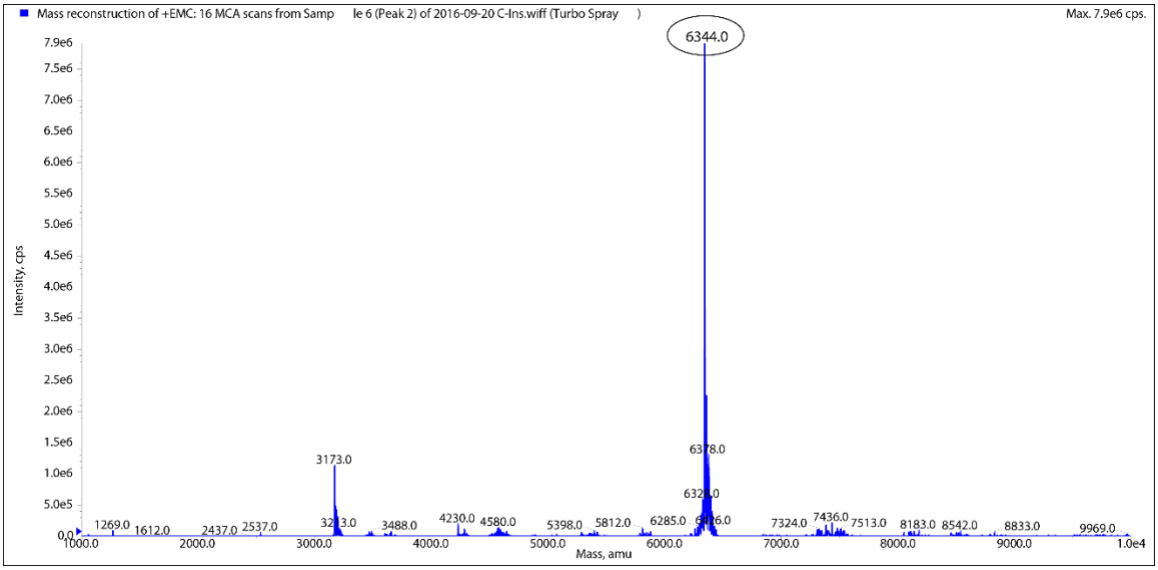

Figure 141: MS of CIMA. The product mass is seen at $[M]^{+}$=6344.0 (calc. for 6339.2).

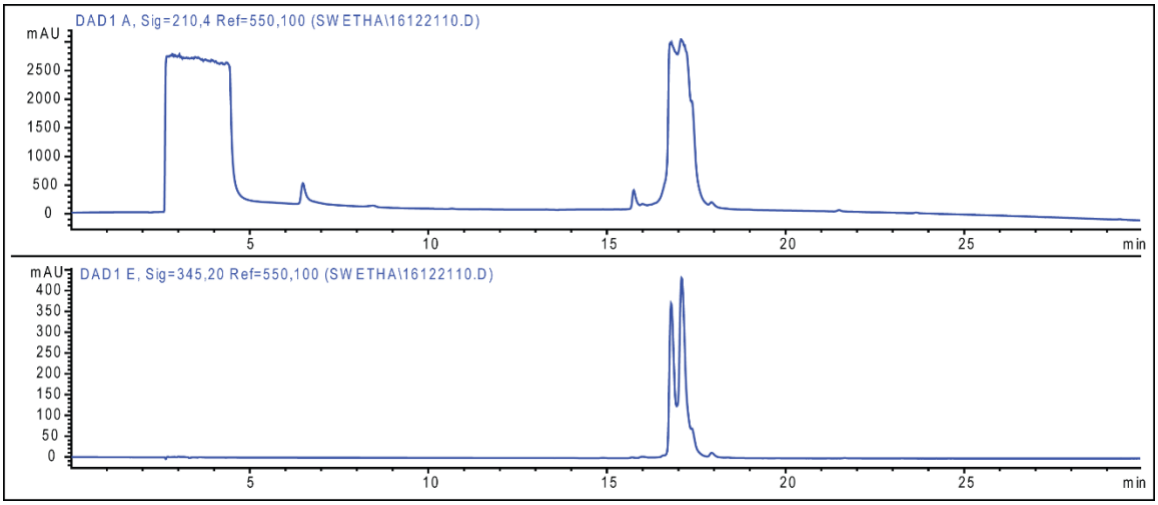

Figure 142: HPLC chromatogram of purified CIMA. The twin peaks are two isomers of CIMA.

<u>Determining the site of conjugation on insulin</u>

We were observing two prominent isomeric peaks for CIMA in HPLC, peak # 2 being slightly in excess. The conjugation of coumarin to insulin occurs via carbamate linkage as evident from the mass spectrum as opposed to ester linkage because carbamate also introduced C=O which adds a mass of 28 amu. There are three primary amines on

insulin which could be involved. The carbonate formation could also happen on possible threonine and serine residues but less likely. Three possible amines are – terminal amine on chain A of Glycine, terminal amine of phenylalanine on chain B and the side chain of B29 lysine on chain B. We initially tried reducing insulin with DTT and analyzing the separated chains using the mass spec to identify whether conjugation solely occurring on chain B or chain A is involved as well. There was an issue with this procedure, it was seen that DTT treatment was hydrolyzing coumarin group from insulin. Initial DTT concentration was 0.72 M. Even reducing it to 50 mM did not help. Later, we used trypsin and GluC to digest insulin into smaller peptide fragments to map the sites of modification. To perform these studies, both the isomers of CIMA were purified individually using RP-HPLC. Analytical method – reversed-phase HPLC (flow rate 0.4 mL min^{-1}, runtime 30 min with 5 min post-run), solvent A (0.1% TFA in H_2O), solvent B (0.1% TFA in ACN), gradient 0 % B to 100% B over 30 min, C18 Hypersil column (5 µm, 150 × 3.2 mm, Agilent), retention time: 17-18 min for both the isomers. Refer to Figure 143 for the chromatogram of the crude mixture and Figure 144 for chromatogram of purified isomers.

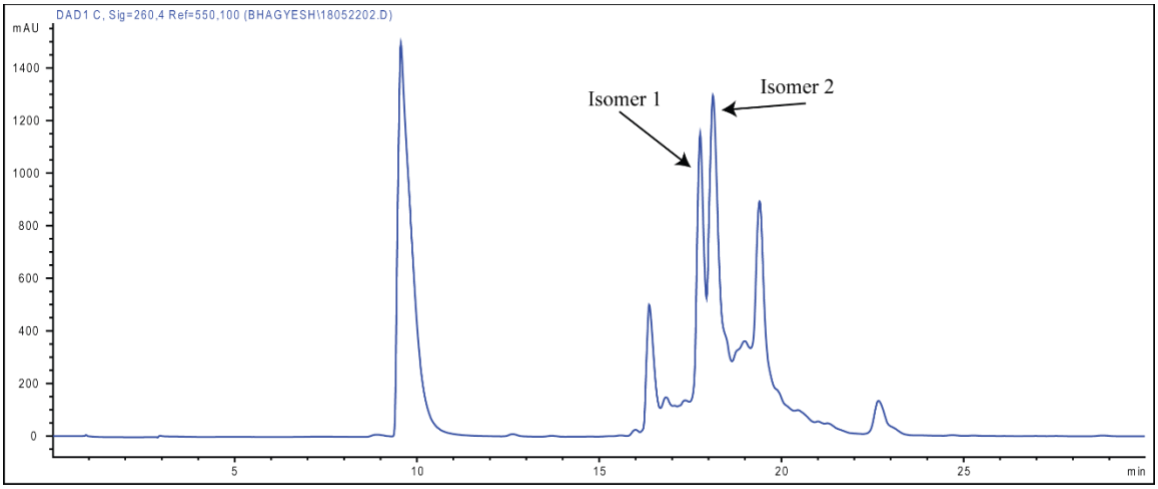

Figure 143: HPLC chromatogram of the crude reaction mixture of insulin by coumarin azide.

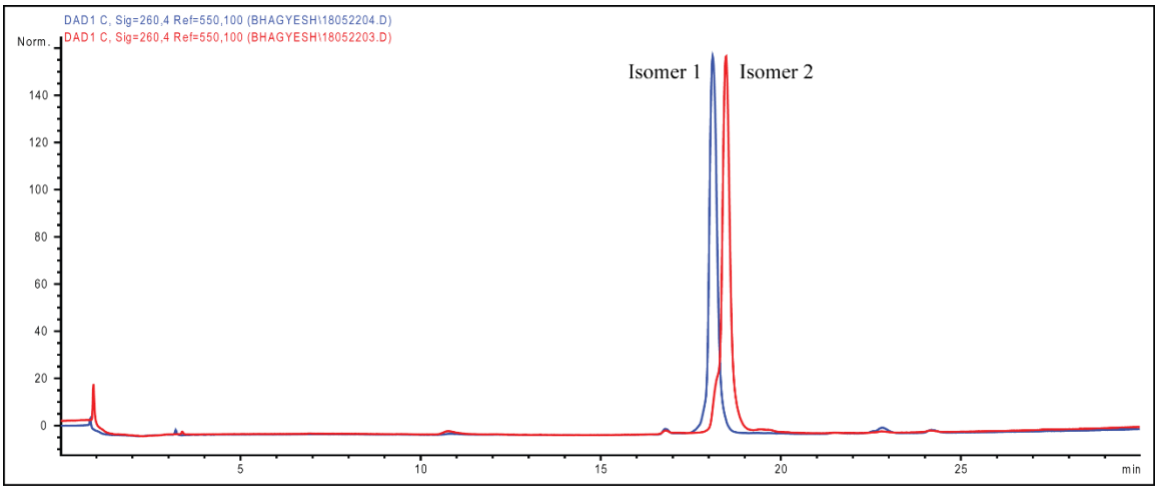

Figure 144: HPLC chromatogram of CIMA isomer 1 and 2 overlaid (and normalized) on top of each other.

Digestion using trypsin

Trypsin (Fisher Scientific, catalog # 90057) and 4 mg insulin were mixed with 4 mL 0.1 M Tris-HCl, pH=8.5; the concentration was 0.172 mM. 20 µg trypsin was dissolved in 20 µL 1 mM HCl solution. This 20 µL enzyme was mixed with 0.5 mL protein substrate. The reaction was incubated for 17 hours at 37 ºC and analyzed by HPLC and mass spectrometry.

The expected masses for the digested fragments are enlisted in Figure 145 and Table 7. HPLC chromatogram for the crude digestion mixture (Figure 146) shows two prominent peaks: a smaller peak 1 and a taller peak 2 at 14.5 and 16.2 min respectively. In the negative ion mode, peak 1 showed a mass of 857.7 amu which corresponds to fragment 2. Fragment 2 GFFYTPK has a mass of 858.4 (Figure 147). While peak 2 shows a mass of 4870 which corresponds to larger fragment 1. The expected mass is 4865.5 (Figure 148). After confirming that the digestion protocol was working on native insulin, we proceeded further to digest CIMA.

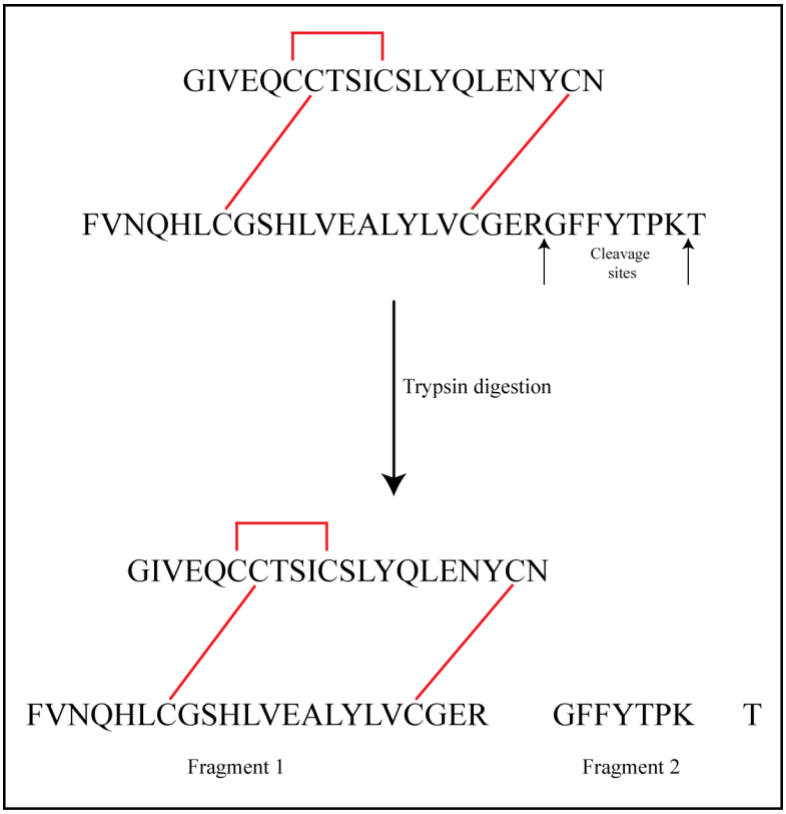

Figure 145: Trypsin digestion of insulin.

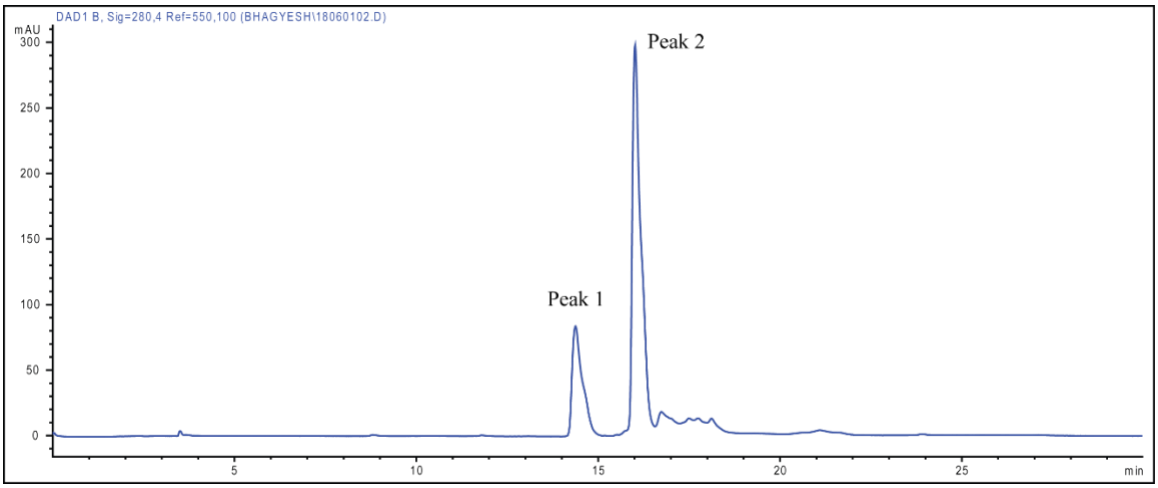

Figure 146: HPLC chromatogram of trypsin digestion of native insulin.

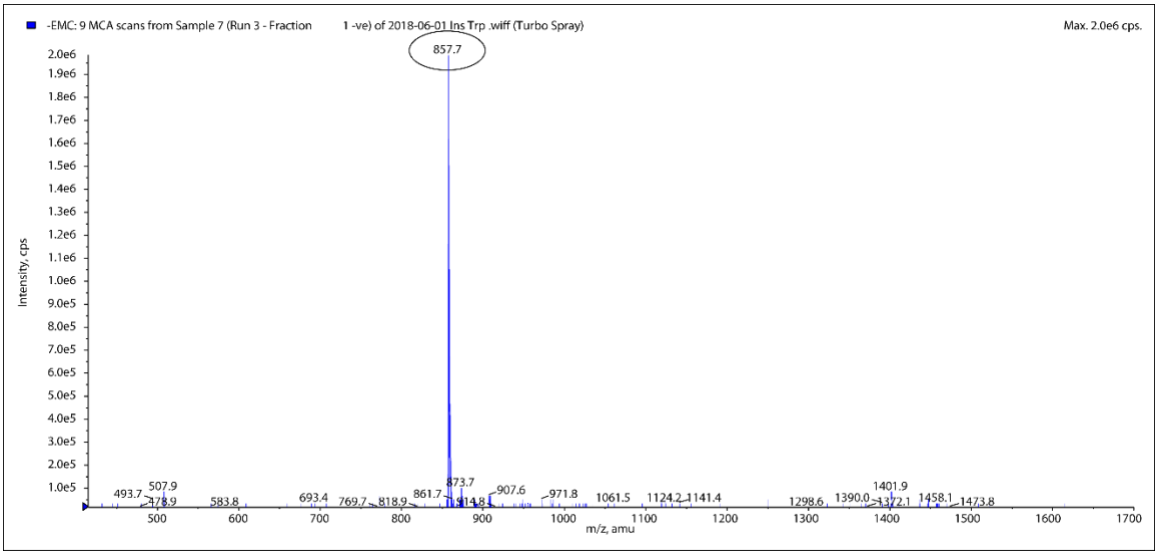

Figure 147: MS infusion of peak 1 (Figure 146) of digestion of insulin by trypsin.

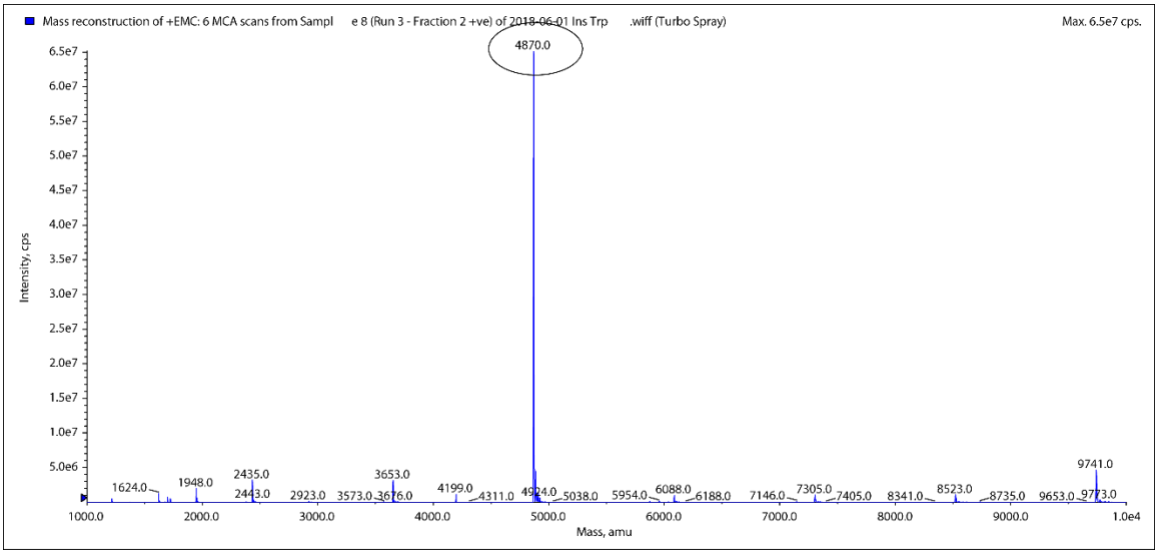

Figure 148: MS infusion of peak 2 (Figure 146) of digestion of insulin by trypsin.

CIMA isomer 1 digestion by trypsin

A stock solution of CIMA isomer 1 was prepared in DMSO (concentration = 8.47 mM). 5.1 µL of CIMA isomer 1 from its stock solution was mixed with 0.25 mL 0.1 M Tris-HCl, pH=8.5, the concentration here was 0.172 mM. Trypsin 10 µg was dissolved in 10 µL 1 mM HCl solution and was mixed with 0.25 mL protein substrate. The reaction was

incubated for 17 hours at 37 ºC and analyzed by HPLC and mass spectrometry.

Figure 149 shows the HPLC chromatogram of CIMA isomer 1 digestion by trypsin. It showed two main peaks of interest. Based on the knowledge of retention times, peak 1 corresponds to unmodified fragment 2. Upon MS analysis, it showed the mass of ($[M]^-$ = 857.5) of unmodified fragment 2 suggesting that the modification should be on fragment 1 (Figure 150). Also, peak 2 showed a signal at 380 nm suggesting that it should have a coumarin chromophore attached to it. Upon MS analysis, the peaks corresponding to modified fragment 1 with coumarin (Figure 151) were observed. The predicted masses and m/z are calculated in Table 7.

Table 7: Fragments of CIMA after trypsin cleavage.

Fragments	Sequence	Mass	Total mass after caging	M/4 for 4^+ charges	M/5 for 5^+ charges
1	GIVEQCCTSICSLYQLENYCN + FVNQHLCGSHLVEALYLVCGER	4865.5	5396.7	1349.2	1079.3
2	GFFYTPK	858.4	1389.6		

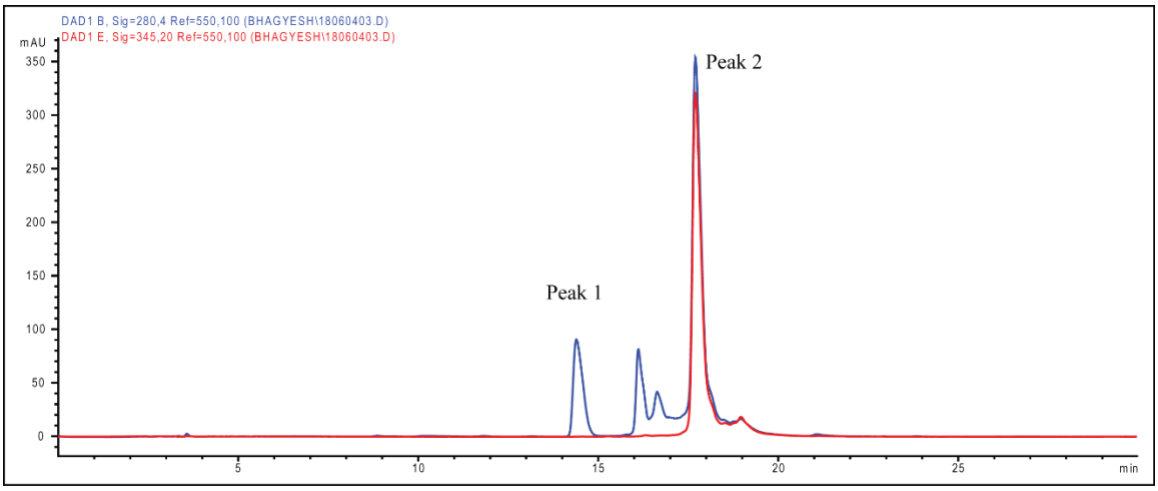

Figure 149: HPLC chromatogram of CIMA isomer 1 digestion by trypsin.

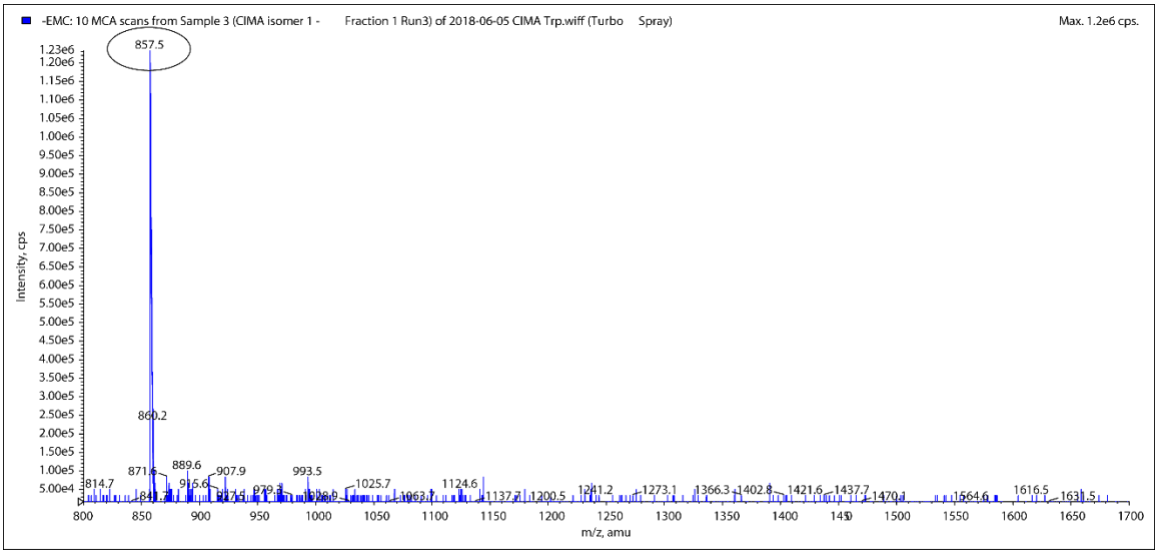

Figure 150: MS infusion of peak 1 (Figure 149) of digestion of CIMA 1 by trypsin.

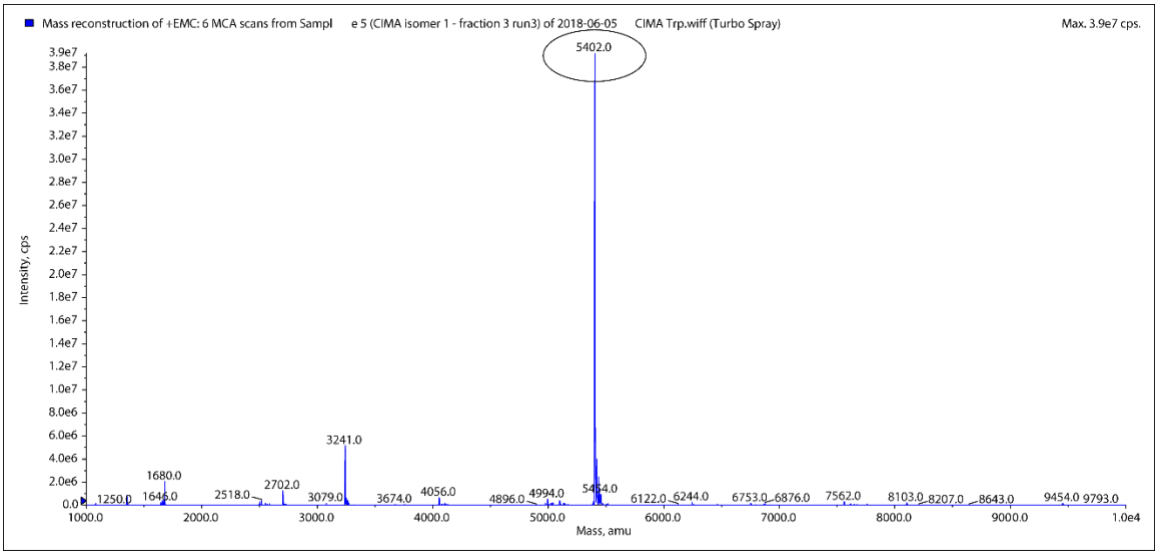

Figure 151: MS infusion of peak 2 (Figure 149) of digestion of CIMA 1 by trypsin.

CIMA isomer 2 digestion by trypsin

A stock solution of CIMA isomer 2 was prepared in DMSO (concentration = 7.79 mM). 5.52 µL of CIMA isomer 2 from its stock solution was mixed with 0.25 mL 0.1 M Tris-HCl, pH=8.5, the concentration was 0.17 mM. 10 µg trypsin was dissolved in 10 µL 1 mM HCl solution and it was mixed with 0.25 mL protein substrate. The reaction was incubated for 3 hours at 37 ºC and analyzed by HPLC and mass spectrometry.

The digestion time for isomer 2 was shortened to 3 hours because the data was not informative when the digestion was performed for overnight. In Figure 152, the crude digestion mixture is run on HPLC; 3 major peaks were observed and collected for infusion in MS. Peak 1 shows a mass of 4870 corresponding the unmodified fragment 1 (Figure 153). This suggests that the conjugation must be on fragment 2 for this CIMA isomer. Peak 2 includes two distinct peaks when infused into MS showed the mass of undigested CIMA (Figure 154). Three hours digestion time is probably not enough for complete digestion of CIMA, hence we observed undigested CIMA as peak 2. Peak 3 showed a mass of 1490.3

which corresponds to the mass of peptide fragment GFFYTPKT + the mass of conjugated coumarin (Figure 155). Ideally, trypsin would cut after K and T should not be in the fragment. Since the conjugation is occurring on K, the bulky coumarin moiety is sterically hindering trypsin cleavage at T.

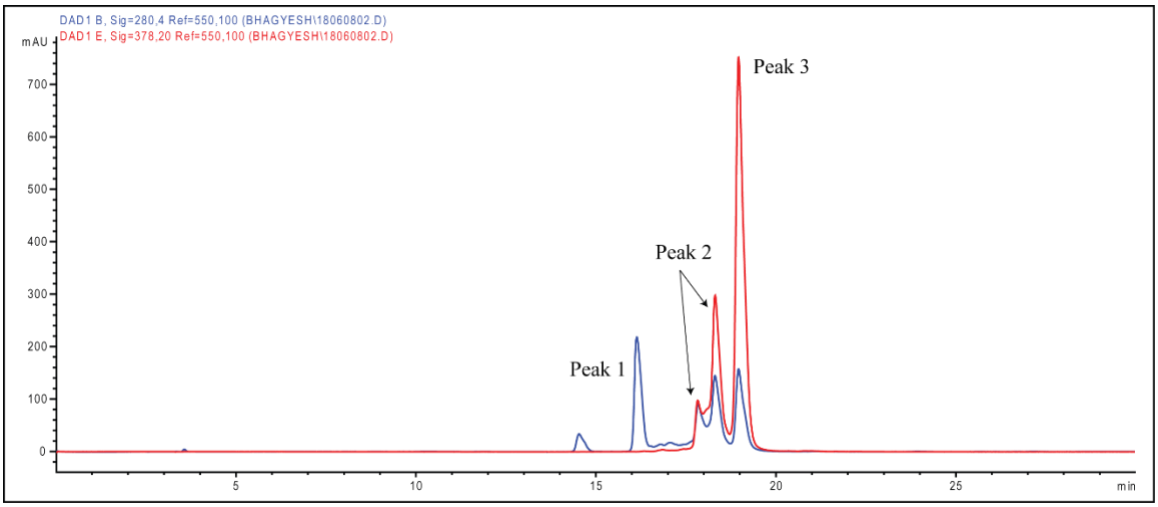

Figure 152: HPLC chromatogram of CIMA isomer 2 digestion by trypsin.

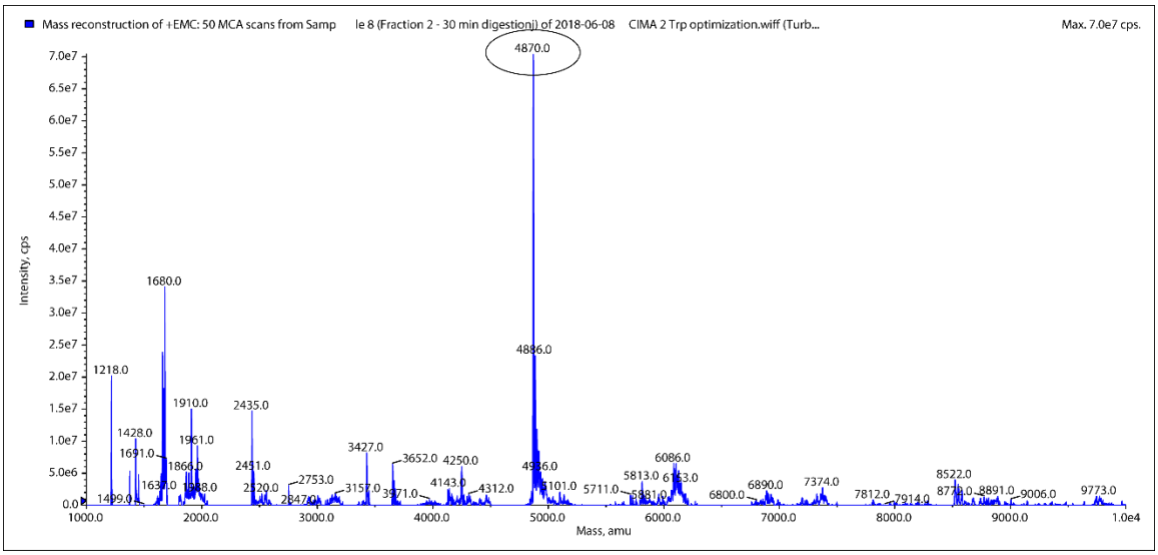

Figure 153: MS infusion of peak 1 (Figure 152) of digestion of CIMA isomer 2 by trypsin.

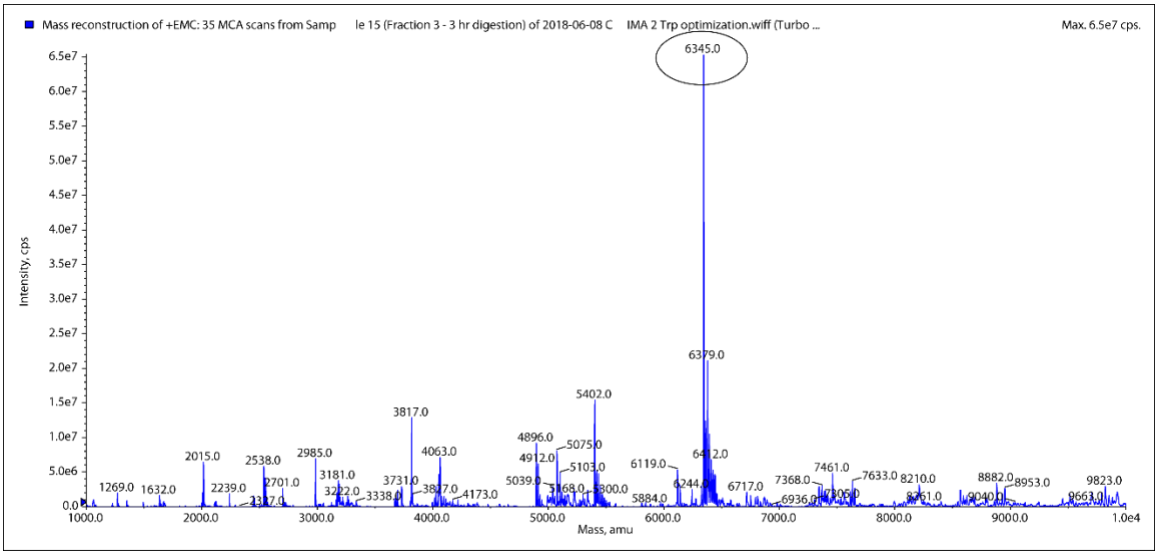

Figure 154: MS infusion of peak 2 (Figure 152) of digestion of CIMA isomer 2 by trypsin.

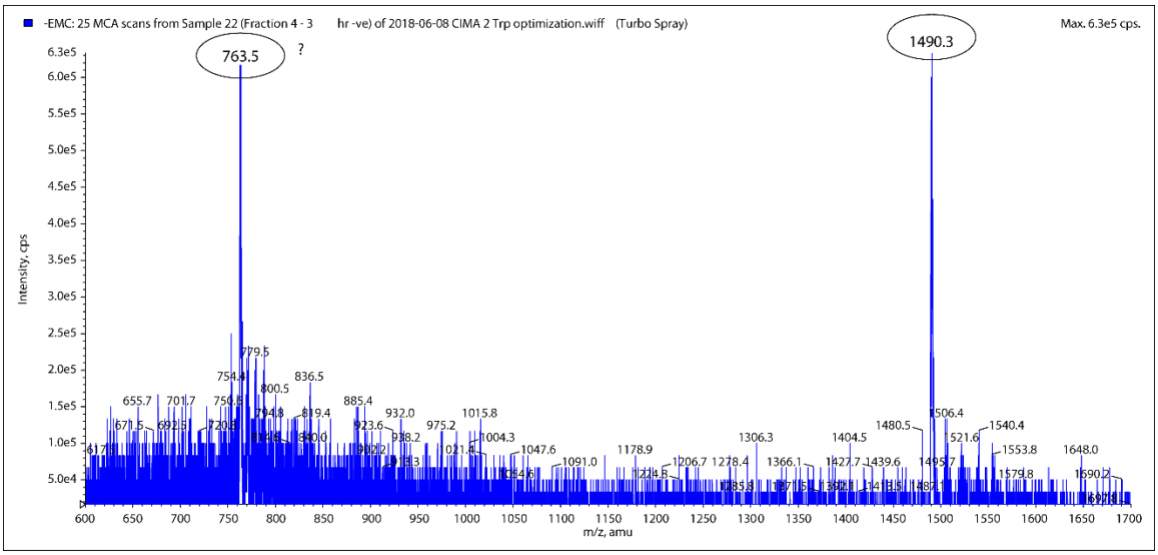

Figure 155: MS infusion of peak 1 (Figure 152) of digestion of CIMA isomer 2 by trypsin.

The results from trypsin digestion experiment were very useful and revealed the sites of conjugation. In the case of isomer 1, the conjugation is most likely on one of the amines of either chain A or chain B. The conclusion is summarized in Figure 156.

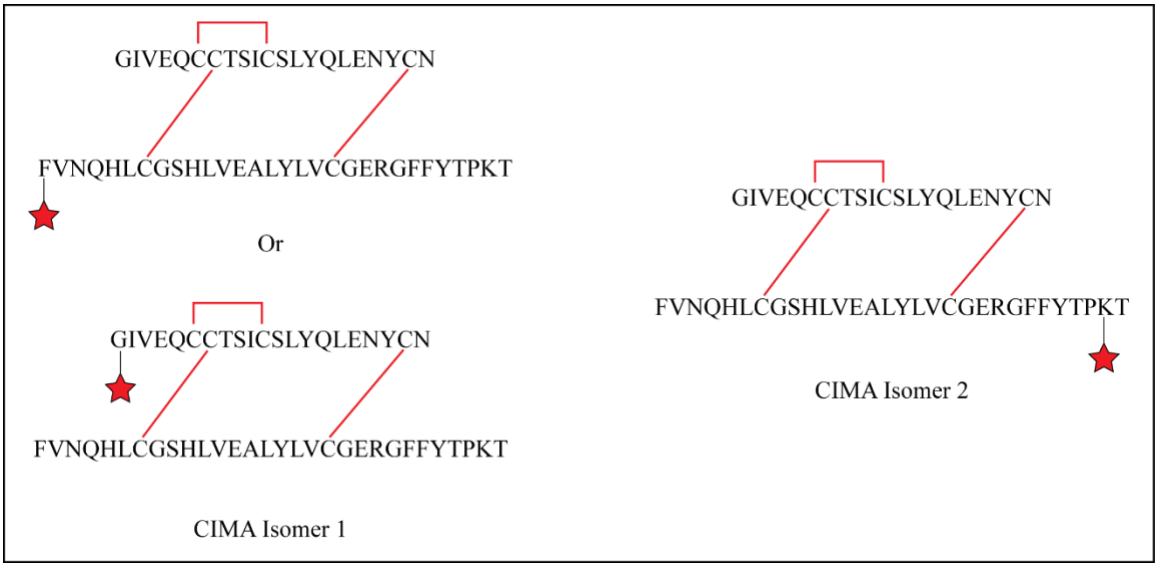

Figure 156: Possible sites of conjugation (red stars), based on the trypsin digestion results.

Digestion of insulin by GluC

The trypsin digestion experiment helped to locate the site of conjugation for CIMA isomer 2, it is likely on K of fragment 2 of chain B. However, it couldn't specify the site on isomer 1. Hence, we decided to use another protease GluC. GluC protease specifically cleaves on the C terminal side after a glutamic acid residue. Since GluC has a different pattern of proteolysis and it would help to locate whether the conjugation is on chain A or chain B of isomer 1 (Figure 157 and Table 8).

Endoproteinase GluC (catalog # P8100s) was purchased from New England Biolabs. 50 µg of GluC was dissolved in 50 µL of milliQ water and 13 aliquots of 3.84 µL were prepared in 13 tubes. The aliquots were stored in -80 ºC until used. The following reagents were mixed to initiate the digestion of insulin; 0.1 mL water + 0.1 mL 2x buffer provided with the kit + 3.84 µL enzyme + 17.2 µL of 1 mM insulin solution prepared in DMSO. It was allowed to run overnight. Finally, the peaks were collected on HPLC and

analyzed by MS to determine the digestion fragments (Figure 158 - Figure 160).

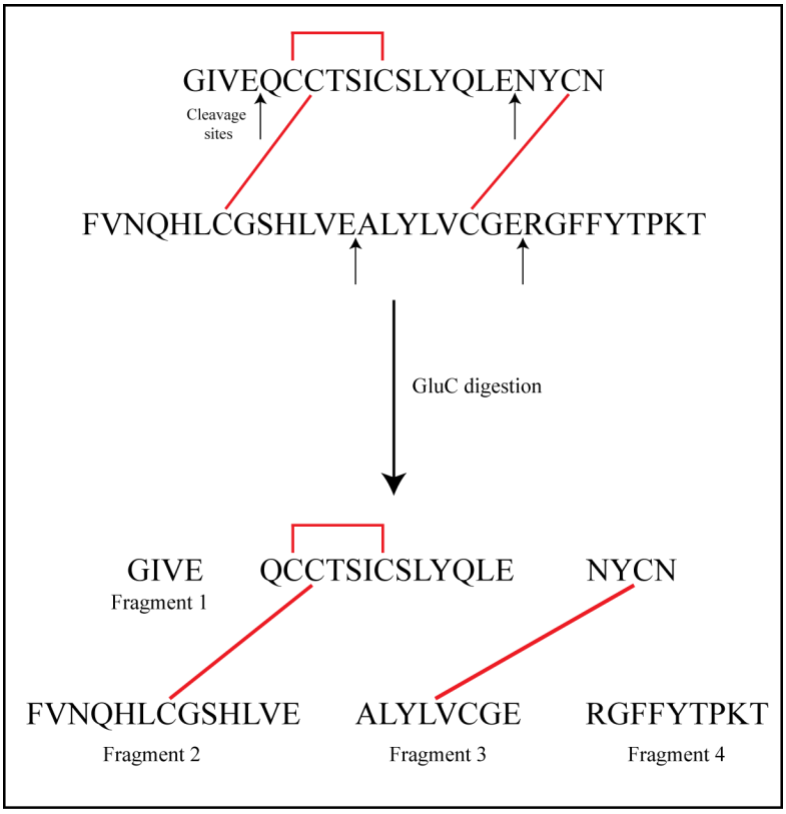

Figure 157: Insulin digestion by GluC.

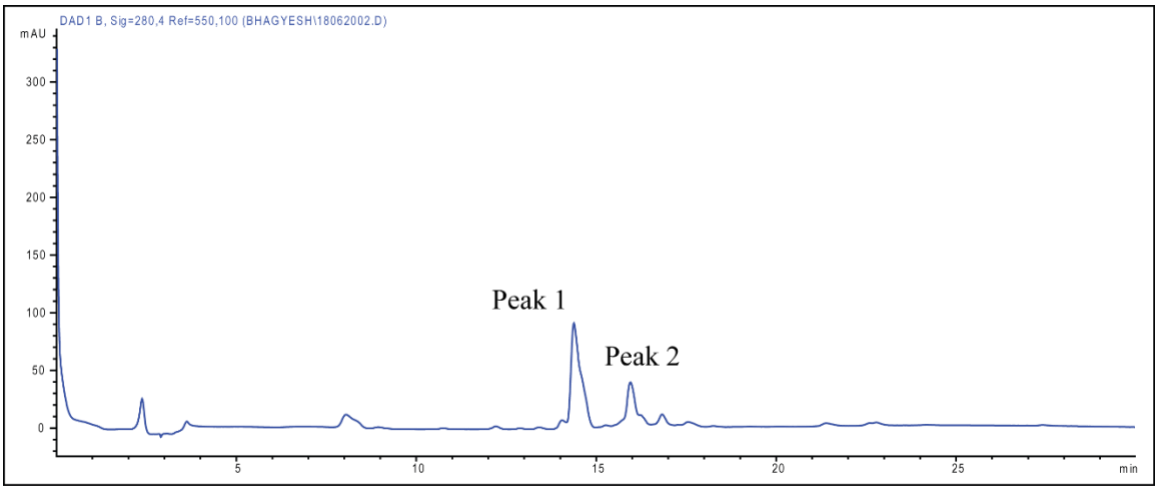

Figure 158: HPLC chromatogram of digestion mixture of insulin by GluC.

Table 8: GluC digestion fragments of insulin and their masses.

Fragment	Sequence	Total mass	Charged state [M/2]	Total mass after conjugation
1	GIVE	416.2	-	947.2
2	QCCTSICSLYQLE + FVNQHLCGSHLVE	2972.2	1486.1	3503
3	RGFFYTPKT	1115.5		
4	NYCN+ ALYLVCGE	1378.5	689.2	-

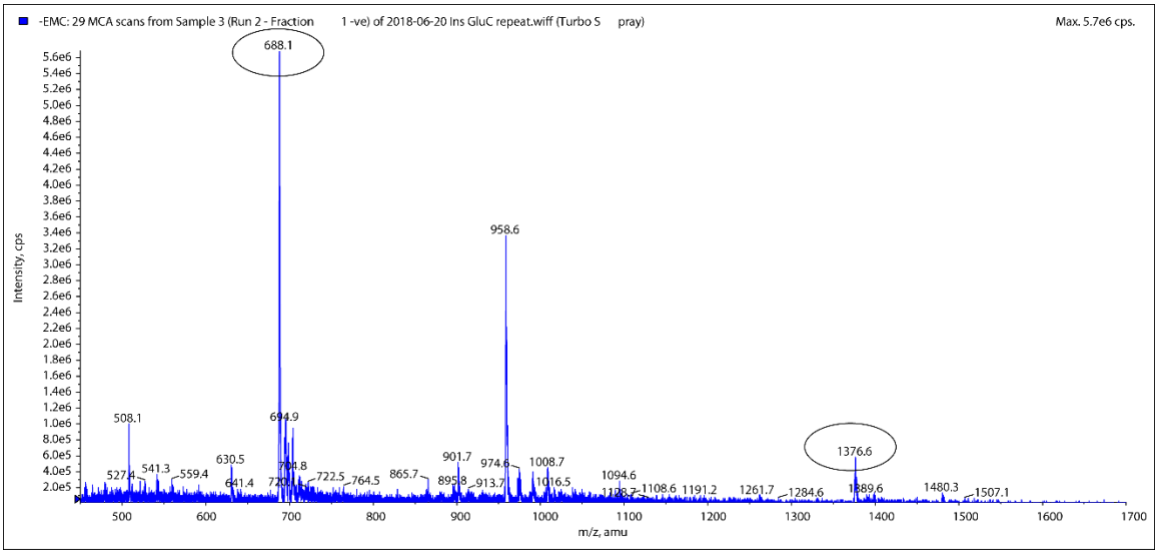

Figure 159: MS infusion of peak 1 (Figure 158) of digestion of insulin by GluC.

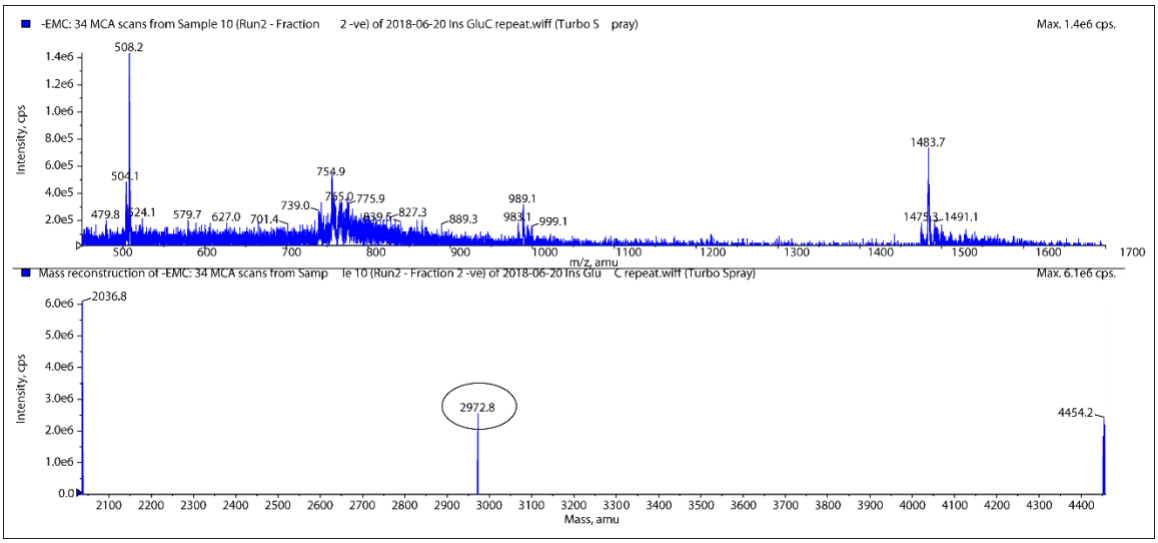

Figure 160: MS infusion of peak 2 (Figure 158) of digestion of insulin by GluC.

CIMA 1 digestion by GluC

A stock solution of CIMA isomer 1 was prepared in DMSO (concentration = 8.467 mM). 1.84 µL of CIMA isomer 1 from its stock solution was mixed with 0.1 mL of 2x digestion buffer, 0.1 mL of milliQ water and 3.84 µg GluC. The reaction was incubated for 3 hours at 37 ºC and analyzed by HPLC (Figure 161), peak 1 was collected and characterized by mass spectrometry. It showed the correct mass of fragment GIVE caged with photocleavable group (Figure 162). To further confirm the identity of peak 1, the fraction collected from HPLC was photolyzed using 405 nm. After the photolysis, the caged peptide was released, and we observe the mass of uncaged peptide GIVE in MS (Figure 163). Conclusions from the protease digestion and MS analysis are summarized in Figure 164.

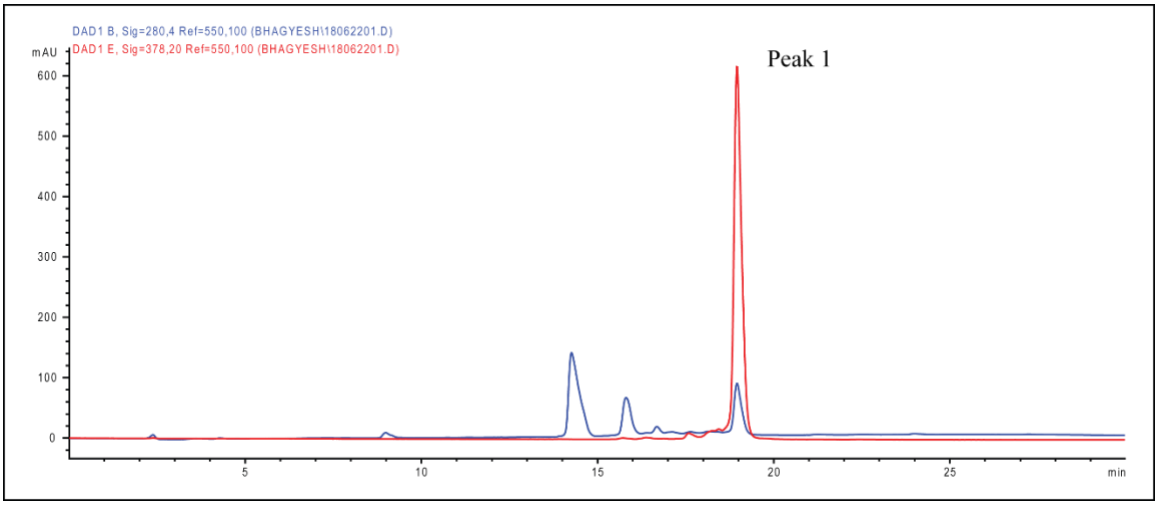

Figure 161: HPLC chromatogram of CIMA isomer 1 by GluC protease.

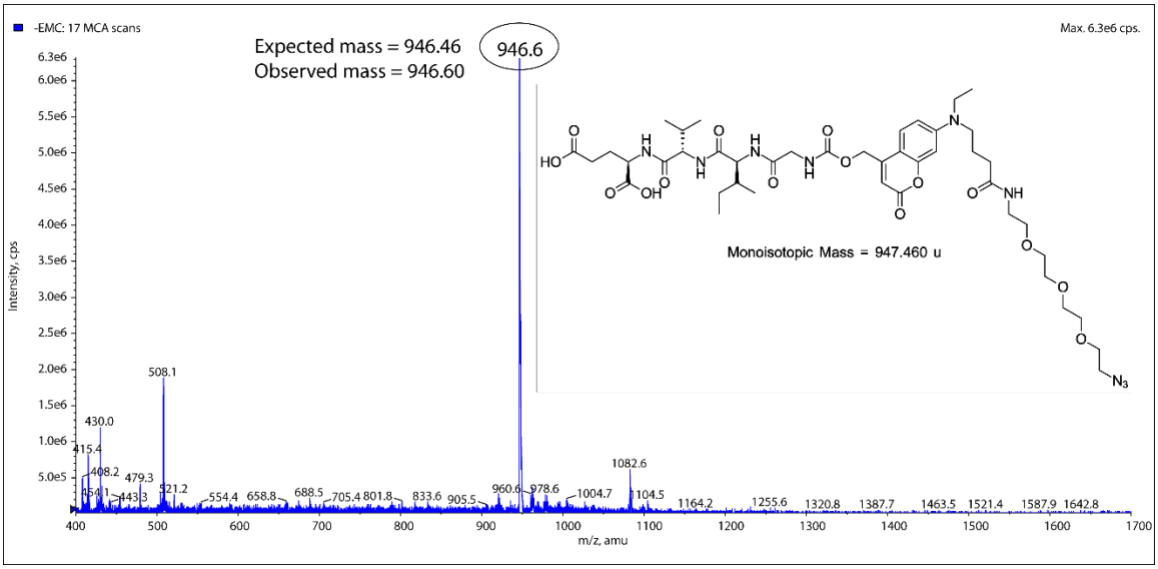

Figure 162: MS infusion of peak 1 (Figure 161) of digestion of CIMA isomer 1 by GluC.

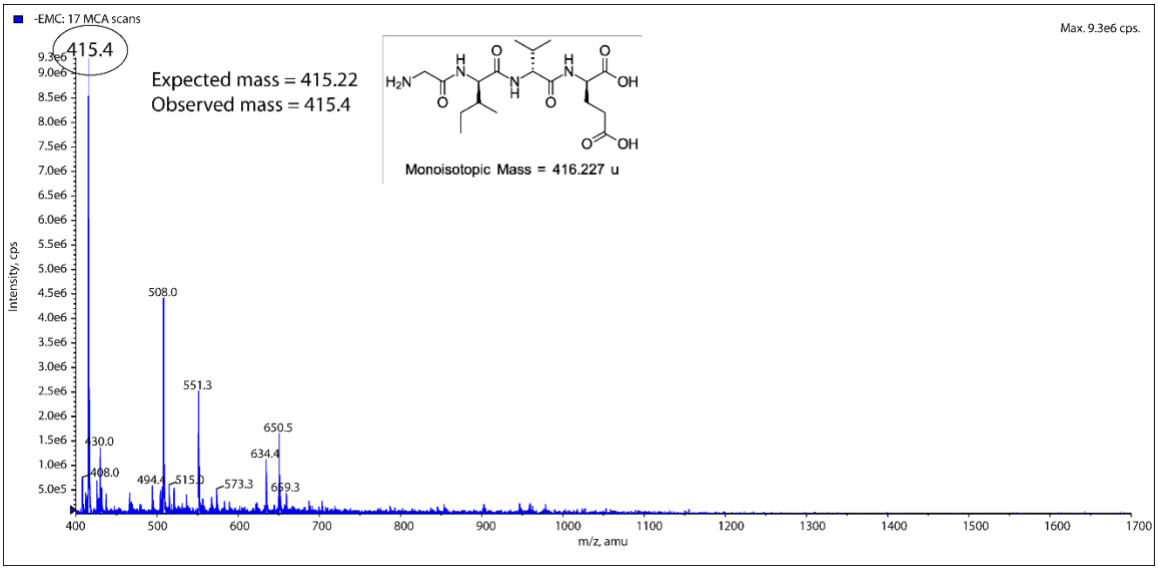

Figure 163: MS infusion of peak 1 (Figure 161 and Figure 162) after exposing it to 405 nm LED for 15 min.

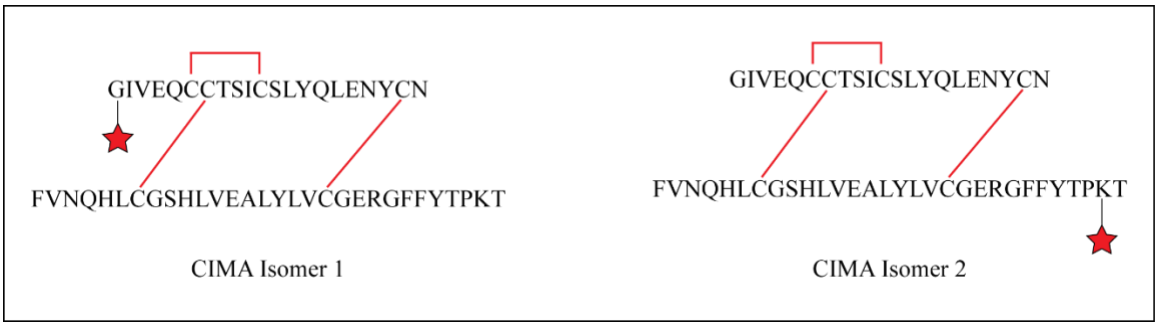

Figure 164: The sites of conjugation on insulin in both CIMA isomers. Coumarin is being conjugated to CIMA isomer 1 on terminal amine of chain A and on B29 lysine in the case of CIMA isomer 2.

Measuring molar extinction coefficients of coumarin carbamate and insulin

The experiment was set up to determine the molar extinction coefficient of coumarin carbamate. The molar extinction coefficient of 4-{N-ethyl[4-(hydroxymethyl)-7-coumarinyl]amino}-1-(2-{2-[2-(2-azidoethoxy)ethoxy]ethoxy}ethylamino)-1-butanone (coumarin azide) could not be used for this purpose because there is an increase in the

absolute molar extinction coefficient once the carbamate is formed. Hence it was decided to cage a test molecule to coumarin azide to measure its molar extinction coefficient. The caged molecule (shown in Figure 165) was synthesized using the same CDI conjugation chemistry used for caging insulin. The crude reaction mixture was run on prep HPLC and the desired product was purified. After drying the HPLC fractions, the dried product was dissolved in DCM and the organic layer was extracted with water to remove TFA salt. The HPLC chromatogram is shown in Figure 166.

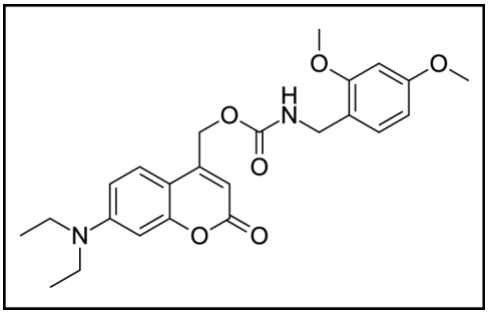

Figure 165: Test molecule used for determining the molar extinction coefficient of coumarin caged test molecule.

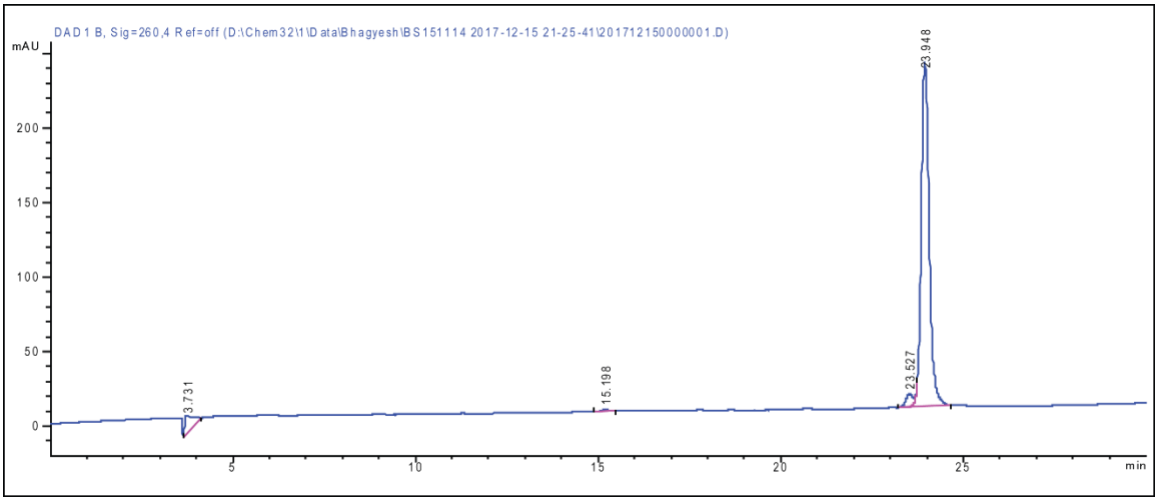

Figure 166: HPLC chromatogram of purified coumarin caged test molecule on prep HPLC.

To measure the extinction coefficient, the dried residue of test molecule was dissolved in DMSO and aliquoted in three Eppendorf tubes. DMSO was evaporated in speedvac overnight to eliminate DMSO completely. The weight of the compound was recorded and dissolved in a known volume of DMSO and theoretical concentration was calculated. From the stock solutions, serial dilutions were performed to create solutions of different concentrations. The absorbance measurements were performed on each dilution and plotted against concentration. The results of three independent replicates are shown in Figure 167. The average slope of 3 plots was 19770 with a standard deviation of 34.2.

Extinction coefficient of caged coumarin = 19800 $M^{-1}cm^{-1}$

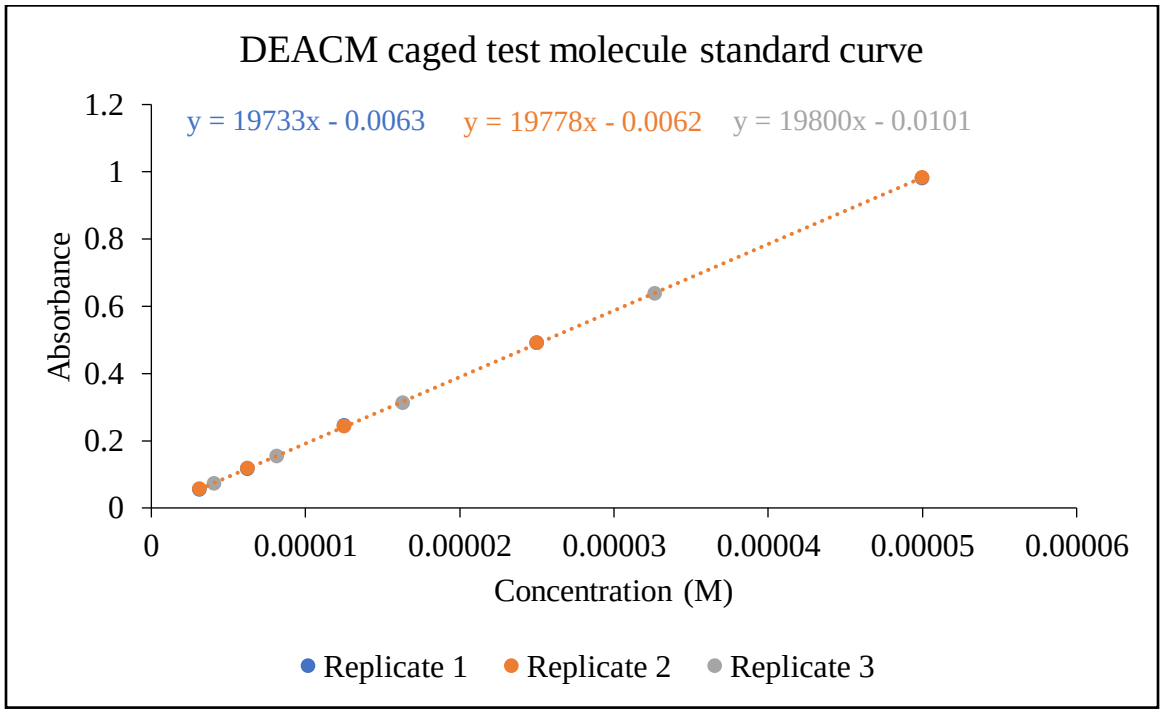

Figure 167: The standard curves of different dilutions from caged DEACM in triplicate.

Measurement of photolysis rate constant of CIMA

This experiment was aimed at measuring photolytic rate kinetics of CIMA in solution. It would be interesting to compare the rate with DMNPE insulin photolysis rate

which was reported earlier.[29] We decided to use PBS as a solvent for performing the photolysis as it closely mimics the physiological solvent. However, CIMA is fairly non-polar and hence a small amount of DMSO was added to maintain its solubility. For photolysis, a stock solution of CIMA of 10.23 mM was used. Final concentration of CIMA was kept at 1 mM adding 8.8 µL stock solution + 1.2 µL DMSO + 80 µL PBS. The photolysis was performed in a microcentrifuge tube at a distance of 5 cm from the 405 nm LED. At every time point, 10 µL solution was removed, diluted to 80 µL using DMSO and injected (25 µL) in HPLC for analysis. A standard curve of insulin on HPLC was used to determine the amount of insulin being uncaged due to photolysis. All chromatograms from one of the replicates are overlaid and shown in Figure 168. The concentration of insulin at each time point was measured and averaged from triplicates. It was plotted against time in Kaleidagraph®.

$$A = A0(1 - e^{-k1.t})$$

The plot is shown in Figure 169. Calculated kinetic rate constant is k_1 = 0.0184 sec^{-1} and fits the expected first order kinetics.

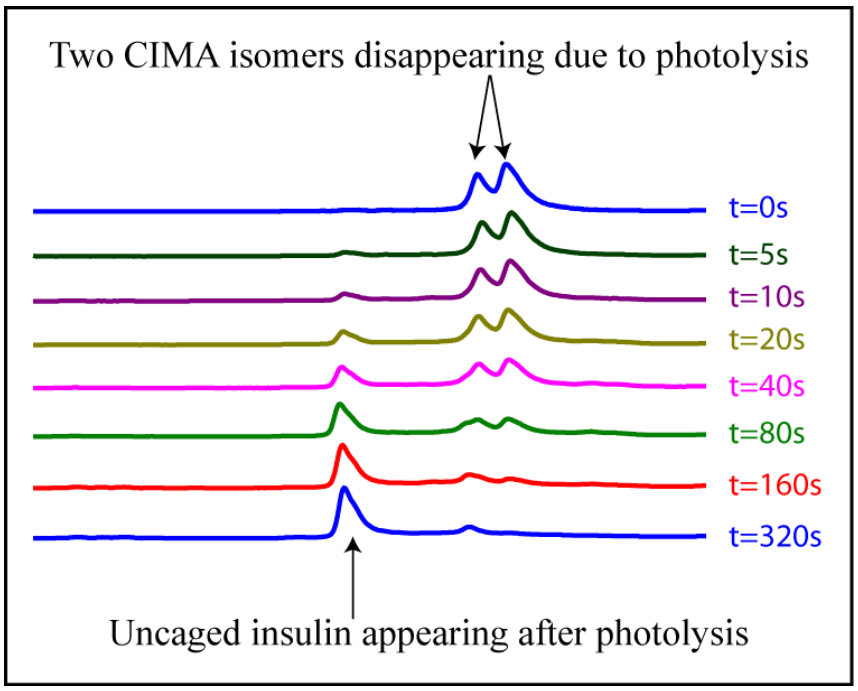

Figure 168: HPLC chromatograms of CIMA solution phase photolysis overlaid.

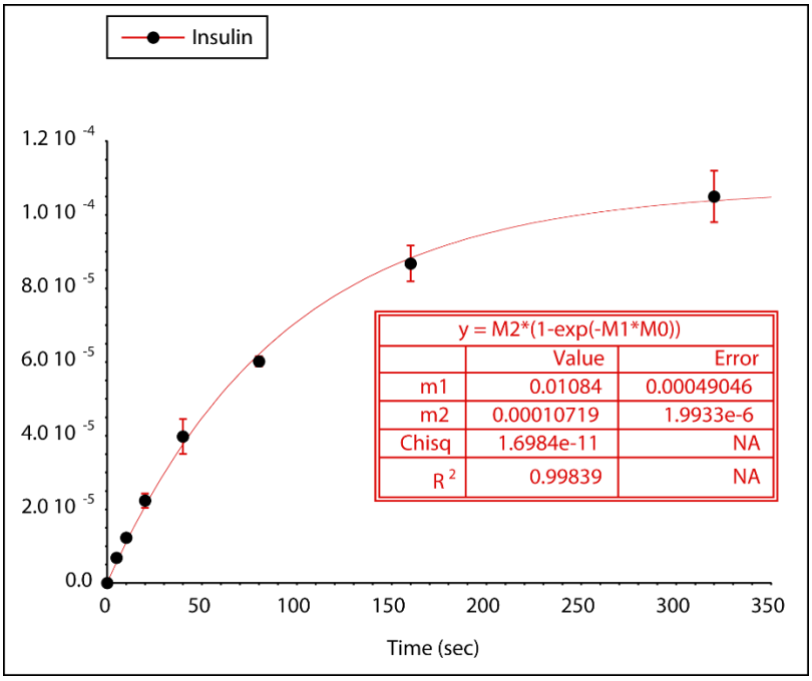

Figure 169: Plot of insulin concentration versus time during CIMA solution phase photolysis by 405 nm light.

Synthesis and characterization of insulin trimer

The trimer species were purified using a size exclusion column (Yarra 3 µm SEC-2000 LC column 300 × 7.8 mm). ESI-MS (m/z): $[M]^+$ calculated for, 20,008.89; found, 20,023.00 (Figure 170); HPLC purification method – size exclusion HPLC (flow rate 0.5 mL min^{-1}, runtime 16 min with 3 min post-run), solvent A (H_2O), solvent B (0.1% TFA in ACN), gradient 45 % B isocratic over 16 min, elution time – 10.7-11.4 min (Figure 171).

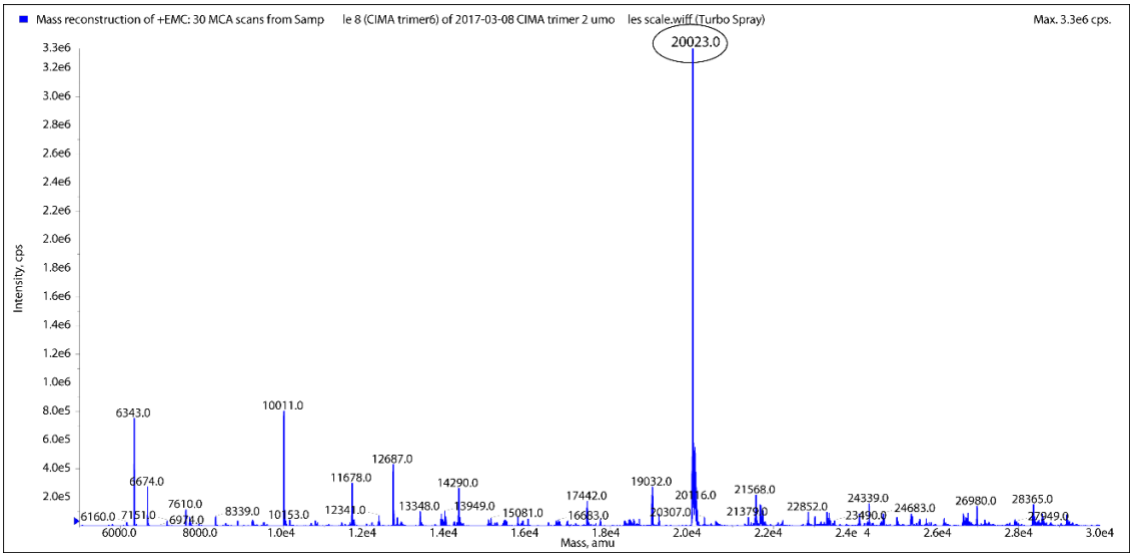

Figure 170: The mass spec of insulin trimer. The trimer is seen at $[M]^+$=20023 (calc. for 20009).

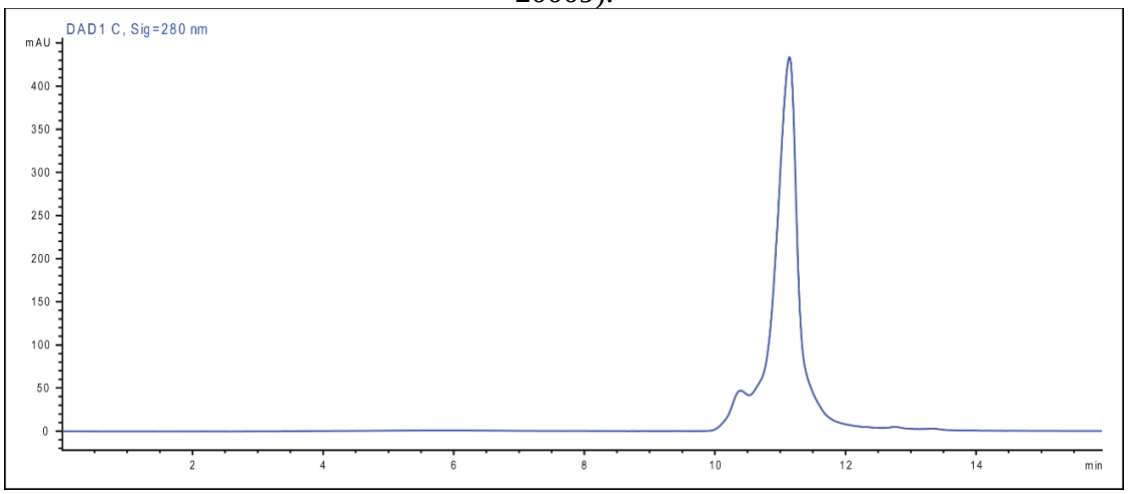

Figure 171: The analytical chromatogram of purified insulin trimer on the size exclusion column.

Preparation of insulin trimer particles

The insulin trimer was synthesized as described above. However, once all DMSO was evaporated from the tube containing trimer, the remaining material used to get stuck as a film. It was hard to remove and always a heterogeneous mixture of variable sizes and shapes. To make it uniform, we thought of grinding this material down to get small particles with a narrow size particle distribution. For this, a smaller motored pestle was used (Argos Technologies, catalog # A0001). Typically, to prepare particles, insulin trimer solution in DMSO was added to a microcentrifuge tube. DMSO was evaporated using speed-vac. 150 µL PBS was added and ground using the pestle for about 4 min. The suspension was centrifuged heavily, and supernatant PBS was removed. Then fresh PBS was added as required. This procedure was performed just before using this material. The particles could be kept in -20 ºC after preparing in bulk.

Optimization of particle size of trimer particles

To achieve the smallest particle size and narrower distribution, we tried grinding particles for different lengths of time using the procedure described above. Briefly, trimer containing 10 nmol of CIMA was dried in a microcentrifuge tube. These particles were suspended in 33 µL of PBS. The particles were ground using motor pestle for 30 seconds, 1 min, 2 min, 4 min and 6 minutes in different tubes. This 33 µL was further diluted approximately 200x after grinding for particle size measurements using Zetasizer.

As seen in Figure 172, there was no significant difference in grinding time either on particle size or PDI. The standard deviation, however, decreased as the grinding time increased. Based on this, we decided to keep the grinding time to 4 minutes to achieve the smallest particle size with a narrow size distribution. To test the ease of injection of these

particles into injection via needle-syringe, this suspension of particles in PBS was passed through a syringe having a 31G needle. The particles passed through it without any resistance. There were no particles seen stuck inside the syringe. Because of this, we decided to use these for animal studies.

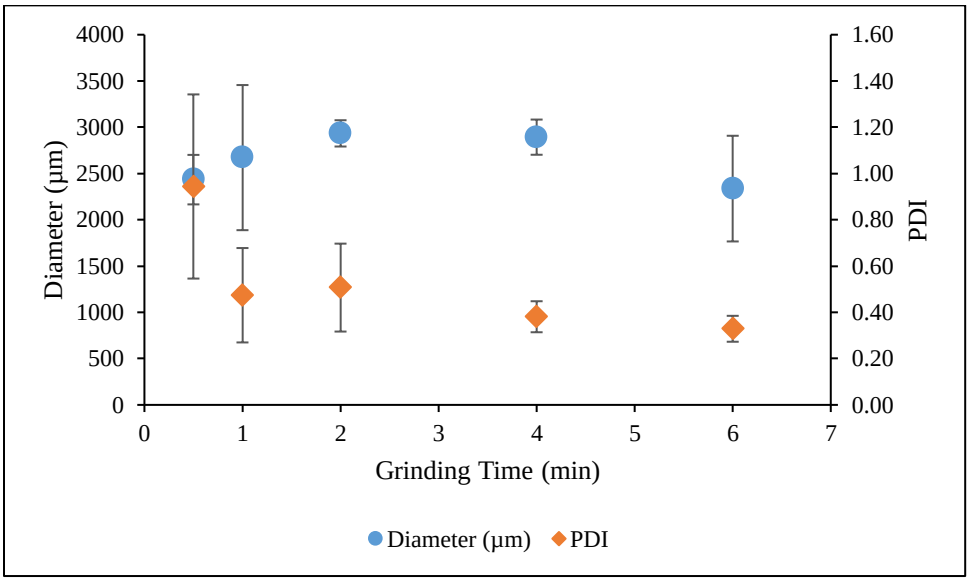

Figure 172: Particle sizes of coumarin insulin trimer particles as measured using Zetasizer.

Final analysis of particle size of trimer used for *in-vivo* studies

For the final measurements of particle size, the trimer pellets were milled as described earlier. Briefly, the solution of insulin trimer in DMSO containing 140 nmol of insulin was aliquoted into 3 tubes and dried overnight in a speed vac. To dried pellet, 0.15 mL of PBS was added, and particles were milled for 4 minutes. Additional 0.3 mL of PBS was used and added to current suspension after washing the plastic probe. Measured pH at this point was approximately 6.3, it was raised to 7.2 using 1 N NaOH. The tubes were centrifuged for one min at 7000 rpm, and the entire supernatant was taken out. 50 µL of fresh PBS was added and vortexed to suspend particles. The suspension was diluted

approximately 2000-fold in PBS and this solution was used to measure the particle size. Average size was calculated from triplicate measurements.

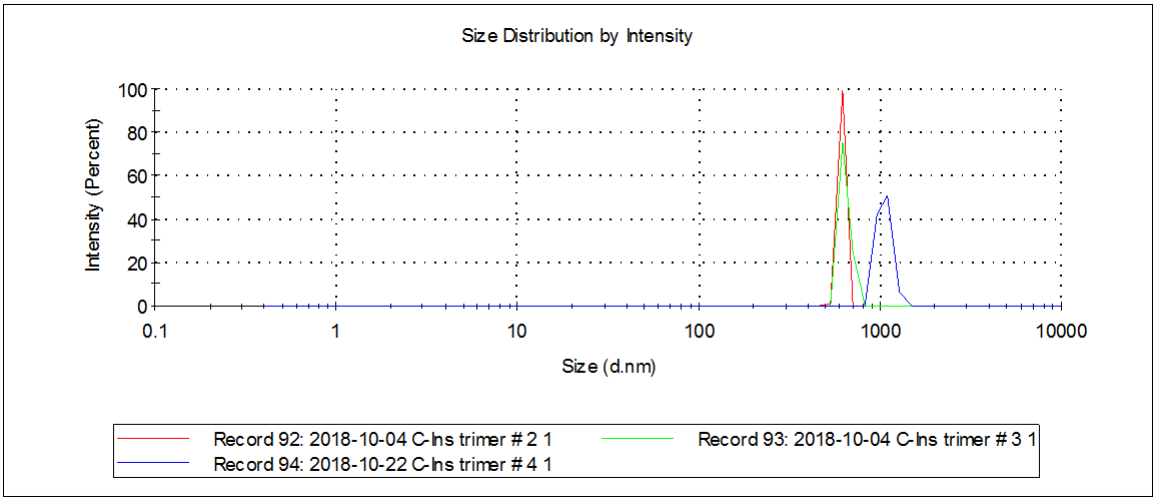

Figure 173: Measurement of particle size of insulin trimer using DLS.

Average diameter = 2461 nm with PDI of 0.7 (Figure 173).

Solubility studies

This experiment was aimed at measuring the solubility of coumarin insulin trimer in PBS at pH 7.2 and comparing it with native insulin. The rationale was to measure how much insoluble insulin is in the form of trimer versus free insulin in aqueous solvents at pH 7.2. Less solubility is desirable as it would precipitate out and remain localized at the site of injection.

To measure the solubility limit of the trimer, trimer pellet containing 140 nmol of insulin was dried in three tubes in speed-vac. 150 µL of PBS was added to it. Using the motorized pestle (Argos Technologies, catalog # A0001), it was ground into particles for 4 min. 0.3 mL additional PBS was used to wash the plastic probe and added to the original solution. PH was adjusted to 7.2 using 1 N NaOH. It was centrifuged for 3 min at 13000 rpm. The supernatant was carefully removed using gel loading pipette tip and remaining

particles were suspended in 70 µL PBS. It was kept for vortexing at speed 6 on Vortex Genie # 2 (Fisher Scientific) for two hours. The samples were centrifuged again at 14000 rpm for 3 min. 1 µL of supernatant was diluted in DMSO and the absorbance measurements were performed using UV-VIS spectrophotometer at 380 nm using coumarin $\varepsilon_{380\ nm}$ = 59300 $M^{-1}cm^{-1}$.

The solubility limit of insulin was determined in a similar manner except 10 mg insulin was weighed and suspended in 0.2 mL PBS in three tubes. pH was adjusted to 7.2 and vortexed in the same manner. The absorbance was recorded in PBS because the extinction coefficient of insulin was measured in PBS. $\varepsilon_{280\ nm}$ = 5200 $M^{-1}cm^{-1}$. The maximum solubility of trimer measured = 1.01 µM and the maximum solubility of insulin measured = 2.14 mM. The solubility of insulin trimer was 2115-fold less compared to native insulin (Figure 174).

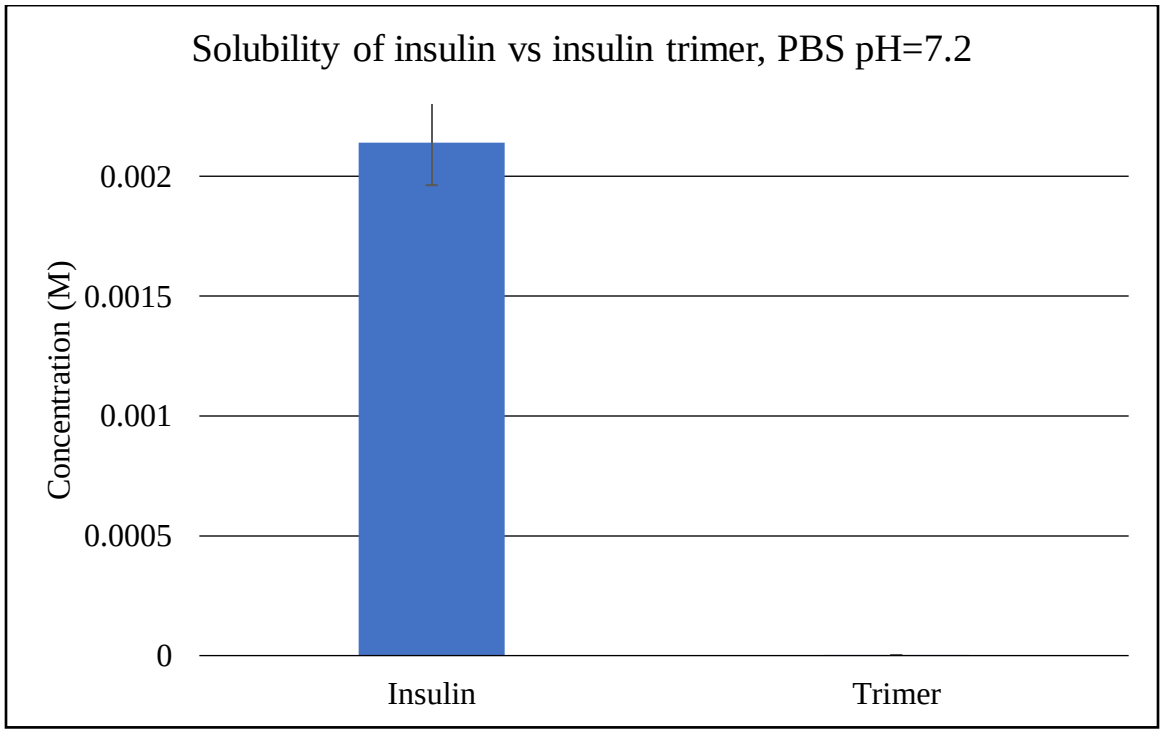

Figure 174: The solubility difference between insulin versus insulin trimer in PBS at pH 7.2.

In-vitro photolysis of insulin trimer

At this point, we performed *in-vitro* photolysis of coumarin trimer material using 405 nm LED. The aim was to mimic the photolysis under light/dark conditions as reported here.[29] We noticed that the Tentagel® resin behaved very differently from the ChemMatrix ® resin when subjected to *in-vitro* photolysis.[73] Significant leaching was observed from Tentagel® resin which was not expected. This might be because insulin that is being released saturates PBS and we know that insulin has moderate solubility in PBS. As additional insulin is released, it cannot be solubilized due to saturation limit and as we replace fresh PBS, previously released but insoluble insulin gets solubilized and we see extended release profiles. Due to this, we decided to remove complete supernatant at each time point rather than removing 50% as performed earlier for the analysis of first-generation material. The procedure is described in the next paragraph.

A solution of insulin trimer in DMSO containing 140 nmol of insulin was aliquoted into 3 tubes and dried overnight in a speed vac. To the dried pellet, 0.15 mL of PBS was added, and particles were milled for 4 minutes. Additional 0.3 mL of PBS was used and added to current suspension for washing the plastic probe. The measured pH at this point was approximately 6.3 and raised to 7.2 using 1 N NaOH. The entire suspension was transferred into glass tubes (Fisher Scientific, 1 mL). The tubes were centrifuged for one min at 7000 rpm, and the entire supernatant was taken out. 0.1 mL of buffer was added to the suspension, vortexed briefly and centrifuged in the same manner. The supernatant was collected and labeled as t=0'. At each time point, 0.1 mL buffer was added, vortexed, centrifuged and the supernatant was collected. At t=0 and t=60, a brief illumination was performed for two minutes each by keeping the vial at 6.4 cm from the 405 nm LED. The

samples were stored in -80 ºC. The samples were analyzed by loading 5 µL of the total 100 µL of collected supernatant on a gel and running SDS-PAGE. Band intensities were measured using Photoshop®. For the control samples, an aluminum foil was kept between LED and samples to prevent exposure to light. To quantify the number of moles of insulin released, different amounts of insulin were loaded into wells to plot a standard curve. This plot was used to measure the amount of insulin in samples. Control samples resulted in no bands. The cumulative insulin release is plotted in Figure 175.

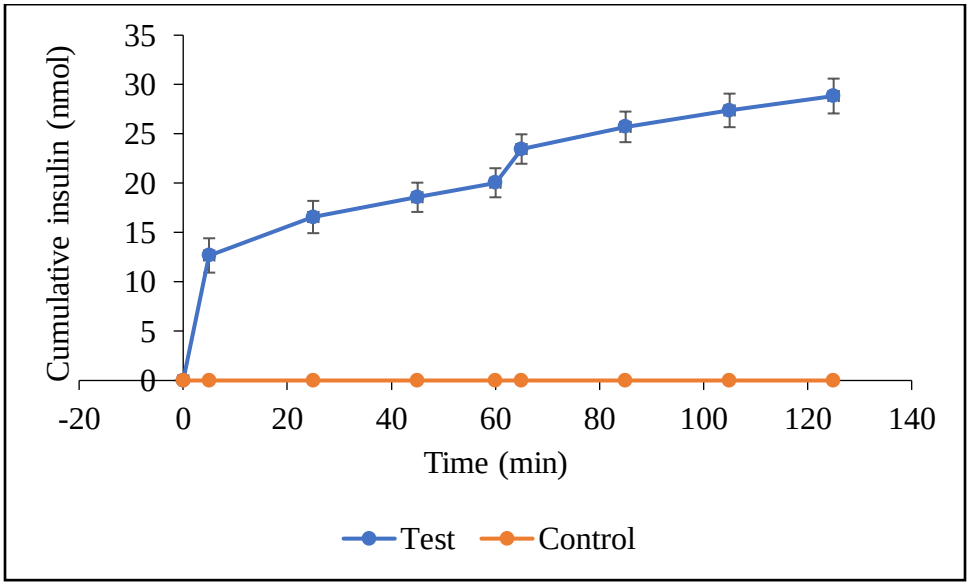

Figure 175: Cumulative insulin release from *in-vitro* photolysis of coumarin insulin trimer suspension. Experimental samples are in blue while the controls are in orange.

This *in-vitro* photolysis is somewhat similar to what we observed with the Tentagel resin with first-generation material. Even after stopping the light exposure, insulin still comes off from the material and plateaus much later than desired. The low solubility of insulin in PBS is probably responsible for this. When we expose the material to light, a certain amount of insulin is released but not all of it can solubilize in the given volume of PBS. Because of this solubility issue, it precipitates out and when we centrifuge it at 7000

rpm for a minute, the solubilized portion comes off in the supernatant, which is then measured in the gel. The precipitated portion settled at the bottom after centrifugation and it gets solubilized later when fresh PBS is added for the next time point. That is why we see such a plot. Likely, a similar phenomenon could happen in an animal model as insulin may not be completely released in the bloodstream all at once. Although we might observe a quick burst into the blood, the release time may be prolonged. The lag could be accounted when creating a mathematical model of PAD insulin release kinetics in the future, thus the release could be predicted and fine-tuned.

Optimization of 405 nm setup for avoiding high temperatures

As coumarin can be photocleaved using blue light, we planned on using 405 or 450 nm LED for performing the photolysis. The inverse square plot of 405 nm LED was plot as described earlier. This was taken when the animal studies were being performed in March 2018 (Figure 176).

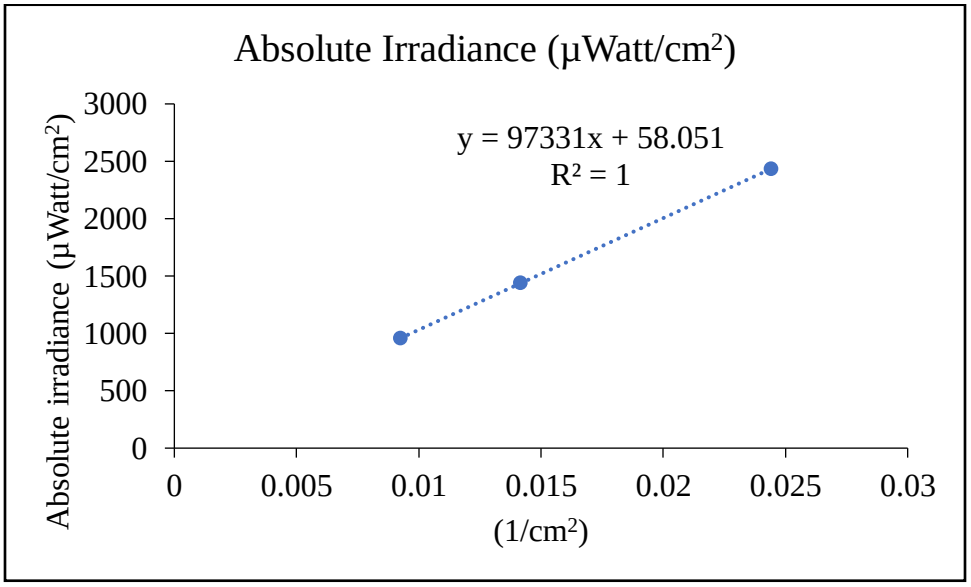

Figure 176: Absolute irradiance of 405 nm LED (taken in March 2018).

405 nm LED temperature measurements

The temperature measurements were performed using a flat temperature probe from Klein Tools. The *in-vitro* temperature measurements were performed by keeping the probe flat and holding a LED right on top of it on a wooden surface.

The temperature went very high, much higher than expected. Within 10 seconds, it went higher than 200 ºF (Figure 177) from room temperature. We were planning to perform 2-min irradiation for the animal studies, but that would have been too much. In pilot studies, it was found out that, even 7-8 seconds of irradiation was enough to cause a skin injury.

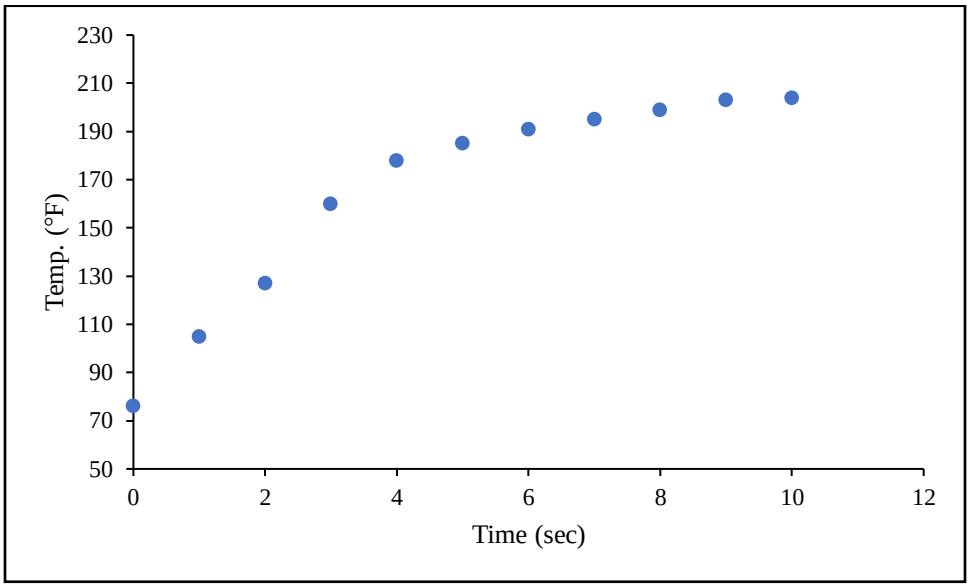

Figure 177: Temperature of 405 nm LED as measured by a flat temperature probe.

To get around this problem, we increased the distance between the LED and the base plate. To achieve this, Dr. Friedman designed smaller wooden spacers of 0.63 cm height with magnets so that it can be put between the LED and the base plate to increase the overall distance. The time course of temperature was measured again with this new setup and compared with the previous one without spacers (Figure 178).

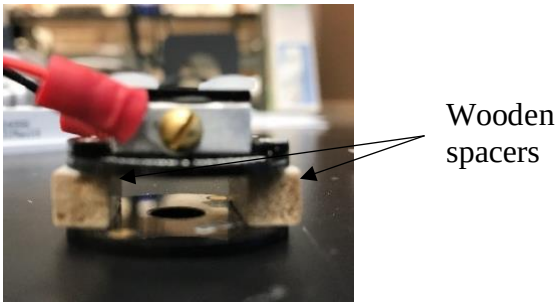

Figure 178: The LED design was modified by inserting wooden spacers in between two black discs.

The temperature did not increase much with the help of spacers and below 130 ºF even after irradiation of one minute (Figure 179). This change occurred because as we increased the distance approximately three times, the light intensity decreased 89% the original intensity. Also, the elevation allows space through which the heat escape, as opposed to a closed area with the compact LED on the surface. We estimated these temperatures would be tolerable to the skin.

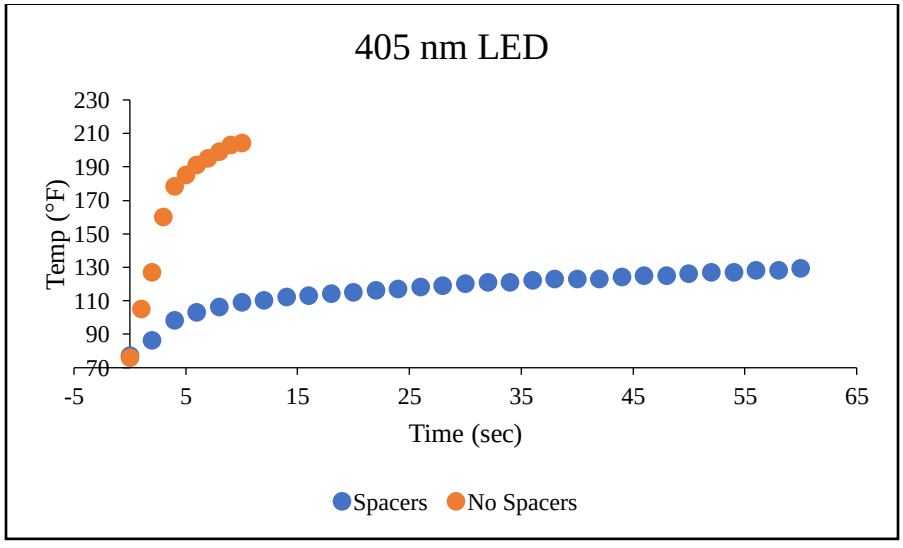

Figure 179: Temperature curve of 405 nm LED with and without spacers.

Thermal studies using LEDs on skin

The higher the energy being delivered to the depot in less amount of time, the more insulin will be released from the depot. Keeping the LED as close to the skin as possible and irradiating for a longer duration would ensure that the depot is being delivered the maximum amount of energy. We varied both the distance and time as these two parameters could be manipulated easily. Ideally, one could also alter the energy output of LEDs but here the aim is to vary the distance. In these studies, we are trying to measure what is the increase in temperature as we vary the distance between LED and skin as well as the duration of irradiation.

Dr. Friedman designed a scaffold which has 6 holes of 7 mm diameter each, through which the light passes for these experiments. A set of magnets were inserted surrounding the holes to add spacers of different heights to vary the distance (Figure 180). To measure the skin temperature, we utilized a FLIR ONE PRO infrared camera which could be operated by attaching to an iPhone. The images can be processed in software (provided by the company) to measure localized temperature. In all experiments, the holes were irradiated for specific periods of time at a certain distance. After irradiation, the LED was removed immediately, and a picture was taken. Thus, we measured heating occurring on the skin (Figure 181).

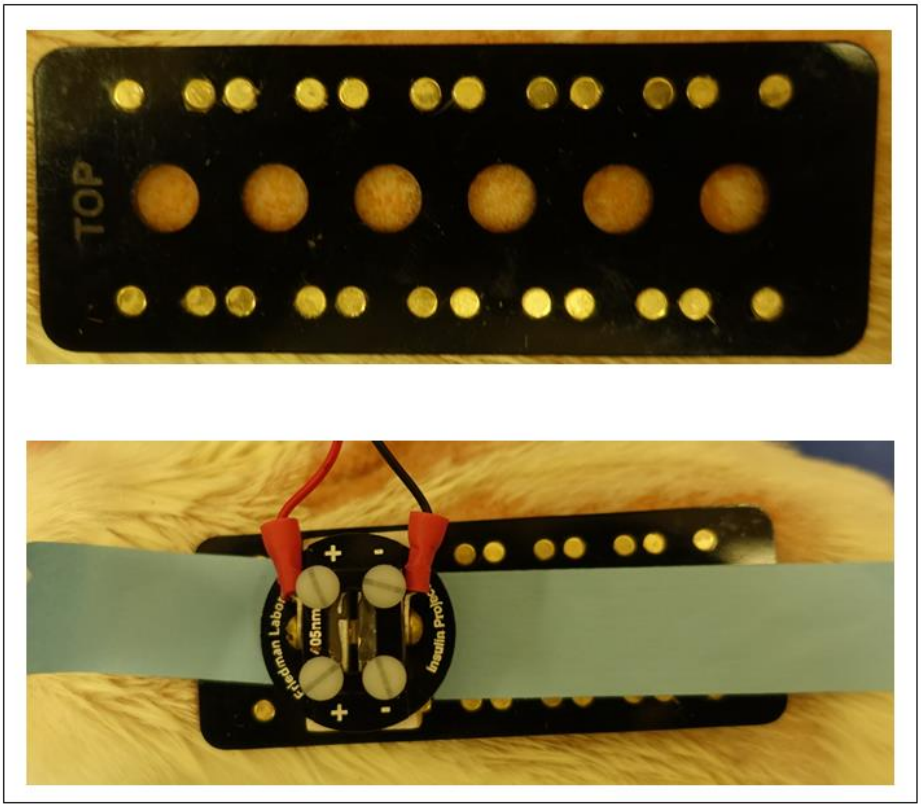

Figure 180: The scaffold used for the thermal studies (top). It was glued to the skin. The golden dots are magnets. LED was aligned over the open circle through a spacer (bottom). An opaque tape was placed over remaining open circles to prevent exposure to light when irradiating a spot.

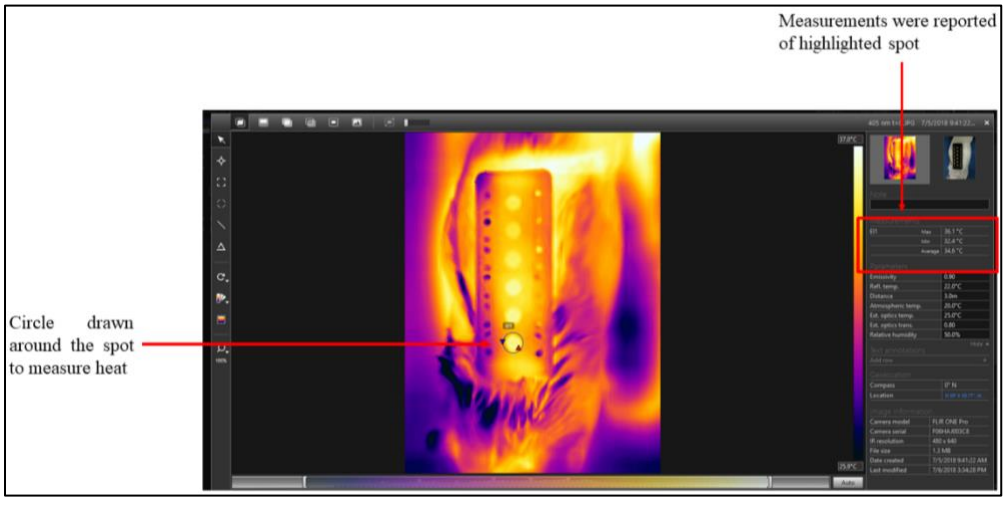

Figure 181: A screenshot of image processing in the FLIR Pro software. To measure the temperature of a spot, a circle was drawn around that and the measurements were recorded.

Attempt 1 for the thermal measurements

For the first attempt, we used both 405 nm and 450 nm LED. For spacers, we used the wooden spacers mentioned above. The total distance with two discs and wooden spacers was 0.95 cm. Time points selected were 0, 0.5, 1, 2, 4, 8 minutes.

We monitored if there was any visible injury on the skin. As seen in Figure 182, there were no visible signs of phototoxicity on the skin with 405 nm LED. The heat measurements for LEDs are plotted in Figure 183 and Figure 182. The temperature increase was modest going from body temperature to low 40s in Celsius in the case of 405 nm LED. Then it stayed nearly constant for 8 minutes time. However, the light of higher wavelength (450 nm) generated more heat and higher temperatures within a minute. No injury was seen with 405 nm LED irradiation, this makes sense at temperatures generated using 405 nm are not high and seemed to be tolerable by the skin. Surprisingly, although the temperatures are higher only by a few degrees centigrade in the case of 450 nm, we observed a significant amount of skin damage for higher durations of irradiation. It is interesting to note that 8 min of irradiation with 405 nm LED doesn't cause skin damage and temperatures plateau around 43 ºC, while even two minutes irradiation with 450 nm LED cases visible skin damage and the temperature was approximately 48 ºC. The estimated relationship between distance and energy is calculated in Table 9 and Table 10.

.

Table 9: Distances and corresponding absolute irradiance of 405 nm LED.

Type of spacer	Distance of spacer	Total distance	Inverse square of the distance	Absolute irradiance (W/cm^2)
No spacer	NA	2 × 1/16” = 1/8” ≈ 3.2 mm	(1/ $(0.32)^2$) = 9.76	0.950556
2 magnets	2 × 1/16” = 1/8”	1/8” + (2 × 1/16”) = 1/4” = 6.35 mm	1/ $(0.635)^2$ = 2.48	0.241439
2 magnets	2 × 1/16” = 1/8”	1/8” + (2 × 1/16”) = 1/4” = 6.35 mm	1/ $(0.635)^2$ = 2.48	0.241439

Table 10: Distances and corresponding absolute irradiance of 450 nm LED.

Type of spacer	Distance of spacer	Total distance	Inverse square of the distance	Absolute irradiance (W/cm^2)
No spacer	NA	2 × 1/16” = 1/8” ≈ 3.2 mm	(1/ $(0.32)^2$) = 9.76	1.848724
2 magnets	2 × 1/16” = 1/8”	1/8” + (2 × 1/16”) = 1/4” = 6.35 mm	1/ $(0.635)^2$ = 2.48	0.469316
Wood spacers	1/4”	1/4” + (2 × 1/16”) =0.375” =9.5 mm	1/ $(0.95)^2$ = 1.11	0.209556

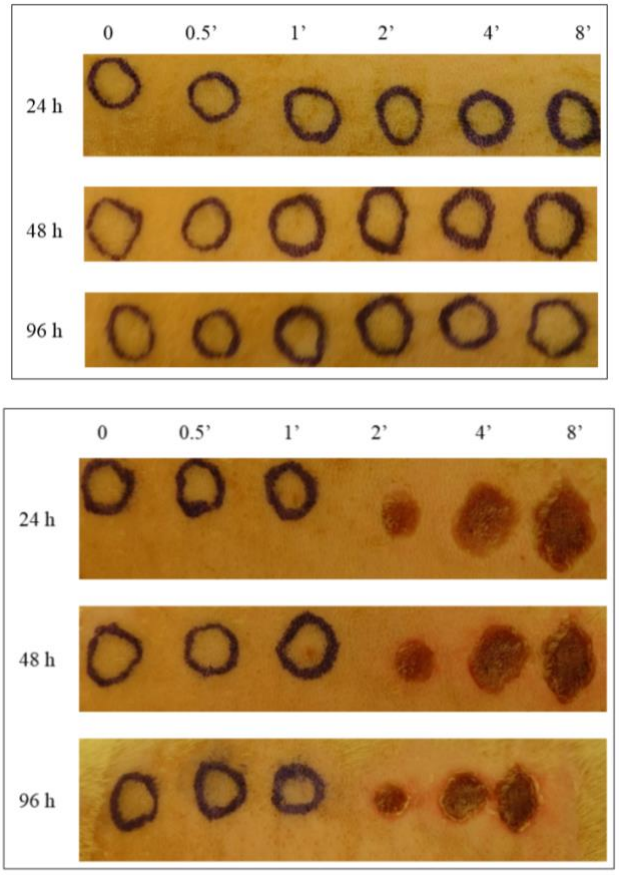

Figure 182: Pictures of irradiated skin spots which were irradiated using 405 nm (top) and 450 nm (bottom) for different periods of time. The pictures were taken after 24h, 48h and 96 hours.

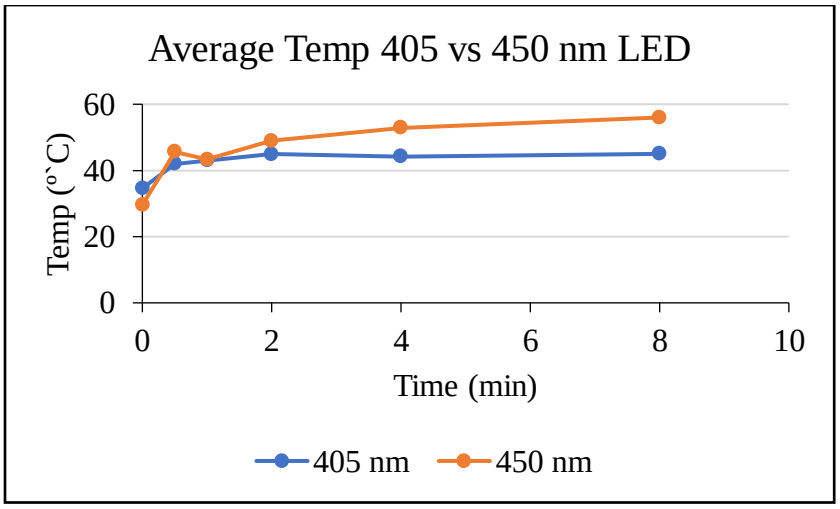

Figure 183: Average temperature on rat skin (inside 7 mm holes) after illumination with 405 nm and 450 nm LEDs at 0.95 cm distance (wooden spacers).

Attempt 2 with 405 nm LED varying the distance

Because 450 nm LED showed a significant level of skin damage, we decided not to use 450 nm in future thermal studies. Also, for *in-vivo* studies, we will be using 405 nm LED so 450 nm was not a priority at the point. We varied the distance between LED and the skin – one of the spacers was a wooden spacer (total distance = 0.95 cm) and the other was 2 × 1/16" magnetic spacer (total distance = 0.63 cm). The time durations were kept the same as earlier. The plots are shown in Figure 184 and skin images are in Figure 186. As seen earlier, for the wooden spacers, the temperature was slightly lower than 45 ºC and it didn't result in any scabs. However, with the lesser distance, temperatures went up as high at 51 ºC and even a two minutes irradiation was not tolerated. These studies provide a temperature range in which we should perform the animal studies when using these LEDs. Also, they help establish a correlation between temperature and skin damage. For example, a temperature of 43-44 ºC is harmless over 8 minutes but a temperature above 47-48 ºC burns the skin within two minutes. The skin samples irradiated using 405 nm LED didn't show any signs of heat burns visually. We also performed histology using hematoxylin and eosin staining to see any difference between unirradiated and 8 min irradiated skin sample. The skin was excised 72 hours post-irradiation. As seen from Figure 185, the irradiated sample didn't show any adverse reaction when compared with the control.

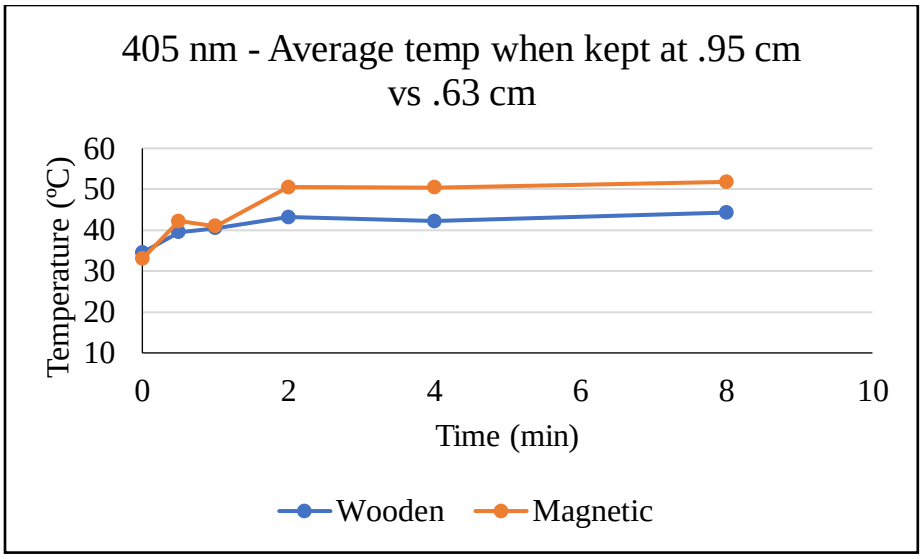

Figure 184: Average temperature on rat skin (inside 7 mm holes) after illumination with 405 nm LEDs at 0.95 cm distance (wooden spacers) and 0.63 cm distance (2 × 1/16" magnetic spacers).

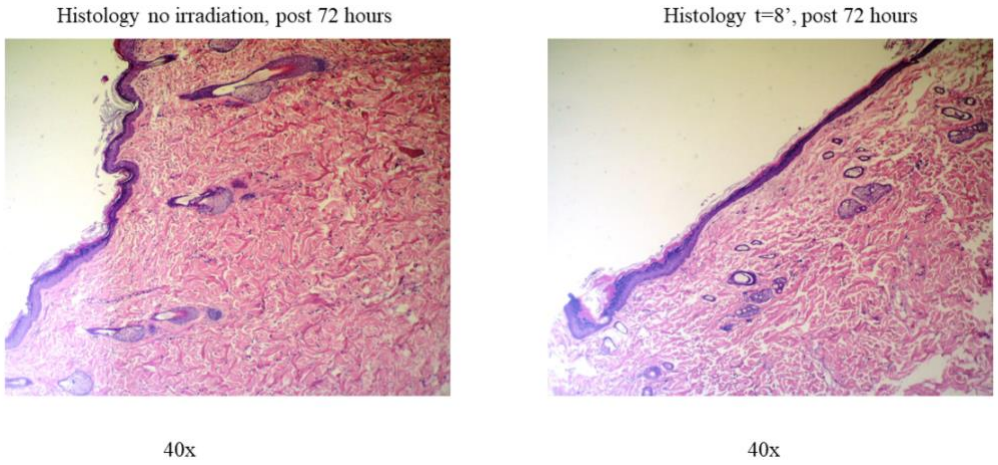

Figure 185: Histology of excised skin samples which were irradiated using 405 nm LED at 0.95 cm distance.

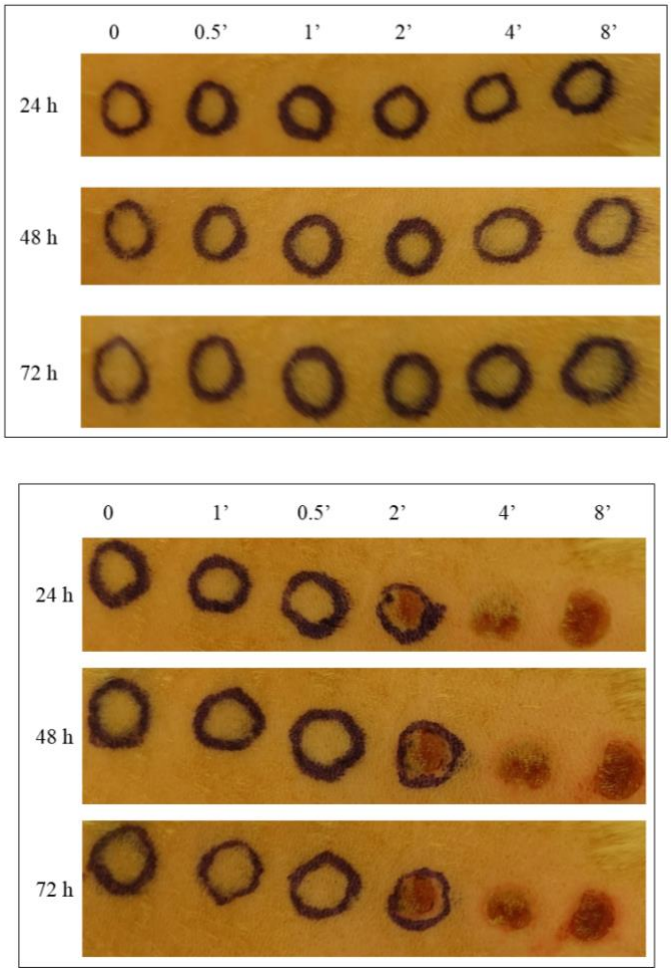

Figure 186: Pictures of irradiated skin spots which were irradiated using 405 nm LED at 0.96 cm distance (top) and at 0.63 cm distance (bottom) for different periods of time. The pictures were taken after 24h, 48h and 72 hours.

In-vivo studies with coumarin trimer material

Once the heating issues related to LED were resolved, and we saw insulin being released in *in-vitro* setting, we tried to repeat the *in-vivo* studies using second-generation coumarin material, and longer wavelength 405 nm LED. There were the following differences compared to the earlier setting when first-generation material was tested in Chapter 3 –

i. Here due to the small size of the particles as opposed resin particles, smaller size needle could be used. Hence, we used the 31G needle as opposed to a 27G needle.
ii. The wooden spacers were used to deal with the excess heat.
iii. The longer wavelength is being used here as mentioned.
iv. The rats were ordered from Harlan labs earlier, but the vendor was changed to Charles River.
v. All glucometers were brand new (Freestyle). Earlier, glucometers from One Touch were old.

Pilot studies

In the following *in-vivo* pilot study, a material containing 133 nmol of insulin suspended in 65 µL sterile PBS (which was filtered through 0.22 µm syringe filters) was injected using a 31G needle. After injecting the depot, 20 min period was given to see any signs of immediate leaching. Then 1 min irradiation was performed after 20 min post-injection and 24 hours as well. The aim was to see how active the depot is after 24 hours.

One minute of irradiation using the wooden spacers was good enough to cause a robust therapeutic response in an animal but did not cause any scabs due to overheating. Hence, we decided to use a one min duration. In previous studies, we failed to see any response after irradiation post-24-hour injection. However, we observed a better response here (Figure 187). The C_{max} after 24 hours was only 20% of the first irradiation when insulin concentrations were compared. The BG response was proportional to the insulin response in both cases. In this first irradiation, approximately 82% BG reduction was seen while in the second irradiation, 35% response was seen. The material was performing better compared to first-generation material.

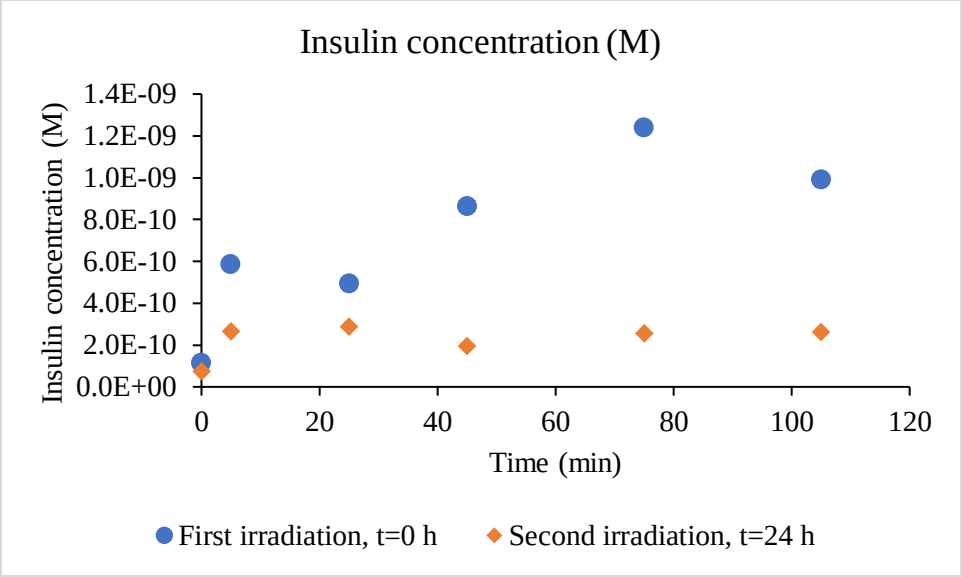

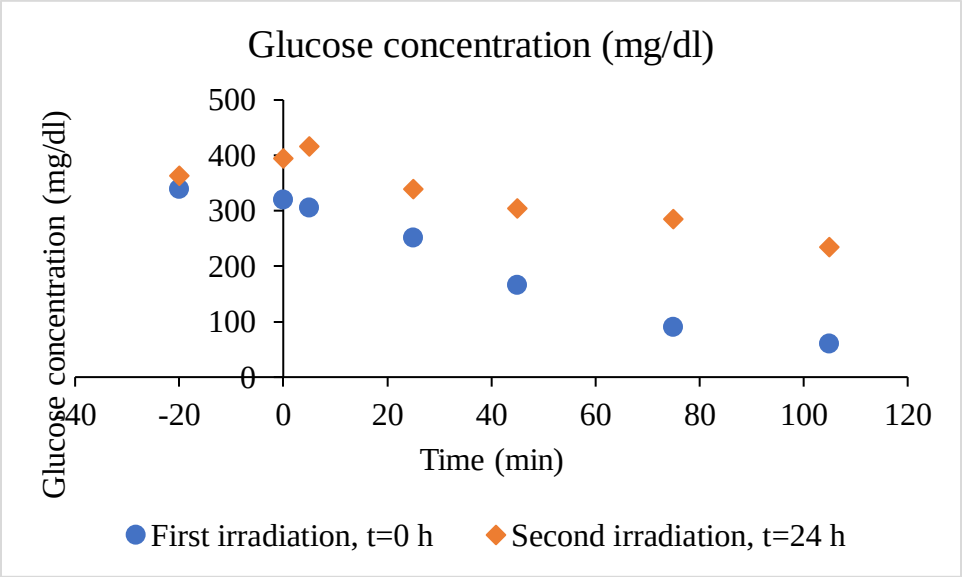

Figure 187: Comparison of results of irradiation performed at t=0 and t=24 hours. The top plot compares insulin released due to irradiation, and the bottom plot compares the reduction in blood glucose.

***In-vivo* studies in replicates**

The pilot studies were encouraging and based on the results, we decided to pursue animal studies in replicates. These were the parameters decided for performing the *in-vivo* studies.

i. The particles were small enough to pass through a 31G needle as demonstrated earlier. However, a 31G needle is quite thin and rat skin is hard. Sometimes the injection would be incomplete and there is a need to pull out the needle from the skin and re-inject at a nearby site. At this point, the needle became blunt and it couldn't be re-inserted into the skin. Due to this issue, we decided to use a 27G needle which is sturdier and could be reused.

ii. The wooden spacers were used to deal with the excess heat. The total distance between LED and skin was ≈ 0.95 cm.

iii. The rats were ordered from Harlan labs for the first-generation material, but the vendor was changed to Charles River.

iv. Instead of performing single irradiation for 1 minute at t=0, we decided to perform two irradiation – at t=0 and at t=65 min each for the duration of 30 seconds.

v. All glucometers were brand new (Freestyle®). For the first-generation material studies, glucometers from One Touch® were old.

vi. The diameter of the hole of the base plate was increased from 0.35 cm to 0.775 cm. The diameter of the injected depot was larger than 0.35 cm hole used for its irradiation. Hence, the depot was being irradiated incompletely. To correct this, the diameter was increased to ensure all depot material is being irradiated.

The results for the replicates are reported below in Figure 188. In one of the experimental

replicates, the final time point of t=125 was not measured. Although, that time point is statistically significant with a p-value of 0.003 with unequal sample size using the t-test, in the plot below, the rest of the values were plotted with an equal sample size of four. Hence the star symbol used for showing statistically significant points is removed from the plot. I have also plotted it after dropping a poor data set (Figure 189).

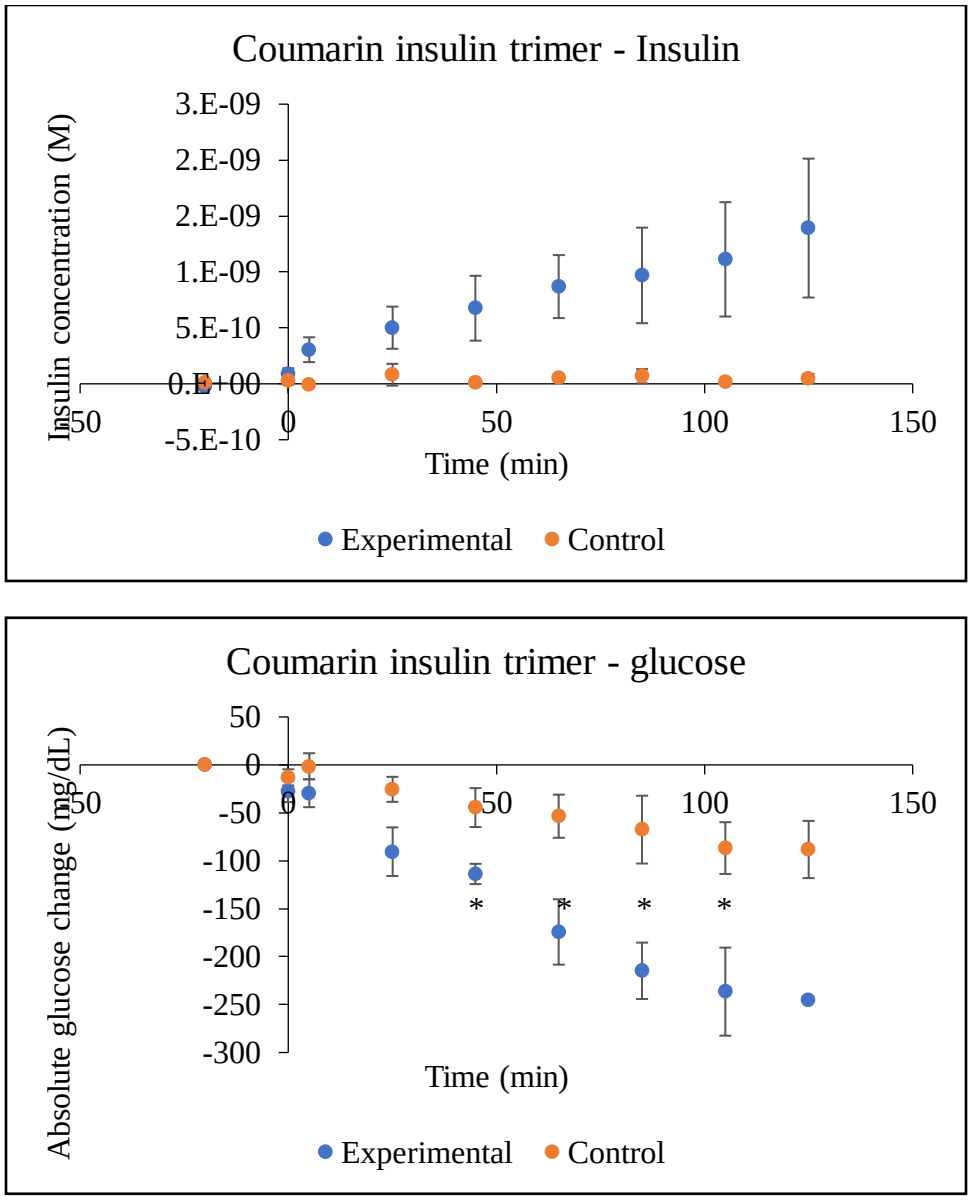

Figure 188: Average concentrations of insulin and glucose from *in-vivo* studies of coumarin insulin trimer (N=4). The irradiation was performed for 30 seconds each at t=0' and t=65'. The statistically significant points $p<0.05$ are shown by an asterisk.

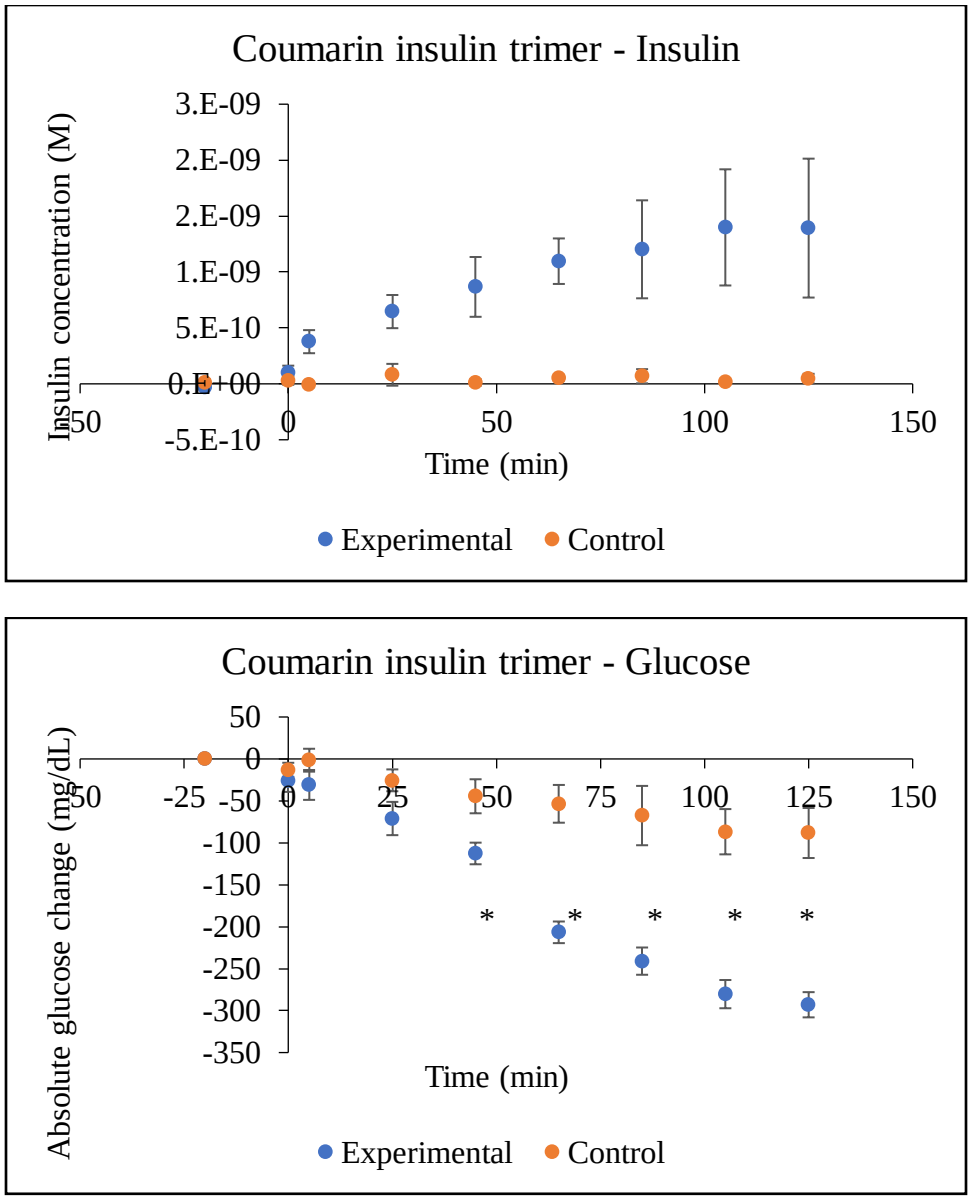

Figure 189: Average concentrations of insulin and glucose from *in-vivo* studies of coumarin insulin trimer (N=3, after dropping a poor data set). The irradiation was performed for 30 seconds each at t=0' and t=65'. The statistically significant points $p<0.05$ are shown by an asterisk.

The second-generation material was performing significantly better compared to first-generation material. The improvements are summarized below.

i. % w/w density of first-generation PAD material was 9% w/w. In the case of the trimer, it is increased to ≈ 87% w/w. This is an approximately 10-fold increase in

density. In the given loading of the depot, we can load 10 times more insulin at a given time.

ii. Calculation of energy being delivered for irradiation –

Table 11: Calculation for LED energy output in both studies

For first-generation materials	
Irradiation intensity at the skin	0.71 W/cm^2
Area irradiated circle pi*(.35cm)^2	0.385 cm^2
Duration of irradiation	240 seconds
Total energy 0.71 × 0.385 × 240	65.6 J
For second-generation materials	
Irradiation intensity at the skin	0.11 W/cm^2
Area irradiated circle pi*(.775cm)^2	1.88 cm^2
Duration of irradiation	60 seconds
Total energy 0.11 × 0.385 × 60	12.4 J

For the second-generation materials, the total energy that is being delivered at the depot size is 5.3-fold less compared to first-generation material.

iii. Calculations for the area under the curve –

We performed the calculations for measuring the area under the curve for insulin concentrations for first versus second-generation materials. The AUC is 6 times higher for second-generation material as opposed to first-generation.

Considering a six-fold increase in AUC and 5.3-fold decrease in total energy, we made an estimated improvement of 32-fold improvement in terms of energy and the amount of

insulin being released.

iv. The improvements mentioned above could be measured quantitively. However, there were other qualitative improvements as well. For example, the first gen material was challenging to inject using a 27G needle. However, the trimer particles which are of ≈ 3 µm size could be injected using 27G needle without any resistance or blockage. They also could be injected using a 31G needle which is used by diabetics for insulin administration without any issue.

v. Furthermore, 405 nm light is likely to have reduced phototoxicity compared to 365 nm light in the long-term. It is known that high energy UV radiation can cause DNA damage. It would be interesting to design experiments in the future to determine the extent of phototoxicity and DNA damage caused by the light of this wavelength in the cells.

Histology pictures

We performed histology of the injected depot site. The objective was to visualize the location of the depot. This would give us an idea about the diameter and the depth of injected material. It was challenging to visualize it using hematoxylin and eosin staining, hence Dr. Kover utilized anti-insulin antibodies to stain skin sections. As shown in Figure 190, the depot can be visualized using this staining technique. For this experiment, an injection holding ≈ 44 nmol of insulin in the form of coumarin insulin trimer was made. It resides just below the skin as expected. In the future, such studies could be carried out to follow the fate of injected materials for days, and whether the depot material is migrating away from the injected site.

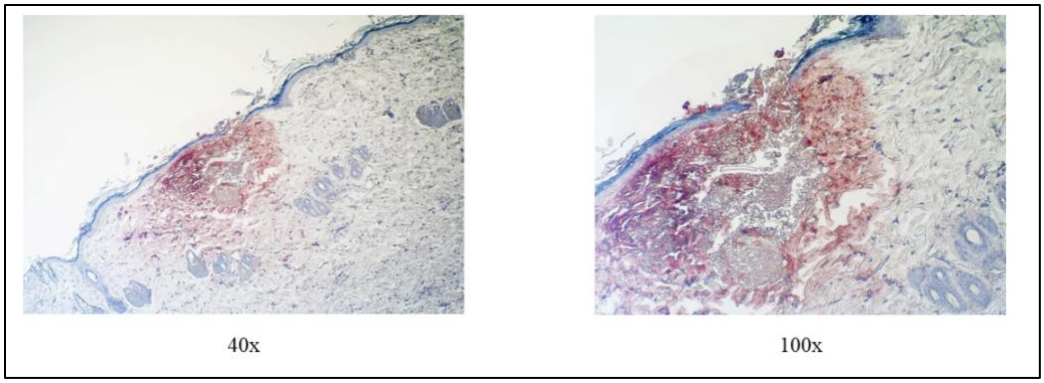

Figure 190: Histology of injected depot site.

In summary, we synthesized advanced material in this project which not only solved existing issues such as low density and injectability but also brought improvements such as faster, more insulin release and low phototoxicity. Furthermore, we demonstrated the efficacy in diabetic animal models. The efforts to improve the coumarin scaffolds have already been undertaken to make redshift the absorption spectrum and increase its quantum yield as demonstrated in this chapter (synthesis route # 3). It would be interesting to see how these newer scaffolds influence the insulin release kinetics *in-vivo*.

Chapter 5

LIGHT ACTIVATED SiRNA NANOPARTICLES

The RNA interference (RNAi) has revolutionized the understanding of the roles of smaller RNA molecules involved in controlling the expression of genes. The mechanism is prevalent in many animals and plants.[99] First reported by Fire et al. in *Caenorhabditis elegans* using microRNA (miRNA),[100] the tool is being widely used for controlling biology processes, phenotypes, identification of biological functions of genes and for the treatment of diseases using gene therapy.

There are mainly two types of RNA molecules involved in RNAi – short interfering RNA (siRNA) and microRNA (miRNA). It is said that 1-5% of the human genome code for miRNA and they all further regulate at least 30% of protein-coding genes.[101] miRNA are known to be associated with critical cellar processes and many diseases including cancer.[102] They provide additional control over the regulation of important pathways and offer fine-tuning through the RNAi machinery. Unlike miRNA, which is coded by the genome, siRNA are exogenous and can be introduced into the cell to trigger RNAi. Significant efforts are underway to develop siRNA-based therapeutics to silence harmful genes for the treatment of diseases like cancer and others.[103] The delivery and possibility of off-target effects remain the major obstacles for the development of such therapeutics in the clinical settings.[104]

Pathways for RNAi using both siRNA and miRNA have been discovered and well understood.[99] Although the biogenesis of miRNA is different from that of siRNA, many of the components overlap. As mentioned already, miRNA is encoded by the genome, then transcribed and released in the nucleus as pri-miRNA. These transcripts are up to 1000 nt

long and can be either single-stranded or double-stranded. The microprocessor complex trims pri-miRNA to yield precursor miRNA (pre-miRNA) in the nucleus which are 65-70 nt in length. Later, it is exported into the cytoplasm to bind to their complementary mRNA (Figure 191).

RNA interference

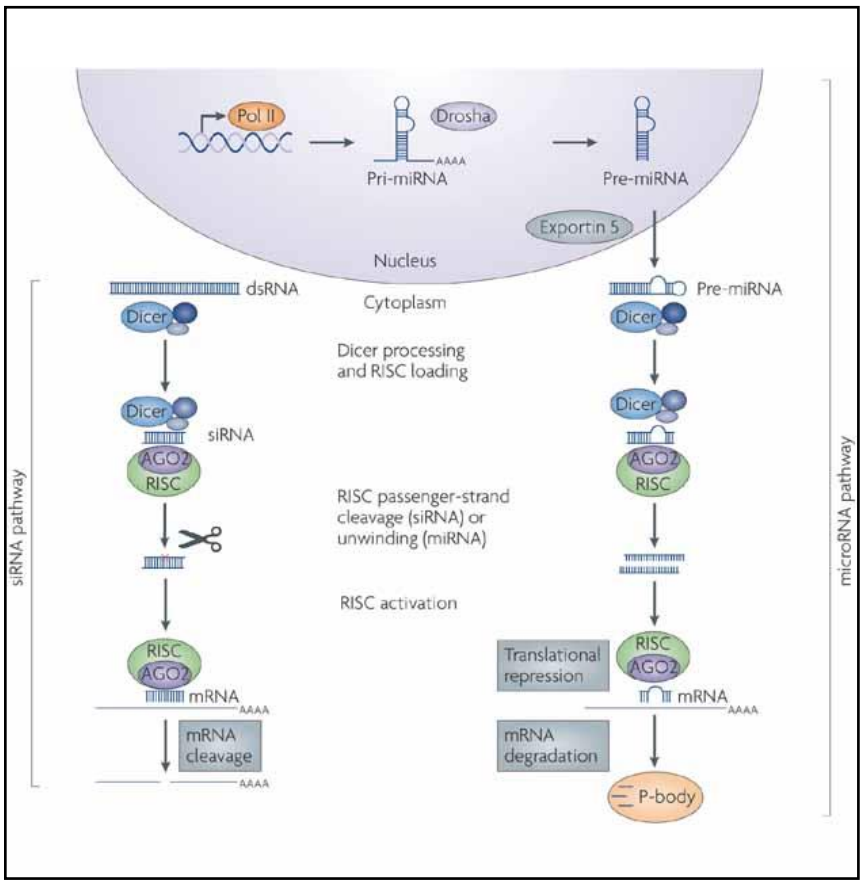

Figure 191: RNAi pathway. Reprinted by permission from Springer Nature.[105]

When miRNA is exported from the nucleus into cytoplasm or siRNA is transfected into the cellular cytoplasm, they both are cleaved by an enzyme named Dicer to excise into short miRNA or siRNA. siRNA is 21-25 nt in length with phosphates on all four termini. This siRNA binds to Argonaute protein which is complexed with other proteins. This assembly of proteins is called the RNA-induced silencing complex (RISC). One of the

strands from siRNA is selected as a guide strand which remains bound to Argonaute while other is discarded. RISC along with guide RNA scans the cytoplasm to bind to mRNA through complementary base pairing. The complementarity does not need to be 100%; the binding still occurs even if there are multiple mismatches. The position, number, and nature of mismatches dictate the silencing efficiency and off-target effects.[106] Upon binding to mRNA, Argonaute cleaves the target strand, silencing the expression of that gene. In some cases, RISC represses the translation to silence the gene expression. There are several attempts to control RNAi for a variety of applications. In our lab, it has been attempted using light.

Light Activated RNA Interference (LARI)

The Friedman lab has pioneered a technique of "light activated RNA interference" (LARI) to control RNAi using light. The concept involves caging siRNA using a photolabile group which renders it inactive and blocks RNAi temporarily by preventing it from binding to RISC. Upon light exposure, photolabile groups come off from siRNA. Now the uncaged siRNA is free to undergo RNAi and cause gene silencing. Using LARI, the spacing, timing, and degree of gene expression can be controlled. LARI has been demonstrated in our lab.[32–34] The schematic is shown in Figure 192.

First, siRNA must be caged with a photolabile group. In the initial experiments, DMNPE was used for caging siRNA. The diazo functionality on DMNPE diazo reacts with the terminal phosphates on siRNA to yield tetra-modified siRNA. Due to the presence of photolabile groups, siRNA fails to form a complex with RISC. Thus, RNAi gets suppressed. Upon exposure to light of a certain wavelength (365 nm in this case), the phosphoester bonds are broken, releasing free siRNA. Released siRNA then binds to RISC

and undergoes RNAi to alter gene expression.

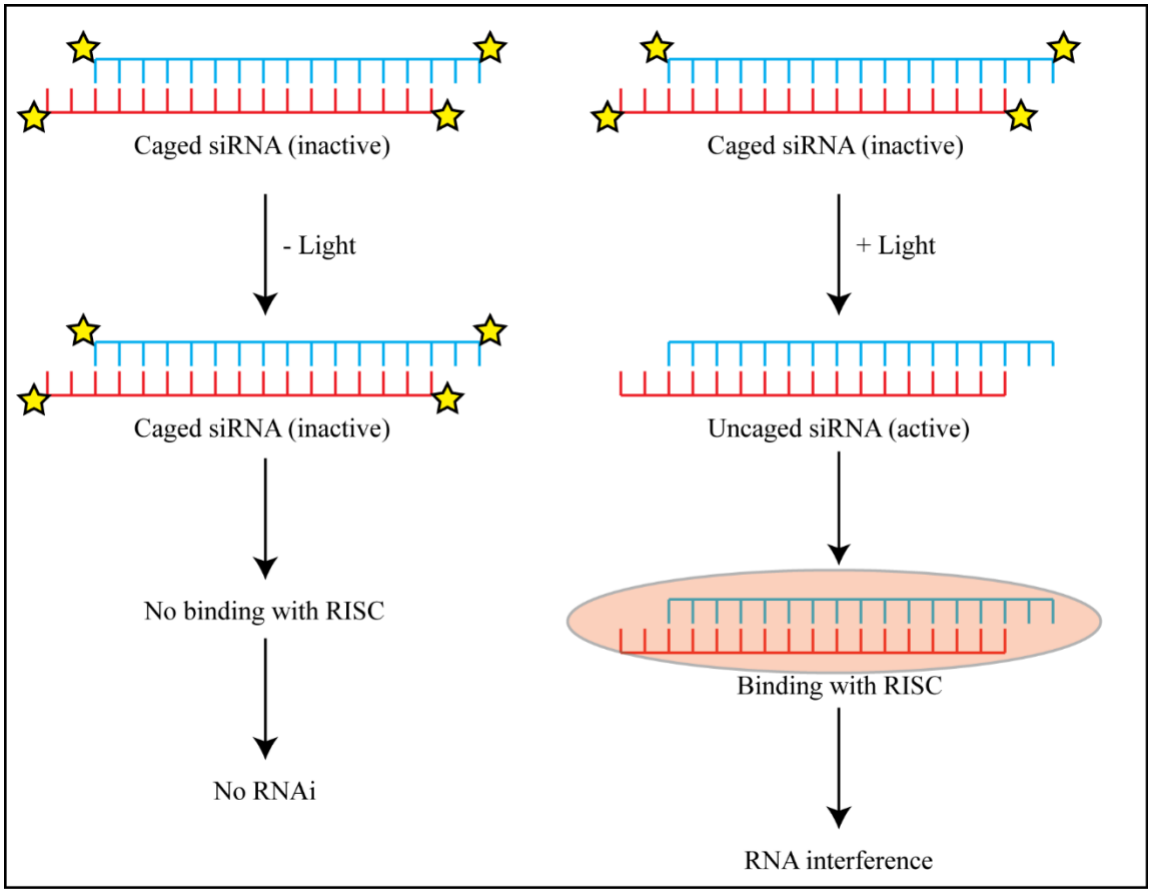

Figure 192: The concept of light activated RNA interference (LARI).

The nature of photolabile groups can be further modified to improve the efficiency of LARI and to increase its dynamic range in response to light. Light-cleavable nucleic acids which could be uncaged using light have been used in dissecting the roles of genes and proteins in understanding biology and to develop therapeutic interventions. In the past 10-15 years, there is substantial interest in developing and utilizing such tools. It has found applications in studying developmental biology,[107,108] micro-patterning of cells in cell culture,[35] therapeutic strategies,[109,110] and to deepen the understanding of cellular biology.[111]

Challenges in siRNA Delivery

Though RNAi is convenient, effective and easy to demonstrate in *in-vitro* cell culture-based studies using siRNA, it is challenging to show similar efficacy in animal models. For the cell culture studies, the major barriers are stability in the serum and permeability through the cell membrane. siRNA can be degraded rapidly by RNase present in the serum and due to its polar charged nature, it cannot cross the lipid bilayer on its own.[112] Using commercially available transfection reagents like Lipofectamine®, both issues can be solved; the formulation protects siRNA from degradation as well as helps it in crossing the lipid bilayer for cytosolic delivery. However, siRNA face host of other challenges *in-vivo*; i) instability against nucleases, ii) attack from the immune system, iii) renal clearance, iv) non-specific protein-binding, and v) inefficient cellular penetration.[113] There is no single solution to solve many of the problems described here hence the *in-vivo* delivery remains challenging. Many of the methods used for *in-vitro* studies are not feasible for *in-vivo* studies. This might be the reasons why there are difficulties in getting approval for siRNA based therapeutics by the FDA.[114,115] Keeping such challenges in mind, we started investigating other possible ways for delivery in the LARI approach.

Nanospheres for enhancing siRNA delivery for LARI applications

Nanospheres are extremely small spherical particles in size ranging from 40-1000 nm in diameter. Typically, their preparation procedures have been optimized to produce such spheres of uniform size across the batch. Both inorganic and organic materials based nanospheres are available commercially. Materials such as glass, polystyrene, polylactide, ceramic, alumina, dextran, poly(methyl methacrylate) (PMMA) are for preparation and

available in many different diameters. Biodegradable materials are also available. Depending on the material, nanosphere surface can be functionalized with either -NH_2 or -COOH groups to covalently conjugate other moieties on top of it. Because of these features, there is an interest in using nanospheres for the purposes of drug delivery.

One of the benefits of using nanospheres is their extremely small size. It is reported that these spheres have good penetrating properties in the cells. Some of the studies showing such evidence are listed in Table 12 below. The ability of cell internalization is seen for nanospheres ranging widely in their size, material, nature of the charge of its surface (cationic or anionic), and tested in different cell lines, etc.

Table 12: Studies demonstrating evidence for internalization of nanospheres into different cell lines.

Author	Size and material	Cell lines	Conclusions
Rejman J. et al.[116]	Fluorescent latex beads (50, 100, 200, 500, 1000 nm)	B16 cells	Beads < 200 nm – Clathrin-mediated endocytosis. Beads > 200 nm – Caveolae-mediated endocytosis.
Santos et al.[117]	Fluorescent –COOH polystyrene (40 – 2000 nm)	HeLa, A549, 1321N1, HCMEC D3, RAW 264.7	Uptake observed of all particles in all cell lines to varying degrees.
Smith et al.[118]	Fluorescent 20 nm – -COOH polystyrene	HeLa, MDCK	Clathrin but not caveolar-mediated endocytosis observed + passive diffusion to some extent. Presence of serum retards uptake.
Ekkapngpisit et al.[119,120]	30 nm –COOH polystyrene 50 nm – NH_2 polystyrene	Ovarian NIH-OVCAR3, SKOV-3 cancer cells	30 nm beads – Not toxicity, no lysosomal localization observed. 50 nm – Toxicity and lysosomal localization observed. Uptake via a caveolae-independent pathway.

Table continued

Author	Size and material	Cell lines	Conclusions
Lai et al.[121]	24, 43 nm –COOH PS	HeLa, HUVEC	43 nm beads – Clathrin-mediated uptake observed. 24 nm beads uptake through non-clathrin, non-caveolae, cholesterol independent pathway. The novel mechanism which doesn't involve endo/lysosomal route and delivery to the perinuclear region.
Lorenz M. R. et al.[122]	168, 206, 337, 489, 1290 nm $–NH_2$ polystyrene	HeLa, MSC (stem cells), Jurkat, KG1a	Uptake is seen without the use of transfection reagent into HeLa, MSC cells. Particles were accumulated in compartments resembling endosomes, cytoplasmic localization wasn't clear.
Musyanovych et al.[123]	80-150 nm PCL, PLLA, PLGA beads	HeLa, Jurkat	The presence of surfactant on particle like SDS has a greater influence than size. PLLA and PCL particles were endocytosed much faster than polystyrene particles.

Table continued

Author	Size and material	Cell lines	Conclusions
Liu et al.[124]	50, 100, 500 nm polystyrene both –COOH and -NH_2 beads	HeLa, NIH 3T3	Uptake was observed with both –COOH and -NH_2 beads. No cytotoxicity observed for –COOH beads. -NH_2 beads showed toxicity by delaying G1 phase and decreasing cyclin expression.
S. Prabha et al.[125]	70 nm, 202 nm PLGA particles encapsulate with a plasmid for transfection	COS-7 cells, HEL293 cells	70 nm sized particles showed a higher level of transfection than 202 nm particles.
Y. Patil et al.[126]	PLGA-PEI encapsulated siRNA - 230±8 nm	MDA-kb2	Addition of cationic PEI in PLGA particles increased the capacity of siRNA encapsulation and its release profile Delivered siRNA in the cytoplasm Particles are serum-stable and no toxicity was observed

Table continued

Author	Size and material	Cell lines	Conclusions
K. Tahara et al.[127]	Chitosan surface modified PLGA NS encapsulated siRNA – 300 nm	A549 cells	Chitosan modification improved delivery profile over plain PLGA nanoparticles and naked siRNA

The features describe above allow flexibility in selecting the system; the size of nanospheres, the material (biodegradable vs non-biodegradable), surface functionality (-COOH vs -NH_2), etc., hence we selected nanospheres for LARI.

The approach here involved conjugating caged siRNA to the surface of nanospheres. This delivery system would have the following advantages –

i. Since the nanospheres have excellent cell penetration properties, it would carry siRNA along with it. This would be important for *in-vivo* studies where traditional transfection reagents have limited efficacy in siRNA delivery.

ii. The entire construct would be very dense and compact. This might render siRNA more resistant towards nucleases due to the steric hindrance.

iii. The LARI as a tool can be applied for an *in-vivo* system using this system.

We describe the route for conjugating caged siRNA to a nanosphere. The reagents used here are the same that were used in the insulin project to immobilize insulin on the solid phase resin. Click chemistry reagents like DBCO can be coupled to the surface with EDC, HOBt chemistry on nanospheres. siRNA can be caged with DDA to synthesize dimod caged siRNA where two azide functionalities will be on each side of siRNA. Upon reacting azide caged siRNA with DBCO conjugated nanospheres, both strands will be

conjugated covalently through the triazole ring. Due to the property of the nanospheres, siRNA will be carried into the cell. In the cells, upon photolysis, siRNA will be uncaged and photoreleased as native siRNA to cause RNAi. The synthesis of individual components is discussed shown in Figure 193 and discussed below. In the future for the purpose of *in-vivo* studies, biodegradable nanospheres should be used which would be degraded and eliminated from the body. Polylactic-co-glycolic acid (PLGA) seems reasonable for such applications and PLGA nanospheres are commercially available.[128]

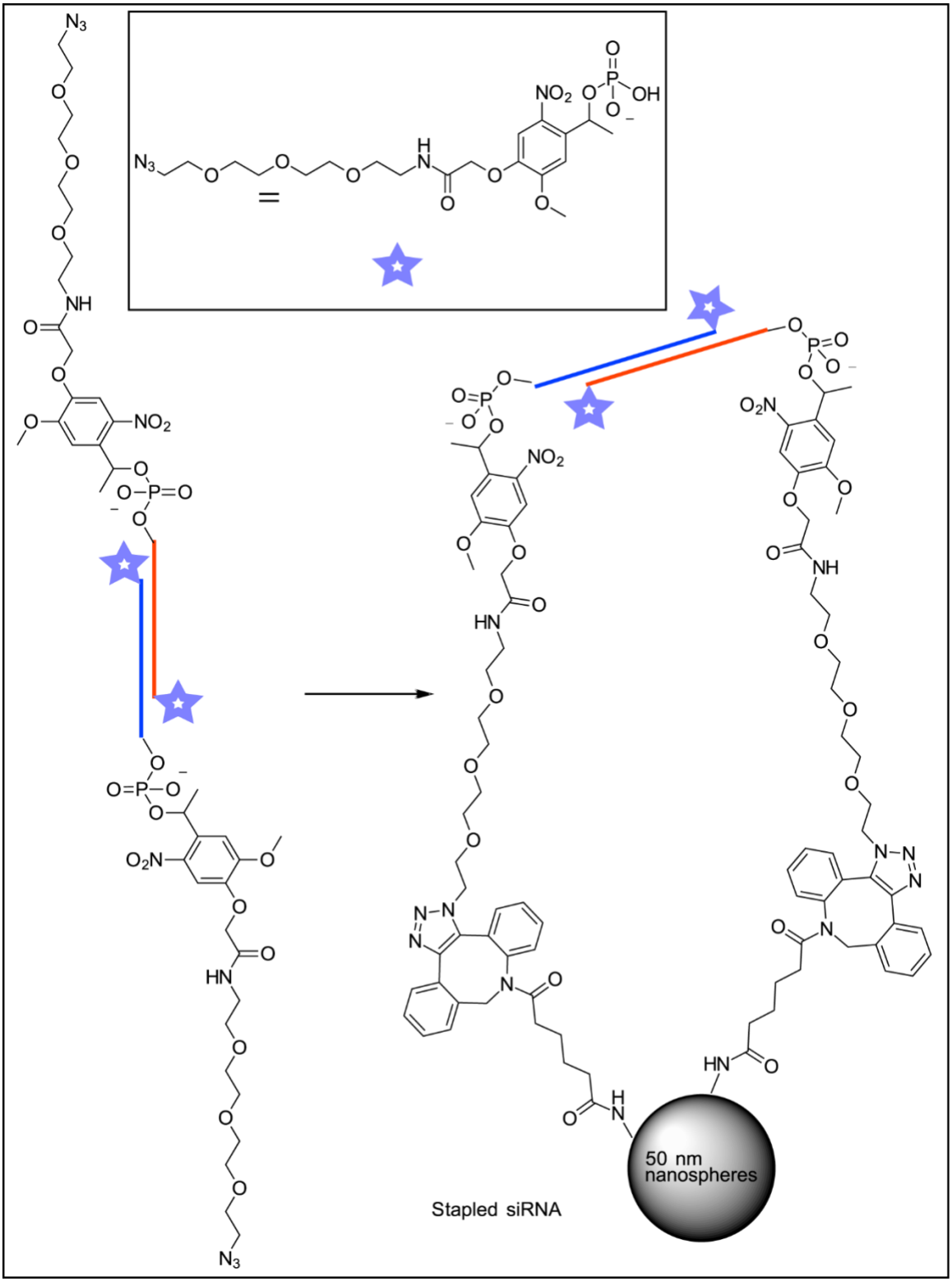

Figure 193: Stapling of caged siRNA on the nanosphere surface.

Cellular uptake of 43 nm nanospheres

Nanospheres were ordered from Polyscience (catalog # 19773-10). The pilot experiment was performed to see if the nanospheres have cell-penetrating ability or not. The nanospheres contained a fluorophore for visualization. In this experiment, the particles were incubated when HeLa cells were at 70% confluency. The concentration of particles was 0 and 200 µg/mL in a 96-well plate. The cells were washed twice using PBS prior to taking images. The images were taken after 27-28 hours after incubation with nanospheres in Dr. Kun Cheng's lab. Both bright-field and fluorescence images were captured (Figure 194).

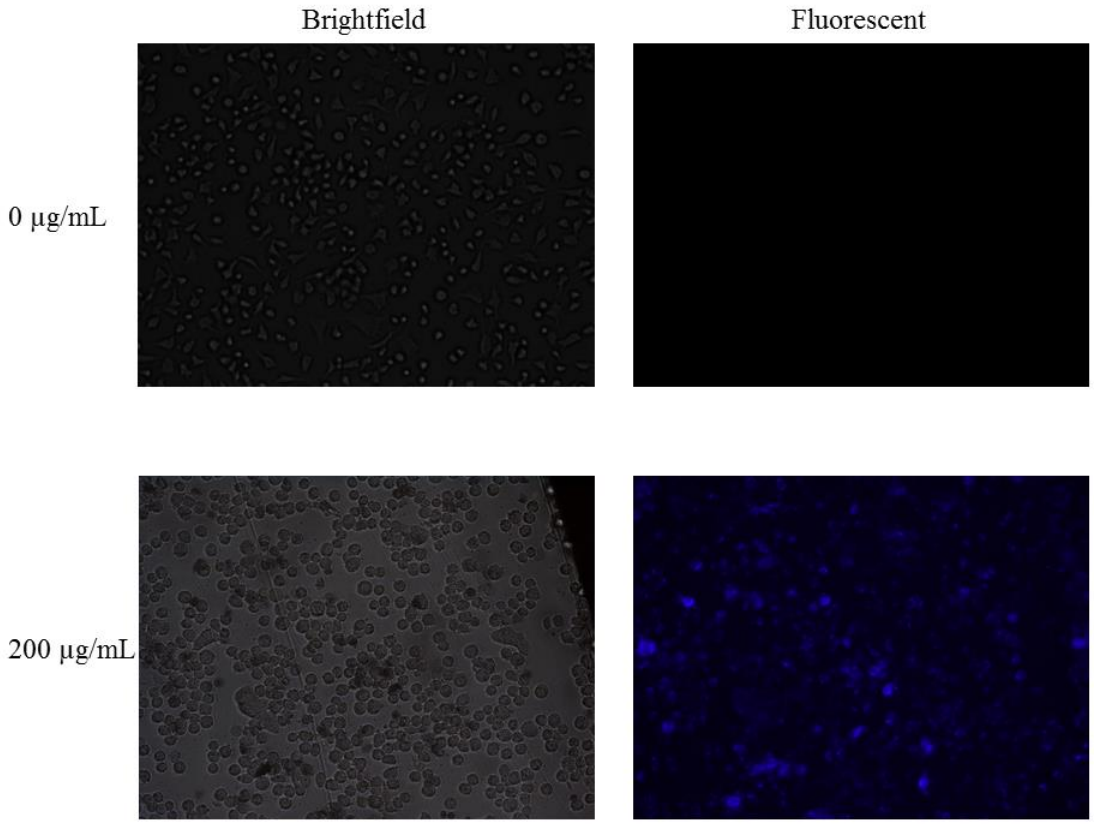

Figure 194: The cellular internalization study of 43 nm nanospheres. The fluorescent can be visualized in cells when incubated at 200 µg/mL concentration.

The experiment was repeated, and very similar results were observed. The exact location of the nanospheres in the cell could be determined using the confocal microscopy i.e. how and where the nanospheres are getting distributed in the cells? Though the images suggest the presence of nanospheres in cells, it left important questions unanswered. 1) Whether the particles are stuck on the outer membrane or inside the cells? 2) Are the nanospheres specifically localized to one more cell organelle or uniformly distributed inside the cells? 3) How much % of the total particles can make it inside? 4) Is there any toxicity due to these particles? Does it affect cell viability? etc. Next, we worked on immobilizing siRNA onto the nanospheres.

Synthesis of dimod caged siRNA

The protocol for caging siRNA was followed as reported.[129] GFP silencing siRNA was used, the sequence is reported in the literature published from the lab previously. 17.83 nmol of each strand of GFP siRNA were mixed to anneal them in Tris-EDTA buffer. (5.57 µmol) N-(2-{2-[2-(2-Azido-ethoxy)-ethoxy]-ethoxy}-ethyl)-2-[4-(1-hydrazono-ethyl)-2-methoxy-5-nitro-phenoxy]-acetamide was added in 48 µL DMSO + 13.45 mg MnO_2 and vortexed for 45 min in the dark. Then it was filtered through celite to remove MnO_2 particles and washed with additional DMSO to wash off unfiltered diazo. Annealed siRNA and diazo were mixed at 25.2 µM and 6.3 mM concentration respectively. The ratio of water: DMSO was 2:1 in the final reaction mixture. The reaction was kept at room temperature for 80 min and divided into 2 equal parts. In each tube, 85 µL 10 M ammonium acetate, 5 µL glycogen (20 mg/ mL) and 0.65 mL ethanol was added. It was incubated in -20 °C freezer overnight. The siRNA pellet was isolated using centrifugation and caged siRNA was purified by HPLC as described in the protocol. The mass spectrum of purified

dimod siRNA is shown in Figure 195 presentation two peaks of caged sense and antisense strand.

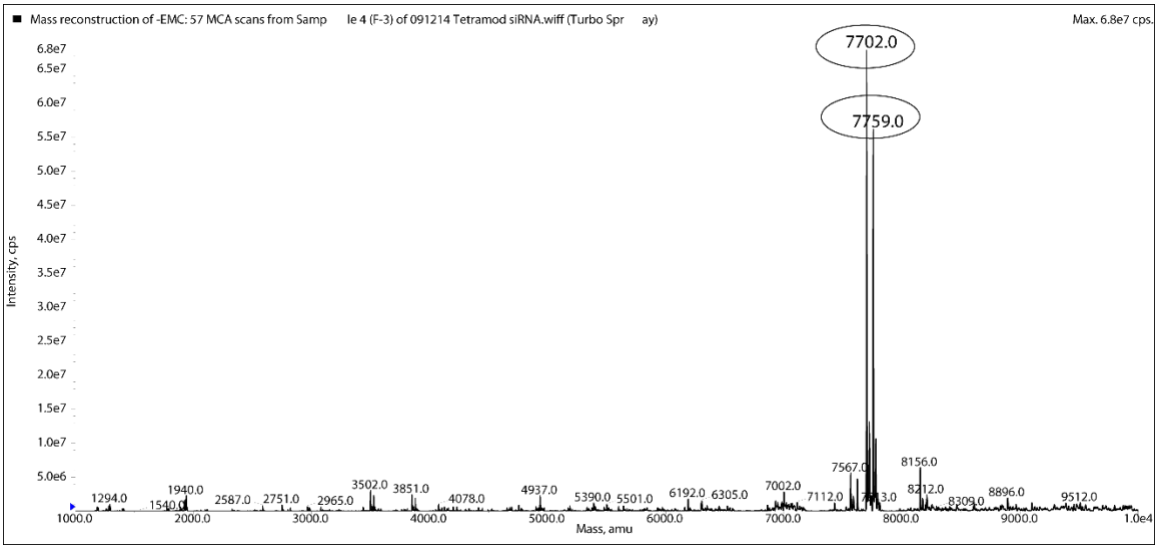

Figure 195: MS of purified dimod siRNA showing each sense and antisense strands modified.

Clicking caged siRNA on nanospheres surfaces

The first step involved conjugating DBCO amine to the nanosphere surface. Because the nanospheres were made from uncrosslinked polystyrene, organic solvents like DMF or NMP could not be used as such solvents would dissolve the nanospheres. Hence the coupling was performed in water under four different conditions using water-soluble coupling agents like EDC, NHS, and sulfo-NHS. The following protocol was followed –

i. Add 0.15 mL 43 nm particle solution in 1.6 mL of 50 mM MES buffer, pH=5.5

ii. Add DBCO amine (1.6 mg, 5.8 µmol) and Triton X-100 at 0.05% concentration.

iii. From this mixture, 436 µL was removed for control.

iv. To the remaining mixture, EDC (4.5 mg, 23 µmol) was added. This was then divided into three tubes of 436 µL.

v. To one tube, only EDC was used for coupling. In the third tube, NHS (3.0 mg, 26

µmol) was added. In the fourth tube, sulfo-NHS (5.0 mg, 23 µmol) was added.

vi. pH was adjusted to 6.5 in all four tubes.

vii. After the overnight reaction, the samples were dialyzed against DI water extensively.

5 µL were taken from all 4 reaction mixtures and mixed with 1 µL of 30 µM caged siRNA solution. The reaction was performed overnight at room temperature and analyzed by PAGE. The nanospheres don't run on PAGE gel as it all gets stuck at the loading site. siRNA however ran, and the bands were visualized using EtBr staining. If siRNA is clicked on the beads, it shouldn't be free and hence shouldn't appear on the gel.

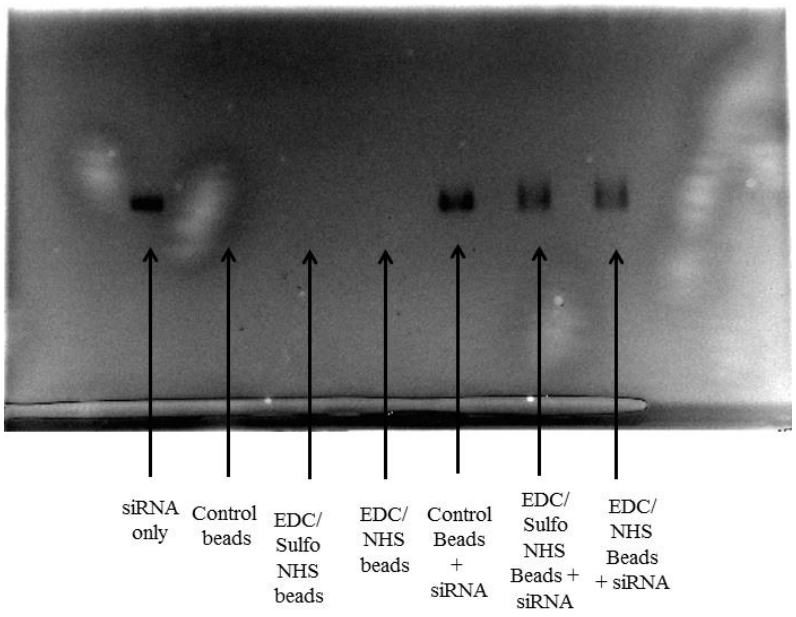

Figure 196: The PAGE analysis of reaction between DBCO conjugated nanospheres and azido caged siRNA.

The gel results were mixed and did not confirm whether the reaction is occurring or measure the reaction yield (Figure 196). The siRNA bands look slightly fainter and diffused than control siRNA band, however, the results were ambiguous and not

encouraging. Because of this lack of confirmation of conjugation and the nanospheres were so tedious to work with, this approach was suspended here.

Preparation of siRNA nanoparticles

Because the reactions with nanospheres were challenging and there was no way to characterize the extent of reactions due to lack of Rink amide linker, another approach was investigated. The concept is to cross-link caged siRNA to make compact siRNA nanoparticles (Figure 197). This siRNA will be caged using photolabile group. When light is irradiated, the nanoparticles will fall apart releasing uncaged siRNA.

The procedure for caging siRNA was very much like what we reported earlier.[129] GFP silencing siRNA was used. 10 nmol of each strand of GFP siRNA were mixed to anneal those together in Tris-EDA buffer. (4.0 mg, 8.3 µmol) N-(2-{2-[2-(2-azido-ethoxy)-ethoxy]-ethoxy}-ethyl)-2-[4-(1-hydrazono-ethyl)-2-methoxy-5-nitro-phenoxy]-acetamide was added in 50 µL DMSO + 20 mg MnO_2 and vortexed for 45 min in the dark. Then it was filtered through celite to remove MnO_2 particles and washed with an additional 0.15 mL DMSO to wash off unfiltered diazo. The concentration of diazo in the filtrate was 38.6 mM as determined using UV-vis spectroscopy. Annealed siRNA and diazo were mixed at 25.8 µM and 6.45 mM concentration respectively. The ratio of water: DMSO was 2:1 in the final reaction mixture. The reaction was kept at room temperature for 80 min and divided into 2 equal parts. In each tube, 82.5 µL 10 M ammonium acetate, 5 µL glycogen and 0.63 mL ethanol was added. It was incubated in -20 °C freezer overnight. siRNA pellet was isolated using centrifugation and caged siRNA was purified by HPLC as described in the protocol (Figure 198).

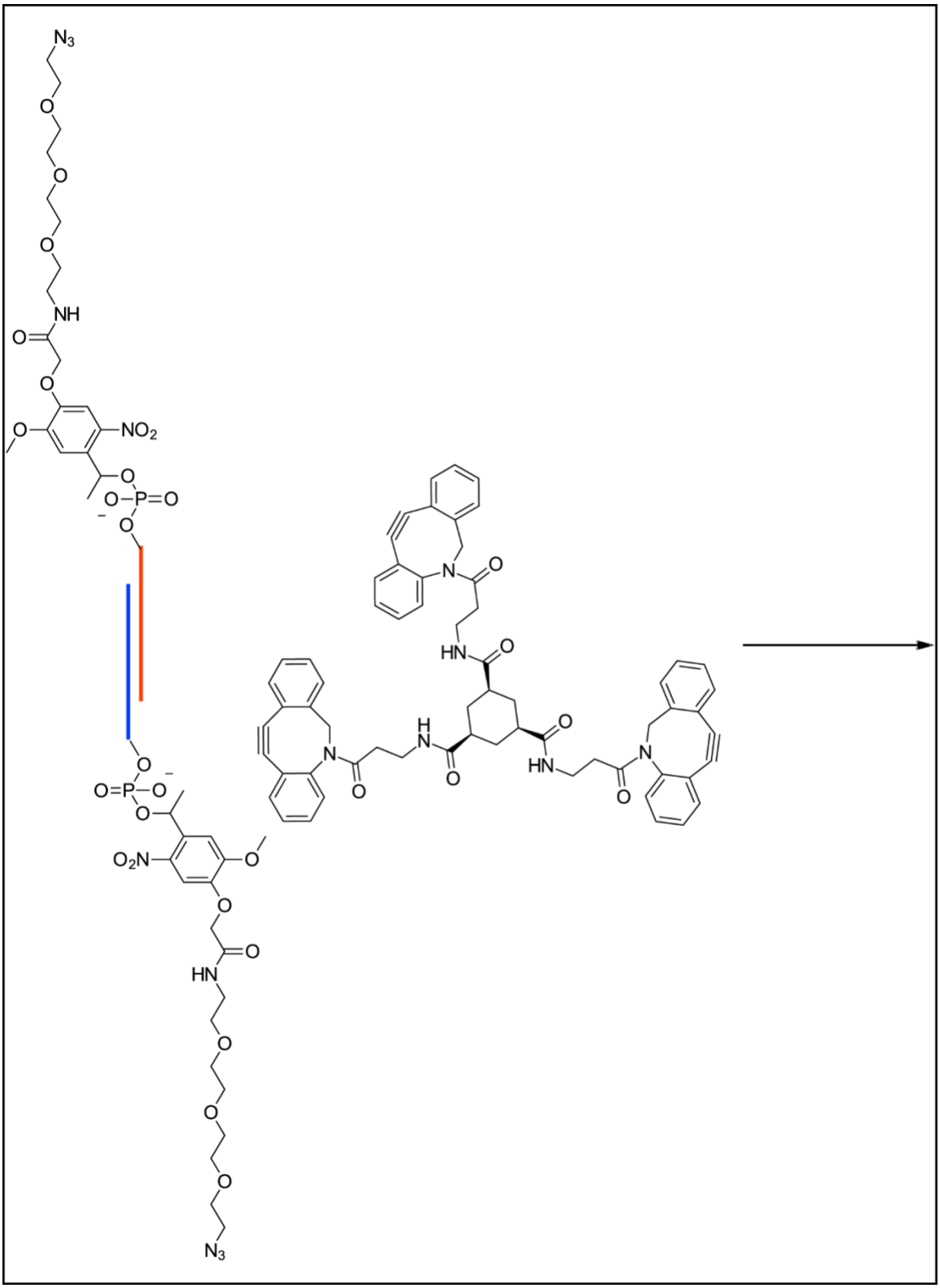

Figure 197: The reaction between dimod caged siRNA and TDL2. Upon multiple intermolecular click reactions, cross-linked siRNA nanoparticles could be formed.

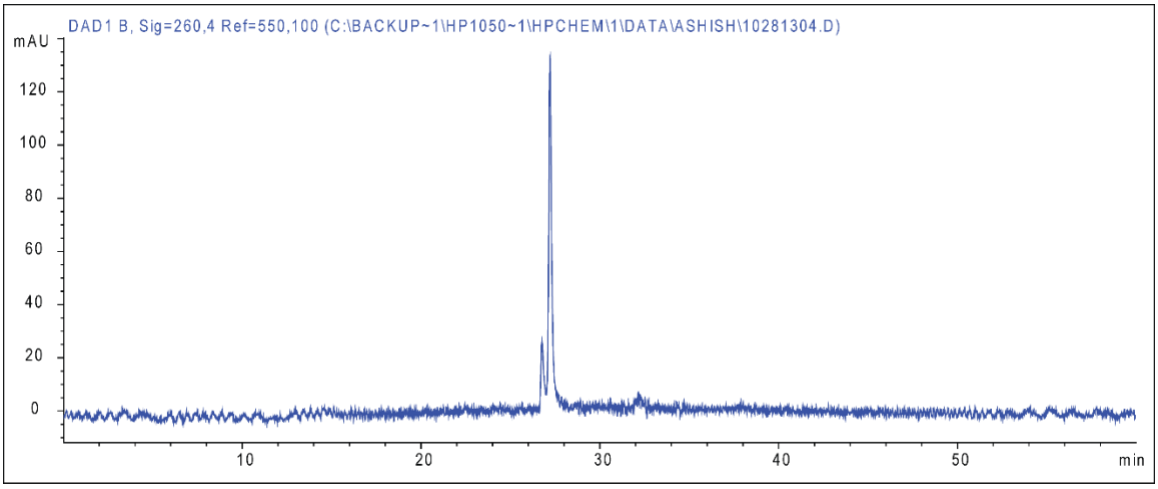

Figure 198: Analytical HPLC of purified dimod caged siRNA.

The synthesis of TD linker # 2 was reported in earlier chapters and published as well.[130] The reaction between caged siRNA and TDL2 was set up by keeping their concentration at 0.16 mM and 0.106 mM respectively in 2:1 mixture of DMSO: water. We monitored the reaction progress every few days. In Figure 199 (below), a gel of reaction mixture after 22 days of incubation is shown.

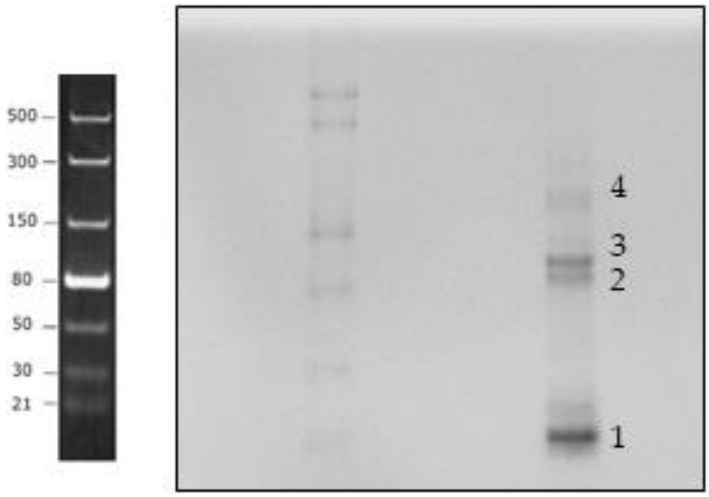

Figure 199: Analysis of higher MW siRNA nanoparticles using gel. Lane 1 shows the MW markers, lane 2 shows the crude mixture of azide caged siRNA + TD linker after 22 days of reaction. Band 1 is unreacted caged siRNA and 2, 3 and 4 are cross-linked siRNA nanoparticles.

The gel results were encouraging on the third day after the reaction; many new higher MW bands were observed which most likely resulted from the cross-linking. The number of moles was too low to perform mass spectrometry analysis. The reaction was continued until 7 days and analyzed later in the same manner. The number of total bands reduced on day 7, the reason is not yet clear. Perhaps the nanoparticles assumed the shape of a tetrahedron or a cube where the edges will be made up of TD linker # 2 and sides will be siRNA. We also photolyzed these formed particles and they underwent uncaging to release native siRNA (data not shown).

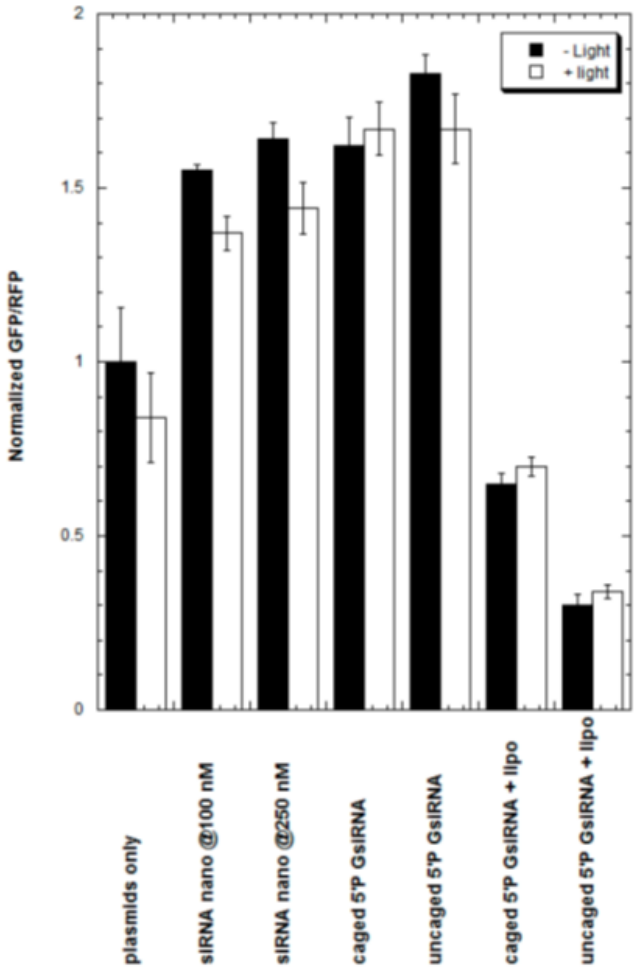

Figure 200: Testing the efficiency of light-activated siRNA nanoparticles in HeLa cells without any transfection reagent.

The materials were tested by Ashish who was collaborating on this project for LARI in the cell culture model using HeLa cells. We were also hoping that the nanoparticles would have cell penetration properties but no response to the GFP signal was observed after incubation and light exposure. No further experiments were performed to troubleshoot this.

Chapter 6

INTRACELLULAR PROTEIN DELIVERY USING PROTEIN PRODRUGS

Introduction and rationale

Development of recombinant DNA technology played a pivotal role in the way protein or peptide-based therapeutics were designed and mass produced. Since the approval of recombinant insulin for the treatment of diabetes in the 1980s, ninety-one protein-based therapeutics have been approved by the FDA.[131] Protein-based therapeutics have advantages over small molecular drugs due to their complex structure and very specific functions. Proteins can be utilized for performing sophisticated roles that small molecules cannot perform. For example, gene editing by CRISPR-cas9. Also, the time required for approval by the FDA is relatively short for proteins as compared to small molecule drugs. On average, protein-based therapeutics take approximately one year less in an approval process.[132] These therapeutics can further be classified broadly as enzymes or hormones e.g., insulin for the treatment of diabetes; antibodies for targeting for such as Trastuzumab for breast cancer therapy, vaccines (cancer vaccines are under developments), etc.

Most of these developed protein therapeutics have extracellular targets. Intracellular delivery remains a big challenge. Small molecules can cross the cell membrane either by active or passive diffusion. Due to the larger size of proteins, it is much more challenging for it to cross the lipid bilayer and make it into the cellular environment. Several strategies have been investigated to deliver macromolecules intracellularly. Some of the strategies can only be utilized for *in-vitro* studies and are impractical for *in-vivo* use. For example, microneedle or electroporation. These are very useful to demonstrate proof

of concept or to study the mechanism of action of a therapeutic. However, their translation from *in-vitro* studies to *in-vivo* studies in rat/mouse has been challenging. Hence there is an urgent need for the development of delivery methods for clinical settings. Intracellular protein delivery could be useful to restore the functions of defective proteins and could be utilized in regenerative medicine, cancer therapy, and intracellular organelle-specific imaging, etc. Below are the few most commonly used methods for the intracellular delivery of proteins.

1. Cell-penetrating peptides (CPP)

One of the earliest discovered CPP was Tat peptide derived from HIV-1 Tat protein.[133] The peptide was found to have excellent cell penetration properties. CPPs are also known as protein transduction domains (PTD). CPPs are rich in positively charged amino acid residues such as arginine, lysine. Positive charges are essential for its cell-penetrating ability. The cell membrane is negatively charged due to the presence of phosphates, sulfates, and carboxylates, etc. Arginine-rich peptide exploits electrostatic interactions to bind tightly to the cell surface due to its cationic nature.[134] The hydrophobicity and secondary structure of the peptide also influence the uptake.[135] By covalently conjugating CPPs with any protein, proteins as large as 120 kDa have been delivered inside the cell.[136] Along with proteins, CPPs are also shown to carry siRNA, antisense oligonucleotides, plasmids, various nanoparticles and fluorescent probes such as quantum dots inside the cells which would otherwise have poor cell-penetrating property on their own. Various mechanisms have been proposed. However, it is not yet obvious what exactly drives it. Table 13 below lists some of widely used CPPs.

Table 13: List of some commonly used CPPs with their sequences.

Peptide name	Peptide sequence	Peptide length
Oligoarginine	RRRRRRRRR	8-15
Penetratin	RQIKIWFQNRRMKWKK	16
Transportan 10	AGYLLGKINLKALAALAKKIL-amide	21
HIV-Tat	YGRKKRRQRRR	11
Transport	GWTLNSAGYLLGKINLKALAALAKKIL	27
VP-22	DAATATRGRSAASRPTERPRARARSASRPRRPVD	34

Although the exact mechanism of CPP is yet unclear, the following mechanisms have been proposed with some evidence.

i. Direct penetration

Direct penetration is an energy-independent process and doesn't need any specific transporters or receptors for internalization. Models such as the inverted micelle model, toroidal pore model, and carpet model (refer to Figure 201), etc. have been investigated.[137,138] Due to the cationic nature of CPPs, they interact and bind with negatively charged moieties like sulfates, phosphates present on the lipid bilayer. After these initial interactions, the peptides are probably internalized through the lipid membrane destabilizing followed by penetration through it. This mechanism dominates when the peptide is present in high concentrations.

ii. Endocytosis

Other than direct translocation, endocytosis is deemed as another pathway for CPP internalization. Cell internalization includes two mechanisms; phagocytosis which involves engulfing particles and pinocytosis which involves uptake of liquids. Pinocytosis could be achieved via these three mechanisms; Clathrin or caveolin-dependent, Clathrin or caveolin-independent, and macropinocytosis, etc.[138] Some of the studies have observed that CPP internalization takes place even at 4 ºC, the temperature at which the receptor-mediated endocytosis would slow down.[139] Because of this, there was a debate which pathway is being utilized by CPPs for penetration. However, with the use of modern techniques, it is being understood that endocytosis is the major pathway. Peptide sequences, concentration and the composition of lipids play important roles as well.

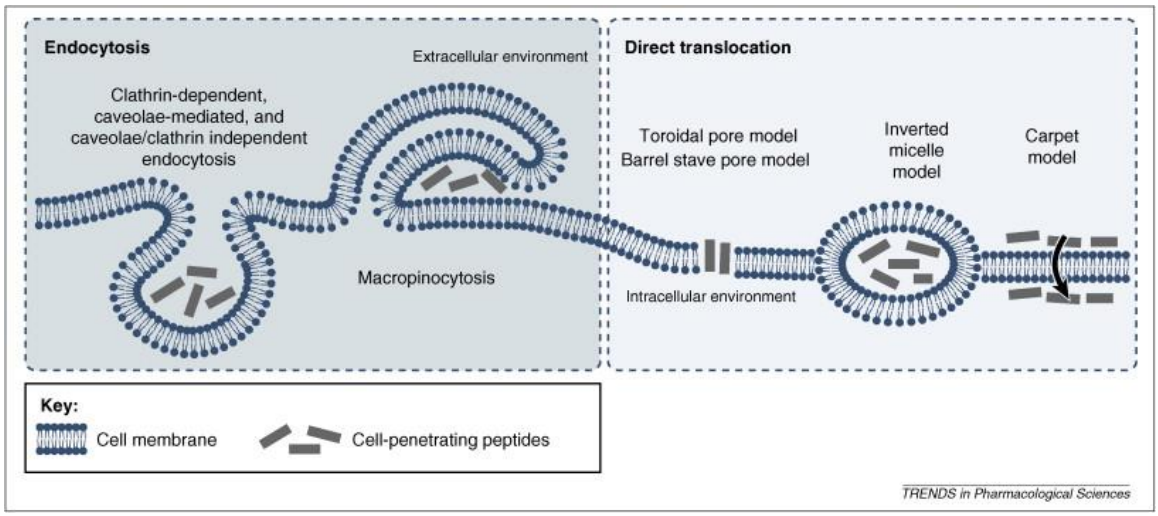

Figure 201: Various proposed mechanisms of internalization of CPPs. Reprinted with permission from Elsevier.[140]

Another unclear aspect of this proposed route is the escape of cargo from the endosome. Once the load is internalized in the endosome, it must be released from the endosome into the cytosol. Otherwise, endosomes mature into lysosomes and degradation might occur in

an acidic environment of the lysozyme or endosomes get recycled with membrane components and cleared from the cellular environment. CPP, when conjugated with fluorophores, delivered intracellularly show localization in the endosomes, not all of it reaches the cytosol. However, with the help of endosome disrupting strategy, cytosolic delivery is often improved. Thus, endosomal escape remains a barrier for the delivery.[141] Hence endosomatic strategies are often incorporated with CPPs to enhance the cytosolic delivery.

2. Nanoparticles

Protein delivery using nanoparticles is a broad field, and it includes cationic lipid-based systems, inorganic nanoparticles, modified proteins nanocarriers, etc. There is significant interest in the development of nanoparticulate formulations because –

i. The nanoparticles can be multifunctional. Due to this, moieties which reduce its immunogenicity, increase its circulation time, facilitate endosomal escape, enhance target-specificity could be included. Furthermore, imaging functionalities can also be included. Thus, the nanoparticles offer much flexibility in the design aspect. While preparing the nanoparticle, factors such as size, shape, zeta potential can be fine-tuned to achieve greater delivery efficiency.

ii. Due to the larger overall size compared to the protein, it can bypass renal clearance and have larger circulation time in the body.

iii. Proteins can be shielded by the nanoparticles by localizing in the inner core of particles to prevent it from degradation.

The existing systems could be further classified into four categories as follows.[142]

1. Cationic lipid-based systems

i. Dioctadecylglycylspermine

ii. BioPORTER which is commercially available

2. Inorganic systems

i. Quantum dots

ii. Gold nanoparticles

iii. Mesoporous silica nanoparticles

iv. Magnetic nanoparticles

v. Single-walled carbon nanotubes

3. Polymer-based systems

i. pH-sensitive systems

ii. PEI based systems

iii. Self-assembling cationic nano gels

4. Protein-based systems

i. Supercharged proteins

ii. Protein nanocapsules

Our approach to solving the problem of protein delivery would fall under the category of the protein-based system as per the above classification.

Preparation of protein prodrugs

Prodrugs are chemically modified versions of the active pharmaceutical ingredient. Prodrugs undergo a reversible transformation in the body to yield the native drug (Figure 202). The modifications are performed for a variety of reasons but primarily to overcome the poor aqueous solubility of a drug, to increase its absorption, to improve pharmacokinetics, to alter its metabolism and to reduce local irritation. The transformation

often occurs enzymatically where an enzyme cleaves the labile linker to release the original drug. There are many chemical linkages through which drugs are conjugated with pro-moieties. The choice of linkage depends on the functionalities presented by the drug. Depending on the functional groups, linkages such as esters, carbonates, carbamates, phosphoesters, oximes, imines, amides ethers, etc. have been used.[143]

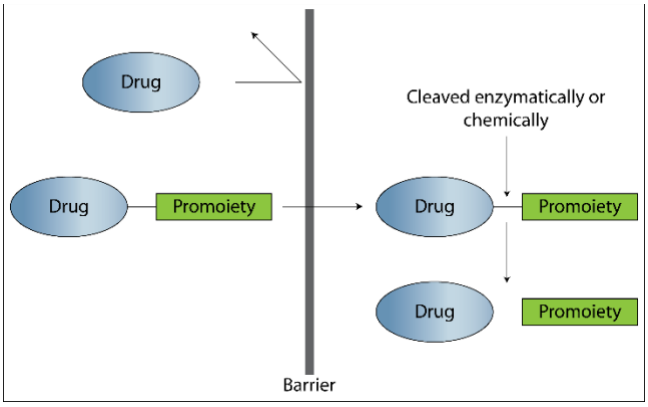

Figure 202: An example of how prodrugs work. In this case, the drug is not able to cross a barrier on its own. However, a prodrug can pass through it and then broken down to yield native drug.

The proposed system here is based on the concept of prodrugs. There are several small molecule-based prodrugs that have been on the markets for decades. However, this concept has not been investigated for proteins in such depth.

The hypothesis of protein-based prodrugs

The main objective behind the preparation of prodrugs is often to improve the pharmacokinetic properties, to alter aqueous solubility, or to reduce local irritation, etc. In our approach, the prodrug concept will be used to enhance the intracellular penetration of proteins (Figure 203). Thus, it would help to achieve the challenging goal of intracellular protein delivery. The prodrug protein itself may or may not have any therapeutic activity. However, once inside the cellular environment, it will be converted to native protein either

chemically or due to enzymatic action.

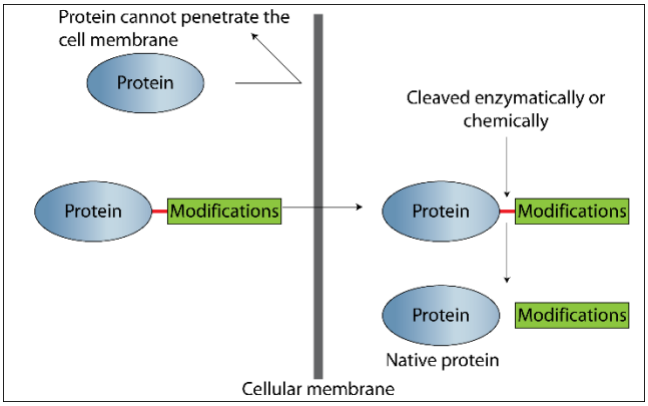

Figure 203: The idea of protein prodrugs. Proteins cannot cross the lipid bilayer on its own. However, it can be delivered inside the cell by chemically modifying it. Once delivered inside, the modifications will be reversed by the action of enzymes or chemically.

The approach is outlined in Figure 204. The key components we require here to test this hypothesis are; 1) A linker which is chemically or enzymatically cleavable; and 2) A modification of the protein which would make it cell permeable. We decided that the linkage here would be an ester-based linkage. The rationale for selecting this was two-fold: i) an ester can be synthesized easily from carboxylic acid functionality by simple coupling reactions, and ii) esterases are present ubiquitously in the body to reverse the modifications.[144]

Proteins have several carboxylic acid functionalities present on their surfaces. The C-terminal, as well as the side chains of aspartic and glutamic acids, provide -COOH groups. Through the linker, a cationic moiety can be introduced on the protein surface. The cationic charge would enhance the cell membrane permeation.[145] It should be noted that, upon esterification of a carboxylic acid group, one negative charge will be quenched. This removal of one charge is equivalent to the addition of a positive charge on the protein. If a protein has 6 -COOH groups and if all 6 get modified, 6 negative charges will be quenched,

or 6 positive charges will be created.

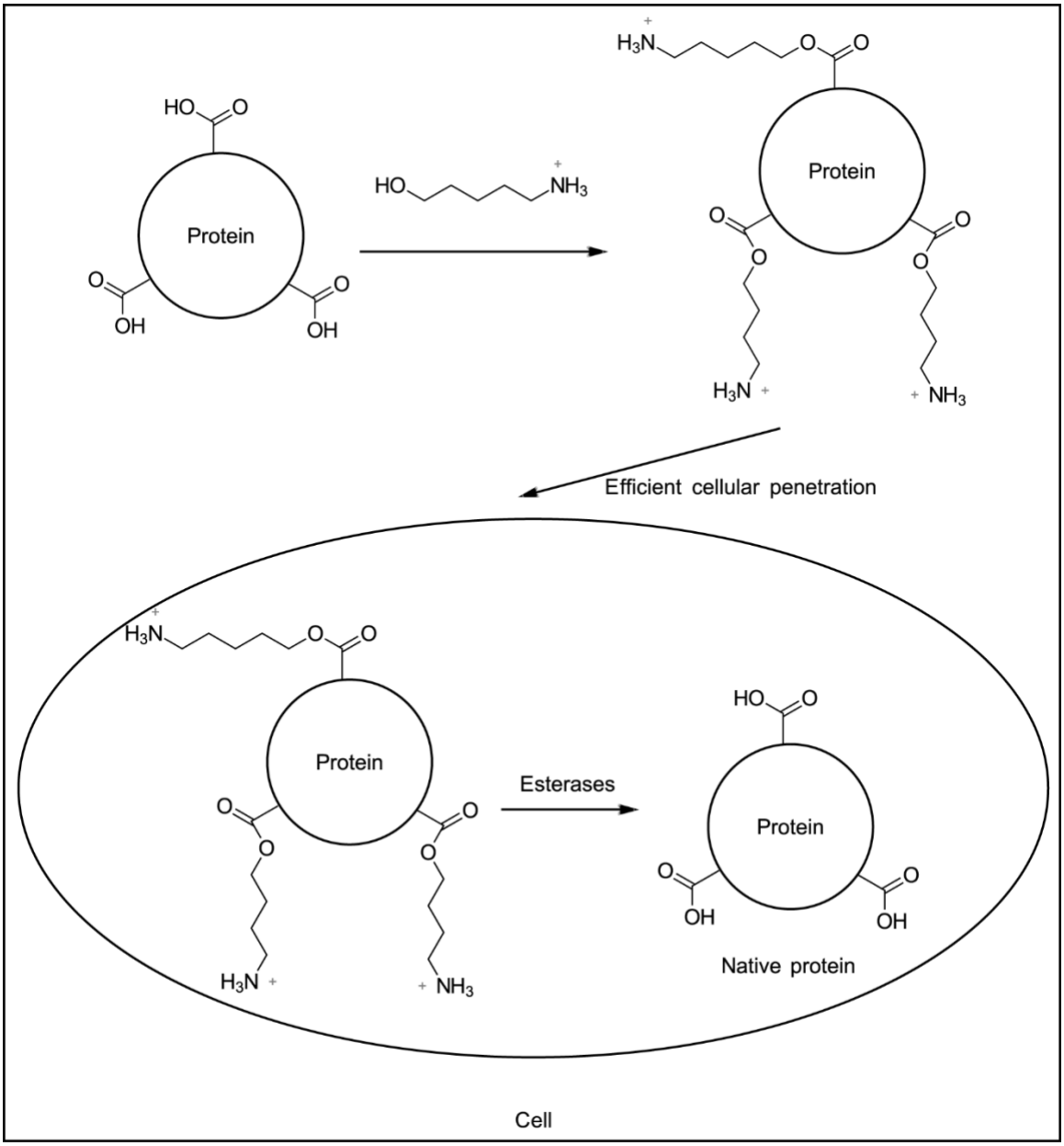

Figure 204: The concept of protein prodrug via an ester linker. The prodrug can be taken up inside the cell by virtue of positive charges. Once internalized, esterases present can hydrolyze the ester bond to yield native protein.

Below are several methods which we pursued to create protein prodrugs for cellular internalization.

Route # 1 – Fischer esterification - Esterification using azido alcohol

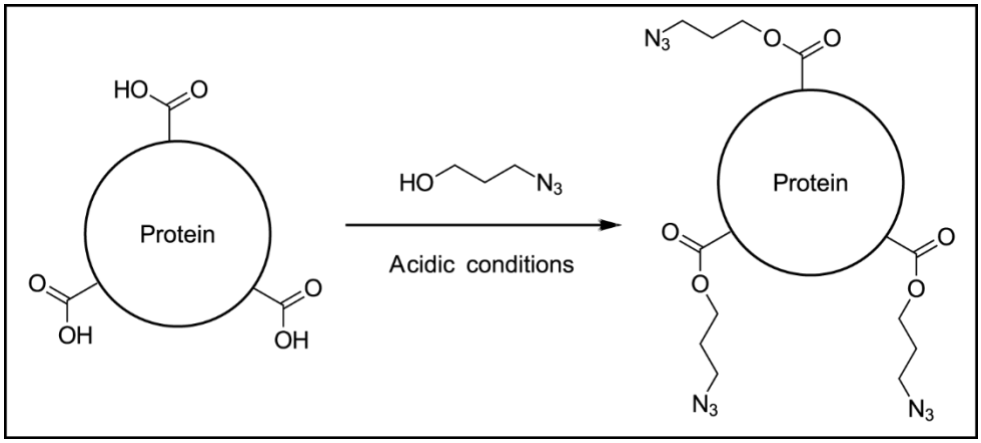

Figure 205: Esterification of insulin with azido alcohol.

We started investigating esterification using the Fischer esterification method under acidic conditions (Figure 205). Low molecular weight alcohols like methanol or ethanol can be coupled to carboxylic acid functionalities on the protein using this approach.[146,147] Insulin was selected as a test protein molecule. Insulin does not represent most proteins because it is a peptide and is extremely small compared to most proteins. Because insulin can be easily analyzed by mass spectrometry (MS) in the HSB building, we decided to use insulin. Once we are reasonably sure that the conjugation and internalization method works with insulin, we can start investigating other proteins. 3-azido propanol was selected as the alcohol. Azide functionality was kept intentionally for introducing a variety of useful functional groups through click chemistry in a facile manner.

The reaction was set up in the following manner. Insulin (4.6 mg, 0.79 µmol) was mixed with 3-Azidopropanol (100 µL, 0.522 mmol) without adding any solvent. Insulin remained insoluble at this point even after vigorous shaking. 2 µL of 37% HCl was added to it and kept on vortex for 10 min. After 10 minutes, insulin was completely solubilized, and the reaction mixture was clear. It was run overnight and analyzed next day by HPLC

and MS. Reversed-phase HPLC (flow rate 0.4 mL min^{-1}, runtime 15 min with 5 min post-run), solvent A (0.1% TFA in H_2O), solvent B (0.1% TFA in ACN), gradient 40% B isocratic for 15 min, retention time: 3 min (Figure 206); C18 Hypersil column (5 µm, 150 × 3.2 mm, Agilent); ESI-MS (m/z); Monoesterified insulin, calculated, 6009.0; found, 6011.0 (Figure 207).

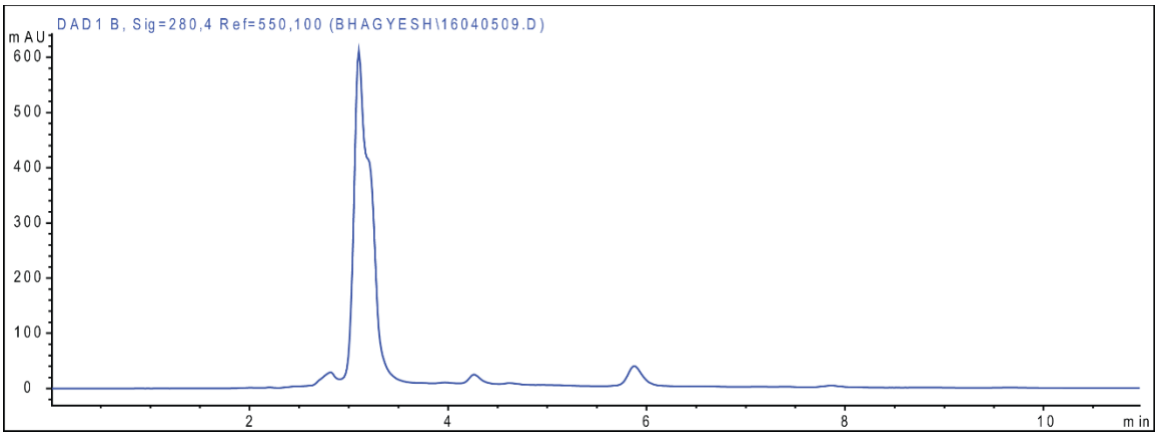

Figure 206: HPLC chromatogram of Insulin + 3-azidopropanol reaction mixture.

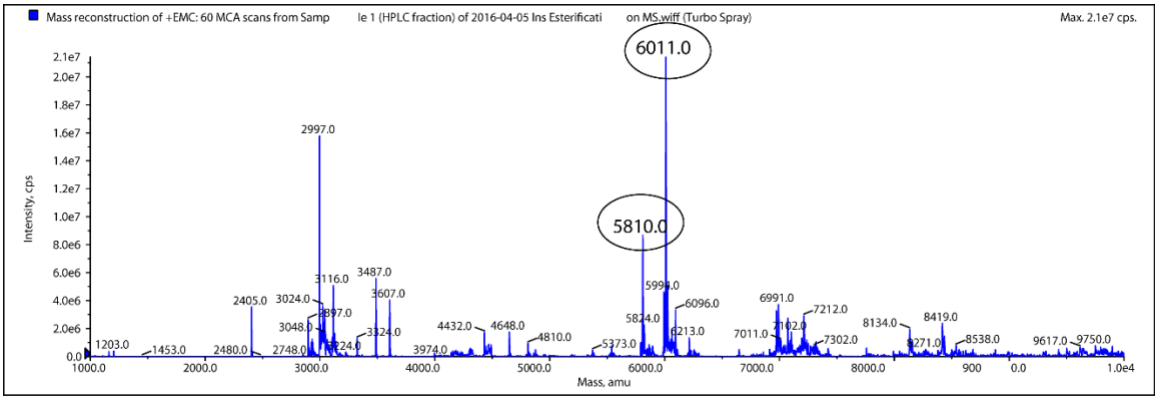

Figure 207: MS of HPLC fraction collected from the chromatogram above. 5810.0 corresponds to native insulin, and 6011.0 corresponds to mono-esterified insulin.

The issue with the above reaction was that the yields were extremely low. Even after using 660 equivalents of alcohol to one equivalent of insulin, only one carboxylic acid group was esterified. The reaction was run for several weeks after this at the room temperature. We

observed di-esterified insulin after 3 weeks (not shown here) when analyzed by MS. This suggested that the reaction progressed but very slowly. We had very limited success in the esterification of all 6 carboxylic acid groups on insulin.

Fischer esterification using methanol

We also tried following the conditions from the insulin esterification article to reproduce the conditions mentioned there.[147] This reaction would result in the synthesis of methyl ester. The final goal is not to synthesize methyl esters of insulin; this reaction was performed just to check what are the yields of the esterification reaction. Insulin (25 mg, 4.3 µL) was dissolved in 2 mL anhydrous methanol, and HCl in methanol was added to a final concentration of 0.115 N. Most insulin was dissolved in methanol but not all, the solution was little turbid. The reaction was analyzed by HPLC followed by MS. Reversed-phase HPLC (flow rate 1 mL min^{-1}, runtime 30 min with 5 min post-run), solvent A (0.1% TFA in H_2O), solvent B (0.1% TFA in ACN), 0 to 100% gradient B isocratic for 30 min; C18 Hypersil column (5 µm, 250 × 4.6 mm, Agilent), retention time: 18-20 min (Figure 209). As seen in the MS analysis (Figure 208), the esterification reaction using methanol was successful. Probably all the -COOH groups on insulin were esterified. This is likely because the reaction was strictly performed under anhydrous conditions and the solvent itself was the reactant. Hence there was a huge excess of methanol and it was present in very high concentration. In MS, after 48 hours, further modifications were seen. We observed 7, 8 and 9 modifications, although there are only 6 -COOH groups on insulin. It is possible that acidic conditions hydrolyzed asparagine and glutamine side chains and free -COOH groups were generated which then underwent esterification reaction. The concentration of HCl, temperature and reaction time could be optimized further to reduce

these side reactions. This was performed to test whether esterification takes place or not under acidic conditions. Though Fischer esterification worked well with methanol, the results were not encouraging when 3-azido propanol was used under identical conditions.

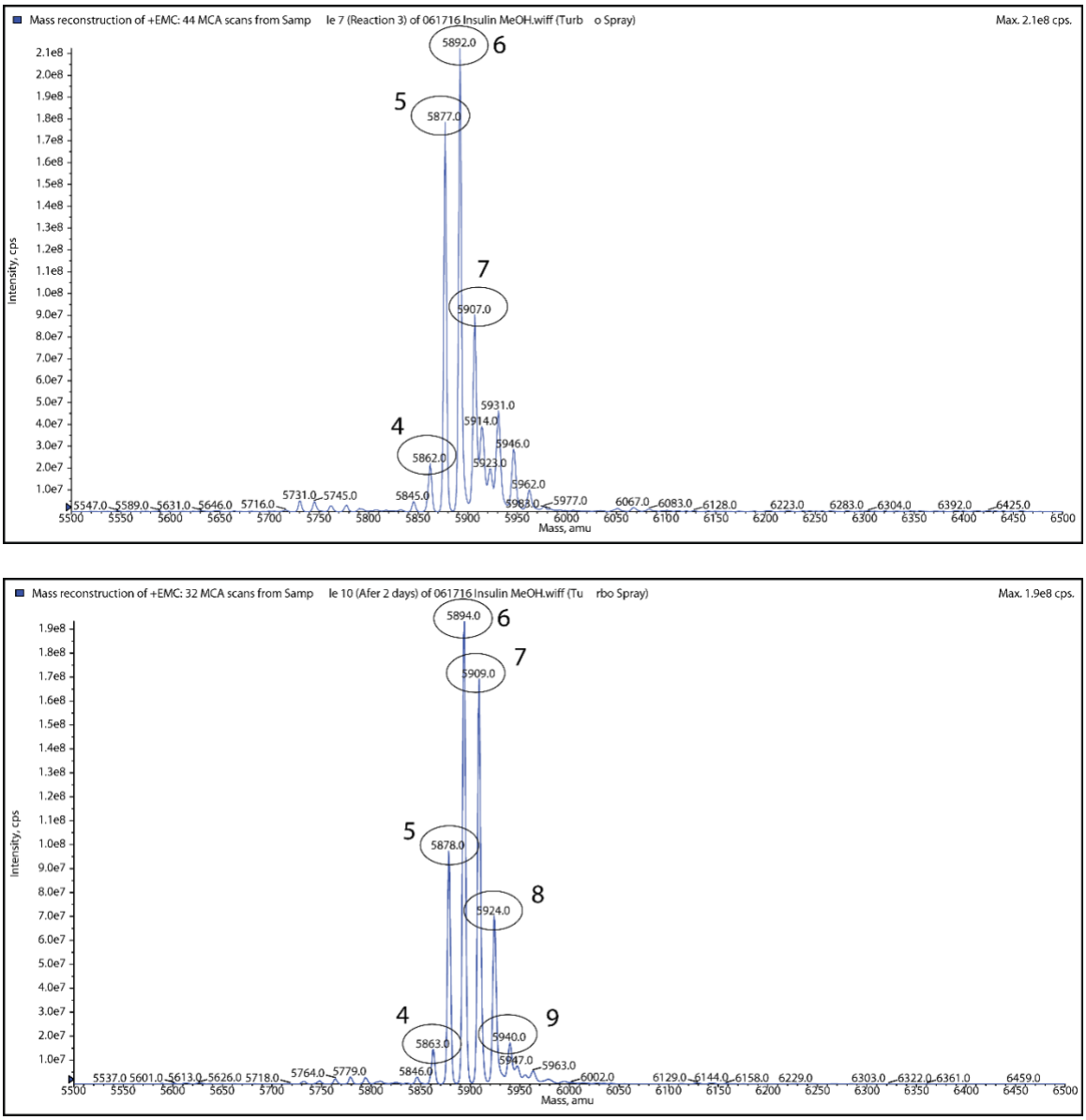

Figure 208: MS analysis of HPLC purified mixture of methyl esters of insulin. The top spectrum is taken after 24 hours of reaction and bottom spectrum after 48 hours. The number annotated refers to the number of carboxylic acids that are esterified by methanol.

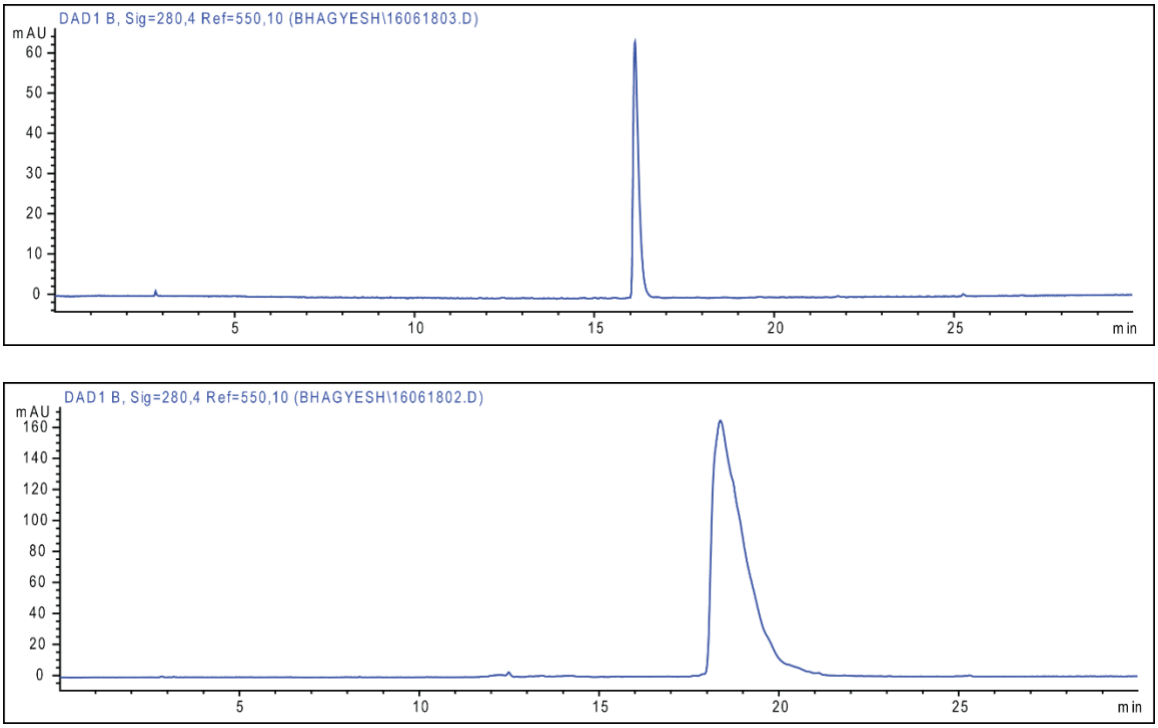

Figure 209: HPLC chromatogram of standard insulin (top) and the crude reaction mixture of methyl esters of insulin (bottom).

Fischer esterification using choline chloride

The next attempt was performed using choline chloride (Figure 210). These were the following reasons for choosing choline chloride for this project –

i. The linker must have two functionalities: alcohol to form an ester bond with the protein and an amino group to introduce positive charges on the protein surface. Choline chloride is very small in MW and has both the functionalities on it.

ii. Furthermore, there is a quaternary amine which will be positively charged under all pH ranges.

iii. Choline chloride forms deep eutectic mixture when mixed with urea, ethylene glycol. Both choline chloride and urea are solid at the room temperature. But when mixed in a 1:2 ratio, it becomes a viscous liquid.[148] Thus, this ionic liquid could act

as a solvent and reactant at the same time in the esterification reaction, like methanol in the esterification reaction reported earlier.

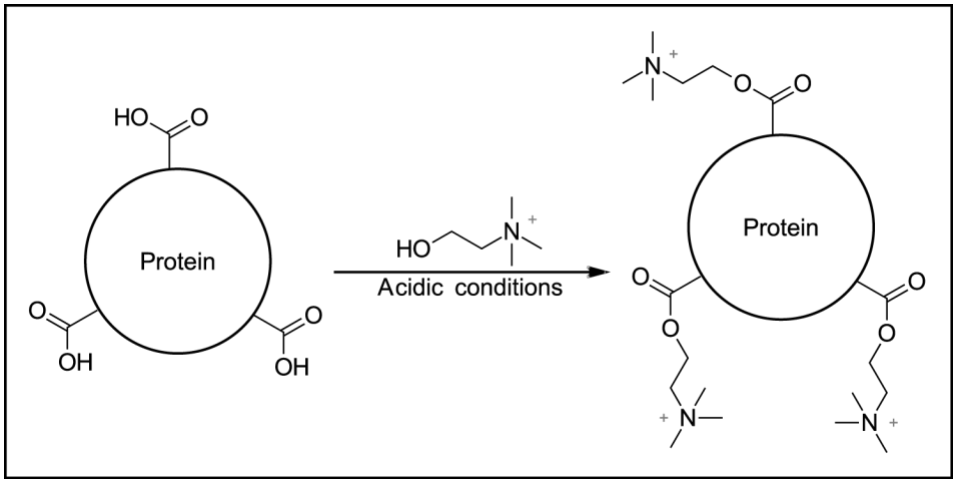

Figure 210: Esterification of insulin using choline chloride.

The ionic liquid can be prepared easily. Insulin was insoluble in the ionic liquid mixture. It cannot be dissolved even after raising the temperature of 50 ºC or after addition of HCl to protonate amines. Because of the solubility issues, we could not continue working on this approach.

Route # 2 –Esterification using diazo

Since the first attempt using Fischer esterification did not exactly work, the diazo route was attempted. The lab has expertise in utilizing diazo for ester formation as performed in the case of siRNA and insulin. Since I have already synthesized DDA earlier, we used the same one here to estimate what is the extent of caging with the diazo (Figure 211).

The reaction of diazo with insulin was performed under two slightly different conditions. Rather than using only DMSO for this reaction, acid was added to lower the

pH. The esterification using diazo and the carboxylic acid is more efficient at lower pH than neutral when all carboxylic acid functionalities are protonated.[149]

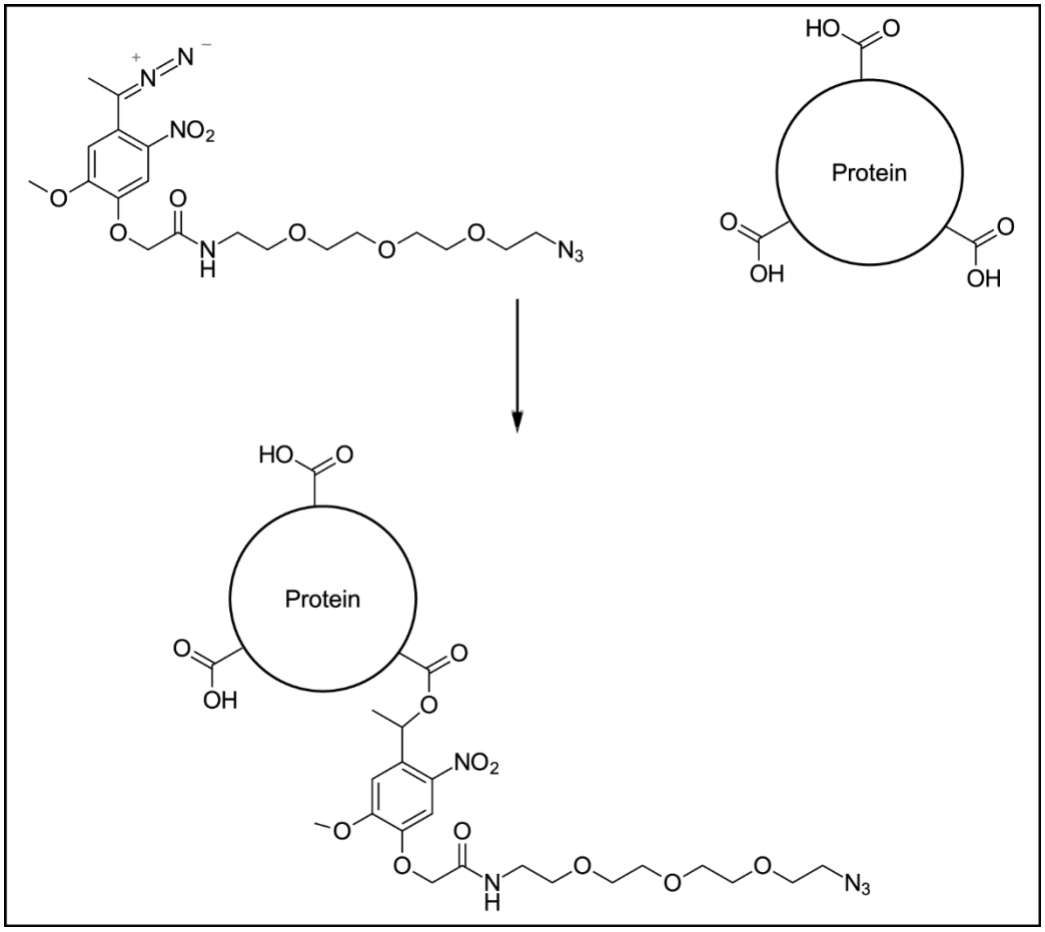

Figure 211: Esterification of insulin using DDA. In the figure, only one of the carboxylic functionalities is undergoing reaction, but all can be modified in this way.

Here, we decided to supply acid/protons in two different ways. Method 1 – in this approach, insulin was treated with pH 2 water for a brief period. This acidic pH probably protonated all the carboxylic acid and amino groups on insulin. Then it was freeze-dried. It is expected that in the dry form, insulin would be protonated completely and would probably stay in a salt form. Method 2 – it involved reducing the pH of the reaction mixture by HCl. HCl in dioxane was used to avoid the presence of water in the reaction. For each

reaction, 2.6 mg (0.447 µmol) insulin was used. Azido hydrazine, used earlier for caging insulin, was used here as shown in the reaction above. Azido hydrazone (43 µmol) in 0.25 mL DMSO was mixed with 105 mg MnO_2. It was vortexed for 45 minutes in the dark and filtered through the celite column to remove particulate MnO_2. Total diazo volume after DMSO washing of the celite column was 1.19 mL. It was split equally into two reaction mixtures for two different conditions mentioned earlier. The pH for condition # 2 was kept at 4.3.

After 24 hours of reaction, insulin + caged insulin products were precipitated by adding cold acetone to the reaction mixture. DMSO and unreacted DDA went into the acetone layer while the insulin + caged insulin precipitated out. It was analyzed using HPLC (Figure 212, Figure 213). Reversed-phase HPLC (flow rate 1 mL min^{-1}, runtime 30 min with 5 min post-run), solvent A (0.1% TFA in H_2O), solvent B (0.1% TFA in ACN), 0 to 100% gradient B isocratic for 30 min; C18 Hypersil column (5 µm, 250 × 4.6 mm, Agilent).

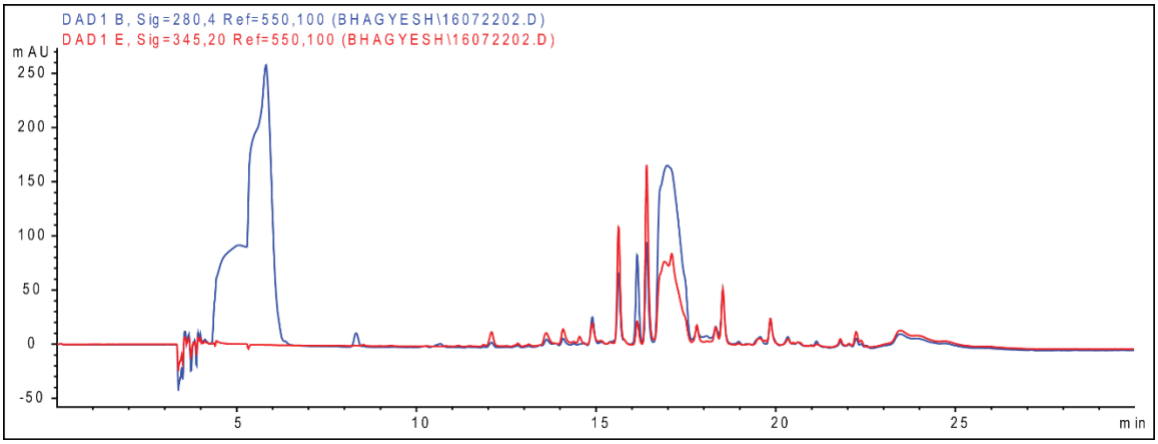

Figure 212: HPLC chromatogram of the reaction mixture after acetone extraction performed using method 1. No reaction is seen.

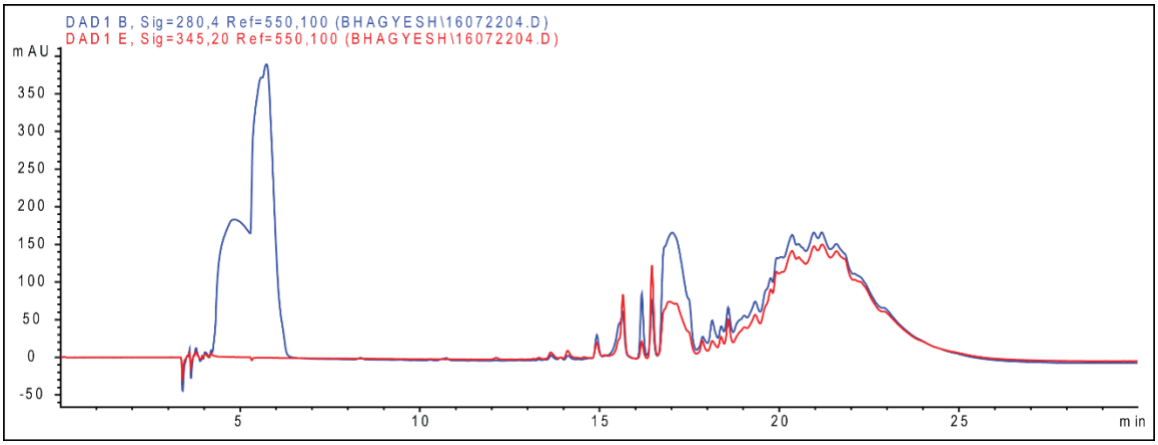

Figure 213: HPLC chromatogram of reaction after acetone precipitation performed using method 2, many modifications were observed.

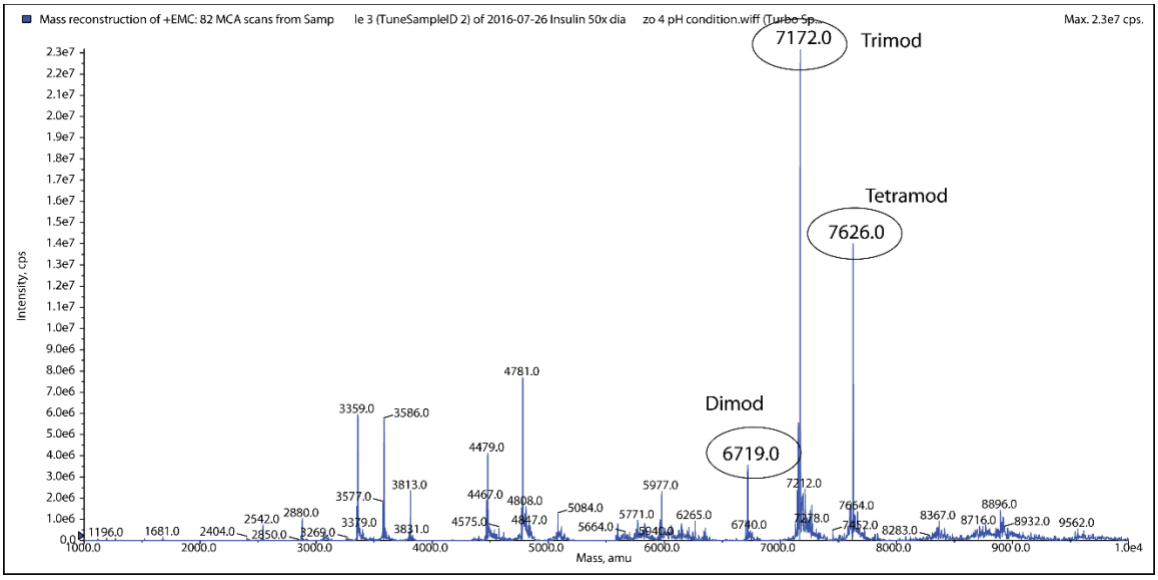

Figure 214: MS analysis of modified insulin collected from the HPLC run.

The reaction performed using method 1 showed no progress. No new peaks corresponding to the products were seen. We don't know the reason yet. However, there were a lot of new peaks in the second reaction. The peaks from 19-25' were collected and infused into MS for analysis. After using a 50× excess of diazo under acidic conditions, the extent of modifications was only 4 per insulin molecule. No traces of pentamodified or

hexamodified insulin were detected in MS (Figure 214). Among the products, trimodified was seen in the highest concentration not tetramodified. This study suggested that it was challenging to get completely hexamodified insulin. For this reaction, 100% DMSO was used. Other proteins will not be compatible with 100% DMSO, and the reaction must be performed in an aqueous solvent. However, the diazo gets easily hydrolyzed in water, so the reaction yields will be significantly lower than what we observed here. Hence, because of these limitations, we started investigating alternative routes other than diazo.

Route # 3 – Esterification using EDC/ DCC

The third approach included using EDC as the coupling reagent. EDC works like DCC except it is water soluble and used in coupling reactions which are performed in aqueous solvents.[150] Insulin (5.0 mg, 0.86 µmol, 3.2 mM), 3-azido propanol (0.99 mmol, 3.6 M, EDC (3.00 mg, 15.5 µmol) and DMAP (0.95 mg, 7.7 µmol) were mixed in DMSO. The reaction was run at room temperature for 48 hours. Reversed-phase HPLC (flow rate 1 mL min^{-1}, runtime 30 min with 5 min post-run), solvent A (0.1% TFA in H_2O), solvent B (0.1% TFA in ACN), 0 to 100% gradient B isocratic for 30 min; C18 Hypersil column (5 µm, 250 × 4.6 mm, Agilent). The analysis is in Figure 215 and Figure 216.

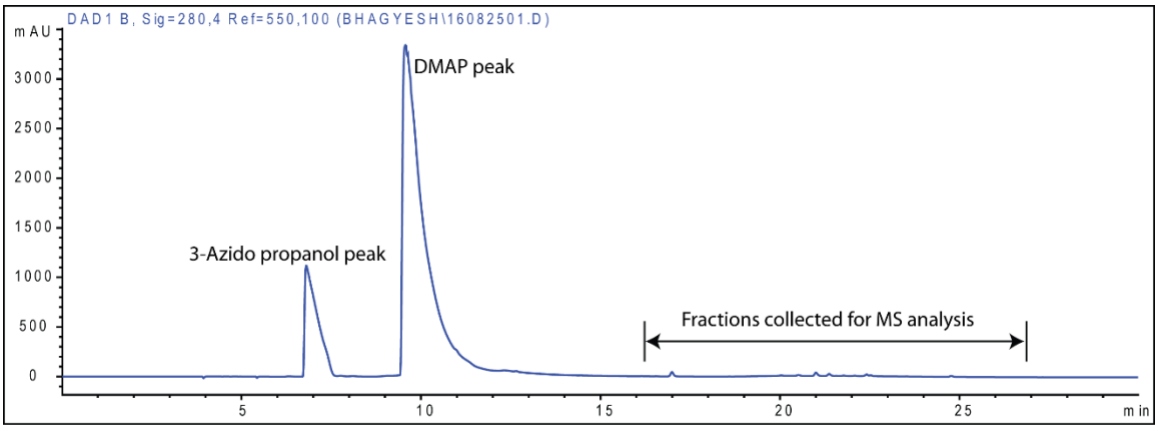

Figure 215: HPLC chromatogram of the crude reaction mixture.

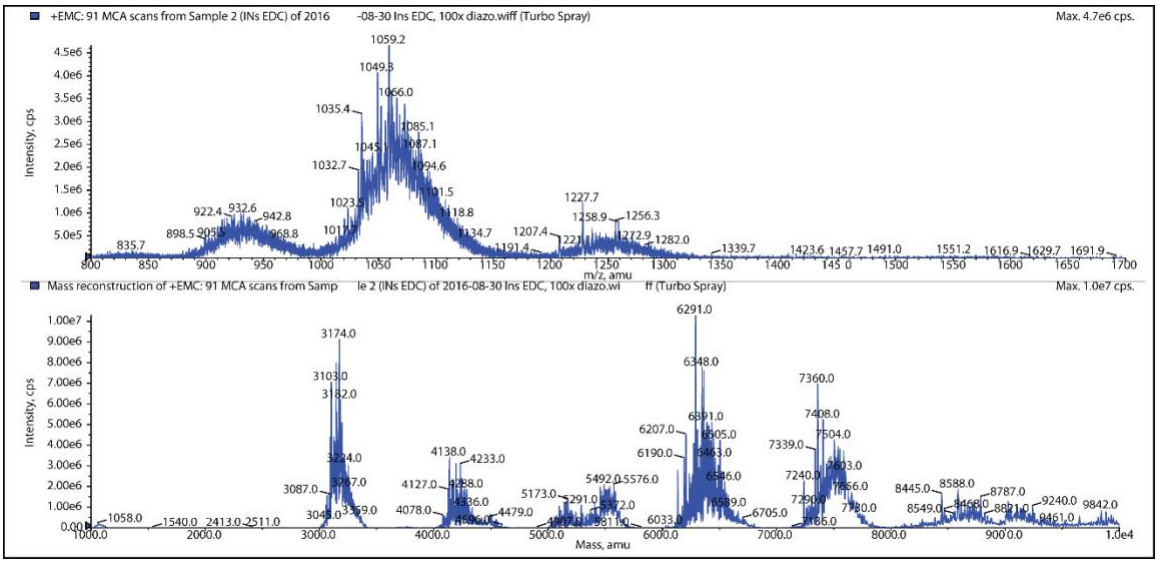

Figure 216: MS analysis of the fraction collected from the chromatogram earlier. No sharp peak corresponding to the product is observed.

Introduction of R9 peptide in the approach – Diazo route

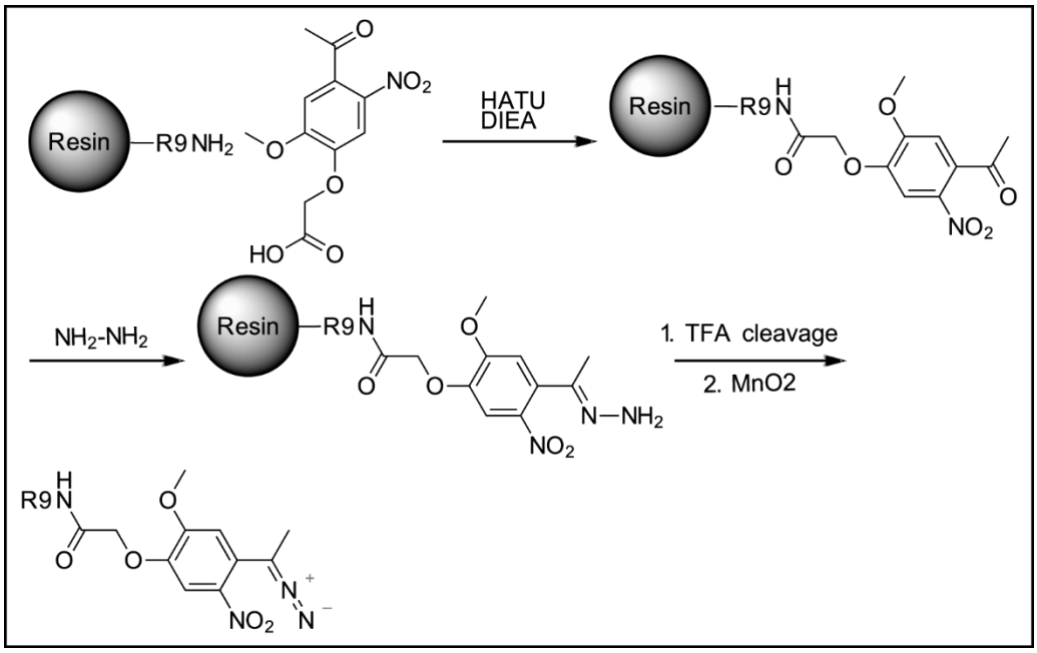

Figure 217: Esterification using diazo. The R9 peptide is conjugated to diazo to facilitate intracellular delivery.

We introduced the R9 peptide in the delivery approach. The cell-penetrating properties of R9-peptide are well documented for carrying cargo inside the cells.[151–153] Hence, we hypothesized that conjugating R9-peptide to the protein through labile ester linkages might succeed. The first attempt was to use diazo for esterification as described here (Figure 217).

The reaction I – Conjugation of NKA of R9-peptide

R9-peptide on the resin was ordered from Peptide 2.0. The first step involved deprotecting FMOC from the peptide using piperidine. The resin (75 mg) was weighed and washed with 0.5 mL DMF thrice; then treated with 0.5 mL of 20% piperidine in DMF thrice for 5 minutes each; then washed again with 0.5 mL DMF five times for 5 minutes each to wash off piperidine. Meanwhile, NKA (40.3 mg, 0.15 mmol), HATU (57 mg, 0.15 mmol) and DIEA (52.2 µL, 0.3 mmol) were mixed in 0.235 mL anhydrous DMF. It was pre-activated for 15 min and added to the resin. The reaction was stopped after an overnight reaction, and the resin was washed with DMF and followed by DCM, dried. A small amount of resin was cleaved using TFA and then analyzed by HPLC and MS. ESI-MS (m/z): $[M]^+$, calc. 1675.0; found, 1675.0 (Figure 218); analytical method – reversed-phase HPLC (flow rate 0.4 mL min^{-1}, runtime 30 min with 5 min post-run), solvent A (0.1% TFA in H_2O), solvent B (0.1% TFA in ACN), 0 to 100% gradient B isocratic for 30 min; C18 Hypersil column (5 µm, 150 × 3.2 mm, Agilent), retention time: 12.2 min (Figure 219).

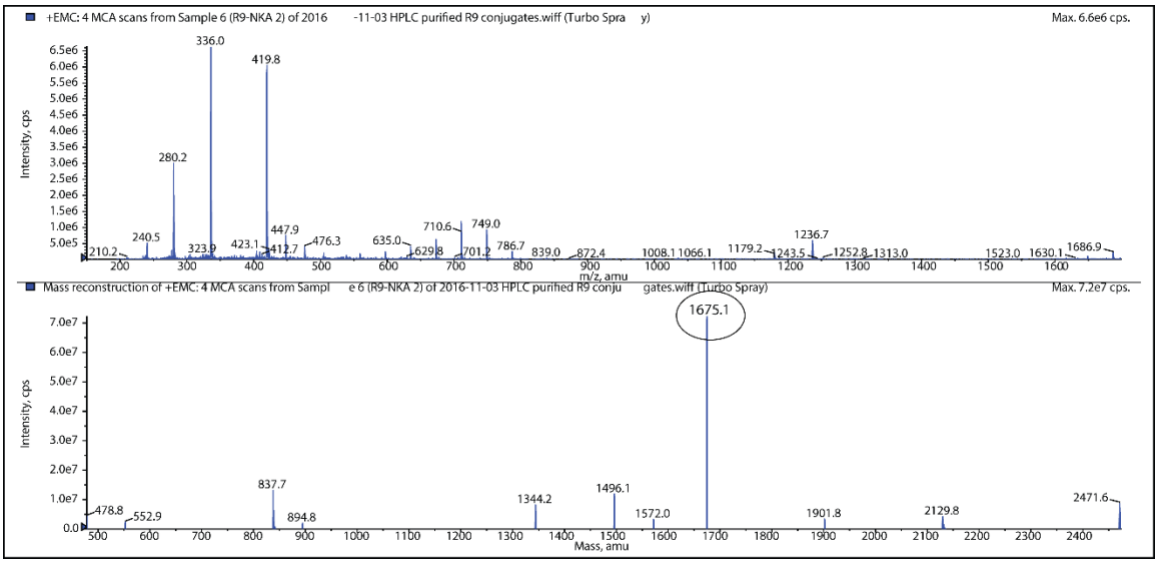

Figure 218: MS of R9-NKA cleaved from the resin using TFA.

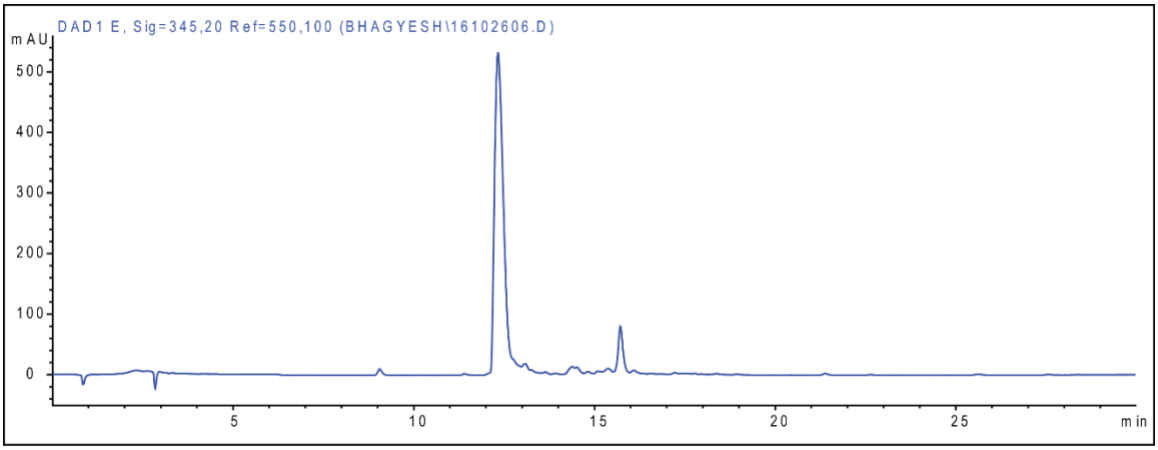

Figure 219: HPLC chromatogram of R9-NKA. Retention time = 12.2 min.

Reaction II – Conversion of R9-NKA to R9-hydrazone

R9-NKA (10 mg resin, 1.43 µmol) was added in Hydrazine monohydrate (2.77 µL, 57.2 µmol) and acetic acid (0.12 µL, 2.14 µmol) in 20µL of EtOH and NMP each. The reaction was run at 50 °C at 1000 rpm shaking in the thermomixer for 24 hours. Then it was washed with DMF followed by DCM 5 times. A small portion was cleaved by TFA for analysis. The reaction was incomplete, but the hydrazone conversion was confirmed.

Higher temperature or excess of acetic acid and hydrazine monohydrate could drive it towards completion. The hydrazone peak was purified using HPLC in multiple runs. Reversed-phase HPLC (flow rate 0.4 mL min^{-1}, runtime 30 min with 5 min post-run), solvent A (0.1% TFA in H_2O), solvent B (0.1% TFA in ACN), 0 to 100% gradient B isocratic for 30 min; C18 Hypersil column (5 µm, 150 × 3.2 mm, Agilent), retention time: 12 min (Figure 220); ESI-MS (m/z): $[M]^+$ calc., 1688.0; found, 1688.0 (Figure 221).

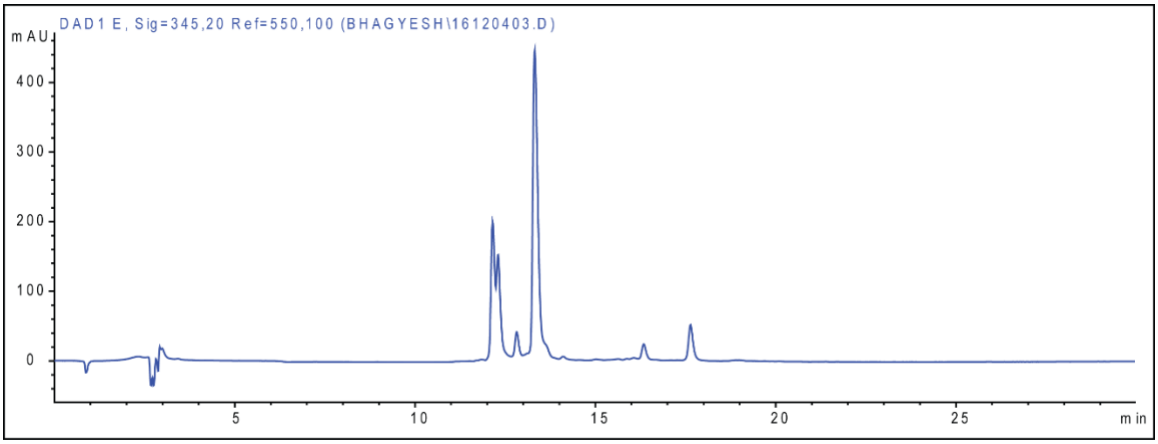

Figure 220: Chromatogram of the crude reaction mixture of hydrazone conversion. The taller peak at 13-14 min is unreacted R9-NKA, and 12 min twin-peaks are R9-hydrazone.

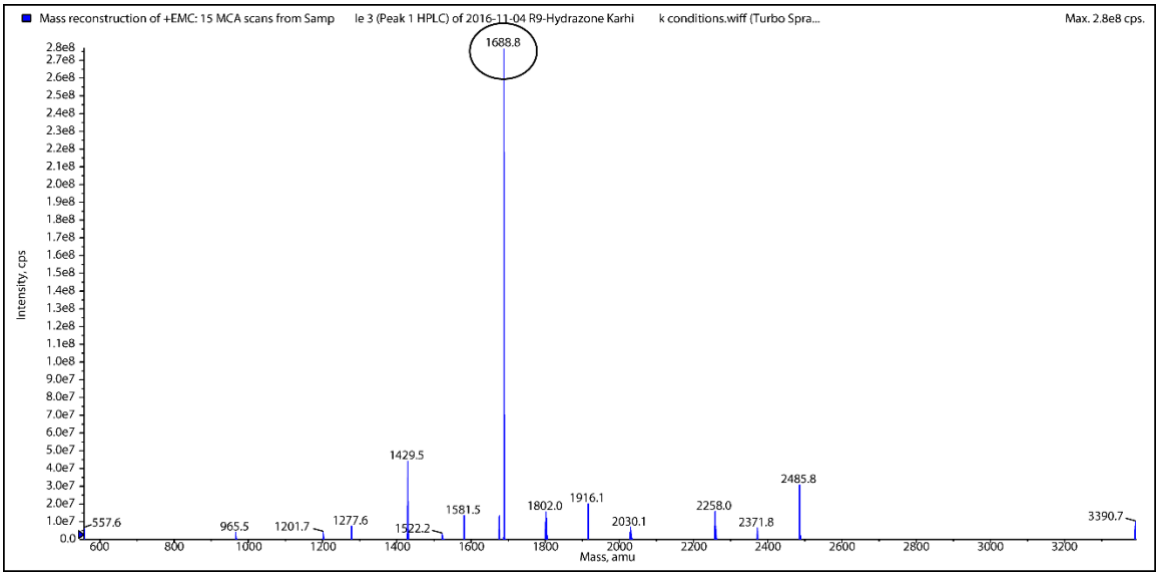

Figure 221: MS of R9-hydrazone. The peaks at 12 min in the chromatogram above were collected and infused in MS.

Reaction III - Conversion of R9-hydrazone to R9-diazo

The conversion of R9-hydrazone to diazo didn't work out well. It was thought that MnO_2 probably also reacts with guanidino groups of arginine to give side products. Due to this, the yield of the diazo reaction is substantially lower with lots of side products. Similar reactions were performed by other lab members and were unable to get the products in a clean manner with higher yields. Due to the challenges, this approach was stopped here.

Introduction of R9 peptide in the approach – Carbamate route

The carbamate route seemed easier than the hydrazone-diazo route. It has been demonstrated in the lab by senior students that small molecules can be caged via carbamate onto the solid phase support. This approach was mentioned in Chapter 1. Insulin, however, failed to undergo coupling reaction in this manner. Hence, we decided to perform TFA cleavage of R9-NAA (alcohol) first and then do the carbamate coupling with insulin in the solution phase. The first reaction of NKA coupling to the resin was described earlier. Here the procedure for the next reactions is described (Figure 222).

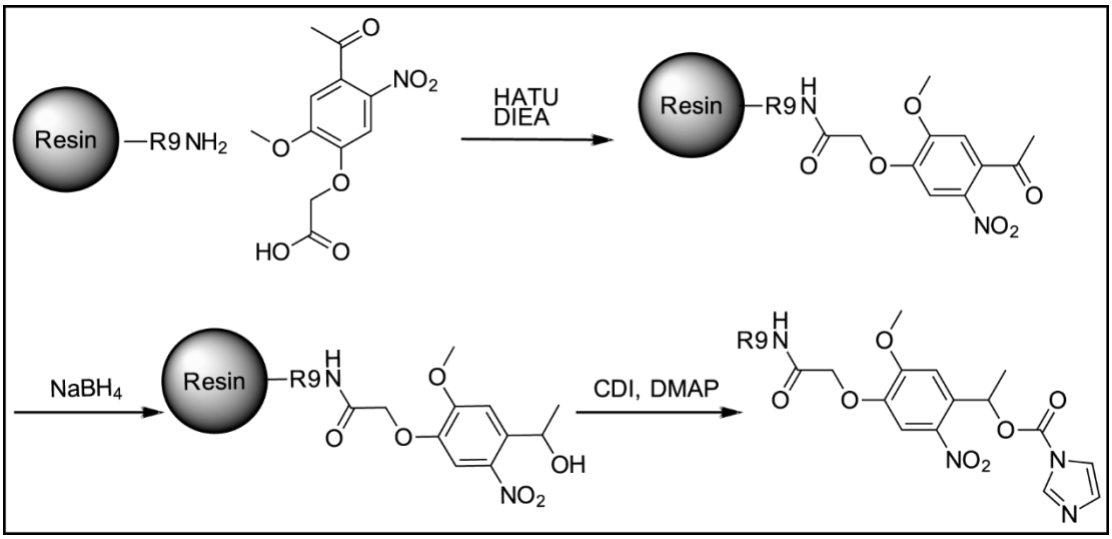

Figure 222: Carbamate route of making carbamate ester of proteins + R9 attachment.

Reaction II – Conversion of the ketone to alcohol

0.1 g R9-NKA resin (13.4 µmol) + $NaBH_4$ (29 µmol, 1.1 mg) were added in 1 mL mixture of ethanol+DMF (1:1) in a small glass reaction vial. The vial kept open to let the *in-situ* generated CO_2 escape. It was stopped after 4 hours. The resin was washed 5 times with DMF followed by DCM. Then a small portion was cleaved using TFA for analysis.

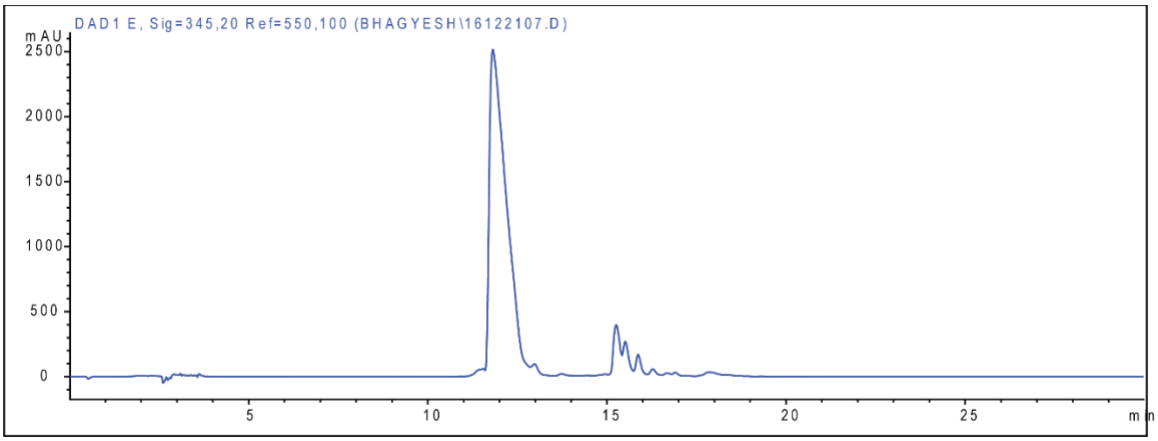

Figure 223: HPLC chromatogram of R9-NAA after reduction with $NaBH_4$. The peak between 11-13 min was collected and analyzed by MS.

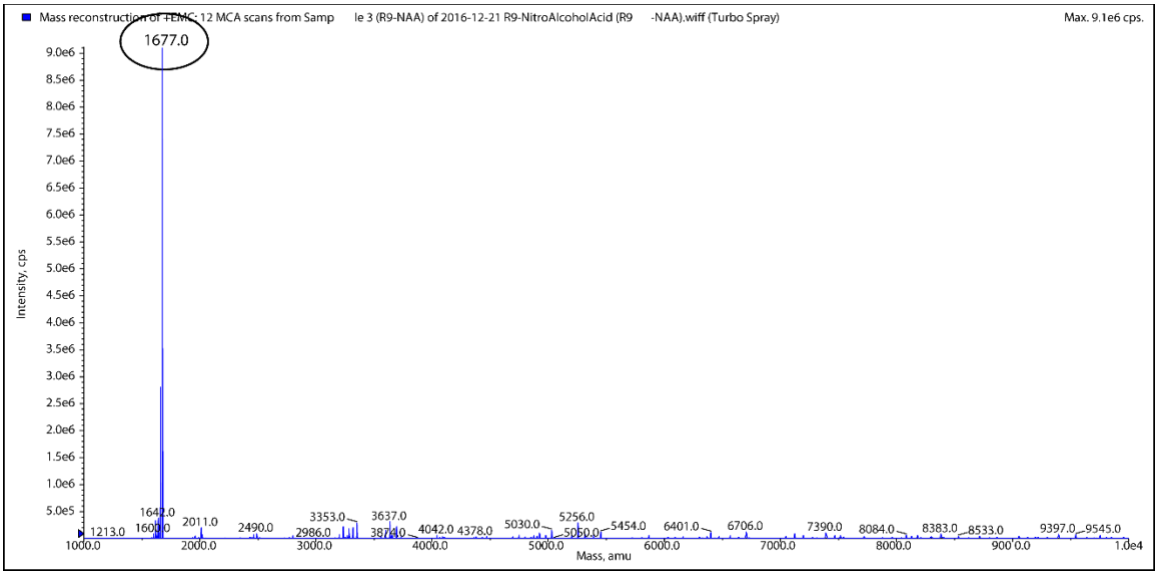

Figure 224: MS of R9-NAA after reduction with $NaBH_4$. This is MS infusion of HPLC peak purified in the figure above.

Reversed-phase HPLC (flow rate 0.4 mL min^{-1}), solvent A (0.1% TFA in H_2O), solvent B (0.1% TFA in ACN), 0 to 100% gradient B isocratic for 30 min; C18 Hypersil column (5 µm, 150 × 3.2 mm, Agilent), retention time: 12 min (Figure 223); ESI-MS (m/z): $[M]^+$ calc., 1677.0, found, 1677.0 (Figure 224).

Reaction III – Caging of insulin by R9-NAA

R9-NAA (0.5 µmol) was added to CDI (0.08 mg, 0.5 µmol), DMAP (0.06 mg, 0.5 µmol) in anhydrous DMSO 14 µL. It was kept for activation at 37 °C for 2 hours. In another tube, insulin (3.0 mg, 0.51 µmol) was dissolved in 0.2 mL DMSO. The activated solution was then added to insulin in DMSO. A similar reaction was also performed in PBS instead of DMSO, but upon addition of all reagents to PBS, a precipitate was observed. Hence the PBS reaction was not analyzed. However, no traces of products were seen in the reaction performed in 100% DMSO (Figure 225). It is plausible that CDI might have some reactivity with guanidino groups preventing it from reacting with the alcohol.

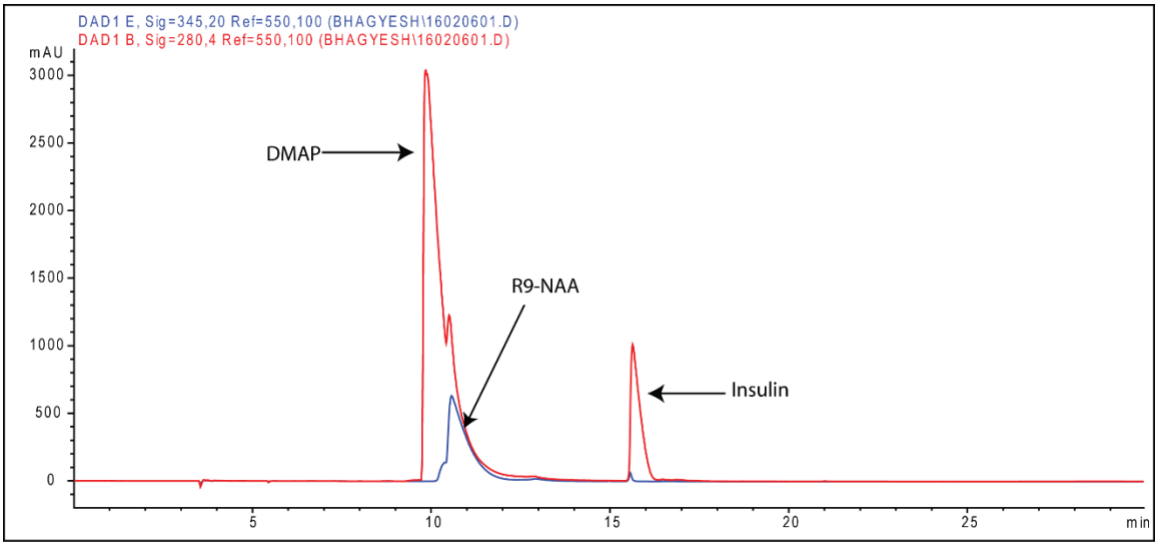

Figure 225: HPLC chromatogram of reaction between R9-NAA and insulin.

The reaction was attempted with different conditions varying the percentage of water in the reaction mixture, pH, etc. However, there was no product detected on HPLC.

Protein nanocapsules

What is a protein nanocapsule?

The idea of "protein nanocapsules" was first published by Yan et al. where they trapped a single protein in a capsule covalently for intracellular protein delivery.[154] First, small linkers were reacted onto the protein surface using amide conjugation chemistry to introduce monomeric acryl cross-linker. Then cross-linking reagents were added to the protein to cross-link all the monomers. The polymerization reaction took place on the protein surface, and it formed a thin polymeric capsule surrounding the protein. Hence it is called "protein nanocapsule." There is flexibility in choosing the desired cross-linkers. The crosslinkers could be designed or selected to have desirable properties. The capsule could be either biodegradable or non-biodegradable or containing positive charges or disulfide bridges or combinations of these things etc. Thus, depending on the protein, its role, route of delivery and the target tissue, the capsule can be modified. Based on this work, stimuli-sensitive nanocapsules have been developed which respond to external environmental stimuli and open to release proteins accordingly. For example – enzyme sensitive,[155] temperature sensitive,[156] light sensitive,[157] etc. protein nanocapsules have been developed. Further work has been performed in this area to create more efficient nanocapsules and is reviewed here.[158] The nanocapsules approach is appealing for several reasons –

1. The polymeric encapsulation of proteins on their surface might render it resistant towards proteases or an immune system of the body and increase its half-life in the

body. The capsule may sterically hinder the access of the proteases to the site of proteolysis. Material such as PEG could be included in the cross-linker which is known to increase circulation time of protein therapeutics in the plasma.[159]

2. The cross-linker could carry positive charges as shown earlier. Decorating protein surfaces with positive charges is strongly proved to enhance protein uptake. Many groups have worked on this idea using a multitude of strategies. Liu group has synthesized "supercharged proteins" by replacing certain amino acid residues with cationic amino acid on the protein surface. These highly cationic proteins are shown to have excellent cell-penetrating properties and also act as carriers to carry cargoes inside the cells with some modifications.[145] Thus, there is no need to biologically engineer proteins to get these charges; the cross-linker would easily impart positive charges on its surface. Also, the charges will be only as a temporary modification, once the protein is internalized, the polymeric capsule would break down, and charges will be separated from the protein. This reversible modification alters the protein structure temporarily until it is internalized or exposed to certain stimuli.
3. The cross-linker could have disulfide linkages which are vulnerable to the reducing environment of the cell. A recent study has used this concept for the intracellular delivery of proteins.[160] Intracellular environment is reducing in nature and disulfides get reduced rapidly. If the nanocapsules are made up of cross-linkers having disulfide bridges, the entire nanocapsules polymers get degraded quickly inside the cells. However, the nanocapsules stay intact outside and protect proteins from undergoing degradation before cellular penetration. The concept has been studied and is being used widely for delivery purposes.[161]

Self-immolative linkers

The strategy of self-immolative linkers (SIL) provides a convenient way and additional control over the release of the drug candidate. Typically, in the case of prodrugs, the drug is modified by a promoiety to alter its pharmacokinetic, physical properties. However, sometimes an additional linker which is called a 'self-immolative linker' is inserted between these two. The conjugated moiety (or promoiety) is connected via a stable but stimuli-sensitive bond i.e. it is stable under normal conditions but cleaved upon exposure to specific stimuli.[162,163] The concept is outlined in Figure 226. The stimuli could be temperature, pH, enzymes (esterases or proteases), light, etc. Once the construct is exposed to certain stimuli, the bond is cleaved exposing the SIL. Until this point, the SIL is inactive but once the conjugated moiety is cleaved off, it undergoes self-cleavage yielding the native drug.

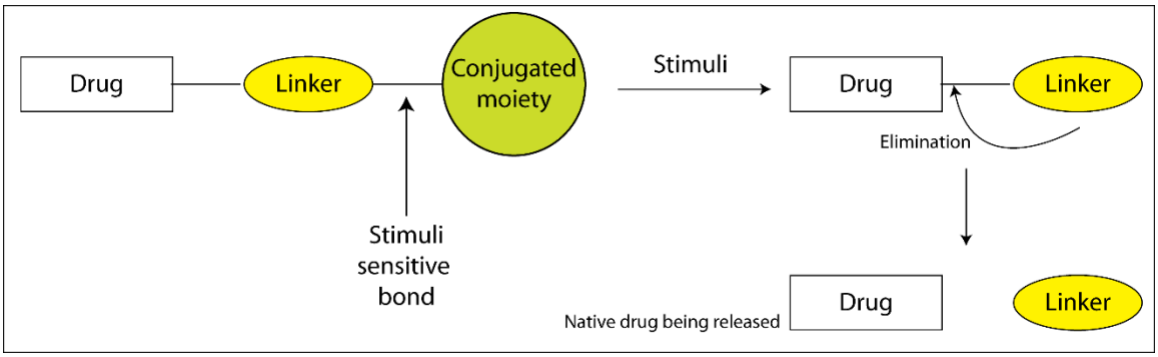

Figure 226: The concept of self-immolative linkers. A moiety is attached to the native drug through the self-immolative linker. Upon exposure to stimuli, the conjugated moiety is cleaved off. At this point, the linker undergoes self-cleavage to release the native drug.

The SEL strategy has been used by different groups for modifying the properties of drug molecules. For example, Pires et al. used this to design a sensor for intracellular thiols (Figure 227).[164] They modified the amines on the fluorophore ring to temporarily quench

its fluorescence. Once it is taken up inside the cells, glutathione reduces the disulfide linkage. The thiol attacks the carbamate, yielding free amino. The free amino group is responsible for the fluorescence and hence upon cellular delivery, fluorescence is restored. The fluorescence signal is proportional to the concentration of glutathione in the cell.

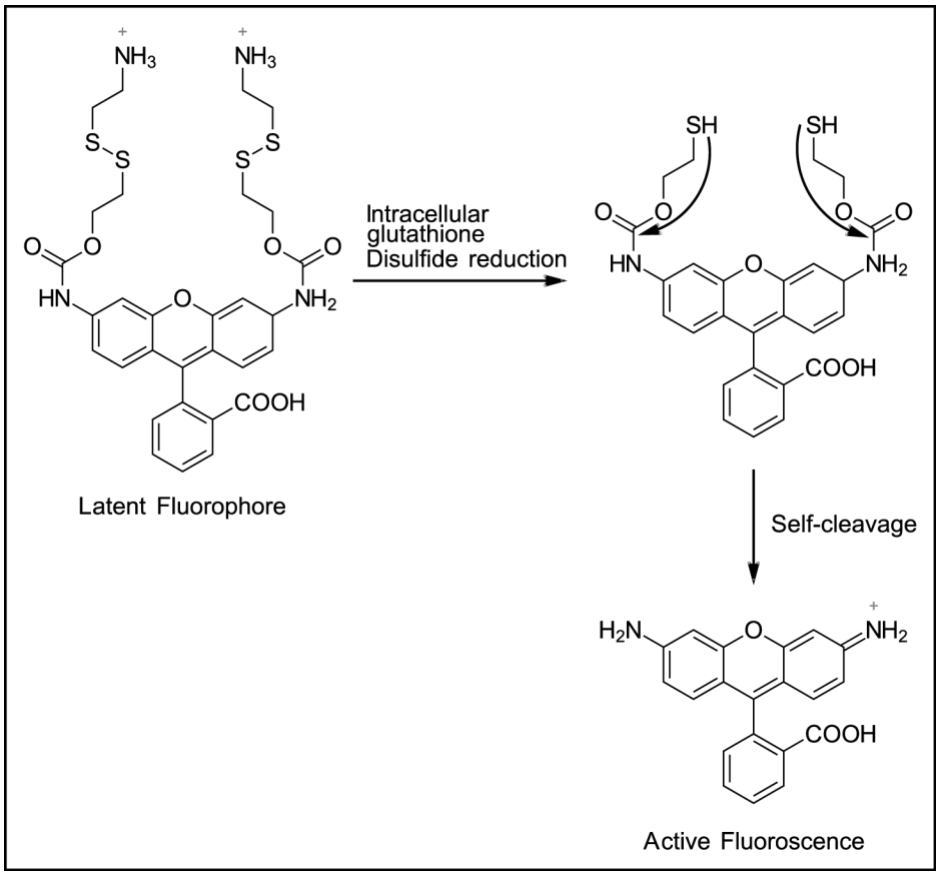

Figure 227: An example of the self-immolative linker. A dye is conjugated through an SEL. The modification makes the fluorescence inactive. The disulfide linkage is reduced once it goes inside the cells. After disulfide reduction, the SIL undergoes self-cleavage to release original dye molecule which is fluorescent. The fluorescence can be detected inside the cells.[164]

The Wender group has attached oligo-arginine peptides to cancer drugs like Taxol, coelenterazine through SIL.[165] By doing so, Taxol can be delivered in cancer-resistant cells by effectively avoiding Pgp efflux pumps. Taxol by itself fails to penetrate in these resistant cell lines due to efflux pumps.[165] Many groups have utilized this system which has been

reviewed already.[166]

We thought of applying the concept of SIL into the protein nanocapsules design. In all the protein nanocapsule designs, the monomer is introduced on the protein surface by modifying the amino groups via an amide bond. These modifications are irreversible as amide bond is very stable compared to an ester. In our approach, we plan to introduce monomers via a carbamate bond which would be reversible. The monomers will be cross-linked to each other via disulfide-containing linkers. The cross-linkers can contain cationic charges to enhance protein uptake inside the cells. When the nanocapsules are taken up inside the cells, reducing environment would trigger disulfide cleavage. The cleavage would expose a free thiol which would undergo self-immolation to cleave the carbamate yielding native protein as opposed to protein modified with all monomers due to amide linkage. The synthetic scheme is outlined below (Figure 228).

The amino groups on any protein can be modified via carbamate linkage with 2-(2-pyridyldithio)ethanol using coupling agents like CDI. The similar reaction was used for caging insulin in the earlier chapter. 2-(2-pyridyldithio)ethanol is an activated disulfide. Any free thiol could displace 2-Pyridinethiol ring and form a new disulfide link. The strategy has been used successfully before.[151] We envision that once multiple amino groups on the protein are modified, a dithiol cross-linker would undergo reactions to cross-link protein on its surface. The cross-linker could be designed as required. The PEG backbone could be included; cationic charges could be added, but it would have to have thiols at each end. Inside the cellular environment, the cross-linking would fall apart exposing free thiols. These thiols would attack carbamate to give free amino groups, yielding native protein inside the cells.

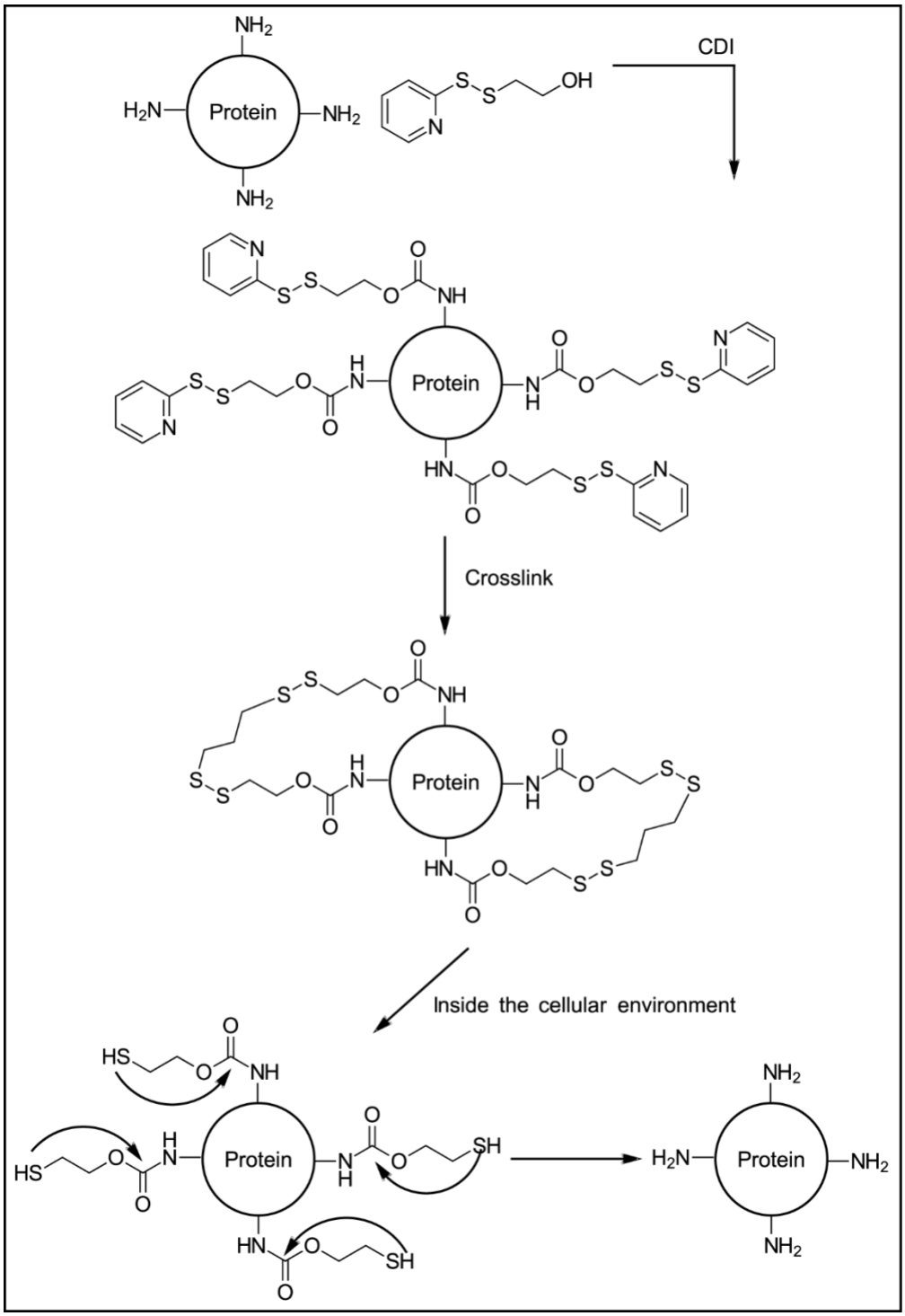

Figure 228: Protein nanocapsules + SIL approach.

Because UMKC does not have any functional MALDI-TOF to analyze protein modifications at this point, we relied on using insulin as a model protein to conduct initial

pilot experiments. The Department of Pharmaceutical Sciences has a functional QTrap 3200 MS on which insulin modifications could be characterized. Below are the experiments with insulin using this strategy.

Synthesis of 2-(2-Pyridyldithio)ethanol

2-Aldrithiol (Sigma-Aldrich, catalog # 143049, 0.47 g, 2.14 mmol) was added to 2.2 mL methanol and purged using N_2 by dipping the needle into it for 1 hour. To this, mercaptoethanol (55 µL, 0.78 mmol) was added using a needle through a rubber septum. The mixture became yellow immediately. It was stirred for next 2 hours. The solvent was evaporated, and it was purified by flash chromatography using 20% ethyl acetate in DCM. Yield = 0.11 g (83%); analytical method – reversed-phase HPLC (flow rate 0.4 mL min^{-1}, runtime 30 min with 5 min post-run), solvent A (0.1% TFA in H_2O), solvent B (0.1% TFA in ACN), 0 to 100% gradient B for 30 min; C18 Hypersil column (5 µm, 150 × 3.2 mm, Agilent), retention time: 13 min (Figure 229); ESI-MS (m/z): $[MH]^+$ calc. for $C_7H_9NOS_2$, 188.0; found, 188.1 (Figure 230).

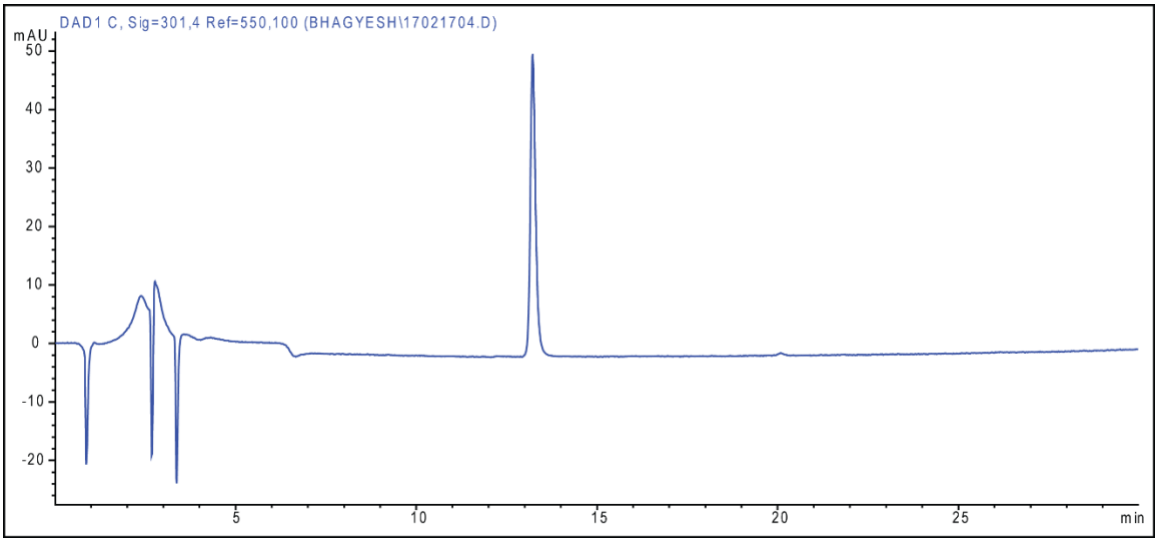

Figure 229: HPLC chromatogram of purified 2-PDE.

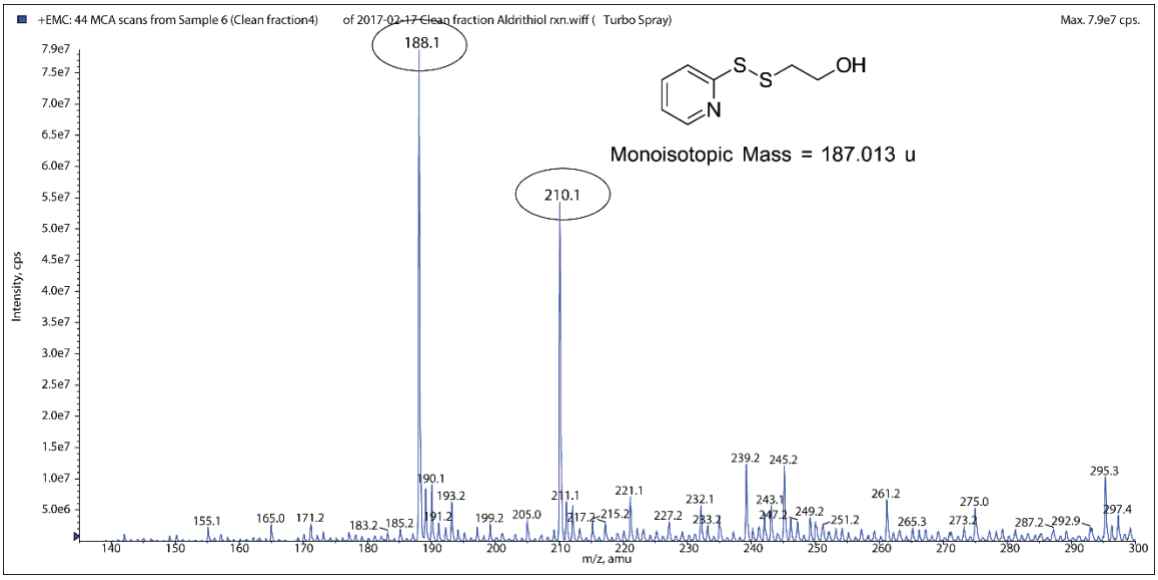

Figure 230: MS-infusion data of 2-PDE. The peak corresponding to 210.1 is a sodium adduct.

Synthesis and purification of insulin PDE dimod

A 2-PDE stock solution of 3.77 M was prepared in anhydrous DMSO. 88 µL of stock solution (330.6 µmol) was mixed with additional 50 µL DMSO to achieve a final concentration of 2.4 M. To this, 53.6 mg (330.8 µmol) of CDI was added and incubated at 37 ºC for 70-75 minutes. After incubation, it was diluted with 0.1 mL additional DMSO to make a final volume of 0.27 mL. This was divided into 4 equal parts. 60 mg insulin (10.33 µmol) was added into 4 glass vials each and dissolved in 4 mL 0.1 M carbonate buffer (pH = 8.95) + 0.1 mL DMSO. Each part of activated CDI was added to insulin solution and incubated at 40 ºC for 24 hours until turbidity was observed. Then it was stored in -20 ºC until purified using prep HPLC. Prep-HPLC method – reversed-phase HPLC (flow rate 2 mL min^{-1}, runtime 40 min with 5 min post-run), solvent A (0.1% TFA in H_2O), solvent B (0.1% TFA in ACN), 0 to 60% gradient B over 40 min; C18 Phenomenex column (5 µm, 250 × 10 mm, Agilent), retention time: 34.4 – 34.9 min; Yield ≈ 4 µmol (9.68%); UV/vis

(DMSO): 280 nm (13800 M^{-1} cm^{-1}); reversed-phase HPLC (flow rate 0.4 mL min^{-1}, runtime 30 min with 5 min post-run), solvent A (0.1% TFA in H_2O), solvent B (0.1% TFA in ACN), 0 to 100% gradient B over 30 min; C18 Hypersil column (5 µm, 150 × 3.2 mm, Agilent), retention time: 19-20 min (Figure 231); ESI-MS (m/z): $[M]^+$ calc. for, 6234.0; found, 6235.0 (Figure 232).

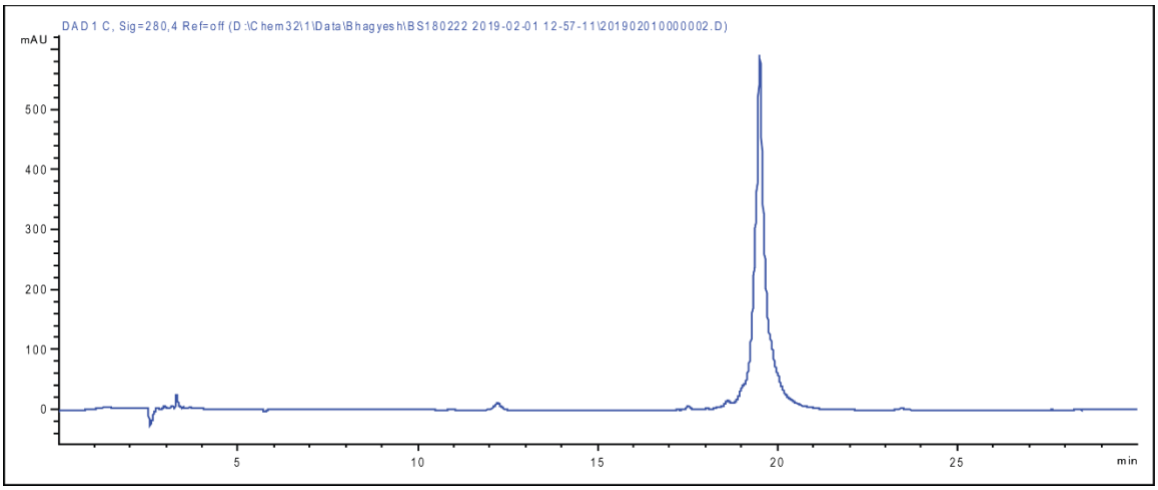

Figure 231: Analytical chromatogram of purified insulin PDE dimod.

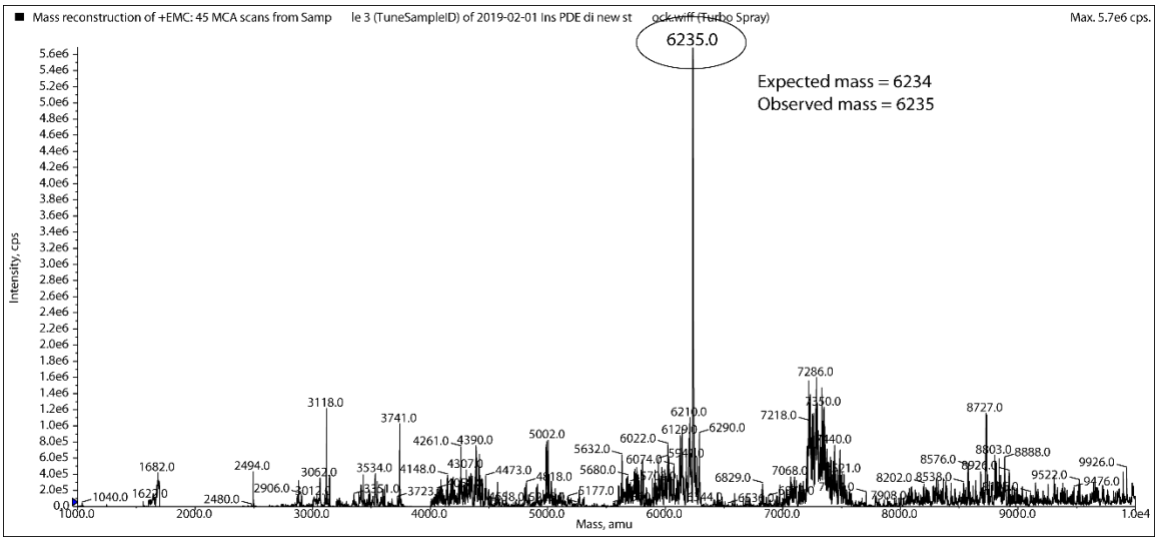

Figure 232: MS of purified insulin PDE dimod.

Cross-linking with dithiols

After synthesizing insulin PDE dimod which has two thiol-sensitive thio-pyridyl groups, the next step was to select dithiols for performing the cross-linking. For intracellular delivery, we would prefer cationic linkers flanking thiols at each end such as CKKKC sequences. This would encapsulate proteins in cationic charges helping cellular penetration. However, first, we thought of testing stability against proteases. The purpose of performing the cross-linking here is to prevent the unwinding of helices by proteases and/or just prevent binding of proteases to proteins. The shorter the cross-linker, the tighter would be the linkage and the greater the degree of resistance against proteases. Hence, we focused on selecting dithiols with the least possible atoms in between. In aliphatic dithiols, we selected ethanedithiol, 1,3-propanedithiol, 1,4-butanedithiol, 2-mercaptoethyl ether. For aromatic dithiols, we used 1,4-benzenedithiol. For dithiols with peptide backbones, we planned to synthesize cysteine dipeptide, both in L and D configuration. All planned dithiols to be used are shown in Figure 233. Except for the cysteine-containing peptides, all reagents were ordered from Sigma-Aldrich and Fisher Scientific.

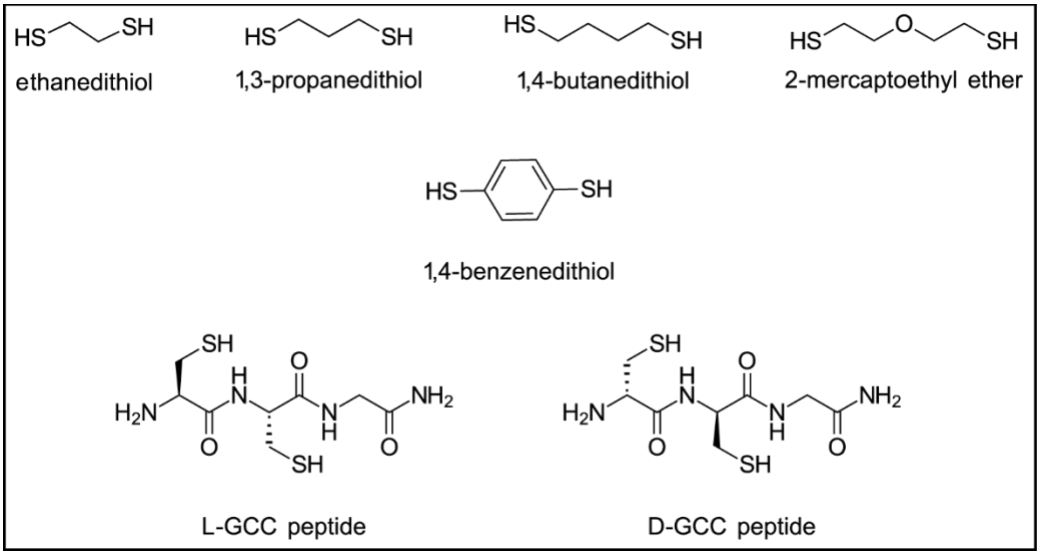

Figure 233: Dithiols that will be used for cross-linking in this approach.

Synthesis of cysteine-containing peptides

Friedman lab has been following a fixed protocol for peptide synthesis for years. However, cysteine has a tendency to undergo racemization during the coupling step.[167] Hence the procedure was modified as reported by Han et al.[168] Significant racemization is observed if cysteine is coupled as the very first amino acid residue on the resin on C-terminus. Hence, we decided to couple a glycine first followed by two cysteines. The reaction conditions are described in Table 14.

Table 14: Conditions used for the synthesis of cysteine-containing peptides.

Step in synthesis	Conditions used
Coupling	Fmoc-Cys (1): HATU (4): HOBt (4): collidine (4) in DCM: DMF (1:1), no pre-activation, 1-hour reaction. Concentration used = 0.2-0.3 M
Fmoc-deprotection	20 % piperidine (2 min and 8 min)
Capping	10 % acetic anhydride + 5% DIPEA in DMF
TFA cleavage	95% TFA + 2.5 % TIPS + 2.5% water, 1 hour

Reversed-phase HPLC (flow rate 0.4 mL min^{-1}, runtime 30 min with 5 min post-run), solvent A (0.1% TFA in H_2O), solvent B (0.1% TFA in ACN), 0 to 100% gradient B over 30 min; C8 Hypersil column (5 μm, 250 × 4.6 mm, Agilent), retention time: 8.3 min (Figure 234); ESI-MS (m/z): $[MH]^+$ calc. for molecular formula = $C_8H_{16}N_4O_3S_2$, 280.1; found, 281.2 (Figure 234).

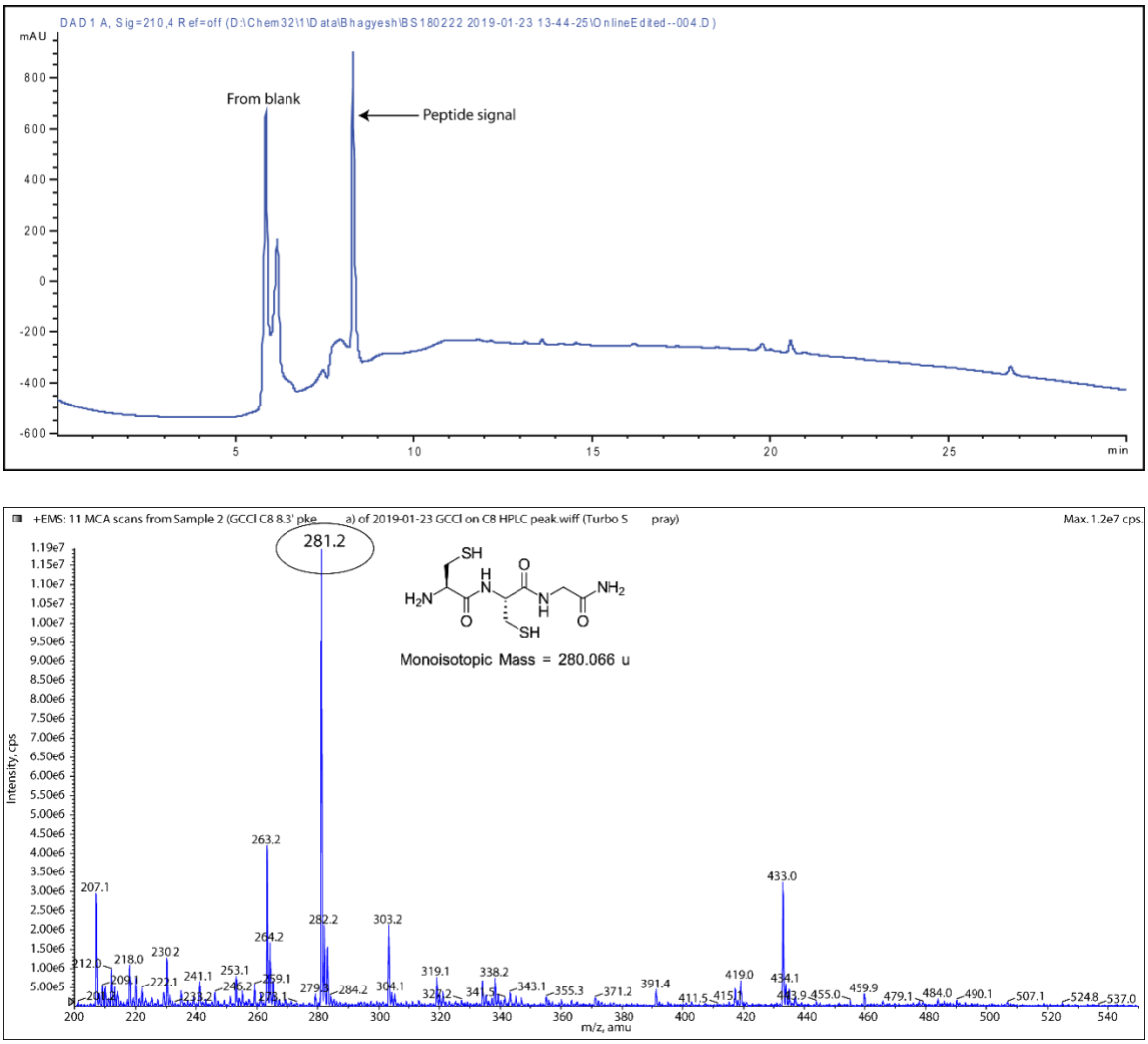

Figure 234: Characterization of L-GCC peptide – HPLC (top) and MS (bottom).

DTNB assay for determination of thiol concentration

We optimized the 5,5′-Dithiobis(2-nitrobenzoic acid) (DTNB) assay for thiol quantitation using Ellman's reagent.[169] To prepare a solution of DTNB reagent, 50 mg of DTNB reagent was added to 1 mL water, vortexed for a few minutes and centrifuged to settle the undissolved amount. The supernatant was taken out and used directly in the assay. For the assay, 12 µL of Ellman's reagent supernatant + 25 µL of 1M Tris-HCl + 0.15 mL of cysteine standard (0-100 µM) were mixed in a 96 well plate. The absorbance was

measured at 405 nm. In the proposed dithiols, we needed this assay to measure the concentration of synthesized peptides i.e. (L-GCC and D-GCC) and DBT as it had poor solubility in DMSO. Along with cysteine standard samples, diluted solutions of dithiols of unknown concentrations were subjected to the assay and their concentrations were determined using the standard curve (Figure 235).

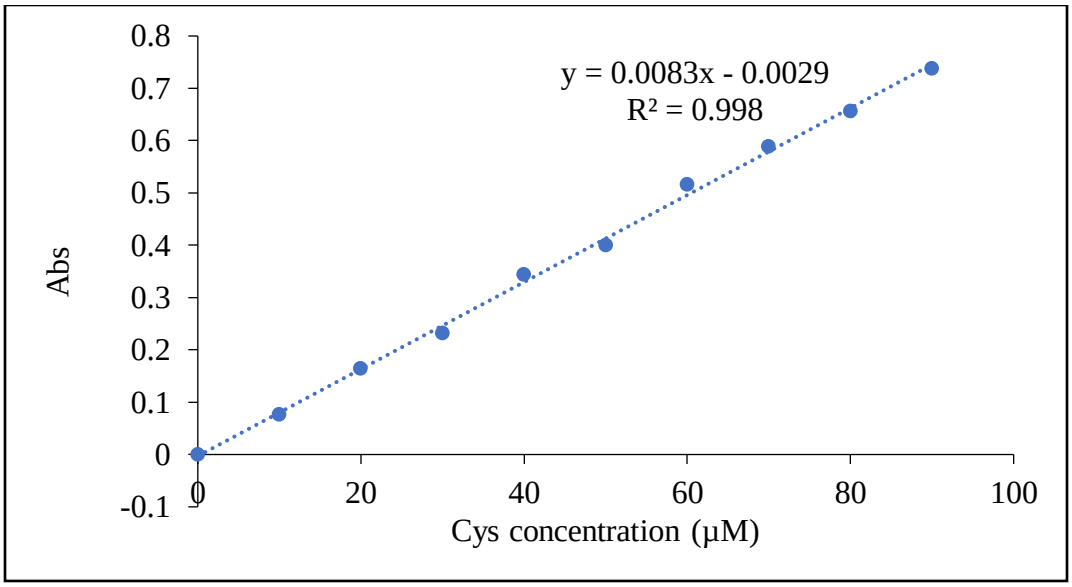

Figure 235: The standard curve of cysteine using Ellman's reagent. The absorbance was measured at 405 nm and plotted against known concentrations of cysteine in water.

Cross-linking on insulin surface

After synthesizing insulin PDE dimod and having dithiols in the lab, we proceeded to confirm whether we could perform cross-link on insulin surface using the selected dithiol candidates. The following reactions were set up with these conditions at a very small scale of approximately 24-40 nmol to just confirm the formation of the product. Insulin PDE dimod was used in the same quantity and the ratio of dithiol: ins PDE dimod was 1:1. Hence, their concentrations were also the same (Table 15). All MS of crude reaction mixtures are shown in Figure 236. All spectra show a single mass consistent with the

desired product. 1,3–propanedithiol reaction didn't show expected mass, only the mass of unreacted starting material was seen. All chromatograms show a cluster of peaks between 18-21' which show the correct mass (Figure 237). Because all chromatograms look similar, I am providing a single representative chromatogram.

Table 15: Concentrations of dithiols and insulin PDE dimod.

Dithiol	Insulin PDE dimod concentration
Ethanedithiol	2.9 mM
1,3-propanedithiol	2.9 mM
1,4-butanedithiol	2.9 mM
2-mercaptoethyl ether	2.9 mM
L-GCC peptide	2.4 mM
1,4-benzenedithiol	1.4 mM

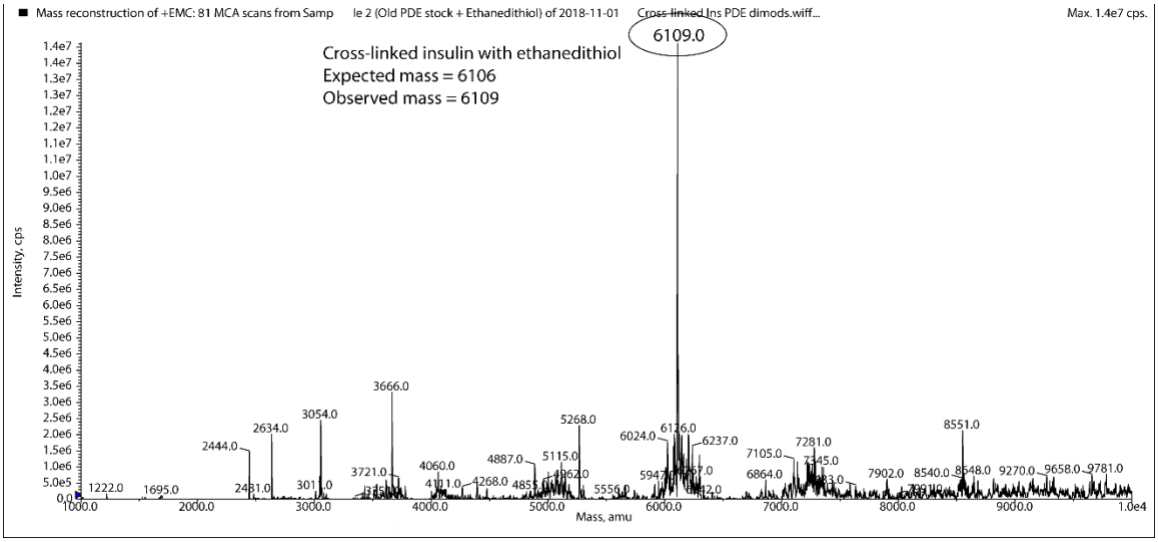

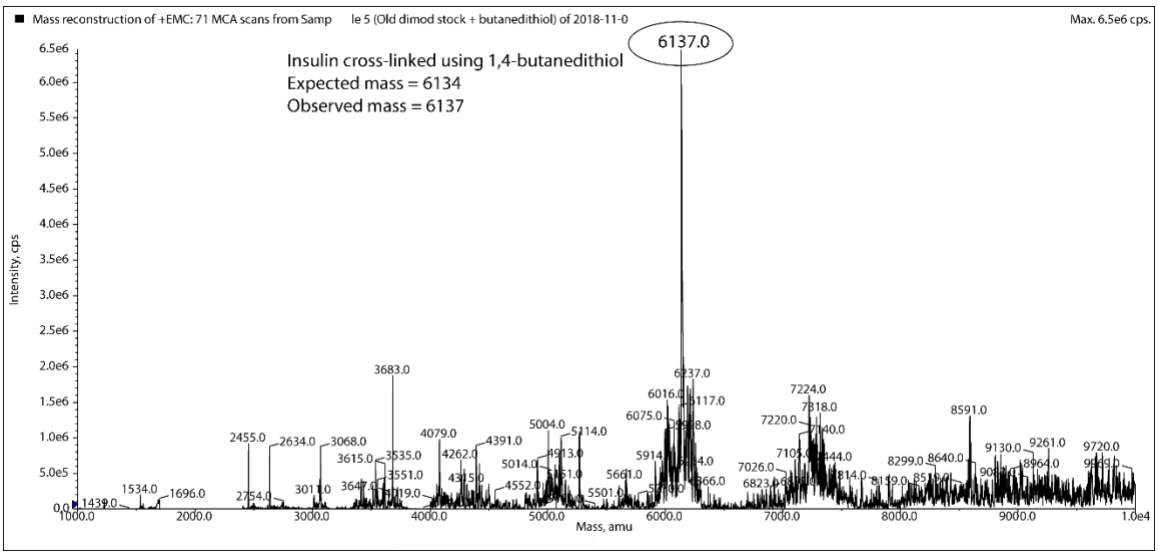
Mass reconstruction of +EMC: 71 MCA scans from Samp le 5 (Old dimod stock + butanedithiol) of 2018-11-0
Max. 6.5e6 cps.
6137.0
Insulin cross-linked using 1,4-butanedithiol
Expected mass = 6134
Observed mass = 6137
Intensity, cps
Mass, amu

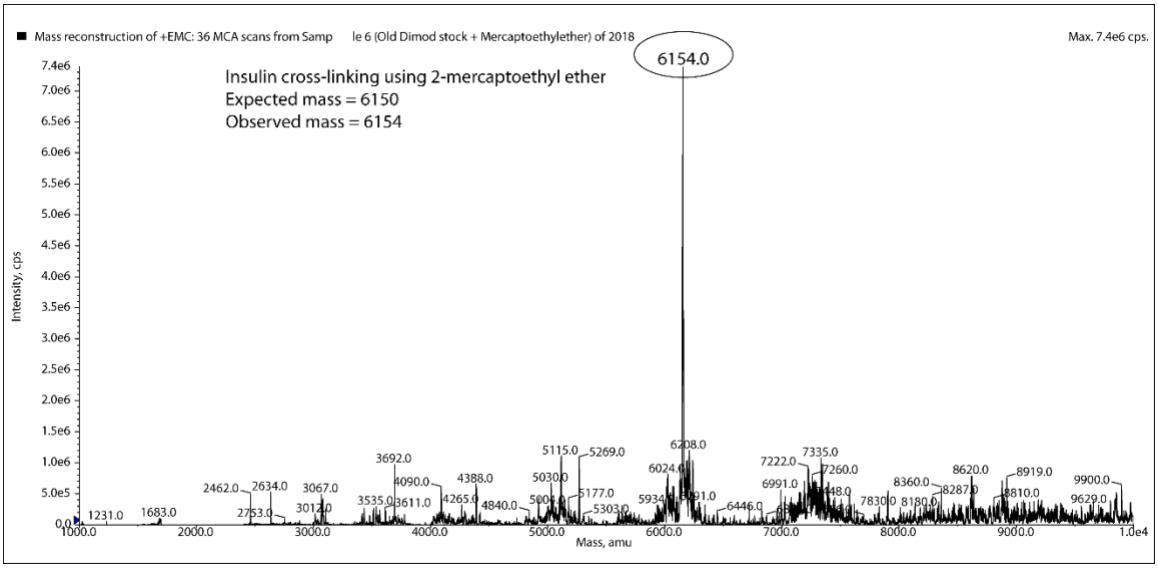
Mass reconstruction of +EMC: 36 MCA scans from Samp le 6 (Old Dimod stock + Mercaptoethylether) of 2018
Max. 7.4e6 cps.
6154.0
Insulin cross-linking using 2-mercaptoethyl ether
Expected mass = 6150
Observed mass = 6154
Intensity, cps
Mass, amu

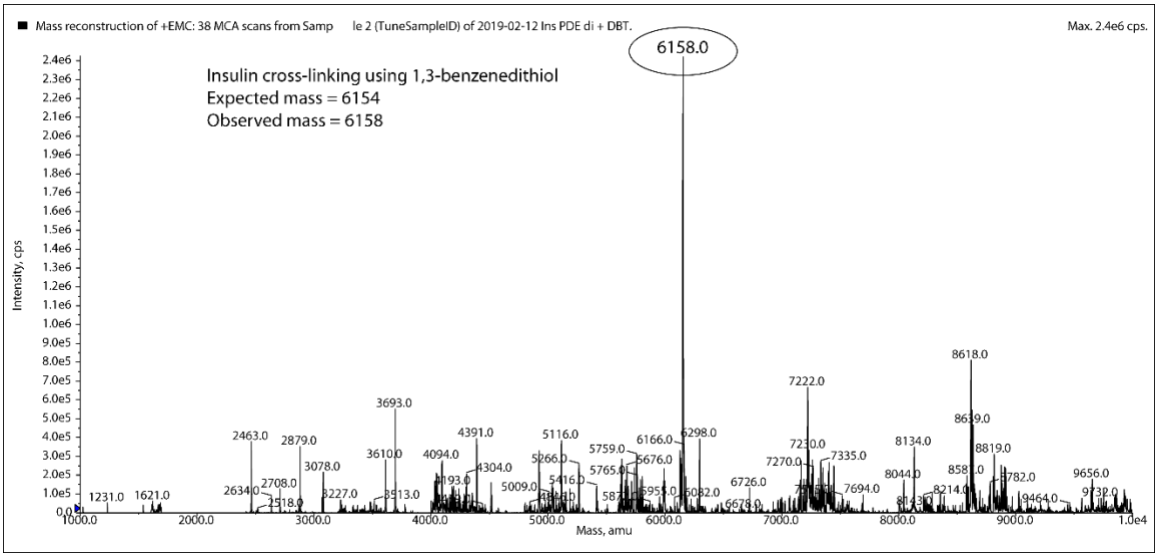
Mass reconstruction of +EMC: 38 MCA scans from Samp le 2 (TuneSampleID) of 2019-02-12 Ins PDE di + DBT.
Max. 2.4e6 cps.
6158.0
Insulin cross-linking using 1,3-benzenedithiol
Expected mass = 6154
Observed mass = 6158
Intensity, cps
Mass, amu

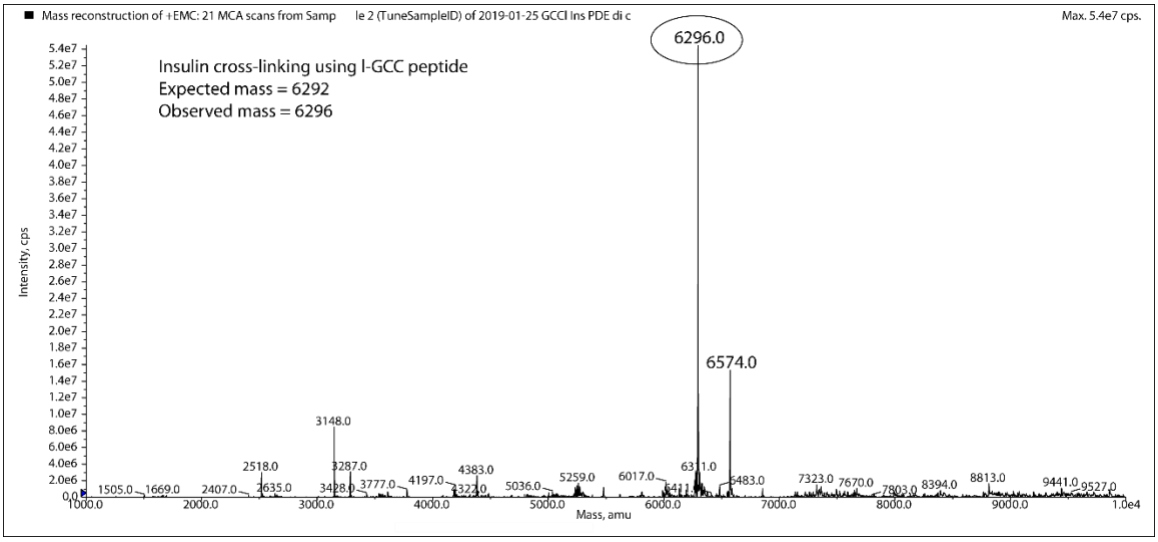

Figure 236: MS of crude mixtures dithiols crosslinking on insulin surface. In all reactions except 1,3-propanedithiol, a single peak consistent with the desired product mass is seen.

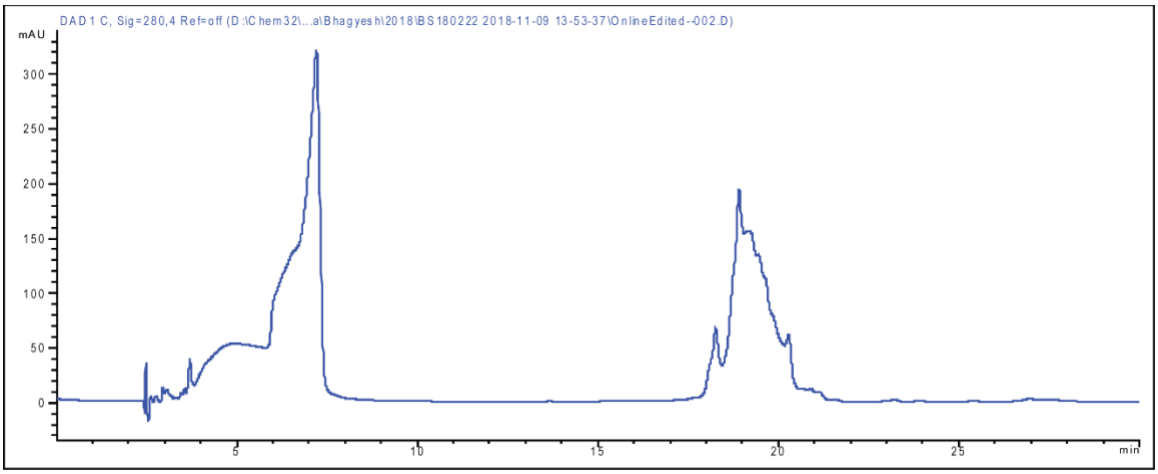

Figure 237: A representative HPLC chromatogram of the crude reaction mixture of ethanedithiol. The desired product is found in the cluster of peaks eluting between 18-20.5'. All chromatograms look very similar and hence only one is shown.

Once after synthesizing and purifying cross-linked species, they will be evaluated for their proteolytic stability by testing against serum or proteases such as pepsin, trypsin, chymotrypsin, carboxypeptidase A comparing with native insulin. The characterization could be performed via gel, HPLC and MS.

Summary and future direction of the project

In Chapter 6, several chemical approaches to improve intracellular delivery of proteins are reported. For protein modifications, enzyme cleavable linkers were used – esters linkages are cleavable by esterases and disulfide linkages are cleavable by glutathione reductase (these are present intracellularly). In addition, the selected linkers are cationic in nature, making the target protein positively charged. Cationic charges help in cytosolic delivery of cargo. For the studies, insulin was used as a model protein because of ease of MS and HPLC characterization and significant experience with the chemistry of insulin. The most recent work involves multiple modifications of insulin using 2-(2-pyridyldithio)ethanol through carbamate linkage and cross-linking the reacted groups through dithiol cross-linkers. I purified doubly modified insulin and performed the cross-linking using several dithiol cross-linkers (Figure 233). The MS characterization is shown in Figure 236. These linkers are neutral in charge and may stabilize the protein from proteases; the next step is to test the stability of these cross-linked species against proteases such as trypsin, chymotrypsin, carboxypeptidase A, pepsin, etc. Finally, we would synthesize cationic dithiol peptides where lysine sequences would offer positive charges flanked by two cysteines required for cross-linking. We would purify cationic cross-linked species and test them for their ability to cross the lipid bilayer and reach the cytosol.

Dear Dr. Sarode:

Thank you for contacting ACS Publications Support.

Your permission request is granted and there is no fee for this reuse. In your planned reuse, you must cite the ACS article as the source, add this direct link <https://pubs.acs.org/doi/10.1021/acs.molpharmaceut.6b00633>, and include a notice to readers that further permissions related to the material excerpted should be directed to the ACS.

I hope this information helped. Please let me know if I can be of further assistance.

Sincerely,

Norvin C. Corbillon
ACS Customer Services and Information
https://help.acs.org/

JOHN WILEY AND SONS LICENSE TERMS AND CONDITIONS

Apr 25, 2019

This Agreement between University of Missouri-Kansas City -- Bhagyesh Sarode ("You") and John Wiley and Sons ("John Wiley and Sons") consists of your license details and the terms and conditions provided by John Wiley and Sons and Copyright Clearance Center.

License Number	4576050454175
License date	Apr 25, 2019
Licensed Content Publisher	John Wiley and Sons
Licensed Content Publication	Macromolecular Bioscience
Licensed Content Title	Polymerizing Insulin with Photocleavable Linkers to Make Light-Sensitive Macropolymer Depot Materials
Licensed Content Author	Bhagyesh R. Sarode, Piyush K. Jain, Simon H. Friedman
Licensed Content Date	May 12, 2016
Licensed Content Volume	16
Licensed Content Issue	8
Licensed Content Pages	9
Type of Use	Dissertation/Thesis
Requestor type	Author of this Wiley article
Format	Print and electronic
Portion	Full article
Will you be translating?	No
Title of your thesis / dissertation	Synthesis, Characterization and In-vivo Testing of Photoactivatable Insulin Depots for Continuously Variable and Minimally Invasive Insulin Delivery
Expected completion date	May 2019
Expected size (number of pages)	
Requestor Location	University of Missouri-Kansas City 2464 Charlotte street HSB, Room 3232 KANSAS CITY, MO 64108 United States Attn: University of Missouri-Kansas City
Publisher Tax ID	EU826007151
Total	**0.00 USD**
Terms and Conditions	

ELSEVIER LICENSE
TERMS AND CONDITIONS

Apr 25, 2019

This Agreement between University of Missouri-Kansas City -- Bhagyesh Sarode ("You") and Elsevier ("Elsevier") consists of your license details and the terms and conditions provided by Elsevier and Copyright Clearance Center.

License Number	4576050562047
License date	Apr 25, 2019
Licensed Content Publisher	Elsevier
Licensed Content Publication	Trends in Pharmacological Sciences
Licensed Content Title	In vivo biodistribution and efficacy of peptide mediated delivery
Licensed Content Author	Peter Järver,Imre Mäger,Ülo Langel
Licensed Content Date	Nov 1, 2010
Licensed Content Volume	31
Licensed Content Issue	11
Licensed Content Pages	8
Start Page	528
End Page	535
Type of Use	reuse in a thesis/dissertation
Intended publisher of new work	other
Portion	figures/tables/illustrations
Number of figures/tables/illustrations	1
Format	both print and electronic
Are you the author of this Elsevier article?	No
Will you be translating?	No
Original figure numbers	Figure 2. Both endocytic, and in certain circumstances, direct translocation routes account for CPP uptake.
Title of your thesis/dissertation	Synthesis, Characterization and In-vivo Testing of Photoactivatable Insulin Depots for Continuously Variable and Minimally Invasive Insulin Delivery
Publisher of new work	University of Missouri-Kansas City
Expected completion date	May 2019
Requestor Location	University of Missouri-Kansas City 2464 Charlotte street HSB, Room 3232 KANSAS CITY, MO 64108 United States Attn: University of Missouri-Kansas City
Publisher Tax ID	98-0397604
Total	**0.00 USD**
Terms and Conditions	

SPRINGER NATURE LICENSE
TERMS AND CONDITIONS

Apr 25, 2019

This Agreement between University of Missouri-Kansas City -- Bhagyesh Sarode ("You") and Springer Nature ("Springer Nature") consists of your license details and the terms and conditions provided by Springer Nature and Copyright Clearance Center.

License Number	4576050698268
License date	Apr 25, 2019
Licensed Content Publisher	Springer Nature
Licensed Content Publication	Nature Reviews Drug Discovery
Licensed Content Title	Pursuit of a perfect insulin
Licensed Content Author	Alexander N. Zaykov, John P. Mayer, Richard D. DiMarchi
Licensed Content Date	Mar 18, 2016
Licensed Content Volume	15
Licensed Content Issue	6
Type of Use	Thesis/Dissertation
Requestor type	academic/university or research institute
Format	print and electronic
Portion	figures/tables/illustrations
Number of figures/tables/illustrations	1
High-res required	no
Will you be translating?	no
Circulation/distribution	<501
Author of this Springer Nature content	no
Title	Synthesis, Characterization and In-vivo Testing of Photoactivatable Insulin Depots for Continuously Variable and Minimally Invasive Insulin Delivery
Institution name	University of Missouri-Kansas City
Expected presentation date	May 2019
Portions	Figure 1: Structure and sequences of human insulin and analogues.
Requestor Location	University of Missouri-Kansas City 2464 Charlotte street HSB, Room 3232 KANSAS CITY, MO 64108 United States Attn: University of Missouri-Kansas City
Total	**0.00 USD**
Terms and Conditions	

SPRINGER NATURE LICENSE
TERMS AND CONDITIONS

Apr 25, 2019

This Agreement between University of Missouri-Kansas City -- Bhagyesh Sarode ("You") and Springer Nature ("Springer Nature") consists of your license details and the terms and conditions provided by Springer Nature and Copyright Clearance Center.

License Number	4576050638454
License date	Apr 25, 2019
Licensed Content Publisher	Springer Nature
Licensed Content Publication	Nature Reviews Drug Discovery
Licensed Content Title	Interfering with disease: a progress report on siRNA-based therapeutics
Licensed Content Author	Antonin de Fougerolles, Hans-Peter Vornlocher, John Maraganore, Judy Lieberman
Licensed Content Date	Jun 1, 2007
Licensed Content Volume	6
Licensed Content Issue	6
Type of Use	Thesis/Dissertation
Requestor type	academic/university or research institute
Format	print and electronic
Portion	figures/tables/illustrations
Number of figures/tables/illustrations	1
High-res required	no
Will you be translating?	no
Circulation/distribution	<501
Author of this Springer Nature content	no
Title	Synthesis, Characterization and In-vivo Testing of Photoactivatable Insulin Depots for Continuously Variable and Minimally Invasive Insulin Delivery
Institution name	University of Missouri-Kansas City
Expected presentation date	May 2019
Portions	Figure 1: Mechanism of RNA interference in mammalian cells.
Requestor Location	University of Missouri-Kansas City 2464 Charlotte street HSB, Room 3232 KANSAS CITY, MO 64108 United States Attn: University of Missouri-Kansas City
Total	**0.00 USD**
Terms and Conditions	

SPRINGER NATURE LICENSE
TERMS AND CONDITIONS

Apr 25, 2019

This Agreement between University of Missouri-Kansas City -- Bhagyesh Sarode ("You") and Springer Nature ("Springer Nature") consists of your license details and the terms and conditions provided by Springer Nature and Copyright Clearance Center.

License Number	4576050755546
License date	Apr 25, 2019
Licensed Content Publisher	Springer Nature
Licensed Content Publication	Nature Reviews Molecular Cell Biology
Licensed Content Title	Regulation of glucose transport by insulin: traffic control of GLUT4
Licensed Content Author	Dara Leto, Alan R. Saltiel
Licensed Content Date	May 23, 2012
Licensed Content Volume	13
Licensed Content Issue	6
Type of Use	Thesis/Dissertation
Requestor type	academic/university or research institute
Format	print and electronic
Portion	figures/tables/illustrations
Number of figures/tables/illustrations	1
High-res required	no
Will you be translating?	no
Circulation/distribution	<501
Author of this Springer Nature content	no
Title	Synthesis, Characterization and In-vivo Testing of Photoactivatable Insulin Depots for Continuously Variable and Minimally Invasive Insulin Delivery
Institution name	University of Missouri-Kansas City
Expected presentation date	May 2019
Portions	The figure in Box 1 | Muscle and adipose tissue in energy homeostasis
Requestor Location	University of Missouri-Kansas City 2464 Charlotte street HSB, Room 3232 KANSAS CITY, MO 64108 United States Attn: University of Missouri-Kansas City
Total	**0.00 USD**
Terms and Conditions	

REFERENCES

1. Sonksen, P.; Sonksen, J. Insulin: Understanding Its Action in Health and Disease. *Br. J. Anaesth.* **2000**, *85*, 69–79. https://doi.org/10.1093/bja/85.1.69.

2. Smith, U. Impaired ('diabetic') Insulin Signaling and Action Occur in Fat Cells Long before Glucose Intolerance--Is Insulin Resistance Initiated in the Adipose Tissue? *Int. J. Obes. Relat. Metab. Disord.* **2002**, *26*, 897–904. https://doi.org/10.1038/sj.ijo.0802028.

3. Tokarz, V. L.; MacDonald, P. E.; Klip, A. The Cell Biology of Systemic Insulin Function. *J. Cell Biol.* **2018**, *217*, 2273–2289. https://doi.org/10.1083/jcb.201802095.

4. Gray, S. M.; Meijer, R. I.; Barrett, E. J. Insulin Regulates Brain Function, but How Does It Get There? *Diabetes* **2014**, *63*, 3992–3997. https://doi.org/10.2337/db14-0340.

5. Leto, D.; Saltiel, A. R. Regulation of Glucose Transport by Insulin: Traffic Control of GLUT4. *Nat. Rev. Mol. Cell Biol.* **2012**, *13*, 383–396. https://doi.org/10.1038/nrm3351.

6. Hua, Q. X.; Shoelson, S. E.; Kochoyan, M.; Weiss, M. A. Receptor Binding Redefined by a Structural Switch in a Mutant Human Insulin. *Nature* **1991**, *354*, 238–241. https://doi.org/10.1038/354238a0.

7. Huang, X. F.; Arvan, P. Intracellular Transport of Proinsulin in Pancreatic Beta-Cells. Structural Maturation Probed by Disulfide Accessibility. *J. Biol. Chem.* **1995**, *270*, 20417–20423. https://doi.org/10.1074/jbc.270.35.20417.

8. Leibiger, B.; Wahlander, K.; Berggren, P. O.; Leibiger, I. B. Glucose-Stimulated Insulin Biosynthesis Depends on Insulin-Stimulated Insulin Gene Transcription. *J. Biol. Chem.* **2000**, *275*, 30153–30156. https://doi.org/10.1074/jbc.M005216200.

9. Zaykov, A. N.; Mayer, J. P.; DiMarchi, R. D. Pursuit of a Perfect Insulin. *Nat. Rev. Drug Discov.* **2016**, *15*, 425–439. https://doi.org/10.1038/nrd.2015.36.

10. Fu, Z.; Gilbert, E. R.; Liu, D. Regulation of Insulin Synthesis and Secretion and Pancreatic Beta-Cell Dysfunction in Diabetes. *Curr. Diabetes Rev.* **2013**, *9*, 25–53. https://doi.org/10.2174/1573399811309010025.

11. Cantley, J.; Ashcroft, F. M. Q&A: Insulin Secretion and Type 2 Diabetes: Why Do β-Cells Fail? *BMC Biol.* **2015**, *13*, 33. https://doi.org/10.1186/s12915-015-0140-6.

12. Teraoku, H.; Lenzen, S. Dynamics of Insulin Secretion from EndoC-BH1 β-Cell Pseudoislets in Response to Glucose and Other Nutrient and Nonnutrient Secretagogues. *J. Diabetes Res.* **2017**, *2017*, 2309630. https://doi.org/10.1155/2017/2309630.

13. Home, P. D. Plasma Insulin Profiles after Subcutaneous Injection: How Close Can We Get to Physiology in People with Diabetes? *Diabetes Obes. Metab.* **2015**, *17*, 1011–1020. https://doi.org/10.1111/dom.12501.

14. Papatheodorou, K.; Papanas, N.; Banach, M.; Papazoglou, D.; Edmonds, M. Complications of Diabetes 2016. *J. Diabetes Res.* **2016**, *2016*, 6989453. https://doi.org/10.1155/2016/6989453.

15. Alberti, K. G.; Zimmet, P. Z. Definition, Diagnosis and Classification of Diabetes Mellitus and Its Complications. Part 1: Diagnosis and Classification of Diabetes Mellitus Provisional Report of a WHO Consultation. *Diabet. Med.* **1998**, *15*, 539–553. https://doi.org/10.1002/(SICI)1096-9136(199807)15:7<539::AID-DIA668>3.0.CO;2-S.

16. Danaei, G.; Finucane, M. M.; Lu, Y.; Singh, G. M.; Cowan, M. J.; Paciorek, C. J.; Lin, J. K.; Farzadfar, F.; Khang, Y.-H.; Stevens, G. A.; et al. National, Regional, and Global Trends in Fasting Plasma Glucose and Diabetes Prevalence since 1980: Systematic Analysis of Health Examination Surveys and Epidemiological Studies with 370 Country-Years and 2·7 Million Participants. *Lancet* **2011**, *378*, 31–40. https://doi.org/10.1016/S0140-6736(11)60679-X.

17. Atkinson, M. A.; Eisenbarth, G. S.; Michels, A. W. Type 1 Diabetes. *Lancet* **2014**, *383*, 69–82. https://doi.org/10.1016/S0140-6736(13)60591-7.

18. Chiang, J. L.; Kirkman, M. S.; Laffel, L. M. B.; Peters, A. L.; Type 1 Diabetes Sourcebook Authors. Type 1 Diabetes through the Life Span: A Position Statement of the American Diabetes Association. *Diabetes Care* **2014**, *37*, 2034–2054. https://doi.org/10.2337/dc14-1140.

19. Orozco, L. J.; Buchleitner, A. M.; Gimenez-Perez, G.; Roqué I Figuls, M.; Richter, B.; Mauricio, D. Exercise or Exercise and Diet for Preventing Type 2 Diabetes Mellitus. *Cochrane Database Syst. Rev.* **2008**, No. 3, CD003054. https://doi.org/10.1002/14651858.CD003054.pub3.

20. Diabetes Control and Complications Trial Research Group; Nathan, D. M.; Genuth, S.; Lachin, J.; Cleary, P.; Crofford, O.; Davis, M.; Rand, L.; Siebert, C. The Effect of Intensive Treatment of Diabetes on the Development and Progression of Long-Term Complications in Insulin-Dependent Diabetes Mellitus. *N. Engl. J. Med.* **1993**, *329*, 977–986. https://doi.org/10.1056/NEJM199309303291401.

21. Evans, M.; Schumm-Draeger, P. M.; Vora, J.; King, A. B. A Review of Modern Insulin Analogue Pharmacokinetic and Pharmacodynamic Profiles in Type 2 Diabetes: Improvements and Limitations. *Diabetes Obes. Metab.* **2011**, *13*, 677–684. https://doi.org/10.1111/j.1463-1326.2011.01395.x.

22. Kaplan, W.; Rodriguez, L. M.; Smith, O. E.; Haymond, M. W.; Heptulla, R. A. Effects of Mixing Glargine and Short-Acting Insulin Analogs on Glucose Control. *Diabetes Care* **2004**, *27*, 2739–2740.

23. Hirsch, I. B. Insulin Analogues. *N. Engl. J. Med.* **2005**, *352*, 174–183. https://doi.org/10.1056/NEJMra040832.

24. Shah, R. B.; Patel, M.; Maahs, D. M.; Shah, V. N. Insulin Delivery Methods: Past, Present and Future. *Int. J. Pharm. Investig.* **2016**, *6*, 1–9. https://doi.org/10.4103/2230-973X.176456.

25. Al-Tabakha, M. M.; Arida, A. I. Recent Challenges in Insulin Delivery Systems: A Review. *Indian J. Pharm. Sci.* **2008**, *70*, 278–286. https://doi.org/10.4103/0250-474X.42968.

26. Colquitt, J. L.; Green, C.; Sidhu, M. K.; Hartwell, D.; Waugh, N. Clinical and Cost-Effectiveness of Continuous Subcutaneous Insulin Infusion for Diabetes. *Health Technol. Assess.* **2004**, *8*, iii, 1–171. https://doi.org/10.3310/hta8430.

27. Retnakaran, R.; Hochman, J.; DeVries, J. H.; Hanaire-Broutin, H.; Heine, R. J.; Melki, V.; Zinman, B. Continuous Subcutaneous Insulin Infusion versus Multiple Daily Injections: The Impact of Baseline A1c. *Diabetes Care* **2004**, *27*, 2590–2596. https://doi.org/10.2337/diacare.27.11.2590.

28. Millstein, R.; Becerra, N. M.; Shubrook, J. H. Insulin Pumps: Beyond Basal-Bolus. *Cleve. Clin. J. Med.* **2015**, *82*, 835–842. https://doi.org/10.3949/ccjm.82a.14127.

29. Jain, P. K.; Karunakaran, D.; Friedman, S. H. Construction of a Photoactivated Insulin Depot. *Angew. Chem.* **2013**, *52*, 1404–1409. https://doi.org/10.1002/anie.201207264.

30. Klán, P.; Šolomek, T.; Bochet, C. G.; Blanc, A.; Givens, R.; Rubina, M.; Popik, V.; Kostikov, A.; Wirz, J. Photoremovable Protecting Groups in Chemistry and Biology: Reaction Mechanisms and Efficacy. *Chem. Rev.* **2013**, *113*, 119–191. https://doi.org/10.1021/cr300177k.

31. Hermkens, P. H. H.; Ottenheijm, H. C. J.; Rees, D. Solid-Phase Organic Reactions: A Review of the Recent Literature. *Tetrahedron* **1996**, *52*, 4527–4554. https://doi.org/10.1016/0040-4020(96)00216-5.

32. Shah, S.; Rangarajan, S.; Friedman, S. H. Light-Activated RNA Interference. *Angew. Chem.* **2005**, *44*, 1328–1332. https://doi.org/10.1002/anie.200461458.

33. Shah, S.; Jain, P. K.; Kala, A.; Karunakaran, D.; Friedman, S. H. Light-Activated RNA Interference Using Double-Stranded SiRNA Precursors Modified Using a Remarkable Regiospecificity of Diazo-Based Photolabile Groups. *Nucleic Acids Res.* **2009**, *37*, 4508–4517. https://doi.org/10.1093/nar/gkp415.

34. Jain, P. K.; Shah, S.; Friedman, S. H. Patterning of Gene Expression Using New Photolabile Groups Applied to Light Activated RNAi. *J. Am. Chem. Soc.* **2011**, *133*, 440–446. https://doi.org/10.1021/ja107226e.

35. Kala, A.; Jain, P. K.; Friedman, S. H. Patterning of Cells through Patterning of Biology. *Mol. Biosyst.* **2014**, *10*, 1689–1692. https://doi.org/10.1039/c3mb70587k.

36. Holmes, C. P. Model Studies for New O-Nitrobenzyl Photolabile Linkers: Substituent Effects on the Rates of Photochemical Cleavage. *J. Org. Chem.* **1997**, *62*, 2370–2380. https://doi.org/10.1021/jo961602x.

37. Ito, K.; Maruyama, J. Studies on Stable Diazoalkanes as Potential Fluorogenic Reagents. II. Ring-Fused 4-Diazomethylcoumarins. *Chem. Pharm. Bull.* **1986**, *34*, 390–395. https://doi.org/10.1248/cpb.34.390.

38. Chou, D. H.-C.; Webber, M. J.; Tang, B. C.; Lin, A. B.; Thapa, L. S.; Deng, D.; Truong, J. V.; Cortinas, A. B.; Langer, R.; Anderson, D. G. Glucose-Responsive Insulin Activity by Covalent Modification with Aliphatic Phenylboronic Acid Conjugates. *Proc Natl Acad Sci USA* **2015**, *112*, 2401. https://doi.org/10.1073/pnas.1424684112.

39. Agard, N. J.; Prescher, J. A.; Bertozzi, C. R. A Strain-Promoted [3 + 2] Azide−Alkyne Cycloaddition for Covalent Modification of Biomolecules in Living Systems. *J. Am. Chem. Soc.* **2004**, *126*, 15046–15047. https://doi.org/10.1021/ja044996f.

40. Jewett, J. C.; Bertozzi, C. R. Cu-Free Click Cycloaddition Reactions in Chemical Biology. *Chem. Soc. Rev.* **2010**, *39*, 1272–1279. https://doi.org/10.1039/B901970G.

41. Alconcel, S. N. S.; Baas, A. S.; Maynard, H. D. FDA-Approved Poly(Ethylene Glycol)–Protein Conjugate Drugs. *Polym. Chem.* **2011**, *2*, 1442. https://doi.org/10.1039/c1py00034a.

42. Webster, R.; Elliott, V.; Park, B. K.; Walker, D.; Hankin, M.; Taupin, P. PEG and PEG Conjugates Toxicity: Towards an Understanding of the Toxicity of PEG and Its Relevance to PEGylated Biologicals. In *PEGylated Protein Drugs: Basic Science and Clinical Applications*; Veronese, F. M., Ed.; Birkhäuser Basel: Basel, 2009; pp 127–146. https://doi.org/10.1007/978-3-7643-8679-5_8.

43. Qin, A.; Lam, J. W. Y.; Tang, B. Z. Click Polymerization. *Chem. Soc. Rev.* **2010**, *39*, 2522–2544. https://doi.org/10.1039/b909064a.

44. Le Droumaguet, B.; Velonia, K. Click Chemistry: A Powerful Tool to Create Polymer-Based Macromolecular Chimeras. *Macromol. Rapid Commun.* **2008**, *29*, 1073–1089. https://doi.org/10.1002/marc.200800155.

45. Arseneault, M.; Wafer, C.; Morin, J.-F. Recent Advances in Click Chemistry Applied to Dendrimer Synthesis. *Molecules* **2015**, *20*, 9263–9294. https://doi.org/10.3390/molecules20059263.

46. Golas, P. L.; Matyjaszewski, K. Marrying Click Chemistry with Polymerization: Expanding the Scope of Polymeric Materials. *Chem. Soc. Rev.* **2010**, *39*, 1338–1354. https://doi.org/10.1039/b901978m.

47. Tasdelen, M. A. Diels–Alder "Click" Reactions: Recent Applications in Polymer and Material Science. *Polym. Chem.* **2011**, *2*, 2133. https://doi.org/10.1039/c1py00041a.

48. Binder, W. H.; Sachsenhofer, R. 'Click' Chemistry in Polymer and Material Science: An Update. *Macromol. Rapid Commun.* **2008**, *29*, 952–981. https://doi.org/10.1002/marc.200800089.

49. Benson, S. W. *The Foundations of Chemical Kinetics*; R.E. Krieger: Malabar, Fla, 1982.

50. Smith, G. D.; Swenson, D. C.; Dodson, E. J.; Dodson, G. G.; Reynolds, C. D. Structural Stability in the 4-Zinc Human Insulin Hexamer. *Proc. Natl. Acad. Sci. U.S.A.* **1984**, *81*, 7093–7097. https://doi.org/10.1073/pnas.81.22.7093.

51. Xu, Y.; Yan, Y.; Seeman, D.; Sun, L.; Dubin, P. L. Multimerization and Aggregation of Native-State Insulin: Effect of Zinc. *Langmuir* **2012**, *28*, 579–586. https://doi.org/10.1021/la202902a.

52. Simpson, D.; McCormack, P. L.; Keating, G. M.; Lyseng-Williamson, K. A. Insulin Lispro: A Review of Its Use in the Management of Diabetes Mellitus. *Drugs* **2007**, *67*, 407–434. https://doi.org/10.2165/00003495-200767030-00006.

53. Manallack, D. T.; Andrews, P. R.; Woods, E. F. Design, Synthesis, and Testing of Insulin Hexamer-Stabilizing Agents. *J. Med. Chem.* **1985**, *28*, 1522–1526. https://doi.org/DOI: 10.1021/jm00148a025.

54. Dunn, M. F. Zinc-Ligand Interactions Modulate Assembly and Stability of the Insulin Hexamer-a Review. *Biometals* **2005**, *18*, 295–303. https://doi.org/10.1007/s10534-005-3685-y.

55. Berenson, D. F.; Weiss, A. R.; Wan, Z.-L.; Weiss, M. A. Insulin Analogs for the Treatment of Diabetes Mellitus: Therapeutic Applications of Protein Engineering. *Ann. N. Y. Acad. Sci.* **2011**, *1243*, E40–E54. https://doi.org/10.1111/j.1749-6632.2012.06468.x.

56. Noble, S. L.; Johnston, E.; Walton, B. Insulin Lispro: A Fast-Acting Insulin Analog. *Am. Fam. Physician* **1998**, *57*, 279–286, 289–292.

57. Worrall, D. S.; Olefsky, J. M. The Effects of Intracellular Calcium Depletion on Insulin Signaling in 3T3-L1 Adipocytes. *Mol. Endocrinol.* **2002**, *16*, 378–389. https://doi.org/10.1210/mend.16.2.0776.

58. Sweeney, G.; Somwar, R.; Ramlal, T.; Volchuk, A.; Ueyama, A.; Klip, A. An Inhibitor of P38 Mitogen-Activated Protein Kinase Prevents Insulin-Stimulated Glucose Transport but Not Glucose Transporter Translocation in 3T3-L1 Adipocytes and L6 Myotubes. *J. Biol. Chem.* **1999**, *274*, 10071–10078. https://doi.org/10.1074/jbc.274.15.10071.

59. Chavez, J. A.; Summers, S. A. Characterizing the Effects of Saturated Fatty Acids on Insulin Signaling and Ceramide and Diacylglycerol Accumulation in 3T3-L1 Adipocytes and C2C12 Myotubes. *Arch. Biochem. Biophys.* **2003**, *419*, 101–109. https://doi.org/10.1016/j.abb.2003.08.020.

60. Wang, Y.; Nishina, P. M.; Naggert, J. K. Degradation of IRS1 Leads to Impaired Glucose Uptake in Adipose Tissue of the Type 2 Diabetes Mouse Model TALLYHO/Jng. *J. Endocrinol.* **2009**, *203*, 65–74. https://doi.org/10.1677/JOE-09-0026.

61. Fang, X.-K.; Gao, J.; Zhu, D.-N. Kaempferol and Quercetin Isolated from Euonymus Alatus Improve Glucose Uptake of 3T3-L1 Cells without Adipogenesis Activity. *Life Sci.* **2008**, *82*, 615–622. https://doi.org/10.1016/j.lfs.2007.12.021.

62. Wu, X.; Ge, H.; Lemon, B.; Weiszmann, J.; Gupte, J.; Hawkins, N.; Li, X.; Tang, J.; Lindberg, R.; Li, Y. Selective Activation of FGFR4 by an FGF19 Variant Does Not Improve Glucose Metabolism in Ob/Ob Mice. *Proc. Natl. Acad. Sci. U.S.A.* **2009**, *106*, 14379–14384. https://doi.org/10.1073/pnas.0907812106.

63. Li, L.-S.; Babendure, J. L.; Sinha, S. C.; Olefsky, J. M.; Lerner, R. A. Synthesis and Evaluation of Photolabile Insulin Prodrugs. *Bioorg. Med. Chem. Lett.* **2005**, *15*, 3917–3920. https://doi.org/10.1016/j.bmcl.2005.05.112.

64. Lenzen, S. The Mechanisms of Alloxan- and Streptozotocin-Induced Diabetes. *Diabetologia* **2008**, *51*, 216–226. https://doi.org/10.1007/s00125-007-0886-7.

65. Szkudelski, T. The Mechanism of Alloxan and Streptozotocin Action in B Cells of the Rat Pancreas. *Physiol. Res.* **2001**, *50*, 537–546.

66. Baskin, J. M.; Prescher, J. A.; Laughlin, S. T.; Agard, N. J.; Chang, P. V.; Miller, I. A.; Lo, A.; Codelli, J. A.; Bertozzi, C. R. Copper-Free Click Chemistry for Dynamic in Vivo Imaging. *Proc. Natl. Acad. Sci. U.S.A.* **2007**, *104*, 16793–16797. https://doi.org/10.1073/pnas.0707090104.

67. Chang, P. V.; Prescher, J. A.; Sletten, E. M.; Baskin, J. M.; Miller, I. A.; Agard, N. J.; Lo, A.; Bertozzi, C. R. Copper-Free Click Chemistry in Living Animals. *Proc. Natl. Acad. Sci. U.S.A.* **2010**, *107*, 1821–1826. https://doi.org/10.1073/pnas.0911116107.

68. Codelli, J. A.; Baskin, J. M.; Agard, N. J.; Bertozzi, C. R. Second-Generation Difluorinated Cyclooctynes for Copper-Free Click Chemistry. *J. Am. Chem. Soc.* **2008**, *130*, 11486–11493. https://doi.org/10.1021/ja803086r.

69. Jewett, J. C.; Sletten, E. M.; Bertozzi, C. R. Rapid Cu-Free Click Chemistry with Readily Synthesized Biarylazacyclooctynones. *J. Am. Chem. Soc.* **2010**, *132*, 3688–3690. https://doi.org/10.1021/ja100014q.

70. Liu, L.; Zhou, C.; Xia, X.; Liu, Y. Self-Assembled Lecithin/Chitosan Nanoparticles for Oral Insulin Delivery: Preparation and Functional Evaluation. *Int. J. Nanomed.* **2016**, *11*, 761–769. https://doi.org/10.2147/IJN.S96146.

71. Qinna, N. A.; Badwan, A. A. Impact of Streptozotocin on Altering Normal Glucose Homeostasis during Insulin Testing in Diabetic Rats Compared to Normoglycemic Rats. *Drug Des. Dev. Ther.* **2015**, *9*, 2515–2525. https://doi.org/10.2147/DDDT.S79885.

72. Sonaje, K.; Lin, K.-J.; Wey, S.-P.; Lin, C.-K.; Yeh, T.-H.; Nguyen, H.-N.; Hsu, C.-W.; Yen, T.-C.; Juang, J.-H.; Sung, H.-W. Biodistribution, Pharmacodynamics and Pharmacokinetics of Insulin Analogues in a Rat Model: Oral Delivery Using PH-Responsive Nanoparticles vs. Subcutaneous Injection. *Biomaterials* **2010**, *31*, 6849–6858. https://doi.org/10.1016/j.biomaterials.2010.05.042.

73. Sarode, B. R.; Kover, K.; Tong, P. Y.; Zhang, C.; Friedman, S. H. Light Control of Insulin Release and Blood Glucose Using an Injectable Photoactivated Depot. *Mol. Pharm.* **2016**, *13*, 3835–3841. https://doi.org/10.1021/acs.molpharmaceut.6b00633.

74. Kvam, E.; Tyrrell, R. M. Induction of Oxidative DNA Base Damage in Human Skin Cells by UV and near Visible Radiation. *Carcinogenesis* **1997**, *18*, 2379–2384. https://doi.org/10.1093/carcin/18.12.2379.

75. Enninga, I. C.; Groenendijk, R. T. L.; Filon, A. R.; Zeeland, A. A. van; Simons, J. W. I. M. The Wavelength Dependence of u.v.-Induced Pyrimidine Dimer Formation, Cell Killing and Mutation Induction in Human Diploid Skin Fibroblasts. *Carcinogenesis* **1986**, *7*, 1829–1836. https://doi.org/10.1093/carcin/7.11.1829.

76. Tyrrell, R. M.; Pidoux, M. Singlet Oxygen Involvement in the Inactivation of Cultured Human Fibroblasts by UVA (334 Nm, 365 Nm) and near-Visible (405 Nm) Radiations. *Photochem. Photobiol.* **1989**, *49*, 407–412. https://doi.org/10.1111/j.1751-1097.1989.tb09187.x.

77. D'Orazio, J.; Jarrett, S.; Amaro-Ortiz, A.; Scott, T. UV Radiation and the Skin. *Int. J. Mol. Sci.* **2013**, *14*, 12222–12248. https://doi.org/10.3390/ijms140612222.

78. de Gruijl, F. R. Skin Cancer and Solar UV Radiation. *Eur. J. Cancer* **1999**, *35*, 2003–2009. https://doi.org/10.1016/S0959-8049(99)00283-X.

79. Armstrong, B. K.; Kricker, A. The Epidemiology of UV Induced Skin Cancer. *J. Photochem. Photobiol.* **2001**, *63*, 8–18. https://doi.org/10.1016/S1011-1344(01)00198-1.

80. Wieboldt, R.; Ramesh, D.; Jabri, E.; Karplus, P. A.; Carpenter, B. K.; Hess, G. P. Synthesis and Characterization of Photolabile O-Nitrobenzyl Derivatives of Urea. *J. Org. Chem.* **2002**, *67*, 8827–8831. https://doi.org/10.1021/jo0201373.

81. Bley, F.; Schaper, K.; Görner, H. Photoprocesses of Molecules with 2-Nitrobenzyl Protecting Groups and Caged Organic Acids. *Photochem. Photobiol.* **2008**, *84*, 162–171. https://doi.org/10.1111/j.1751-1097.2007.00215.x.

82. Swann, P. F. The Toxicology of Nitrate, Nitrite Andn-Nitroso Compounds. *J. Sci. Food Agric.* **1975**, *26*, 1761–1770. https://doi.org/10.1002/jsfa.2740261119.

83. Loh, Y. H.; Jakszyn, P.; Luben, R. N.; Mulligan, A. A.; Mitrou, P. N.; Khaw, K.-T. N-Nitroso Compounds and Cancer Incidence: The European Prospective Investigation into Cancer and Nutrition (EPIC)-Norfolk Study. *Am. J. Clin. Nutr.* **2011**, *93*, 1053–1061. https://doi.org/10.3945/ajcn.111.012377.

84. Furuta, T.; Wang, S. S.; Dantzker, J. L.; Dore, T. M.; Bybee, W. J.; Callaway, E. M.; Denk, W.; Tsien, R. Y. Brominated 7-Hydroxycoumarin-4-Ylmethyls: Photolabile Protecting Groups with Biologically Useful Cross-Sections for Two Photon Photolysis. *Proc. Natl. Acad. Sci. U.S.A.* **1999**, *96*, 1193–1200. https://doi.org/10.1073/pnas.96.4.1193.

85. Jung, H. S.; Han, J.; Lee, J.-H.; Lee, J. H.; Choi, J.-M.; Kweon, H.-S.; Han, J. H.; Kim, J.-H.; Byun, K. M.; Jung, J. H.; et al. Enhanced NIR Radiation-Triggered Hyperthermia by Mitochondrial Targeting. *J. Am. Chem. Soc.* **2015**, *137*, 3017–3023. https://doi.org/10.1021/ja5122809.

86. Hagen, V.; Dekowski, B.; Nache, V.; Schmidt, R.; Geissler, D.; Lorenz, D.; Eichhorst, J.; Keller, S.; Kaneko, H.; Benndorf, K.; et al. Coumarinylmethyl Esters for Ultrafast Release of High Concentrations of Cyclic Nucleotides upon One- and Two-Photon Photolysis. *Angew. Chem.* **2005**, *44*, 7887–7891. https://doi.org/10.1002/anie.200502411.

87. Geissler, D.; Kresse, W.; Wiesner, B.; Bendig, J.; Kettenmann, H.; Hagen, V. DMACM-Caged Adenosine Nucleotides: Ultrafast Phototriggers for ATP, ADP, and AMP Activated by Long-Wavelength Irradiation. *ChemBioChem* **2003**, *4*, 162–170. https://doi.org/10.1002/cbic.200390027.

88. Huang, Q.; Bao, C.; Ji, W.; Wang, Q.; Zhu, L. Photocleavable Coumarin Crosslinkers Based Polystyrene Microgels: Phototriggered Swelling and Release. *J. Mater. Chem.* **2012**, *22*, 18275. https://doi.org/10.1039/c2jm33789d.

89. Fournier, L.; Aujard, I.; Le Saux, T.; Maurin, S.; Beaupierre, S.; Baudin, J.-B.; Jullien, L. Coumarinylmethyl Caging Groups with Redshifted Absorption. *Chem.: Eur. J.* **2013**, *19*, 17494–17507. https://doi.org/10.1002/chem.201302630.

90. Fournier, L.; Gauron, C.; Xu, L.; Aujard, I.; Le Saux, T.; Gagey-Eilstein, N.; Maurin, S.; Dubruille, S.; Baudin, J.-B.; Bensimon, D.; et al. A Blue-Absorbing

Photolabile Protecting Group for in Vivo Chromatically Orthogonal Photoactivation. *ACS Chem. Biol.* **2013**, *8*, 1528–1536. https://doi.org/10.1021/cb400178m.

91. Holzer, A. M.; Athar, M.; Elmets, C. A. The Other End of the Rainbow: Infrared and Skin. *J. Investig. Dermatol.* **2010**, *130*, 1496–1499. https://doi.org/10.1038/jid.2010.79.

92. Shembekar, V. R.; Chen, Y.; Carpenter, B. K.; Hess, G. P. A Protecting Group for Carboxylic Acids That Can Be Photolyzed by Visible Light. *Biochemistry* **2005**, *44*, 7107–7114. https://doi.org/10.1021/bi047665o.

93. Babin, J.; Pelletier, M.; Lepage, M.; Allard, J.-F.; Morris, D.; Zhao, Y. A New Two-Photon-Sensitive Block Copolymer Nanocarrier. *Angew. Chem.* **2009**, *48*, 3329–3332. https://doi.org/10.1002/anie.200900255.

94. Eckardt, T.; Hagen, V.; Schade, B.; Schmidt, R.; Schweitzer, C.; Bendig, J. Deactivation Behavior and Excited-State Properties of (Coumarin-4-Yl)Methyl Derivatives. 2. Photocleavage of Selected (Coumarin-4-Yl)Methyl-Caged Adenosine Cyclic 3',5'-Monophosphates with Fluorescence Enhancement. *J. Org. Chem.* **2002**, *67*, 703–710. https://doi.org/10.1021/jo010692p.

95. Siddiki, A. A.; Takale, B. S.; Telvekar, V. N. One Pot Synthesis of Aromatic Azide Using Sodium Nitrite and Hydrazine Hydrate. *Tetrahedron Lett.* **2013**, *54*, 1294–1297. https://doi.org/10.1016/j.tetlet.2012.12.112.

96. Azagarsamy, M. A.; Anseth, K. S. Wavelength-Controlled Photocleavage for the Orthogonal and Sequential Release of Multiple Proteins. *Angew. Chem.* **2013**, *52*, 13803–13807. https://doi.org/10.1002/anie.201308174.

97. Thorson, M. K.; Majtan, T.; Kraus, J. P.; Barrios, A. M. Identification of Cystathionine β-Synthase Inhibitors Using a Hydrogen Sulfide Selective Probe. *Angew. Chem.* **2013**, *52*, 4641–4644. https://doi.org/10.1002/anie.201300841.

98. Lai, Y.-T.; Chang, Y.-Y.; Hu, L.; Yang, Y.; Chao, A.; Du, Z.-Y.; Tanner, J. A.; Chye, M.-L.; Qian, C.; Ng, K.-M.; et al. Rapid Labeling of Intracellular His-Tagged Proteins in Living Cells. *Proc. Natl. Acad. Sci. U.S.A.* **2015**, *112*, 2948–2953. https://doi.org/10.1073/pnas.1419598112.

99. Agrawal, N.; Dasaradhi, P. V. N.; Mohmmed, A.; Malhotra, P.; Bhatnagar, R. K.; Mukherjee, S. K. RNA Interference: Biology, Mechanism, and Applications. *Microbiol. Mol. Biol. Rev.* **2003**, *67*, 657–685. https://doi.org/10.1128/MMBR.67.4.657-685.2003.

100. Fire, A.; Xu, S.; Montgomery, M. K.; Kostas, S. A.; Driver, S. E.; Mello, C. C. Potent and Specific Genetic Interference by Double-Stranded RNA in Caenorhabditis Elegans. *Nature* **1998**, *391*, 806–811. https://doi.org/10.1038/35888.

101. Macfarlane, L.-A.; Murphy, P. R. MicroRNA: Biogenesis, Function and Role in Cancer. *Curr. Genom.* **2010**, *11*, 537–561. https://doi.org/10.2174/138920210793175895.

102. Lu, M.; Zhang, Q.; Deng, M.; Miao, J.; Guo, Y.; Gao, W.; Cui, Q. An Analysis of Human MicroRNA and Disease Associations. *PLoS One* **2008**, *3*, e3420. https://doi.org/10.1371/journal.pone.0003420.

103. Ozcan, G.; Ozpolat, B.; Coleman, R. L.; Sood, A. K.; Lopez-Berestein, G. Preclinical and Clinical Development of SiRNA-Based Therapeutics. *Adv. Drug Deliv. Rev.* **2015**, *87*, 108–119. https://doi.org/10.1016/j.addr.2015.01.007.

104. Gavrilov, K.; Saltzman, W. M. Therapeutic SiRNA: Principles, Challenges, and Strategies. *Yale J. Biol. Med.* **2012**, *85*, 187–200.

105. de Fougerolles, A.; Vornlocher, H.-P.; Maraganore, J.; Lieberman, J. Interfering with Disease: A Progress Report on SiRNA-Based Therapeutics. *Nat. Rev. Drug Discov.* **2007**, *6*, 443–453. https://doi.org/10.1038/nrd2310.

106. Jackson, A. L.; Linsley, P. S. Recognizing and Avoiding SiRNA Off-Target Effects for Target Identification and Therapeutic Application. *Nat. Rev. Drug Discov.* **2010**, *9*, 57–67. https://doi.org/10.1038/nrd3010.

107. Shestopalov, I. A.; Sinha, S.; Chen, J. K. Light-Controlled Gene Silencing in Zebrafish Embryos. *Nat. Chem. Biol.* **2007**, *3*, 650–651. https://doi.org/10.1038/nchembio.2007.30.

108. Tang, X.; Maegawa, S.; Weinberg, E. S.; Dmochowski, I. J. Regulating Gene Expression in Zebrafish Embryos Using Light-Activated, Negatively Charged Peptide Nucleic Acids. *J. Am. Chem. Soc.* **2007**, *129*, 11000–11001. https://doi.org/10.1021/ja073723s.

109. Lucas, T.; Schäfer, F.; Müller, P.; Eming, S. A.; Heckel, A.; Dimmeler, S. Light-Inducible AntimiR-92a as a Therapeutic Strategy to Promote Skin Repair in Healing-Impaired Diabetic Mice. *Nat. Commun.* **2017**, *8*, 15162. https://doi.org/10.1038/ncomms15162.

110. Tan, X.; Li, B. B.; Lu, X.; Jia, F.; Santori, C.; Menon, P.; Li, H.; Zhang, B.; Zhao, J. J.; Zhang, K. Light-Triggered, Self-Immolative Nucleic Acid-Drug Nanostructures. *J. Am. Chem. Soc.* **2015**, *137*, 6112–6115. https://doi.org/10.1021/jacs.5b00795.

111. Ankenbruck, N.; Courtney, T.; Naro, Y.; Deiters, A. Optochemical Control of Biological Processes in Cells and Animals. *Angew. Chem.* **2018**, *57*, 2768–2798. https://doi.org/10.1002/anie.201700171.

112. Wang, J.; Lu, Z.; Wientjes, M. G.; Au, J. L.-S. Delivery of SiRNA Therapeutics: Barriers and Carriers. *AAPS J.* **2010**, *12*, 492–503. https://doi.org/10.1208/s12248-010-9210-4.

113. Wittrup, A.; Lieberman, J. Knocking down Disease: A Progress Report on SiRNA Therapeutics. *Nat. Rev. Genet.* **2015**, *16*, 543–552. https://doi.org/10.1038/nrg3978.

114. Kanasty, R.; Dorkin, J. R.; Vegas, A.; Anderson, D. Delivery Materials for SiRNA Therapeutics. *Nat. Mater.* **2013**, *12*, 967–977. https://doi.org/10.1038/nmat3765.

115. Lorenzer, C.; Dirin, M.; Winkler, A.-M.; Baumann, V.; Winkler, J. Going beyond the Liver: Progress and Challenges of Targeted Delivery of SiRNA Therapeutics. *J. Control. Release* **2015**, *203*, 1–15. https://doi.org/10.1016/j.jconrel.2015.02.003.

116. Rejman, J.; Oberle, V.; Zuhorn, I. S.; Hoekstra, D. Size-Dependent Internalization of Particles via the Pathways of Clathrin- and Caveolae-Mediated Endocytosis. *Biochem. J.* **2004**, *377*, 159–169. https://doi.org/10.1042/BJ20031253.

117. dos Santos, T.; Varela, J.; Lynch, I.; Salvati, A.; Dawson, K. A. Quantitative Assessment of the Comparative Nanoparticle-Uptake Efficiency of a Range of Cell Lines. *Small* **2011**, *7*, 3341–3349. https://doi.org/10.1002/smll.201101076.

118. Smith, P. J.; Giroud, M.; Wiggins, H. L.; Gower, F.; Thorley, J. A.; Stolpe, B.; Mazzolini, J.; Dyson, R. J.; Rappoport, J. Z. Cellular Entry of Nanoparticles via Serum Sensitive Clathrin-Mediated Endocytosis, and Plasma Membrane Permeabilization. *Int. J. Nanomed.* **2012**, *7*, 2045–2055. https://doi.org/10.2147/IJN.S29334.

119. Ekkapongpisit, M.; Giovia, A.; Follo, C.; Caputo, G.; Isidoro, C. Biocompatibility, Endocytosis, and Intracellular Trafficking of Mesoporous Silica and Polystyrene Nanoparticles in Ovarian Cancer Cells: Effects of Size and Surface Charge Groups. *Int. J. Nanomed.* **2012**, *7*, 4147–4158. https://doi.org/10.2147/IJN.S33803.

120. Ekkapongpisit, M.; Giovia, A.; Nicotra, G.; Ozzano, M.; Caputo, G.; Isidoro, C. Labeling and Exocytosis of Secretory Compartments in RBL Mastocytes by Polystyrene and Mesoporous Silica Nanoparticles. *Int. J. Nanomed.* **2012**, *7*, 1829–1840. https://doi.org/10.2147/IJN.S29034.

121. Lai, S. K.; Hida, K.; Chen, C.; Hanes, J. Characterization of the Intracellular Dynamics of a Non-Degradative Pathway Accessed by Polymer Nanoparticles. *J. Control. Release* **2008**, *125*, 107–111. https://doi.org/10.1016/j.jconrel.2007.10.015.

122. Lorenz, M. R.; Holzapfel, V.; Musyanovych, A.; Nothelfer, K.; Walther, P.; Frank, H.; Landfester, K.; Schrezenmeier, H.; Mailänder, V. Uptake of Functionalized, Fluorescent-Labeled Polymeric Particles in Different Cell Lines and Stem Cells.

Biomaterials **2006**, *27*, 2820–2828. https://doi.org/10.1016/j.biomaterials.2005.12.022.

123. Musyanovych, A.; Schmitz-Wienke, J.; Mailänder, V.; Walther, P.; Landfester, K. Preparation of Biodegradable Polymer Nanoparticles by Miniemulsion Technique and Their Cell Interactions. *Macromol. Biosci.* **2008**, *8*, 127–139. https://doi.org/10.1002/mabi.200700241.

124. Liu, Y.; Li, W.; Lao, F.; Liu, Y.; Wang, L.; Bai, R.; Zhao, Y.; Chen, C. Intracellular Dynamics of Cationic and Anionic Polystyrene Nanoparticles without Direct Interaction with Mitotic Spindle and Chromosomes. *Biomaterials* **2011**, *32*, 8291–8303. https://doi.org/10.1016/j.biomaterials.2011.07.037.

125. Prabha, S.; Zhou, W.-Z.; Panyam, J.; Labhasetwar, V. Size-Dependency of Nanoparticle-Mediated Gene Transfection: Studies with Fractionated Nanoparticles. *Int. J. Pharm.* **2002**, *244*, 105–115. https://doi.org/10.1016/S0378-5173(02)00315-0.

126. Patil, Y.; Panyam, J. Polymeric Nanoparticles for SiRNA Delivery and Gene Silencing. *Int. J. Pharm.* **2009**, *367*, 195–203. https://doi.org/10.1016/j.ijpharm.2008.09.039.

127. Tahara, K.; Yamamoto, H.; Hirashima, N.; Kawashima, Y. Chitosan-Modified Poly(D,L-Lactide-Co-Glycolide) Nanospheres for Improving SiRNA Delivery and Gene-Silencing Effects. *Eur. J. Pharm. Biopharm.* **2010**, *74*, 421–426. https://doi.org/10.1016/j.ejpb.2009.12.007.

128. Makadia, H. K.; Siegel, S. J. Poly Lactic-Co-Glycolic Acid (PLGA) as Biodegradable Controlled Drug Delivery Carrier. *Polymers* **2011**, *3*, 1377–1397. https://doi.org/10.3390/polym3031377.

129. Kala, A.; Jain, P. K.; Karunakaran, D.; Shah, S.; Friedman, S. H. The Synthesis of Tetra-Modified RNA for the Multidimensional Control of Gene Expression via Light-Activated RNA Interference. *Nat. Protoc.* **2014**, *9*, 11–20. https://doi.org/10.1038/nprot.2013.165.

130. Sarode, B. R.; Jain, P. K.; Friedman, S. H. Polymerizing Insulin with Photocleavable Linkers to Make Light-Sensitive Macropolymer Depot Materials. *Macromol Biosci* **2016**, *16*, 1138–1146. https://doi.org/10.1002/mabi.201500471.

131. Kinch, M. S. An Overview of FDA-Approved Biologics Medicines. *Drug Discov. Today* **2015**, *20*, 393–398. https://doi.org/10.1016/j.drudis.2014.09.003.

132. Reichert, J. M. Trends in Development and Approval Times for New Therapeutics in the United States. *Nat. Rev. Drug Discov.* **2003**, *2*, 695–702. https://doi.org/10.1038/nrd1178.

133. Vivès, E.; Brodin, P.; Lebleu, B. A Truncated HIV-1 Tat Protein Basic Domain Rapidly Translocates through the Plasma Membrane and Accumulates in the Cell Nucleus. *J. Biol. Chem.* **1997**, *272*, 16010–16017. https://doi.org/10.1074/jbc.272.25.16010.

134. Brock, R. The Uptake of Arginine-Rich Cell-Penetrating Peptides: Putting the Puzzle Together. *Bioconjugate Chem.* **2014**, *25*, 863–868. https://doi.org/10.1021/bc500017t.

135. Bechara, C.; Sagan, S. Cell-Penetrating Peptides: 20 Years Later, Where Do We Stand? *FEBS Lett.* **2013**, *587*, 1693–1702. https://doi.org/10.1016/j.febslet.2013.04.031.

136. Mäe, M.; Langel, U. Cell-Penetrating Peptides as Vectors for Peptide, Protein and Oligonucleotide Delivery. *Curr. Opin. Pharmacol.* **2006**, *6*, 509–514. https://doi.org/10.1016/j.coph.2006.04.004.

137. Trabulo, S.; Cardoso, A. L.; Mano, M.; De Lima, M. C. P. Cell-Penetrating Peptides-Mechanisms of Cellular Uptake and Generation of Delivery Systems. *Pharmaceuticals* **2010**, *3*, 961–993. https://doi.org/10.3390/ph3040961.

138. Madani, F.; Lindberg, S.; Langel, U.; Futaki, S.; Gräslund, A. Mechanisms of Cellular Uptake of Cell-Penetrating Peptides. *J. Biophys.* **2011**, *2011*, 414729. https://doi.org/10.1155/2011/414729.

139. Jiao, C.-Y.; Delaroche, D.; Burlina, F.; Alves, I. D.; Chassaing, G.; Sagan, S. Translocation and Endocytosis for Cell-Penetrating Peptide Internalization. *J. Biol. Chem.* **2009**, *284*, 33957–33965. https://doi.org/10.1074/jbc.M109.056309.

140. Järver, P.; Mäger, I.; Langel, Ü. In Vivo Biodistribution and Efficacy of Peptide Mediated Delivery. *Trends Pharmacol. Sci.* **2010**, *31*, 528–535. https://doi.org/10.1016/j.tips.2010.07.006.

141. Erazo-Oliveras, A.; Muthukrishnan, N.; Baker, R.; Wang, T.-Y.; Pellois, J.-P. Improving the Endosomal Escape of Cell-Penetrating Peptides and Their Cargos: Strategies and Challenges. *Pharmaceuticals* **2012**, *5*, 1177–1209. https://doi.org/10.3390/ph5111177.

142. Gu, Z.; Biswas, A.; Zhao, M.; Tang, Y. Tailoring Nanocarriers for Intracellular Protein Delivery. *Chem. Soc. Rev.* **2011**, *40*, 3638–3655. https://doi.org/10.1039/c0cs00227e.

143. Rautio, J.; Kumpulainen, H.; Heimbach, T.; Oliyai, R.; Oh, D.; Järvinen, T.; Savolainen, J. Prodrugs: Design and Clinical Applications. *Nat. Rev. Drug Discov.* **2008**, *7*, 255–270. https://doi.org/10.1038/nrd2468.

144. Liederer, B. M.; Borchardt, R. T. Enzymes Involved in the Bioconversion of Ester-Based Prodrugs. *J. Pharm. Sci.* **2006**, *95*, 1177–1195. https://doi.org/10.1002/jps.20542.

145. Thompson, D. B.; Cronican, J. J.; Liu, D. R. Engineering and Identifying Supercharged Proteins for Macromolecule Delivery into Mammalian Cells. *Methods Enzymol.* **2012**, *503*, 293–319. https://doi.org/10.1016/B978-0-12-396962-0.00012-4.

146. Mommaerts, W. F. H. M.; Neurath, H. Insulin Methyl Ester. I. Preparation and Properties. *J. Biol. Chem.* **1950**, *185*, 909–917.

147. Fraenkel-Conrat, H.; Olcott, H. S. Esterification of Proteins with Alcohols of Low Molecular Weight. *J. Biol. Chem.* **1945**, *161*, 259–268.

148. Yadav, A.; Pandey, S. Densities and Viscosities of (Choline Chloride + Urea) Deep Eutectic Solvent and Its Aqueous Mixtures in the Temperature Range 293.15 K to 363.15 K. *J. Chem. Eng. Data* **2014**, *59*, 2221–2229. https://doi.org/10.1021/je5001796.

149. Mix, K. A.; Raines, R. T. Optimized Diazo Scaffold for Protein Esterification. *Org. Lett.* **2015**, *17*, 2358–2361. https://doi.org/10.1021/acs.orglett.5b00840.

150. Valeur, E.; Bradley, M. Amide Bond Formation: Beyond the Myth of Coupling Reagents. *Chem. Soc. Rev.* **2009**, *38*, 606–631. https://doi.org/10.1039/B701677H.

151. Liu, J.; Gaj, T.; Patterson, J. T.; Sirk, S. J.; Barbas, C. F. Cell-Penetrating Peptide-Mediated Delivery of TALEN Proteins via Bioconjugation for Genome Engineering. *PLoS ONE* **2014**, *9*, e85755. https://doi.org/10.1371/journal.pone.0085755.

152. Guterstam, P.; Madani, F.; Hirose, H.; Takeuchi, T.; Futaki, S.; El Andaloussi, S.; Gräslund, A.; Langel, U. Elucidating Cell-Penetrating Peptide Mechanisms of Action for Membrane Interaction, Cellular Uptake, and Translocation Utilizing the Hydrophobic Counter-Anion Pyrenebutyrate. *Biochim. Biophys. Acta* **2009**, *1788*, 2509–2517. https://doi.org/10.1016/j.bbamem.2009.09.014.

153. Kristensen, M.; Birch, D.; Mørck Nielsen, H. Applications and Challenges for Use of Cell-Penetrating Peptides as Delivery Vectors for Peptide and Protein Cargos. *Int. J. Mol. Sci.* **2016**, *17*. https://doi.org/10.3390/ijms17020185.

154. Yan, M.; Du, J.; Gu, Z.; Liang, M.; Hu, Y.; Zhang, W.; Priceman, S.; Wu, L.; Zhou, Z. H.; Liu, Z.; et al. A Novel Intracellular Protein Delivery Platform Based on Single-Protein Nanocapsules. *Nat. Nanotechnol.* **2010**, *5*, 48–53. https://doi.org/10.1038/nnano.2009.341.

155. Liu, Y.; Du, J.; Yan, M.; Lau, M. Y.; Hu, J.; Han, H.; Yang, O. O.; Liang, S.; Wei, W.; Wang, H.; et al. Biomimetic Enzyme Nanocomplexes and Their Use as

Antidotes and Preventive Measures for Alcohol Intoxication. *Nat. Nanotechnol.* **2013**, *8*, 187–192. https://doi.org/10.1038/nnano.2012.264.

156. Wei, W.; Du, J.; Yan, M.; Hu, Z.; Lu, Y. Thermo-Responsive Protein Nanocapsules for Effective Enzyme Recycling and Delivery. *J. Control. Release* **2013**, *172*, e115–e116. https://doi.org/10.1016/j.jconrel.2013.08.277.

157. Gu, Z.; Biswas, A.; Joo, K.-I.; Hu, B.; Wang, P.; Tang, Y. Probing Protease Activity by Single-Fluorescent-Protein Nanocapsules. *ChemComm* **2010**, *46*, 6467–6469. https://doi.org/10.1039/c0cc01439g.

158. Ye, Y.; Yu, J.; Gu, Z. Versatile Protein Nanogels Prepared by In Situ Polymerization. *Macromol. Chem. Phys.* **2016**, *217*, 333–343. https://doi.org/10.1002/macp.201500296.

159. Pisal, D. S.; Kosloski, M. P.; Balu-Iyer, S. V. Delivery of Therapeutic Proteins. *J. Pharm. Sci.* **2010**, *99*, 2557–2575. https://doi.org/10.1002/jps.22054.

160. Li, J.; Zhang, L.; Liu, Y.; Wen, J.; Wu, D.; Xu, D.; Segura, T.; Jin, J.; Lu, Y.; Wang, H. An Intracellular Protein Delivery Platform Based on Glutathione-Responsive Protein Nanocapsules. *ChemComm* **2016**, *52*, 13608–13611. https://doi.org/10.1039/c6cc05099a.

161. Saito, G.; Swanson, J. A.; Lee, K.-D. Drug Delivery Strategy Utilizing Conjugation via Reversible Disulfide Linkages: Role and Site of Cellular Reducing Activities. *Adv. Drug Deliv. Rev.* **2003**, *55*, 199–215. https://doi.org/10.1016/S0169-409X(02)00179-5.

162. Alouane, A.; Labruère, R.; Le Saux, T.; Schmidt, F.; Jullien, L. Self-Immolative Spacers: Kinetic Aspects, Structure-Property Relationships, and Applications. *Angew. Chem.* **2015**, *54*, 7492–7509. https://doi.org/10.1002/anie.201500088.

163. Jones, L. R.; Goun, E. A.; Shinde, R.; Rothbard, J. B.; Contag, C. H.; Wender, P. A. Releasable Luciferin-Transporter Conjugates: Tools for the Real-Time Analysis of Cellular Uptake and Release. *J. Am. Chem. Soc.* **2006**, *128*, 6526–6527. https://doi.org/10.1021/ja0586283.

164. Pires, M. M.; Chmielewski, J. Fluorescence Imaging of Cellular Glutathione Using a Latent Rhodamine. *Org. Lett.* **2008**, *10*, 837–840. https://doi.org/10.1021/ol702769n.

165. Dubikovskaya, E. A.; Thorne, S. H.; Pillow, T. H.; Contag, C. H.; Wender, P. A. Overcoming Multidrug Resistance of Small-Molecule Therapeutics through Conjugation with Releasable Octaarginine Transporters. *Proc. Natl. Acad. Sci. U.S.A.* **2008**, *105*, 12128–12133. https://doi.org/10.1073/pnas.0805374105.

166. Blencowe, C. A.; Russell, A. T.; Greco, F.; Hayes, W.; Thornthwaite, D. W. Self-Immolative Linkers in Polymeric Delivery Systems. *Polym. Chem.* **2011**, *2*, 773–790. https://doi.org/10.1039/C0PY00324G.

167. Siedler, F.; Weyher, E.; Moroder, L. Cysteine Racemization in Peptide Synthesis: A New and Easy Detection Method. *J. Pept. Sci.* **1996**, *2*, 271–275. https://doi.org/10.1002/psc.83.

168. Han, Y.; Albericio, F.; Barany, G. Occurrence and Minimization of Cysteine Racemization during Stepwise Solid-Phase Peptide Synthesis(1)(,)(2). *J. Org. Chem.* **1997**, *62*, 4307–4312. https://doi.org/10.1021/jo9622744.

169. Ellman, G. L. Tissue Sulfhydryl Groups. *Arch. Biochem. Biophys.* **1959**, *82*, 70–77. https://doi.org/10.1016/0003-9861(59)90090-6.

VITA

Bhagyesh R. Sarode was born on 21st February 1990 in Palghar, India. He completed his high school education at Aryan High School in Palghar, India. He completed his higher secondary education at the D. G. Ruparel College of Arts, Science and Commerce in Mumbai, India. Most recently, he obtained a Bachelor of Pharmacy from the Institute of Chemical Technology in Mumbai, India.

He joined the University of Missouri Kansas City in 2012 to pursue an interdisciplinary doctoral degree in pharmaceutical sciences in the laboratory of Professor Simon H. Friedman. Upon completion of his degree requirements, Mr. Bhagyesh plans to continue his career in life sciences and to pursue further research interests.